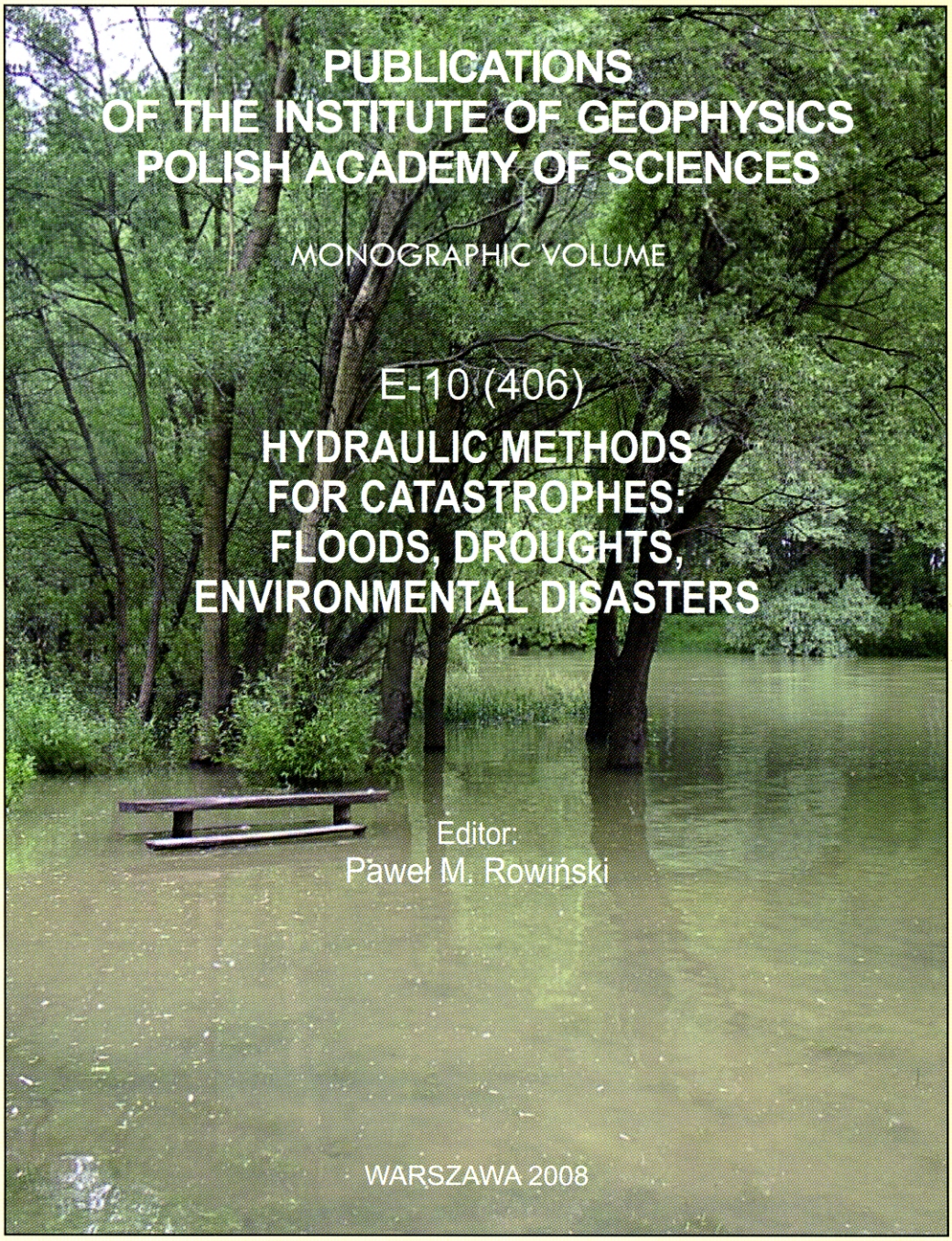
PUBLICATIONS
OF THE INSTITUTE OF GEOPHYSICS
POLISH ACADEMY OF SCIENCES
MONOGRAPHIC VOLUME
E-10 (406)
HYDRAULIC METHODS
FOR CATASTROPHES:
FLOODS, DROUGHTS,
ENVIRONMENTAL DISASTERS
Editor:
Paweł M. Rowiński
WARSZAWA 2008

INSTITUTE OF GEOPHYSICS
POLISH ACADEMY OF SCIENCES

PUBLICATIONS OF THE INSTITUTE OF GEOPHYSICS POLISH ACADEMY OF SCIENCES

MONOGRAPHIC VOLUME

E-10 (406)
HYDRAULIC METHODS FOR CATASTROPHES: FLOODS, DROUGHTS, ENVIRONMENTAL DISASTERS

Editor:
Paweł M. Rowiński

WARSZAWA 2008

Editorial Office
Instytut Geofizyki Polskiej Akademii Nauk
ul. Księcia Janusza 64, 01-452 Warszawa, Poland

SUBSCRIPTION
Subscription orders should be addressed directly to the Editorial Office.
The list of issues to be published in 2008 is on the inside back cover.

Circulation: 200 copies

ISBN-978-83-88765-79-7 ISSN-0138-0133

Camera ready copy prepared by:
Dział Infromacji i Wydawnictw Naukowych, Instytutu Geofizyki PAN
Printed and bound by:
PPH Remigraf sp. z o.o., Ratuszowa 11, 03-450 Warszawa

PUBLS. INST. GEOPHYS. POL. ACAD. SC., E-10 (406), 2008

Hydraulic Methods for Catastrophes: Floods, Droughts, Environmental Disasters

Preface

Paweł M. ROWIŃSKI

Institute of Geophysics Polish Academy of Sciences
Ks. Janusza 64, 01-452 Warszawa, Poland
e-mail: pawelr@igf.edu.pl

The overall theme of the 28th School of Hydraulics was **Hydraulic Methods For Catastrophes: Floods, Droughts, Environmental Disasters**. Most of the presentations were therefore devoted to a variety of problems that may contribute to increase our knowledge in the description or prediction of extreme situations that we deal with in aquatic environment and where hydraulic methods offer important solutions. All the papers presented during the School (after thorough review procedure) are presented in this volume.

Four keynote lectures were delivered during the event. Professor Gareth Pender from Heriot-Watt University from Edinburgh, UK, gave a talk on the developments in flood plain inundation modelling. His brilliant talk was devoted to flood risk management on a Scottish national scale. One of the discussed aspects was flooding in urban areas causing considerable economic and social losses. That problem was also a subject of another talk of Professor Wojciech Majewski from the Institute of Meteorology and Water Management discussed from the perspective of an important Polish harbour city of Gdańsk. Professor Jarosław Napiórkowski from the Institute of Geophysics of the Polish Academy of Sciences considered the question whether natural and artificial flood impulses sustain high level of biodiversity in inundated river terraces. Doctor Jochen Aberle from the Technical University of Braunschweig from Germany and the Secretary of Hydraulic Instrumentation Section of IAHR gave an excellent overview of measurement techniques for the estimation of cohesive sediment erosion, particularly pronounced during a flood event.

The 28th International School of Hydraulics took place at the Podewils Castle in a small town of Krąg, the largest 15th century Knight's Castle in Pomerania, the only castle on water in Poland. It is an unusually picturesque building set in ornamental grounds and is counted among the most interesting and beautiful ancient buildings in Europe. That fantastic surrounding created an unforgettable atmosphere of the meeting. A tradition of the schools of hydraulics is also a study tour and this time it was the tour along the River Słupia offering extremely favourable conditions for power industry. Research on the use of the rivers' energy was carried out as early as in the middle of 19th century in that area and the conference participants could admire the original, old-fashioned machines and facilities, carefully maintained and tended, which are still working in the still existing hydro power stations.

I wish to take this opportunity to express my appreciation to the members of the Scientific Committee, namely Professors Włodzimierz Czernuszenko, Janusz Kubrak, Wojciech Majewski, Marek Mitosek, Jarosław Napiórkowski and Romuald Szymkiewicz, for their contributions to the technical program and thorough review of all the papers. All the organization of the School was coordinated by Monika Kalinowska, Anna Łukanowska and Anna Zdunek, and I wish to thank for their unfailing support which ensured the success of the meeting. I would also like to acknowledge the financial support provided by the Institute of Geophysics of the Polish Academy of Sciences and the Committee of Water Resources Management of the Polish Academy of Sciences and the Brewery Company *Kompania Piwowarska*. This year school was carried out under the auspices of the Committee for Water Resources Management of the Polish Academy of Sciences and the International Association of Hydraulic Engineering and Research (IAHR).

PUBLS. INST. GEOPHYS. POL. ACAD. SC., E-10 (406), 2008

Measurement Techniques for the Estimation of Cohesive Sediment Erosion

Jochen ABERLE

Leichtweiß-Institut für Wasserbau
Beethovenstr. 51a, 38106 Braunschweig, Germany
e-mail: j.aberle@tu-bs.de

Abstract

This paper provides an overview on measurement techniques related to cohesive sediment erosion. Important hydraulic parameters governing the erosion potential of cohesive sediments are defined and methods for the determination of these parameters in field studies are discussed. An overview over the available in situ technology is given. For this purpose, the in situ instruments are classified in recirculating flumes, straight flow-through flumes, and miscellaneous devices. Hydraulic working principles, advantages and disadvantages of the devices are described. Results of recent comparative studies are summarized.

1. Introduction

The dynamical behavior of cohesive sediments is an important issue for many hydraulic engineering applications such as the estimation of erosion and sedimentation in aquatic environments and artificial water bodies. This issue is also important for ecological and environmental applications, since cohesive sediments may affect the health of aquatic ecosystems by degrading water clarity, smothering benthic communities, and acting as a secondary source of pollution. For example, during floods or other natural or artificial re-suspension events, contaminated sediment particles may be mobilized and released into the water phase, affecting water quality and the ecosystem. Thus, the understanding of cohesive sediment erodibility is a prerequisite for the development of sustainable management strategies for both fresh- and saltwater environments.

The erosive potential of cohesive sediments is governed by the interaction between the cohesive strength of the sediment bed and the acting fluid force. Thus, compared to sand dynamics, cohesive sediment dynamics are much more complicated due to the complexity of relevant physical, chemical, and biological processes and their

spatial and temporal variability. For example, Berlamont *et al*. (1993) proposed a list of 28 parameters for the characterization of cohesive sediments. A significant proportion of the current knowledge on the erosion potential of mud has been gained from laboratory studies (Black and Paterson 1997). However, laboratory studies have the significant shortcoming that physical, chemical, and biological/microbiological sediment properties cannot be simulated accurately (e.g., Young and Southard 1978, Amos *et al*. 1992a, Widdows *et al*. 1998, Paterson and Black 1999, Black *et al*. 2002). Testing field sediment samples in laboratory experiments is also not a complete solution to the problem as during sampling and transportation from the field to the laboratory the properties of the samples may be significantly changed. Thus, the application of laboratory results for field assessments, computer modeling, and/or theoretical developments is often not appropriate. In contrast, the data required for such tasks should be collected directly in the field over undisturbed beds (Black and Paterson 1997).

The objective of this paper is to provide an overview on measurement techniques and hydraulic instrumentation related to cohesive sediment erosion. In a first step, important hydraulic parameters governing the erosion potential of cohesive sediments are defined and methods for the determination of these parameters in field studies are discussed. Then, the state-of-the-art in situ technology is broadly reviewed and results from comparative studies found in the literature are presented. Finally, limitations and needs for further studies are discussed. It is worth mentioning that it is not the scope to provide detailed comments on the influence of biological and chemical parameters on cohesive sediment erosion – a review on this topic can be found in Paterson and Black (1999) and Black *et al*. (2002).

2. Background

The main purpose of investigations related to cohesive sediment erosion is the determination of the critical erosive shear stress and erosion rates. The physical processes governing cohesive sediment erosion provide the basis for the development and application of adequate methods and instruments.

2.1 Erosion rate

The surface erosion rate E is defined as the mass of sediment eroded per unit bed area per unit time and it is related to the temporal change in bed elevation, dz/dt, as:

$$E = -\rho_d(z)\frac{dz}{dt} \tag{1}$$

where z = bed elevation with an arbitrary origin (positive upwards), t = time, and ρ_d = dry bulk density of bed material (e.g., Mehta and Partheniades 1982). Alternatively, E can be estimated considering the sediment flux from a defined bed section. The sediment flux consists of two components, resuspension rate E_R and bed load rate E_B. The first component, E_R, refers to sediments which are directly transported in suspension after being eroded and the second component, E_B, refers to sediments (or aggre-

gates) which move as bed load. Thus, for open systems (i.e., eroded sediments are washed out of the flume and are not accumulated in the erosion channel), the continuity equation for the solid phase can be written according to (Debnath *et al*. 2007):

$$\underbrace{\frac{\partial(HC)}{\partial t} + q\frac{\partial C}{\partial x}}_{E_R} + \underbrace{\frac{\partial q_B}{\partial x}}_{E_B} = \underbrace{-\rho_d(z)\frac{dz}{dt}}_{E} \tag{2}$$

where C = suspended sediment concentration (SSC), H = channel height or flow depth, q = specific water discharge, q_B = specific bed load, and x = longitudinal coordinate along the flow direction positive with an arbitrary origin.

According to Eq. (2), erosion rate can be measured by two independent methods. The first method, related to the right-hand side of Eq. (2), is monitoring the evolution of bed elevation with time. This method requires information on $\rho_d(z)$ which may be obtained from bed samples. A drawback of this method is the limited accuracy of bed monitoring techniques when being applied in muddy environments. Optical systems are influenced by turbidity and acoustic systems need, in general, a sufficient amount of sand in the bed mixture for adequate signal strength, i.e., their applicability in pure muddy environments without any sand in the bed material is restricted. Nonetheless, recent studies showed that such measurements provide new insights into the erosion process of mud-sand mixtures (e.g., Debnath *et al*. 2007, Plew *et al*. 2007).

An alternative approach for the determination of dz/dt in laboratory investigations is the use of special flumes with an open-bottomed test section, through which a coring tube containing the sediment sample can be inserted (e.g., Jepsen *et al*. 1997, Kern *et al*. 1999, Roberts *et al*. 2003). The shear caused by the flow causes sediment erosion in the core and, therefore, the sediments are continually moved upwards during the measurements by an operator so that the sediment-water interface remains level with the flume bottom. Erosion rate is recorded as the upward movement of the sediments in the coring tube. However, a disadvantage of this method is the abrupt change in roughness of the boundary between the flume floor and the sediment core (Roberts *et al*. 2003).

The second method to estimate erosion rate is related to the left hand side of Eq. (2) and consists of sediment flux measurements, i.e., SSC and bed load. So far, the bed load component has been neglected in most cohesive sediment studies as it has often been assumed that fine grained sediments are entrained directly into suspension under most flow conditions. However, recent studies showed that bed load may, in principle, contribute significantly to total erosion (Mitchener and Torfs 1996, Aberle *et al*. 2004, Debnath *et al*. 2007). For example, Mitchener and Torfs (1996) found for mud-sand mixtures that muddy layers are eroded predominantly directly into suspension, whereas sand layers are eroded into bed load. Moreover, for pure cohesive and consolidated beds, large aggregates or lumps of bed material may be transported as bed load. However, direct field measurements of E_B over cohesive beds (in terms of eroded mass) are sophisticated and a satisfying measurement system is not yet available. Therefore, Debnath *et al*. (2007) and Plew *et al*. (2007) used Eq. (2) to estimate the bed load component E_B from measurements of E and E_R.

The erosion rate due to resuspension, E_R, is generally estimated from turbidity measurements using turbidimeters (e.g., Optical Backscatters (OBS) or photodetectors). The corresponding readings are calibrated against SSC, where SSC is usually determined from water samples. Thus, knowing the suspended sediment concentration, flow depth, and flow rate, the resuspension rate E_R can be calculated.

2.2 Experimental procedure and data interpretation

Both in situ and laboratory measurements of cohesive sediment erosion are often based on an experimental procedure in which shear stress is increased stepwise to constant levels during fixed time steps or intervals, usually 10 to 20 min (e.g., Parchure and Mehta 1985, Amos *et al.* 1992a, Aberle *et al*. 2003). During these time intervals, erosion rates are estimated using the aforementioned methods. A typical time series of flow velocity and SSC is displayed in Fig. 1. The figure shows that at the beginning of each experimental step (interval) with an increased flow velocity (and hence bed shear stress), erosion rate is often initially high and then decreases with time. In the literature, such a behavior has been associated with two potential mechanisms: (1) the structure of the (consolidated) bed; and (2) transient hydrodynamic effects. Aberle *et al*. (2006) investigated the significance of transient hydrodynamic effects analyzing velocity data obtained by Acoustic Doppler Velocimeter (ADV) measurements and concluded that these effects can be neglected. Thus, the erosion pattern shown in Fig. 1 is most likely solely due to the structure of the bed (see also Zreik *et al*. 1998, Krone 1999). This becomes also obvious from Eq. (1), in which $\rho_d(z)$ is a significant parameter.

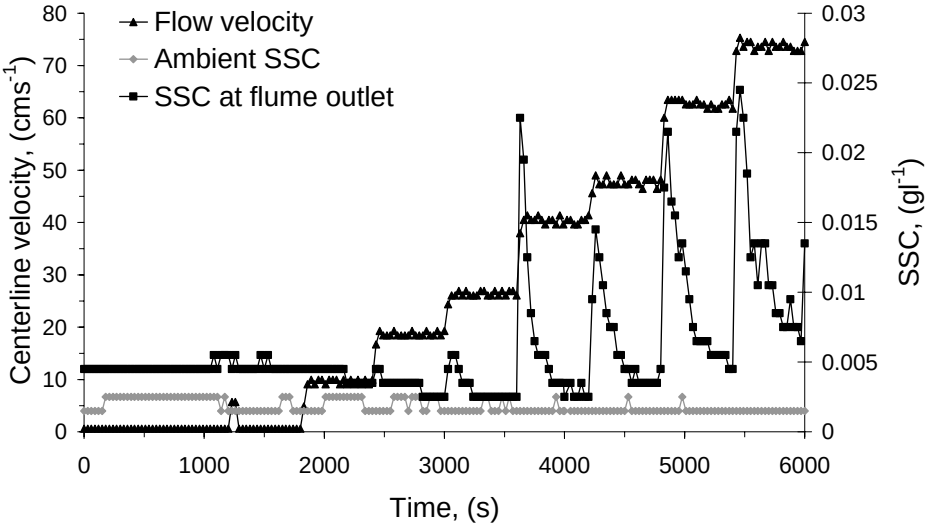

Fig. 1. Time series of the centreline flow velocity in an erosion channel (measured by an Ott-flow meter; triangles), ambient SSC (diamonds), and SSC at the end of the erosion channel (squares) for an experiment carried out in the Styx River near Christchurch, New Zealand. Once the critical threshold for erosion is exceeded, erosion increases sharply at the onset of each velocity level and then decreases.

The erosion process of cohesive beds is often classified using two erosion types (e.g., Paterson and Black 1999). Depth-limited (type I) erosion occurs due to a large vertical gradient in the bed shear strength, which depends on a number of factors such as sediment characteristics, deposition history, and consolidation. In this case, erosion ceases when the bed erodes down to the level where the bed shear strength τ_s within the consolidated bed is in equilibrium with the applied bed shear stress (e.g., erosion event at 3500 s in Fig. 1). After erosion of the upper sediment layer, the initial erosion rate may still be high in further experimental steps, but then erosion rate may reduce and reach a constant value (e.g., erosion event at 4300 s in Fig. 1). In this case the erosion process can be described as sharing features from two erosion types, depth-limited erosion (type I) and steady-state (i.e., constant) erosion, defined as type II erosion. Steady-state erosion (type II) is characterized by a constant erosion rate and is expected for uniform beds when the bed shear strength does not change with sediment depth (e.g., Mehta and Partheniades 1982, Parchure and Mehta 1985, Zreik *et al.* 1998). It is worth mentioning that the shared erosion type shown in Fig. 1 may be an artefact of the experimental procedure, as one may infer that the time duration for each velocity step of 10 min in Fig. 1 is insufficient for the condition $\tau_B = \tau_s$ to be attained (Aberle *et al*. 2006).

The erosion types and associated formulas describing the erosion mechanisms have been introduced to support interpretation of experimental data and to calculate erosion rates from such data. Several formulations have been derived in which erosion rate is described in terms of the excess bed shears stress concept, i.e., erosion occurs as long as bed shear stress is larger than the critical stress at the bed. Using a power law function, this concept can be formulated as:

$$E = M(z)\left(\tau_b - \tau_c(z)\right)^n \tag{3}$$

where $M(z)$ is an empirical erosion constant with its dimension depending on the exponent n, τ_b is the bed shear stress, and $\tau_c(z)$ is the critical bed shear stress for erosion which may vary with depth z (Maa *et al*. 1998, Ravens and Gschwend 1999, Mehta and Parchure 2000).

However, the use of Eq. (3) for determination of erosion rate is not straightforward because both $M(z)$ and τ_c, and a variety of physical, chemical and biological factors influencing them, are unknown functions of sediment depth (Aberle *et al*. 2004). Furthermore, erosion is a highly dynamical process (see Fig. 1) and there is a lack of consistency in the way the various parameters from field deployments are interpreted. For example, in some investigations E is defined as the initial erosion rate after application of a new bed shear stress (e.g., Amos *et al*. 1992a, Maa *et al*. 1998, Houwing 1999), Ravens and Gschwend (1999) define erosion rate as the rate of sediment resuspension after some initial response has passed, while other investigators averaged erosion rates over each velocity step (e.g., Andersen *et al*. 2002). Obviously, such diverse definitions can result in different values for erosion rate from the same experimental data set, aggravating a direct comparison of the experimental results. Sanford and Maa (2001) developed a time dependent solution for Eq. (3) for $n = 1$ and the special case of a step-wise increase of bed shear stress that incorporates both types

of erosion. This solution was used by Aberle *et al*. (2004, 2006) to develop a method for data interpretation from field studies taking into account the time dependency of the erosion process.

2.3 Bed shear stress estimation

Equation (3) shows that bed shear stress is a key parameter in cohesive sediment studies, since it determines erosion rates and erosion rate parameters. However, estimation of bed shear stress during bed erosion is difficult and, therefore, bed shear stress is generally estimated from calibration curves. These curves are obtained under controlled conditions by determining bed shear stress in the erosion channel using hydrodynamic measurements and relating these estimates to bulk properties of the flow such as mean flow velocity or flow rate. Flow velocity in the erosion channel is usually measured by current meters and/or velocimeters or estimated using the equation of continuity (given the flow rate is known). Methods to determine bed shear stress used in cohesive sediment studies range from direct measurements with skin friction probes to indirect estimates using pipe flow laws (e.g., Moody-Diagram), analyses of the vertical velocity profile and/or near bed turbulence properties, and testing quartz sediment samples with a known critical shear stress for incipient motion (i.e., once the particles start moving, the corresponding critical shear stress is related to the applied forcing mechanism of the apparatus). A detailed description of these methods is beyond the scope of this paper and a review on this topic can be found in Rowiński *et al.* (2005).

So far there is no standard procedure available for bed shear stress calibration of in situ devices. Thus, discrepancies in bed shear stress estimates due to these different methods may be interpreted as an important factor which prevents a rigorous comparison of erosion rates. Another important issue is the influence of roughness, turbulence properties, and flow structure on bed shear stress. The use of calibration curves (which were often obtained over well defined surfaces such as wooden beds or sandpaper; e.g., Aberle *et al*. 2003) implies that the roughness of natural cohesive beds is similar to the roughness used during instrument calibration. However, this is not necessarily the case as the roughness of cohesive beds can be quite variable (e.g., Black and Paterson 1997). Besides, Debnath *et al.* (2007) showed that bed roughness may change significantly during erosion and, therefore, τ_b does not necessarily follow calibration curves.

The influence of turbulence properties on bed shear stress is related to the fact, that most erosion devices are closed conduits and, therefore, the size of the turbulent eddies is not comparable to the eddy-sizes observed under natural flow conditions (Rowiński *et al*. 2005). Furthermore, in environments with high SSC, fluid properties may be altered due to large amounts of particles in the fluid (e.g., Wang and Larsen 1994). Another issue is related to the general flow structure. For example, in estuarine or coastal environments oscillatory wave activity may be the key erosion process instead of shear stress imposed by unidirectional flow (Jepsen *et al*. 2004). Last but not least it must be mentioned that secondary currents in flumes may result in a non-uniform shear stress distribution across the erosion channel (e.g., Gust and Müller 1997). Consequences of all these factors on the estimation of erosion rates have not

been investigated in depth yet in cohesive sediment erosion studies, showing that adequate bed shear stress estimation is still an open question.

3. In situ devices

Various in situ instruments have been built since the 1970's to investigate cohesive sediment dynamics. The design of these instruments has been a compromise between various factors, such as costs, portability, number of required operators, duration of erosion tests, required water supply, fluid flow in the instrument, objective of the investigation, required data, etc. (Black and Paterson 1997). In general, the instruments are operated in either submerged or sub-aerial conditions (i.e., open to the air). When being operated in sub-aerial conditions, additional water supply is often required which may limit the use dependent on the deployment site.

A detailed review on in situ technology available until 1997 can be found in Black and Paterson (1997). Since then, various new devices have been developed and it is the scope of this section to provide an updated overview on the existing in situ technology. For this purpose, the existing instruments are subdivided into two groups: (1) benthic flumes; and (2) miscellaneous devices. Benthic flumes, in turn, are subdivided into recirculating and flow-through types. In the following, the basic principles of the instruments are briefly outlined. For detailed information on each device as well as the deployment protocol, the reader is directed to the corresponding source.

3.1 Recirculating in situ flumes

Recirculating in situ flumes are parallel-walled rectangular channels with either an annular or race-way plan view (see Table 1). When deployed, a skirt or flange around the outer walls prevents penetration of the flume into the bed. Recirculating flumes are closed systems and as erosion proceeds the water inside the flume gradually becomes saturated with suspended sediments. Therefore, the change of concentration C with time t is always non-negative ($dC/dt > 0$) unless sediment deposition occurs or water infiltrates from outside the device.

Table 1

Recirculating in situ flumes

Source	Shape	Instrument name	Use
Peirce *et al*. (1970)	annular	–	sub-aerial
Nowell *et al*. (1985)	race-way	SEADUCT	submerged
Amos *et al*. (1992b)	annular	Sea Carousel	submerged
Houwing and van Rijn (1992)	race-way	ISEF	sub-aerial
Maa *et al*. (1993, 1995)	annular	VIMS Sea Carousel	submerged
Black and Cramp (1995)	race-way	–	sub-aerial
Widdows *et al*. (1998)	annular	PML in situ AF	sub-aerial
Thompson and Amos (2002)	annular	AMF	sub-aerial
Bale *et al*. (2006)	annular	PML MAF	sub-aerial

In annular devices, the channel floor is formed by the natural sediment and the eroding flow is driven by different methods, such as a rotating lid (e.g., Maa *et al*. 1993, Widdows *et al.* 1998), a rotating lid with paddles (e.g., Amos *et al*. 1992, Thompson and Amos 2002, Bale *et al.* 2006), or by paddles (e.g., Peirce *et al*. 1970). An advantage of the annular shape is that the "infinite" flow length results in a fully developed boundary layer. Hence, bed shear stress can be estimated from measured velocity profiles using the logarithmic formula. However, this advantage is offset by inherent secondary currents causing a non-uniform shear stress distribution across the channel. It is worth mentioning that, in laboratory investigations, the effect of secondary currents can be minimized by counter-rotating the outer channel-wall (e.g., Krishnappan 1993, Schweim 2005).

In contrast to the annular geometry, race-way shaped flumes have a relatively long straight open-bottomed test section connected to short high-curvature sections leading to and from a return flow channel with a fixed bed. Race-way flumes are oriented horizontally (Black and Cramp 1995) or vertically (Nowell *et al*. 1985, Houwing and van Rijn 1998) and the flow is driven by a propeller (Black and Cramp 1995), paddles (Houwing and van Rijn 1998), or a pump (Nowell *et al*. 1985). Hence, unlike in annular flumes, suspended flocs in the water column may be broken by the flow driving system. Although it is assumed that the racetrack shape reduces the magnitude of the secondary currents, the boundary layer may not be fully developed in the test section (Houwing and van Rijn 1998).

3.2 Straight benthic flow through flumes

Flow-through flumes, summarized in Table 2, are designed as straight canals or conduits with an open bottom. Most devices consist of a contracting, open-mouthed entrance section, a straight erosion section, and a straight fixed-bed section. They are enclosed by an upper lid or open to the air when used in submerged or sub-aerial conditions, respectively. Similar to recirculating flumes, a skirt or flange around the outer walls prevents penetration of the flume into the bed. Flow-through flumes are open systems and the eroded sediment is lost at the flume outlet. Thus, when erosion ceases SSC decreases and in contrast to recirculating flumes, both $dC/dt < 0$ and $dC/dt > 0$ are possible.

The flow in straight flumes is driven by propellers (Scoffin 1968, Hawley 1991, Aberle *et al*. 2003, Debnath *et al*. 2007, Plew *et al*. 2007), pumps (Young 1977, Manzenrieder 1983, Gust and Morris 1989, Ravens and Gschwend 1999, Krishnappan and Droppo 2006) or by gravity (sub-aerial devices of Grissinger *et al*. 1981, Cowgill 1994). In flumes where water is sucked through the channel, the entrance section is usually designed to be similar to that of a wind tunnel to smooth out entrance effects. As an example for a straight flow-through flume the NIWA in situ flume I, described in detail by Aberle *et al*. (2003), is shown in Fig. 2.

Due to the straight erosion section, effects of secondary currents are assumed to be minimal in straight flumes. On the other hand, straight flow-through flumes are often criticized because the boundary layer may not be fully developed in the test section, which may introduce significant uncertainties in bed shear stress estimates using the logarithmic formula. However, Young and Southard (1978) and Ravens and

Gschwend (1999) pointed out that this effect was not crucial in their studies. The requirement of a fully developed logarithmic profile for estimating the bed shear stresses can be avoided either by using stress probes (Gust and Morris 1989) or by measuring near-bed turbulence parameters (e.g., Aberle *et al*. 2003, Debnath *et al*. 2007).

Table 2
Straight flow through flumes

Source	Name	Use
Scoffin (1968) Neumann *et al*. (1970)	Underwater flume	submerged
Young (1977) Young and Southard (1978)	SEAFLUME	submerged
Grissinger *et al*. (1981)[1]	Portable flume	sub-aerial
Manzenrieder (1983)	Strömungskanal	sub-aerial
Gust and Morris (1989)	SEAFLUME	submerged
Hawley (1991)	–	submerged
Cowgill (1994)[1]	–	sub-aerial
Ravens and Gschwend (1999)	FLUME	submerged
Westrich and Schmid (2003)	EROMOB	submerged
Aberle *et al*. (2003)	NIWA in situ flume I	submerged
Krishnappan and Droppo (2006)		submerged
Debnath *et al*. (2007)	NIWA in situ flume II	submerged
Plew *et al*. (2007)	NIWA in situ flume III	submerged

[1] described in Black and Paterson (1997)

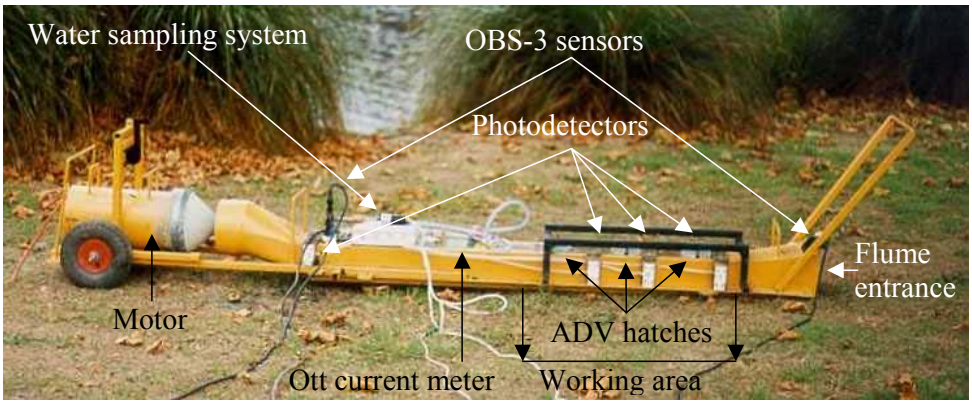

Fig. 2. The NIWA in situ flume I. The flume has been designed as a straight benthic flow-through flume and is equipped with OBS-3 sensors, photodetectors, an Ott current meter, and a water sampling system. Special ADV-hatches allow for ADV calibration measurements inside of the flume. Note that the wheels are uplifted during operation; handles and frames attached to the flume are removable. For a description of the operation of the flume refer to Aberle *et al*. (2003).

3.3 Miscellaneous devices

Miscellaneous devices, summarized in Table 3, are mostly based on alternative methods of assessing the potential for erosion of cohesive beds rather than erosion caused by flowing water. The used methods comprise erosion due to vertical jets (Paterson 1989), vertically oscillating grids (Tsai and Lick 1986, PES), rotating flows in small cylinders (Gust 1991, Schünemann and Kühl 1991), shear strength testing using a shear pad (which is a field-modification of a standard uniaxial shear test instrument; Faas *et al*. 1992), or an erosion bell (Williamson and Ockenden 1996, and SedErode), and shear vane testing (Bassoullet and Le Hir 2007). The footprint of these devices is generally much smaller than the footprint of benthic flumes.

Table 3

Miscellaneous devices

Source	Name	Method
Faas *et al*. (1992)	INSIST	shear pad
Tsai and Lick (1986)	Shaker	oscillating grid
Paterson (1989); Vardy *et al*. (2007) Tolhurst *et al*. (1999)	CSM	vertical jet
Schünemann and Kühl (1991)	EROMES	rotating flow
Gust (1991)	Microcosm	rotating flow
Williamson and Ockenden (1996)	ISIS	erosion bell
Delft Hydraulics[1]	PES	oscillating grid
HR Wallingford[2]	SedErode	erosion bell
Bassoullet and Le Hir (2007)	–	shear vane

[1] described in Cornelisse *et al*. (1997); [2] described in Tolhurst *et al.* (2000)

4. Comparative studies

The listed in situ technology in Tables 1-3 reveals that an abundance of unique instruments has been developed with different operation principles, geometries, and test-section sizes. Bearing in mind the known limitations related to data acquisition and interpretation as well as the problems faced in the field during deployments, surprisingly few comparative studies have been carried out until today. Relevant comparisons, where different instruments have been applied simultaneously over the same sediment, are described by Cornelisse *et al*. (1997), Tolhurst *et al*. (2000) and Widdows *et al.* (2007).

Cornelisse *et al*. (1997) used a kaolinite bed over which PES, EROMES, ISIS, and ISEF were tested (see Table 1 and 3). The results of the tests with these devices were also compared to data obtained in an annular laboratory flume. This comparison showed that all instruments were able to establish an accurate and reproducible value for critical shear stress but that estimates of erosion rate parameters varied significantly, which was partly associated with spatial and temporal variations of bed shear stress

and bed strength. Therefore, Cornelisse *et al*. (1997) concluded that the error in measured erosion rate is mainly related to footprint size of the instruments.

Tolhurst *et al.* (2000) compared Microcosm, ISEF, SedErode, and CSM (see Table 1 and 3) in a natural environment and found that erosion threshold was relatively comparable between these devices. On the other hand, Tolhurst *et al*. (2000) found that erosion rate estimates were not comparable between the different devices, confirming the findings of Cornelisse *et al*. (1997). This fact was attributed to fundamental differences between the erosion devices (e.g., flow structure, bed-shear stress calibration, etc.) as well as to deployment time, and instrument size.

Widdows *et al*. (2007) compared five erosion devices (PML in situ AF, PML MAF, AMF, CSM, and EROMES; see Table 1 and 3) and found good agreement between similar erosion devices (e.g., annular flumes). On the other hand, they identified significant differences comparing the three investigated basic types of erosion devices, confirming again the studies of Cornelisse *et al*. (1997) and Tolhurst *et al*. (2000). Widdows *et al*. (2007) concluded that the main cause of the observed differences is the manner in which the shear stress is applied to the bed. In this context, Debnath *et al*. (2007) found that data obtained from two similar straight flumes deployed at identical locations were comparable, although a time period of three years separated the two measurement series.

5. Summary and conclusions

This paper presents an overview of measurement techniques for the estimation of cohesive sediment erosion. Based on the definition of the surface erosion rate E, relevant physical parameters were identified and methods for their determination briefly described. As several studies have shown that the application of laboratory results for field assessments, computer modeling, and/or theoretical developments is often not appropriate, the main focus was set on a review and summary of existing in situ erosion devices. The influence of biological and chemical parameters on cohesive sediment erosion was not addressed specifically, since the scope of the paper was related to hydraulic instrumentation.

The review of the existing in situ instruments revealed that an abundance of devices exists (thirty of them are listed in this paper) which can be broadly subdivided into benthic flumes and miscellaneous devices. Each device is a unique piece of equipment which was developed according to specific needs and boundary conditions. This means that each individual instrument has its specific advantages and disadvantages and, hence, it is not possible to evaluate which instrument is best. Nonetheless, within the last years the instruments have been steadily improved on the basis of experiences from previous investigations. One such example is the development of the NIWA in situ flumes (see Table 2). The latest prototype, described in Plew *et al*. (2007), may now be used in deeper waters, is lighter, better equipped, and easier to handle than its antecessors.

Comparative studies between different instruments revealed that instruments based on the same principle of operation yield similar results for critical shear stresses and erosion rates. On the other hand, erosion rates obtained with devices based on

different working principles are not directly comparable. In the literature, this has been associated with different factors such as footprint size, mode of bed shear stress application, bed shear stress calibration, etc. It is interesting to note that a direct comparison of a straight in situ flow-through flume with recirculating flumes and/or miscellaneous devices has not yet been carried out under field conditions. This is somewhat surprising, as several types of straight flow-through flumes exist. Thus, to gain more insight into the performance of such instruments and to explore the comparability of the results of the abundance of studies related to cohesive sediment erosion found in the literature, such a comparison would be desirable. Last but not least, it would also be desirable to compare the results of in situ devices with data from specifically designed large scale field experiments in canals or rivers, where hydraulic parameters and erosion are directly assessed during a flood event. Although this is a challenging task, such data should provide further insight into the erosion processes of cohesive beds.

Acknowledgements. This paper is a result of a collaborative effort of the Hydraulic Instrumentation Section of the International Association for Hydraulic Engineering and Research with the International School of Hydraulics.

References

Aberle, J., V. Nikora, S. McLean, C. Doscher, I. McEwan, M. Green, D. Goring, and J. Walsh (2003), Straight benthic flow-through flume for in situ measurement of cohesive sediment dynamics, *J. Hydraul. Eng.* **129**, 1, 63-67.

Aberle, J., V. Nikora, and R. Walters (2004), Effects of bed material properties on cohesive sediment erosion, *Mar. Geol.* **207**, 83-93.

Aberle, J., V. Nikora, and R. Walters (2006), Data interpretation for in situ measurements of cohesive sediment erosion, *J. Hydraul. Eng.* **132**, 6, 581-588.

Amos, C.L., G.R. Daborn, H.A. Christian, A. Atkinson, and A. Robertson (1992a), In situ erosion measurements on fine-grained sediments from the Bay of Fundy, *Mar. Geol.* **108**, 175-196.

Amos, C.L., J. Grant, G.R. Daborn, and K. Black (1992), Sea Carousel – a benthic, annular flume, *Estuar. Coast. Shelf Sci.* **34**, 557-577.

Andersen, T.J., E.-J. Houwing, and M. Pejrup (2002), On the erodibility of fine-grained sediments in an infilling freshwater system. **In:** J.C. Winterwerp, and C. Kranenburg (eds.), *Fine Sediment Dynamics in the Marine Environment*, Elsevier, 315-328.

Bale, A.J., J. Widdows, C.B. Harris, and J.A. Stephens (2006), Measurements of the critical erosion threshold of surface sediments along the Tamar Estuary using a mini-annular flume, *Continent. Shelf Res*., **26**, 1206–1216.

Bassoullet, P., and P. Le Hir (2007), In situ measurements of surficial mud strength: A new vane tester suitable for soft intertidal muds, *Continent Shelf Res* **27**, 1200-1205.

Berlamont, J.E., M.C. Ockenden, E.A. Toorman, and J.C. Winterwerp (1993), The characterisation of cohesive sediment properties, *Coast. Eng.* **21**, 105-128.

Black, K.S., and A. Cramp (1995), A device to examine the in situ response of intertidal cohesive sediment deposits to fluid shear, *Continent Shelf Res.* **15**, 15, 1945-1954.

Black, K.S., and D.M. Paterson (1997), Measurement of the erosion potential of cohesive marine sediments: A review of current in situ technology, *J. Mar. Environ. Eng.* **4**, 43-83.

Black, K.S., T. Tolhurst, D.M. Paterson, and S.E. Hagerthey (2002), Working with natural cohesive sediments, *J. Hydraul. Eng.* **128**, 1, 2-8.

Cornelisse, J.M., H.P.J. Mulder, E.J. Houwing, H.J. Williamson, and G. Witte (1997), On the development of instruments for in situ erosion measurements. **In:** N. Burt, R. Parker, and J. Watts (eds.), *Cohesive Sediments*, John Wiley & Sons Ltd., 175-186.

Cowgill, C.M. (1994), In situ determination of fine grained sediment erodibility, unpublished PhD-thesis, University of Southampton.

Debnath, K., V. Nikora, J. Aberle, B. Westrich, and M. Muste (2007), Erosion of cohesive sediments: Resuspension, bed load, and erosion patterns from field experiments, *J. Hydraul. Eng.* **133**, 5, 508-520.

Faas, R.W., H.A. Christian, and G.R. Daborn (1992), Biological control of mass properties of surficial sediments: an example from Starr's point tidalflat, Minas Basin, Bay of Fundy. **In:** *Nearshore and Estuarine Cohesive Sediment Dynamics*. Springer-Verlag, Berlin, 360-377.

Grissinger, E.H., W.C. Little, and J.B. Murphey (1981), Erodibility of streambank materials of low cohesion, *Transactions ASAE* **24**, 3, 624-630.

Gust, G. (1991), *Fluid Velocity Measurement Instrument*, U.S. Patent No. 4, 986, 122.

Gust, G., and M.J. Morris (1989), Erosion thresholds and entrainment rates of undisturbed in situ sediments, *J. Coast. Res.* **5**, 87-99.

Gust, G., and V. Müller (1997), Interfacial hydrodynamics and entrainment functions of currently used erosion devices. **In:** N. Burt, R. Parker, and J. Watts (eds.), *Cohesive Sediments*, John Wiley & Sons Ltd., 149-174.

Hawley, N. (1991), Preliminary observations of sediment erosion from a bottom resting flume, *J. Great Lake Res.*, **17**, 3, 361-367.

Houwing, E.-J. (1999), Determination of the critical erosion threshold of cohesive sediments on intertidal mudflats along the dutch Wadden Sea coast, *Estuar. Coast. Shelf Sci.* **49**, 545-555.

Houwing, E.-J., and L.C. van Rijn (1998), In situ erosion flume (ISEF): determination of bed-shear stress and erosion of a kaolinite bed, *J. Sea Res.* **39**, 243-253.

Jepsen, R., J. Roberts, and W. Lick (1997), Effects of sediment bulk density on sediment erosion rates, *Water Air Soil Pollut.* **99**, 21-37.

Jepsen, R., J. Roberts, and J. Gailani (2004), Erosion measurements in linear, oscillatory, and combined oscillatory and linear flow regimes, *J. Coast. Res.* **20**, 4, 1096-1101.

Kern, U., I. Haag, V. Schürlein, M. Holzwarth, and B. Westrich (1999), Ein Strömungskanal zur Ermittlung der tiefenabhängigen Erosionsstabilität von Gewässersedimenten: das SETEG-System, *Wasserwirtschaft* **89**, 2, 72-77 (in German).

Krishnappan, B.G. (1993), Rotating circular flume, *J. Hydraul. Eng.* **119**, 6, 758-767.

Krishnappan, B.G., and I.G. Droppo (2006), Use of an in situ erosion flume for measuring stability of sediment deposits in Hamilton Harbour, Canada, *Water Air Soil Pollut.* **6**, 557-567.

Krone, R.B. (1999), Effects of bed structure on erosion of cohesive sediments, *J. Hydraul. Eng.* **125**, 12, 1297-1301.

Maa, J.P.-Y., L.D. Wright, C.-H. Lee, and T.W. Shannon (1993), VIMS Sea Carousel: A field instrument for studying sediment transport, *Mar. Geol.* **115** 271-287.

Maa, J.P.-Y., C.-H. Lee, and F.J. Chen (1995), Bed shear stress measurements for VIMS Sea Carousel, *Mar. Geol.*, **129** 129-136.

Maa, J. P.-Y., L. Sanford, and J.P. Halka (1998), Sediment resuspension characteristics in Baltimore Harbor, Maryland, *Mar. Geol.* **146**, 137-145.

Manzenrieder, H. (1983), Biological stabilization effects on wadden areas from engineering point of view, *Mitt. Leichtweiß-Institut für Wasserbau*, TU Braunschweig, Heft **79**, 135-193.

Mehta, A.J., and E. Partheniades (1982), Resuspension of deposited cohesive sediment beds, *Coastal Engineering*, Cape Town, South Africa, ASCE, Reston, VA, pp. 1569-1588.

Mehta, A.J., and T.M. Parchure (2000), Surface erosion of fine-grained sediment revisited. **In:** B.W. Flemming, and M.T. Delafontaine (eds.), *Muddy Coast Dynamics and Resource Management*, Elsevier, 55-74.

Mitchener, H.J., and H. Torfs (1996), Erosion of mud/sand mixtures, *Coast. Eng.* **29**, 1-25.

Neumann, A.C., C.D. Gebelein, and T.P. Scoffin (1970), The composition, structure and erodability of subtidal mats, Abaco, Bahamas, *J. Sediment. Petrol.* **40**, 1, 274-297.

Nowell, A.R.M., I.N. McCave, and C.D. Hollister (1985), Contributions of Hebble to understanding marine sedimentation, *Mar. Geol.* **66**, 397-409.

Parchure, T.M., and A.J. Mehta (1985), Erosion of soft cohesive sediment deposits, *J. Hydraul. Eng.* **111**, 10, 1308-1326.

Paterson, D.M. (1989), Short-term changes in the erodibility of intertidal cohesive sediments related to the migratory behaviour of epipelic diatoms, *Limnol. Oceanogr.* **34**, 1, 223-234.

Paterson, D.M., and K.S. Black (1999), Water flow, sediment dynamics and benthic biology, *Adv. Ecol. Res.* **29**, 155-193.

Peirce, T.J., R.T. Jarman, and C.N. de Turville (1970), An experimental study of silt scouring, *Proc. Inst. Civ. Eng*. **45**, 231-243.

Plew, D., K. Debnath, J. Aberle, V. Nikora, and G. Cooper (2007), In situ flume for studying cohesive and non-cohesive sediment erosion, *XXXII IAHR Congress, Venice*, Italy, Papers on CD-ROM.

Ravens, T.M., and P.M. Gschwend (1999), Flume measurements of sediment erodibility in Boston Harbor, *J. Hydraul. Eng.* **125**, 10, 998-1005.

Roberts, J.D., R.A. Jepsen, and S.C. James (2003), Measurements of sediment erosion and transport with the adjustable shear stress erosion and transport flume, *J. Hydraul. Eng*. **129**, 11, 862-871.

Rowiński, P.M., J. Aberle, and A. Mazurczyk (2005), Shear velocity estimation in hydraulic research, *Acta Geophys. Pol.* **53**, 4, 567-583.

Sanford, L., and J.P.-Y. Maa (2001), A unified erosion formulation for fine sediments, *Mar. Geol.* **179**, 9-23.

Schünemann, M, and H. Kühl. (1991), A device for erosion-measurements on naturally formed, muddy sediments: The EROMES-System, GKSS Report GKSS 91/E/18, Geesthacht, Germany.

Schweim, C. (2005), *Modellierung und Prognose der Erosion feiner Sedimente*, PhD-thesis, Rheinisch-Westfälisch Technische Hochschule Aachen, Aachen in German.

Scoffin, T.P. (1968), An underwater flume, *J. Sediment. Petrol.* **38**, 244-246.

Thompson, C.E.L., and C.L. Amos (2002), The impact of mobile disarticulated shells of Cerastoderma edulis on the abrasion of a cohesive substrate, *Estuaries* **25**, 2, 204-214

Tolhurst, T.J., K.S. Black, S.A. Shayler, S. Mather, I. Black, K. Baker, and D.M. Paterson (1999), Measuring the in situ erosion shear stress of intertidal sediments with the cohesive strength meter (CSM), *Estuar. Coast. Shelf Sci.* **49**, 281-294.

Tolhurst, T.J., K.S. Black, D.M. Paterson, H.J. Mitchener, G.R. Termaat, and S.A. Shayler (2000), A comparison and measurement standardisation of four in situ devices for determining the erosion shear stress of intertidal sediments, *Continent. Shelf Res.* **20**, 1397-1418.

Tsai, C.-H., and W. Lick (1986), A portable device for measuring sediment resuspension, *J. Great Lakes Res.* **12**, 4, 314-321.

Vardy, S., J.E. Saunders, T.J. Tolhurst, P.A. Davies, and D.M. Paterson (2007), Calibration of the high-pressure cohesive strength meter (CSM), *Continent. Shelf Res.* **27**, 1190-1199.

Wang, Z.Y., and P. Larsen (1994), Turbulent structure of water and clay suspensions with bed load, *J. Hydraul. Eng.* **120**, 5, 577-600.

Westrich, B., and G. Schmid (2003), Development, calibration, and deployment of a mobile in situ sediment erosion testing device, Internal Rep., Univ. of Stuttgart, Institute of Hydraulics, Stuttgart, Germany.

Widdows, J., M.D. Brinsley, N. Bowley, and C. Barret (1998), A benthic annular flume for in situ measurement of suspension feeding/biodeposition rates and erosion potential of intertidal cohesive sediments, *Estuar. Coast. Shelf Sci.* **46**, 27-38.

Widdows, J., P.L. Friend, A.J. Bale, M.D. Brinsley, N.D. Pope, and C.E.L. Thompson (2007), Inter-comparison between five devices for determining erodability of intertidal sediments, *Continent. Shelf Res.* **27**, 1174-1189.

Williamson, H.J., and M.C. Ockenden (1996), ISIS: An instrument for measuring erosion shear stress in situ, *Estuar. Coast. Shelf Sci.* **42**, 1-18.

Young, R.A. (1977), Seaflume: A device for in-situ studies of threshold erosion velocity and erosional behaviour of undisturbed marine muds, *Mar. Geol.* **23**, 11-18.

Young, R.N., and J.B. Southard (1978), Erosion of fine-grained marine sediments: Sea-floor and laboratory experiments, *Geol. Soc. Am. Bull.* **89**, 663-672.

Zreik, D.A., B.G. Krishnappan, J.T. Germaine, O.S. Madsen, and C.C. Ladd (1998), Erosional and mechanical strengths of deposited cohesive sediments, *J. Hydraul. Eng.* **124**, 11, 1076-1085.

Accepted November 13, 2008

PUBLS. INST. GEOPHYS. POL. ACAD. SC., E-10 (406), 2008

Site Verified Contaminant Transport Model as a Mathematical Vehicle for Prevention of the Natural Aquifer Contamination

Andrzej ANISZEWSKI

Szczecin University of Technology
Piastów 50a, 70-310 Szczecin, Poland
e-mail: andrzej.aniszewski@ps.pl

Abstract

To prevent the natural aquifer contamination, the chosen site verification of the practical mathematical model (equation) of conservative contaminant transport in a groundwater stream was presented. This model includes, except of the advection and dispersion processes, the source (negative) term of reversible sorption which can be described by the well-known non-linear Freundlich adsorption isotherm in relation to statics of this process. In this 2D-mathematical model the numerical solution (using the finite difference method) was used, based on the previously calculated values of the longitudinal and transverse dispersion coefficients (D_x, D_y) as well as the non-linear adsorption parameters (K, N). The calculated maximal values of chloride concentrations based on this mathematical model (with and without adsorption term) were compared with the measured chloride concentrations in the piezometers installed in the chosen natural aquifer for the site verification.

1. Introduction

To describe the contaminant concentration fields in a groundwater stream, the practical 2D-model of conservative contaminant transport was worked out in this paper, combining simultaneously advection, dispersion and physical adsorption processes.

To describe the physical adsorption process, the well-known Freundlich non-linear isotherm was accepted, which is widely applied to practice in relation to statics of this process (Chiang 2005, Alvarez 2006).

In the further analysis, based on this presented model (equation), the calculated maximal values of chloride concentrations (with and without adsorption term) were

compared with the measured chloride concentrations in the existing piezometers chosen for the site verification and installed in the natural aquifer.

2. Approach and methods

Concern over the potential for migration of wastes in the subsurface has generated a great deal of interest in the mechanisms responsible for contaminant transport through groundwater systems.

To prevent the deterioration or even catastrophe of groundwater quality, it has become necessary to develop a methodology for description, analyzing, monitoring and predicting (in the form of various mathematical models) the movement of contaminants through the saturated zones (Chiang 2005).

2.1 Description of conservative contaminant transport in groundwater

To describe conservative and passive contaminant transport in groundwater stream incorporating the reversible sorption term, the well-known practical 2D-model was used, resulting from the transport continuity equation (Chiang 2005, Alvarez 2006):

$$\frac{\partial C}{\partial t} + u_x \frac{\partial C}{\partial x} = D_x \frac{\partial^2 C}{\partial x^2} + D_y \frac{\partial^2 C}{\partial y^2} - \frac{\rho}{m} \frac{\partial S}{\partial t}, \tag{1}$$

where: C = the solute concentration in flowing groundwater in aqueous phase (in the local equilibrium conditions); S = the mass of the solute species adsorbed on the grounds per unit bulk dry mass of the porous medium (in the local equilibrium conditions); u_x = component of the average (real) seepage velocity in pore space along the x axis (as pore velocity of groundwater); D_x = component of the longitudinal dispersion coefficient along the x axis; D_y = component of the transverse dispersion coefficient along the y axis; ρ = the bulk density of the porous medium; m = the effective porosity of the porous medium; t = co-ordinate of time; (x, y) = Cartesian co-ordinates of the assumed reference system.

Equation (1) assumes one-dimensional flow of groundwater along the x axis; hence, both the components of the average (real) seepage velocities in pore space ($u_y = u_z = 0$) and the advection terms ($u_y \partial C/\partial y = u_z \partial C/\partial z = 0$) can be neglected.

Assuming also in Eq. (1) the 2D-contaminant transport along the x and y axes, the dispersion term ($D_z \partial^2 C/\partial z^2 = 0$) along the vertical axis z can be treated as negligible, simulating in the further analysis the longitudinal ($D_x \partial^2 C/\partial x^2$) and transverse ($D_y \partial^2 C/\partial y^2$) dispersion of flowing contaminant mass in the aquifer.

The longitudinal and transverse dispersion coefficients (D_x and D_y) which are being considered in Eq. (1), called also the hydrodynamic dispersion coefficients, consist of both the terms representing mechanical dispersion coefficients ($\alpha_L u_x$ and $\alpha_T u_x$) and the effective (modified) molecular diffusion (τD_M) (Chiang 2005).

Thus, the values of hydrodynamic dispersion coefficients take the form:

$$\begin{aligned} D_x &= \alpha_L u_x + \tau D_M \\ D_y &= \alpha_T u_x + \tau D_M \end{aligned} \tag{2}$$

where: (α_L, α_T) = the constants of the longitudinal and the transverse dispersivity along the x and y axes; D_M = the molecular (effective) diffusion coefficient; τ = the dimensionless tortuosity parameter of the porous medium.

The constants of the dispersivity (α_L) and (α_T) depend on the scale (length) of contaminant region (plume) spreading in the aquifer. Detailed description of the dispersivity (α_L) and (α_T), as a macro-dispersion process, is given among other things in (Chiang 2005, Alvarez 2006).

The values of molecular (effective) coefficients (D_M) are generally very low, based on laboratory and site surveys for the various graining (porosity) of the ground media being considered. Thus, in most cases they can be negligible in Eq. (2) for calculations of the hydrodynamic dispersion coefficients (Chiang 2005).

The tortuosity parameter (τ), which expresses the solute mass flow along longer available pathways through the pore space is described in (Zhang 2004).

The ($\partial S/\partial t$) term in Eq. (1) represents generally the negative source term of the reversible sorption (as the adsorption-desorption system) connected with the mass exchange phenomenon, which expresses the relationship $\partial S/\partial t = f(C, S)$ between the mass of the solute species adsorbed on the grounds per unit bulk dry mass of the porous medium (S) and the solute concentration in flowing groundwater in aqueous phase (C) (Chiang 2005, Alvarez 2006).

Making an assumption of the local equilibrium condition between phases – aqueous (free) and sorption (solid) – function $S = f(C)$ implicates that the sorption term ($\partial S/\partial t$) in Eq. (1) can be replaced by the expression ($\partial S/\partial C \cdot \partial C/\partial t$).

Equation (1) may be written in the following form, taking into account the above remark and by factoring out the term ($\partial C/\partial t$):

$$\frac{\partial C}{\partial t}\left(1+\frac{\rho}{m}\frac{\partial S}{\partial C}\right)+u_x\frac{\partial C}{\partial x}=D_x\frac{\partial^2 C}{\partial x^2}+D_y\frac{\partial^2 C}{\partial y^2}. \tag{3}$$

As a result of detailed literature review, in the case of reversible sorption assumption (as negative source term) in Eq. (3) by ($\partial C/\partial t$) term, the constant expression $R = [1 + (\rho/m)\cdot(\partial S/\partial C)]$ will always be found, which is known as the retardation factor in the literature (Chiang 2005, Alvarez 2006).

In the further analysis the well-known empirical equation of the Freundlich isotherm was accepted for the assumption of local equilibrium of concentrations. For such equilibrium-controlled state, it can be assumed that the rate of the reversible adsorption process is equal to zero ($\partial S/\partial t = 0$) in relation to the ground medium with the finite adsorbing capacity (for a constant temperature and negligible value of the irreversible chemical sorption) (Chiang 2005, Alvarez 2006).

The Freundlich non-linear isotherm as a more general equilibrium relationship, assumes that the sorbed concentration (S) is not directly proportional to the dissolved concentration (C). The proportion between concentrations (S) and (C) is fitted in most cases to the exponential relationships with relatively higher concentrations of flowing contaminants in natural groundwater stream in the form (Chiang 2005):

$$S = K \cdot C^N, \tag{4}$$

where: K, N = the parameters of the Freundlich non-linear isotherm; (K = the Freundlich constant; N = the Freundlich exponent, that depends on the solute species, the nature of the porous medium and other conditions of the system).

Taking into account Eq. (4), the advection-diffusion Eq. (3) may be written in the dimensionless form:

$$\frac{\partial C^*}{\partial \tau} + A_1^* \frac{\partial C^*}{\partial \xi} = A_1^* \cdot D_x^* \frac{\partial^2 C^*}{\partial \xi^2} + A_1^* \cdot D_y^* \frac{\partial^2 C^*}{\partial \eta^2} \tag{5}$$

taking also into account the auxiliary dimensionless parameters:

$$\left.\begin{aligned} &\frac{x}{L} = \xi; \quad \frac{y}{L} = \eta; \quad \frac{C}{C_o} = C^*; \quad \frac{u_x t}{L} = \tau; \quad \frac{D_x}{u_x L} = D_x^* \\ &\frac{D_y}{u_x L} = D_y^*; \quad \frac{m}{m + \rho \cdot N \cdot K \cdot C_o^{(N-1)} \cdot C^{*(N-1)}} = A_1^* \end{aligned}\right\} \tag{6}$$

where: L = the measured distance from the source of the contaminant outflow (injection) to the last calculated ground-cross section in the ground, treated as a known length of the solution area in the numerical calculations of the transport equation ($L \cong 105.0\ m$); C_o = the initial measured contaminant concentration in the source of the contaminant outflow (injection) into the chosen natural aquifer, treated as the known initial concentration in the numerical calculations of the transport equation ($C_o \cong 296.0\ g\,m^{-3}$) (Aniszewski 2005).

For numerical solution of Eq. (5), the initial and boundary dimensionless conditions were also assumed in the form:

– initial condition:

$$\left.\begin{aligned} &C^*\left(0 \langle \xi \le \infty, 0 \langle \eta \le \infty, \tau = 0\right) = 0 \\ &C^*\left(\xi = 0, \eta = 0, \tau = 0\right) = 1 \end{aligned}\right\} \tag{7}$$

– boundary conditions:

$$\left.\begin{aligned} &C^*\left(\xi = 0, 0 \langle \eta \le \infty, \tau \rangle 0\right) = 0 \\ &C^*\left(\xi = 0, \eta = 0, \tau \rangle 0\right) = 1 \\ &C^*\left(\xi \to \infty, 0 \langle \eta \le \infty, \tau \rangle 0\right) = 0 \end{aligned}\right\} \tag{8}$$

These conditions, as Eqs. (7) and (8), are related to the considered semi-confined plane of groundwater flow. In this analysis, taking into account the symmetry, the area of flow was considered for ($0 \langle \xi \le \infty$) and ($0 \langle \eta \le \infty$). In the further analysis the asterisk symbol for concentration values has also been neglected ($C^* = C$). For numerical solution of Eq. (5), the differential "upstream" scheme was used, eliminating at the same time the effect of "numerical diffusion" for the Courant number $C_a = 1$ and the effect of "numerical dispersion" for the Peclet number $Pe \le 2$ (satisfying also the consistency, stability and convergence conditions in the solution) (Szymkiewicz 2000, Chiang 2005). Numerical solution of Eq. (5) was obtained for both the earlier calcu-

lated values of the contaminant dispersion coefficients (D_x, D_y) according to Eq. (2), and non-linear adsorption parameters (N, K) according to Eq. (4) (Aniszewski 2005).

Based on the accepted literature numerical values of the longitudinal and transverse dispersivity (α_L, α_T), the numerical values of the contaminant dispersion coefficients according to Eq. (2) are $D_x \cong 7.93 \cdot 10^{-3}$ m^2 s^{-1} and $D \cong 3.96 \cdot 10^{-4}$ m^2 s^{-1}, respectively. However, the numerical values of the non-linear adsorption isotherm parameters according to Eq. (4) are $K \cong 0.4132$ m^3 g^{-1} and $N \cong 0.6122$, respectively, using at the same time sodium chloride (chloride anions Cl^-) as the accepted indicator in the our own, earlier so-called "batch" laboratory research with immobile groundwater (Aniszewski 2005).

2.2 Description of the site verification being considered

From among many conservative indicators determined in the site research by the Institute of Environmental Development in Poznań(chlorides, sulfates, phosphates) for the site verification of Eq. (5), describing contaminant transport in the aquifer, chlorides were chosen in spite of relatively low adsorbing capacity of this indicator in relation to granular materials (Aniszewski 2005, Alvarez 2006). Based on the general literature analysis, it can be concluded that the chloride adsorbing capacity will be relatively greater both in the case of chloride flow in natural aquifers with relatively small graining (for example in sandy ground media) and in the case of appearance in these natural aquifers of admixtures of various substances, for example, with micro-porous structure increasing also the adsorbing capacity of these aquifers (Aniszewski 2005, Alvarez 2006, Singhal 2008).

The source of groundwater contamination in this chosen aquifer were seven real ground lagoons with pre-purified liquid manure inside (Poznań 1982). For the exact examination of contaminant transport into groundwater, a certain number of piezometers were installed nearby the existing ground lagoons (Poznań 1982).

Based on these existing piezometers, the Institute of Environmental Development in Poznańmade testing the concentration values of the chosen contaminant indicators in this natural aquifer, collecting water samples in these piezometers (Poznań 1982). At the same time, in the presented site verification, the zero-value of chloride background concentrations in groundwater was also assumed based on accessible site measurements according to (Poznań 1982).

3. Results

The maximal dimensionless values of chloride concentrations were calculated numerically according to Eq. (5) for times when the contaminant wave front reached the particular four piezometers, respectively counting from the moment of geotextile slotted vertical cracking and the liquid manure direct leaking into the groundwater stream from the ground lagoon No. 4, as the measuring series: November 1981 (Poznań 1982, Aniszewski 2005). The graph of the calculated dimensionless values of chloride concentrations according to Eq. (5) (for negligible and incorporated adsorption, respectively) in the chosen four piezometers (along axis x and for $y = 0$) together with the

measured chloride values in these piezometers is presented in Fig. 1 (Poznań 1982, Aniszewski 2005).

However, the compilation of the maximal calculated values of chloride concentrations, based on the own modified recently calculation program "PCCS – 2", is presented in (Aniszewski 2005).

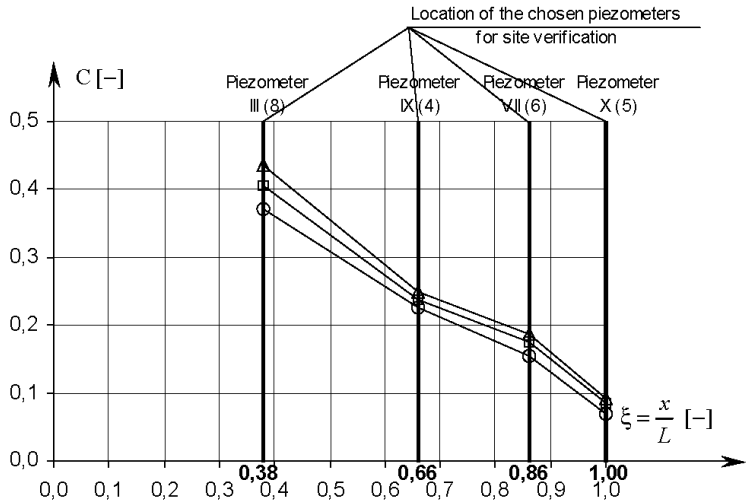

Fig. 1. The maximal values of dimensionless chloride concentrations in the chosen four piezometers: Δ − the values of the concentrations calculated acc. to Eq. (5) for negligible adsorption term, □ – the values of the concentrations calculated acc. to Eq. (5) with incorporated adsorption term, O − the values of the concentrations measured acc. to (Poznań 1982).

4. Discussion

The calculated values of relative deviations in the range of 8.6% – 22.5% between the maximal values calculated according to Eq. (5) (with incorporated adsorption term) and the measured values according to (Poznań 1982) in relation to the measured concentrations, prove the sufficient accuracy of the presented numerical solution of the contaminant transport equation in groundwater stream incorporating also non-linear term of adsorption process.

However, the relative deviations in the range of 3.2% – 8.9% between the maximal calculated values acc. to Eq. (5) (for negligible and incorporated adsorption term, respectively) in relation to the calculated concentrations with incorporated adsorption term, confirm the fact of occurrence of the relatively low, but existing chloride adsorbing capacity in the chosen aquifer. The low chloride adsorbing capacity in the chosen aquifer is compatible with the confirmed nearly negligible adsorption values of such contaminants like chlorides flowing through natural ground media (Aniszewski 2005, Chiang 2005, Alvarez 2006, Singhal 2008).

At the same time, for other kinds of flowing compounds (like sulfates or pesticides), the real values of both adsorbing capacity and the concentration reduction of

such contaminants can be considerably greater, especially in natural sandy aquifers (Aniszewski 2005, Chiang 2005, Alvarez 2006, Singhal 2008).

5. Conclusions

The practical conservative contaminant transport model presented as Eq. (5), combining simultaneously the advection, dispersion and physical reversible adsorption processes, can be used for the engineering calculations of the contaminant concentration fields in the natural sandy aquifers. Practical using of this model for site verifications greatly depends on both the proper mathematical description of all processes and the proper identification of all the required parameters being considered in this equation (Aniszewski 2005).

References

Alvarez, P.J.J., and W. Illman (2006), *Fundamentals of groundwater flow and contaminant transport process. Bioremediation and natural attenuation*. Series: Environmental Science and Technology: A Wiley Interscience Series of Texas and Monographs, John Wiley and Sons, Inc., 612 pp.

Aniszewski, A. (2005), Experimental verification of the contaminant transport in the aquifer incorporating advection, dispersion and sorption processes, *Arch. Hydro-Engin. Environ. Mech.*, Gdańsk **52**, 3, 195-212.

Chiang, W.H. (2005), *3D-Groundwater modeling with PMWIN. A simulation system for modeling groundwater flow and pollution*. Springer-Verlag, Heidelberg-New York, 397 pp.

Poznań (1982), *Results of physico-chemical and bacteriological analyses of water samples together with documentation and conclusions resulted from these analyses for Agricultural Complex "Redło" in Redło*, (manuscript) (in Polish), 23 pp.

Singhal, N., and J. Islam (2008), One-dimensional model for biogeochemical interactions and permeability reduction in soils during leachate permeation, *Journal of Contaminant Hydrology* **96**, 1-4, 32-47.

Szymkiewicz, R. (2000), *Mathematical modeling of the flows in rivers and channels*. Scientific Proceedings, Warsaw (in Polish), 321 pp.

Zhang, Z., and M.L. Brusseau (2004), Nonideal transport of reactive contaminants in heterogeneous porous media: 7. Distributed-domain model incorporating immiscible-liquid dissolution and rate-limited sorption/desorption, *Journal of Contaminant Hydrology* **74**, 1-4, 83-103.

Accepted November 13, 2008

PUBLS. INST. GEOPHYS. POL. ACAD. SC., E-10(406), 2008

Particle-Particle Collision for Lagrangian Modelling of Saltating Grain: Theoretical Background

Robert J. BIALIK and Włodzimierz CZERNUSZENKO
Institute of Geophysics, Polish Academy of Sciences
Ks. Janusza 64, 01-452 Warsaw, Poland
email:rbialik@igf.edu.pl

Abstract

The goal of this paper is to describe the method of application of particle-particle collision for Lagrangian modelling of saltating grain in rivers. The model based on the approach proposed for turbulent gas-solid flow and on statistical physics for inter-particle collision in gases is presented. This approach relies on determination of the velocity of the considered particles after collision with another particle during the saltation. These collisions, which depend on the particle concentration, the particle size, and particle velocity are briefly discussed. The formulas for collision probability and the method for calculation of velocity after collision and direction of considered particles before collision are proposed.

1 Introduction

Sediment transport in bed-load is probably one of the most interesting and important processes in rivers. This phenomenon is associated with many things, like: building dams or bridges, occurrence of scour or even floods. In bed-load layer, the sediment may be transported in three forms: sliding, rolling and saltation. The last of these forms is the most typical motion of sediment (Bagnold , 1956). A number of researchers have been involved in modelling of saltation. The breakthrough works were: Wiberg and Smith (1985), Lee and Hsu (1994), Niño et al. (1994a), Niño and Garcia (1994b), and Niño and Garcia (1998). Apart from the model proposed by Rowiński and Czernuszenko (1999), all of known mathematical models of saltation movement of particle in an open channel or river flow are based on a movement for single grains and do not take into account the vertical concentration and particle - particle interaction. The main aim of this paper is to describe

the way of calculation of particle-particle collision, which also takes into account the vertical particle concentration, often neglected in models that appear in literature but strongly affects the quality of results.

2 Particle motion and problem of inter-particle collision

To describe the behavior of particles suspended or entrained into flowing water, most researchers use the equation of motion of a single spherical particle in a fluid (Bialik and Czernuszenko , 2007). Two works are the most important: Tchen (1947) who synthesized the work of Basset (1883), Boussinesq (1903) and Ossen (1927), and Maxey and Riley (1983) who based on an analysis similar to that of Corssin and Lumley (1956). In order to find the trajectory of particle during the saltation we may solve similar system of equations of motion of a single spherical particle in fluid, which can be described in the following form (Hinze , 1975):

$$\frac{d\overrightarrow{x}}{dt} = \overrightarrow{v} \tag{1}$$

$$m_p \frac{d\overrightarrow{u}}{dt} = \overrightarrow{F_D} + \overrightarrow{F_L} + \overrightarrow{F_M} + \overrightarrow{F_V} + \overrightarrow{F_B} + \overrightarrow{F_G} \tag{2}$$

where m_p is the particle mass, v is the particle translational velocity vector, x is the particle position vector, F_D is the drag force, F_L is the lift force, F_M is the Magnus force, F_V is the virtual or added mass force, F_B is the Basset force and F_G is the buoyancy force. In order to solve this system of equations we also need initial and boundary conditions and fluid velocity which is described by the logarithmic law:

$$u_f(z) = \frac{u_*}{\kappa} \ln \frac{z}{z_0}, \tag{3}$$

where: $\kappa = 0.4$ is the Karman constant, $z_0 = 0.11(\nu u_*) + 0.033 k_s$, and k_s is roughness, which is proportional to the size of the particle. It is necessary to remark that the system of equations (1) and (2) do not take into account the force which might be responsible for particle-particle collision.

Sommerfeld (2003) claimed that deterministic as well as stochastic models could describe inter-particle collisions. Therefore, it is necessary to look for a method of calculation the particle-particle collision in kinetic theory of gases or in statistical physics. There are a lot of studies associated with inter-particle collision in fluid flow in many fields (i.e., engineering or chemistry), which are published in the past, i.e., Oestere and Petitjean (1993) who described collisions in dilute flows, Williams and Crane (1999) who gave a detailed review of process of inter-particle collision, Mei and Hu (1999) who described the geometrical collision for small particles. In opposition to these theoretical studies, a lot

of experiments were carried out in Martin-Luther University of Halle-Wittenberg and were described e.g. by: Sommerfeld (2001), Sommerfeld (2003) and Sommerfeld and Kussin (2003).

On the other hand, it is very interesting that only a few works, which described particle saltation in river, took into account the effect of particle-particle interaction. Schmeeckle et al. (2001) measured the particle impact on an inclined glass plane in water and used elastohydrodynamic theory in order to investigate the mechanics of inter-particle collisions in sediment-transporting flow, whereas Lee et al. (2002) proposed a new two-dimensional continuous saltation model which was able to simulate the continuous saltating trajectories of several particles. In the work (Bialik and Czernuszenko , 2008) we made an attempt to calculate the force responsible for particle-particle collision and showed the possible influence of this force on particle trajectory.

3 Particle-particle collision model

In calculation of particle-particle collision based on turbulent gas-solid flow we may follow the approach proposed by Sommerfeld and Zivković (1992) and Oestere and Petitjean (1993). They developed independently a similar stochastic particle-particle collision model, based on the calculation of the collision probability along the particle trajectory, which was associated with kinetic theory of gases. In this paragraph these two methods will be briefly described. However, in application of these methods to particle movement in rivers we have to change the way of calculation of a few parameters, which were given there.

From kinetic theory of gases we know that two identical particles collide with the following frequency:

$$f_c = \frac{\pi}{4}(d_1 + d_2)^2 \left|\overrightarrow{u_1} - \overrightarrow{u_2}\right| n_p \tag{4}$$

where: d_1 and d_2 are the particle diameters, $|\overrightarrow{u_1} - \overrightarrow{u_2}|$ is the relative velocity between particles and n_p is the number of particles in unit of fluid volume, concentration (number/m^3).

The first method which can be used to calculate the probability of occurrence of collision between two particles in the very small time interval dt was proposed by Sommerfeld (2001):

$$P_S(\Delta t) = \frac{\pi}{4}(d_1 + d_2)^2 \left|\overrightarrow{u_1} - \overrightarrow{u_2}\right| n_p \Delta t \tag{5}$$

This collision probability P_S is calculated as the product of the time step size Δt (which should be smaller than unity) and the collision frequency.

On the other hand, Oestere and Petitjean (1993) proposed that the probability of collision between instants t and $t + dt$ for every particle is:

$$dP = P(t_0, t + dt) - P(t_0, t) = [1 - P(t_0, t)] f_c dt, \tag{6}$$

where $P(t_0, t)$ is the unknown probability. After a few transformations with assumption that $P(t_0, t_0) = 0$ it is easy to obtain the following expression for a probability of a collision which takes place between $\Delta t = t - t_0$:

$$P_{OP}(\Delta t) = 1 - exp[-f_c \Delta t]. \tag{7}$$

It is impossible to apply directly these two solutions, eqs. (5) and (7), to inter-particle collision during saltation in open-channel flow, because we cannot calculate some parameters which appeared there in the same way as they did it in their propositions, especially, the calculation of $\overrightarrow{u_2}$ and n_p.

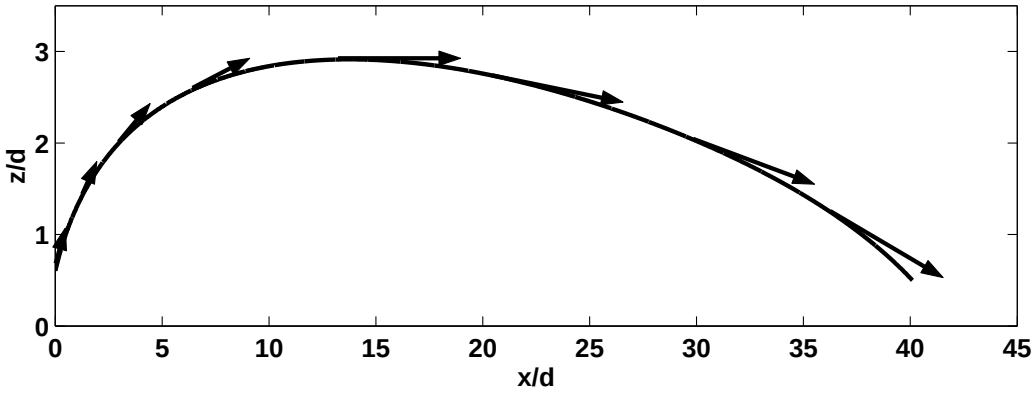

Fig. 1: History of direction and length of particle velocity.

The first step of our method to calculate the probability from eqs. (5) and (7) is to find the value of both components of velocity of second particle which takes part in collision. In order to do this, we use the additional parallel Lagrangian model of saltating grain without the effect of particle-particle collision. In order to determine the velocity components, is important to describe the velocity direction of the particle. Fig. 1 shows the history of v_p for each point on particle trajectory. To find the direction of second particle we used random number generator for a logical value of 0 or 1, which means that when it is 0 then the particle moves upward and when it is 1 the then particle moves in the opposite direction. Exemplary calculated mean component of particle velocity, when the particle moves upward and downward, for particle with d = 0.015 m is shown on Fig. 2. This division is essential, because there are clear differences and the relative velocity between colliding particles has an important influence on value of P.

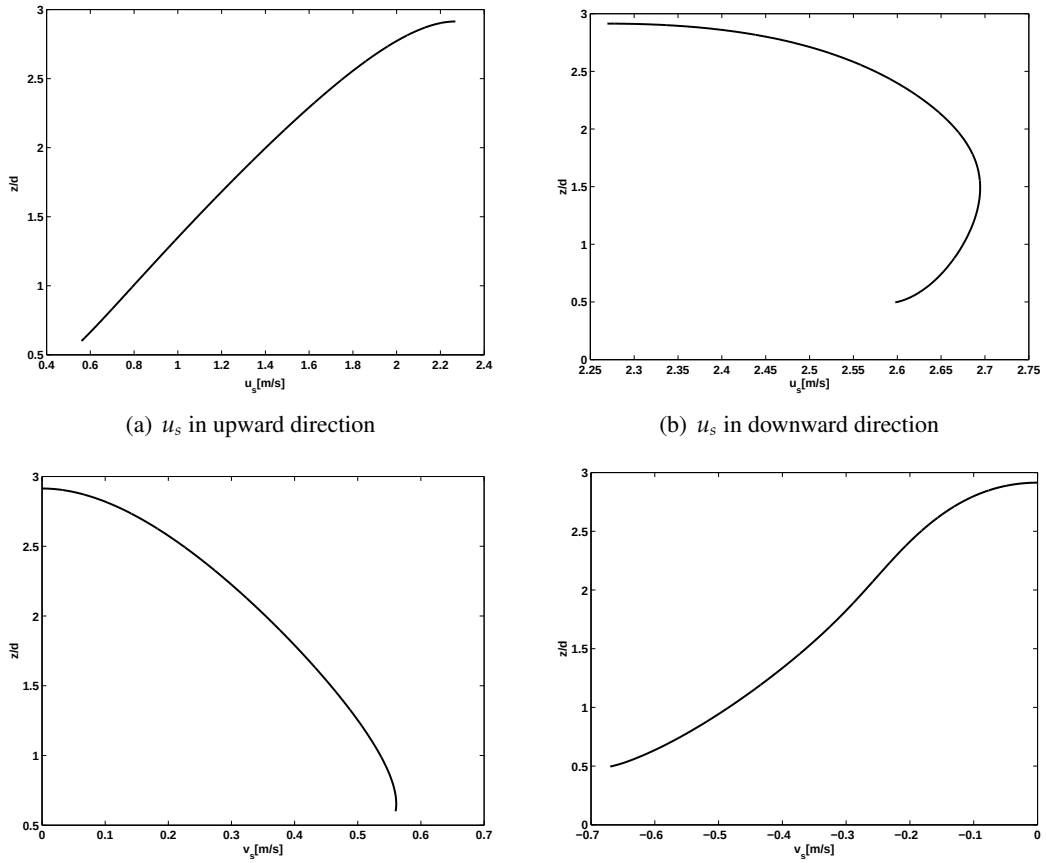

(a) u_s in upward direction

(b) u_s in downward direction

(c) v_s in upward direction

(d) v_s in downward direction

Fig. 2: Exemplary calculated vertical and horizontal velocities of particle with d = 0.015 m from eqs. (1) and (2), when particle moves upward and downward. Initial conditions: $x_o = 0$, $z_o = 0.6d$, $v_o = 2u_*$, $u_o = 2u_*$, $u_* = 0.25[m/s]$.

The next step is to calculate the value of n_p. This is the number of particles per unit volume in the control volume, which means that this number is a function of distance from the bed. In order to do this we also use the additional parallel Lagrangian model of saltating grain without the effect of particle-particle collision. Fig. (3) shows calculated concentration for the particle with d = 0.015 m. If the number of particles which were used to simulation is known, there is no problem to calculate the value of probability in every time step Δt from eqs. (5) or (7). The collision probability P is determined with the use of a random number generator. If $P > RNG$ then the collision is taken into account to our calculation.

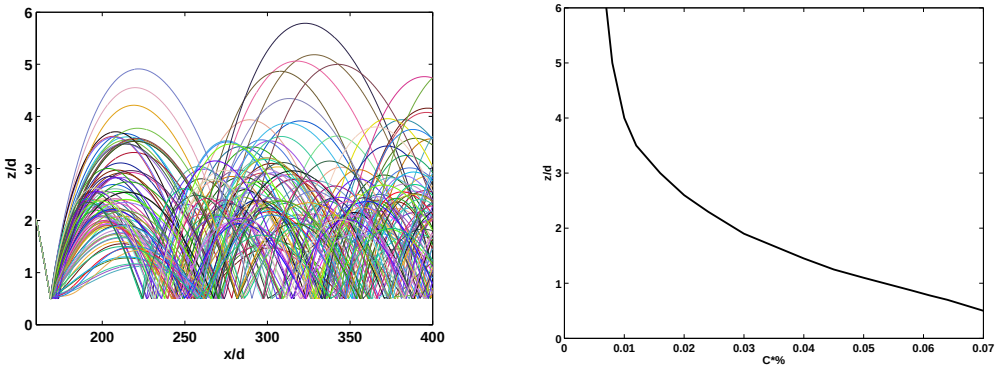

(a) exemplary trajectories (b) concentration (%)

Fig. 3: Exemplary calculated concentration for which particle d = 0.015 m for the following initials condition: $x_o = 0$, $z_o = 0.6d$, $v_o = 2u_*$, $u_o = 2u_*$, $u_* = 0.25[m/s]$.

Finally we have to find the particle velocity after collision. Sommerfeld (2001) proposed the following expression for relation between particle velocity before and after collision for flying particles:

$$u_{out} = u_{in}\left(1 - \frac{1+e}{1+m_1/m_2}\right) \tag{8}$$

$$v_{out} = v_{in}\left(1 - f(1+e)\frac{u_{in}}{v_{in}}\frac{1}{1+m_1/m_2}\right) \tag{9}$$

where: e and f are restitution and friction coefficients, respectively, and m_1 and m_2 are the masses of the saltating and surrounding particles. The index *in* stands for the particle velocity before collision and index *out* denotes the velocity after collision. This relation appears by solving the momentum equations with connection with Coulomb's law of friction. In this assumption the particle rotation is neglected, which means that Magnus force is not considered in the presented model. When $m_1 = m_2$, eqs. (8) and (9) reduce to the following expressions:

$$u_{out} = u_{in}\left(\frac{1-e}{2}\right) \tag{10}$$

$$v_{out} = v_{in} - \left(\frac{f(1+e)u_{in}}{2}\right) \tag{11}$$

Eqs. (10) and (11) can be used for the particle movement in open-channel flow in order to calculate the influence of particle-particle collisions on the shape of particle trajectory.

4 Conclusions

The following points summarize our conclusions.

1. The model proposed here takes into account inter-particle collision effect. This approach, new in fluvial hydraulic, is based on turbulent gas-solid flow and on kinetic theory of gases;

2. Two methods of calculation of probability for the occurrence of a collision between two particles in the time step are shown. It seems to be important to propose the method of choosing the value of time step in the better way, and the further works are needed to define $\overrightarrow{u_2}$ and n_p more precisely in sediment transport in bed-load;

3. The present investigation should be continued since it points to fundamental differences between approaches used in the kinetic theory of gases and in fluvial hydraulics.

Appendix

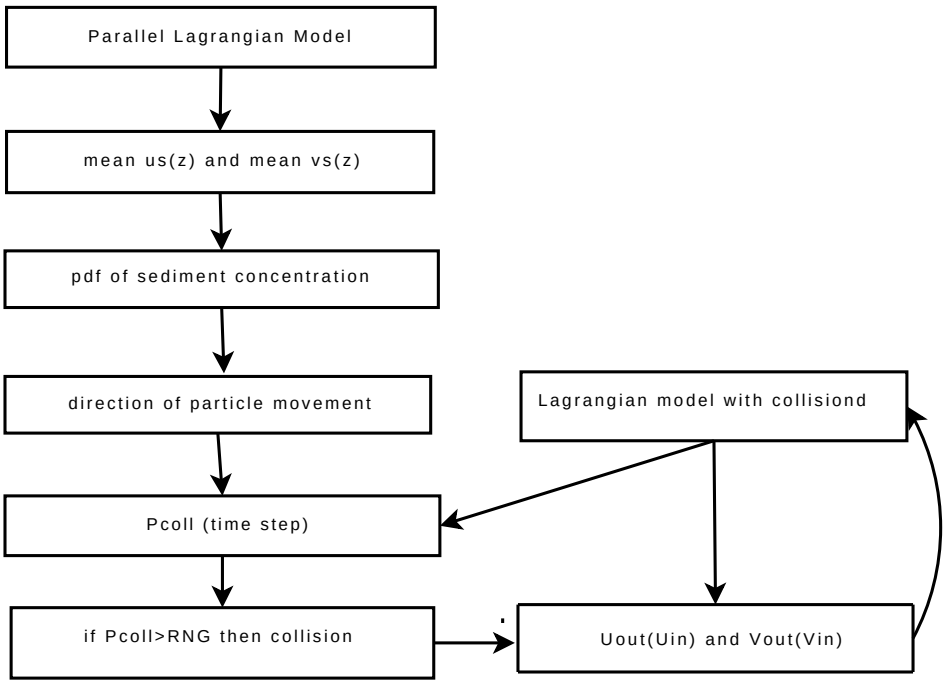

Fig. 4: The diagram of the method used.

Figure 4 shows a diagram of described solution how to include particle-particle collision into Lagrangian modelling of saltating grain. In the proposed method we want to solve numerical Lagrangian model which includes particle-particle collision. The described method requires some parameters like: both components of velocity of the second particle that takes part in collision and the number of particles in considered volume. In order to fix these unknown coefficients we may solve numerically parallel Lagrangian model without collision. In the first step we should fix the velocity that can be calculated based on Monte Carlo simulation, next in the same way we may calculate the concentration of particles, then we can find the probability of occurrences of collision. Finally we can change the velocity of particle after collision from eqs. (10) and (11).

References

Bagnold R.A., (1956), The Flow of Cohesionless Grains in Fluids. Proc. Royal Soc. Philos. Trans. **249**

Basset A.B., (1883), *A Treatise on Hydrodynamics*, Cambridge; Deighton, Bell; (1961), New York, Dover.

Boussinesq J., (1903), *Theorie Analitique de la Chaleur*, Paris, Gauthier-Villars.

Bialik R., Czernuszeko W., (2007), Numerical Analysis of Lagrangian Particle Saltation Model, *Publs. Inst. Geophys. Pol. Acad.* Sc. E-6(401) 21-29.

Bialik R., Czernuszeko W., (2008), 2D numerical model for the bed-load transport of saltating grain, *Proc. River Flow 2008*, 945-952.

Corssin S., Lumely J., (1956), On the equation of motion of solid particles in a turbulent fluid. *Applied Scientific Research*, **A6**,pp. 114

Hinze J.O., (1975), *Turbulence*, McGraw-Hill, USA.

Lee H., Hsu I., (1994), Investigation of saltating particle motion, *Journal of Hydraulic Eng.*, **120**, 831-845.

Lee H.Y., You J.Y., Lin Y.T., (2002), Continuous Saltating Process of Multiple Sediment Particles, *Journal of Hydraulic Eng.*, **128**, 443-450.

Maxey M.R., Riley J.J., (1983), Equation of Motion of a Small Rigid Sphere in a Nonuniform Flow, *Physic Fluids*, **26**(4), 883-889

Mei R., Hu K.C., (1999), On the collision rate of small particles in turbulent flows *J. Fluid Mech.* **391**, 67-89.

Niño Y., Garcia M., Ayala L., (1994a), Gravel Saltation. 1.Experiments, *Water Resour. Research*, **30**(6), 1907-1914.

Niño Y., Garcia M., (1994b), Gravel Saltation. 2.Modeling, *Water Resour. Research*, **30**(6), 1915-1924.

Niño Y., Garcia M., (1998), Using Lagrangian particle saltation observations for bedload sediment transport modelling, *Hydrological Processes*, **12**, 1197-1218.

Oestere B., Petitjean A., (1993), Simulation of particle-to-particle interactions in gas-solid flows, *Int. J. Multiphase Flow*, **19**, 199-211.

Ossen C.W., (1927), *Hydrodynamik*, Leipzig, Akademische Verlagsgescellschafe.

Rowiński P.M., Czernuszenko W., (1999), Modelling of sand grains paths in a turbulent open channel flow, *Proc. 28th IAHR Congress*, Graz, Austria.

Schmeeckle M.W., Nelson J.M., Pitlick J., Bennett J.P., (2001), Interparticle collision of natural sediment grains in water, *Water Resources Research*, **37**(9), 2377-2391.

Sommerfeld M., Zivković G., (1992), Recent advances in the numerical simulation of pneumatic conveying through pipe systems. In: Hirish, et al. (Eds.), *Computational Methods in Applied Science, First European Computational Fluid Dynamics*, Brussels, 201-212.

Sommerfeld M., (2001), Validation of a stochastic Lagrangian modelling approach for inter-particle collisions in homogeneous isotropic turbulence, *Int. J. Multiphase Flow*, **27**, 1829-1858.

Sommerfeld M., (2003), Analysis of collision effect for turbulent gas-particle flow in a horizontal channel: Part I. Particle transport, *Int. J. Multiphase Flow*, **29**, 675-699.

Sommerfeld M., Kussin J., (2003), Analysis of collision effect for turbulent gas-particle flow in a horizontal channel: Part II. Integral roperties and validation, *Int. J. Multiphase Flow*, **29**, 701-718.

Tchen C.M., (1947), *Mean value and correlation problems connected with the motion of small particles suspended in a turbulent fluid*. The Hague: Marinus Nijhoff. (PhD Thesis)

Wiberg, P.L., Smith, J.D., (1985), A theoretical model for saltating grains in water. *J. Geophys. Res.*, **90**(C4), 7341-7345.

Williams J.J.E., Crane R.J., (1983), Particle collision rate in turbulent flow, *Int. J. Multiphase Flow*, **9**, 421-435.

PUBLS. INST. GEOPHYS. POL. ACAD. SC., E-10 (406), 2008

Tracing of Modelled Pollution Originating from Tributaries in the Dobczyce Lake Working under Flood Conditions

Monika GAŁEK and Paweł S. HACHAJ

Institute of Water Engineering and Management
ul. Warszawska 24, 31-155 Kraków, Poland
e-mail: monika.galek@iigw.pl

Abstract

This paper shows an application of the water flow velocity maps model that was designed for the Dobczyce retention water body. The model is used to track simulated pollutants that enter the lake from a number of its tributaries. The idea, its use and sample results are shown. The background model is referenced.

1. The model and the aim

Modeling of water flow in retention lakes is a difficult task. It requires using 2- or even 3-dimensional models which are susceptible to a lot of instabilities caused by our inaccurate knowledge of starting and boundary conditions as well as by the complexity of the task itself. This article does not aspire to present a new model nor to validate one. Instead, the water velocity maps generated by the two-and-a-half dimensional model of the flow in Dobczyce Lake (Hachaj 2007a,b) are treated as given.

The maps are in digital form and they can be represented by the formula:

$$\vec{v} = f\left(x, y, l, \vec{Q}_i\right), \tag{1}$$

where $\vec{v}$ is the planar (horizontal) velocity (it can be either surface velocity or average velocity of a water column in the given location; in this article the average velocity is used), x and y are coordinates of the point of interest where the velocity is calculated, l is the water surface level in the lake, and the vector $\vec{Q}_i$ contains all the discharges of the tributaries of the lake and all the discharges at the sections where water leaves the lake. The "inflows" of positive values of the discharge are the Raba River and a number of streams. The "outflows" of negative values of the discharge are dam sluices,

dam spillways, as well as water supply and power plant inlets. The model works for the full physically reasonable range of all of its parameters.

The aim of this article is to show one of the applications of that model: It presents tracking of the virtual pollutants dissolved in water that may enter the lake from a number of its tributaries. Such an analysis may be helpful in crisis management for the considered lake. The task is done by following the current lines in the lake as they are defined by the velocity field. Overall flooding conditions are assumed to assure that for the whole lake the current is the dominant mean of transport (Hachaj 2008). The examples are made for the water surface level of 272 m above the sea level and the Raba incoming discharge of 1560 m^3/s, which is the design flow for the Dobczyce water body. The procedure can be also applied to other states of the lake and results of such calculations can be verified by field measurements in appropriate conditions.

2. The lake and the methodology

Basic properties of the Dobczyce Lake are as follows (Nachlik *et al*. 2006): It was created by building a dam of 31.6 m height and 617 m length at 60.1 km of the Raba river; its capacity varies between $14.5 \cdot 10^6$ m^3 and $125 \cdot 10^6$ m^3 along with the water surface level – which may change between 256.7 m and 272.6 m above the sea level; the total discharge may be as high as 2717 m^3/s.

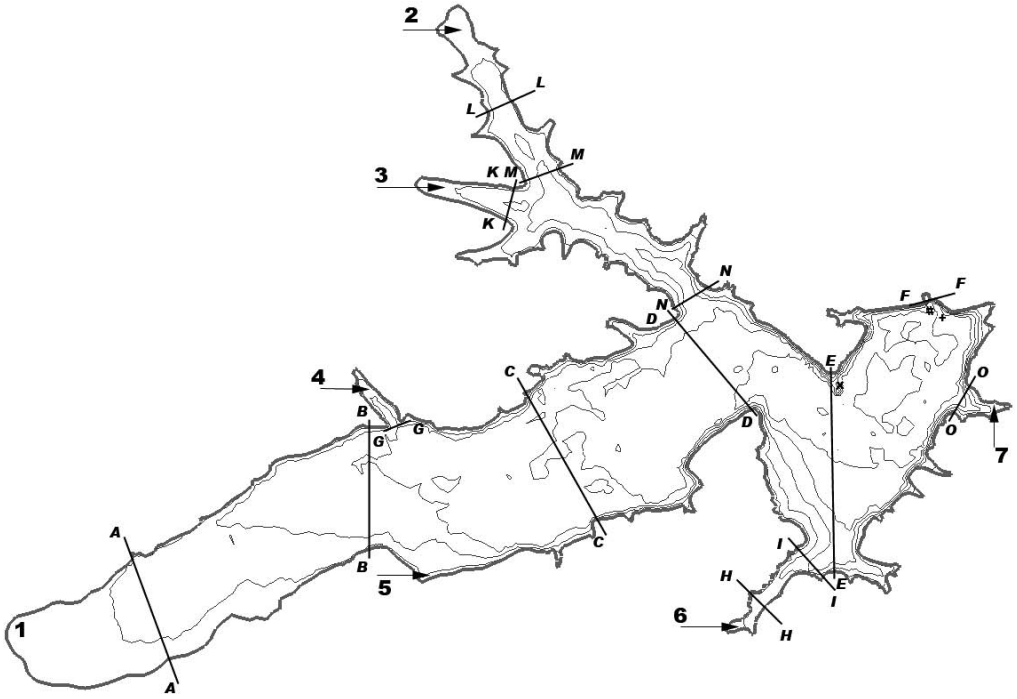

Fig. 1. The shape of the Dobczyce lake for the water level of 272 m a.s.l. Contours denote bed elevation levels of 265, 260, 255, 250 and 245 m a.s.l. The digits denote positions of the tributaries. The letters denote applied cross-sections. The #, +, and x marks denote the outflows.

Figure 1 shows the shape of the lake when the water level is set to 272 m a.s.l. (which is a reasonable value during flood events). The contours provide an insight of the bed shape being drawn at bed elevation values of 265, 260, 255, 250, and 245 meters above the sea level. The digits denote the position of tributaries considered in this article with **1** being the position of the Raba inflow, **2** – the position of the Wolnica inflow (the main side tributary) and **3**-**7** – the positions of several smaller tributary inflows. The approximate dam inlets and spillways position is marked by "#", the power plant inlet position is marked by "**+**", and the water supply inlet position is marked by "**x**". There is also a number of cross-section lines introduced; their markings range from ***A***-***A*** to ***O***-***O***. They are used as check lines during the flow analysis.

In order to track the pollutants the following procedure is used:

1. A few starting points are introduced at the tributary inflow region. They constitute the start of the tracking lines. The choice of those points in that region is basically arbitrary. They should be dispersed to cover a range of possible trajectories. The smoothness of the background model solutions assures that small changes in the starting point location should not cause big changes in trajectories and in fact they do not do so.
2. The velocity field map designed for $l \approx 272$ m are used to track the points along the current lines using a linear formula: $\vec{x}(t+\Delta t) = \vec{x}(t) + \vec{v}(\vec{x}(t), l, \vec{Q}_i) \cdot \Delta t$, where $x(t)$ is the tracking point position in the time t, Δt is the numerical time step and v is the velocity taken from the map as described in eq. (1). Such a procedure gives stable, consistent and reliable results for a wide range of the Δt parameter. If it is set much too high or too low, numerical errors may appear.
3. There is a few of cross-section lines introduced in the lake. When a point being tracked passes such a line, the position and time of this event are recorded, along with the total distance traveled by that point. Note that for different points the distance they travel between two cross-section lines may also be different.
4. Among the points the ones that reach a given cross-section line in the shortest and the longest time are taken to find out the approximate range of spreading the simulated pollution along the current.

3. The results and the remarks

3.1 Time frames

The time frames of the performed simulation can be defined as the time water needs to propagate through the whole lake from the inflow of Raba to the dam outlets. By a comparison of any other flow time to the time scale shown below it can be recognized whether that flow should be considered as "fast" or "slow". The results of simulation of Raba-originating flow are shown in Table 1.

As one can see, the average time the main current passes the whole lake from the Raba inflow to the dam outflows is of the order of 20 hours. The tributaries currents as lying at the sides of the main one are expected to be significantly slower.

Table 1

Average total distance and the time interval for reaching given cross-section lines by the tracking points originating from the Raba river (tributary **1**)

Tributary	Section	Distance [m]	Time [h]	
			min	max
1. RABA	A-A	1165	0.25	0.4
	B-B	3271	2.55	2.75
	C-C	4817	5.25	7.5
	D-D	6212	9.5	13.0
	E-E	7502	11.7	15.3
	F-F	8882	15.4	22.1

3.2 Tributaries flow tracking

The following set of tables and figures presents the results of the simulations of the propagation of pollutants originating from a few of the lake tributaries. The most important inflowing stream is Wolnica. Results obtained for that stream are provided below (Fig. 2. and Table 2). It can be seen that for a real-life event one has approximately 70 hours to neutralize the contamination before it leaves the upper "arm" of the lake and enter its main body. It should be also noted that the current lines run very close to the water supply inlet which make monitoring of water condition in Wolnica very important.

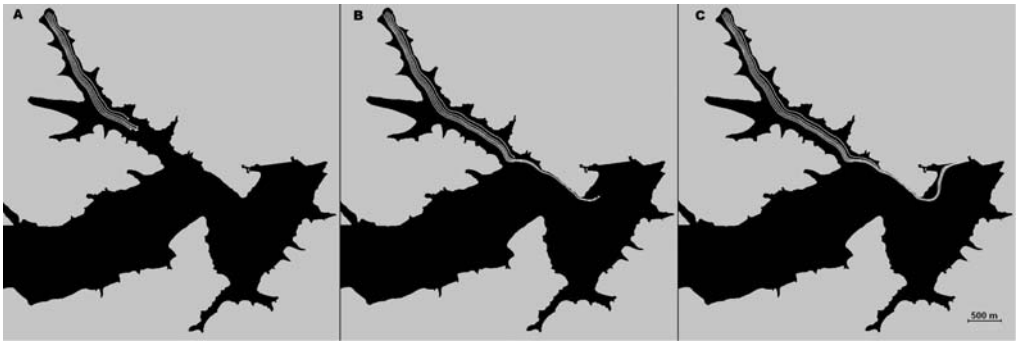

Fig. 2. Tracking of pollutants entering the lake from the tributary **2** (Wolnica). The panels show the situation after 48 hours (A), 90 hours (B) and 122 hours (C) from the event of entering the lake by the pollutants.

For the next tributary (**3**) the overall picture is very similar to the one above. The times are of course different. As that stream is much smaller than Wolnica the tracing points use a significantly longer time interval to reach the ***N-N*** profile as shown in Table 3 below.

The next two tables, 4 and 5, contain data calculated for two side tributaries of the lake: **4** and **5**. For the tributary **5** a figure is included (Fig. 3).

Table 2

Average total distance and the time interval for reaching given cross-section lines by the tracking points originating from the Wolnica stream (tributary **2**)

Tributary	Section	Distance [m]	Time [h]	
			min	max
2. WOLNICA	L-L	915	7.0	8.0
	M-M	1509	21.0	24.0
	N-N	3083	72.0	85.0
	E-E	4445	87.7	104.0
	F-F	5676	100.3	121.6

Table 3

Average total distance and the time interval for reaching given cross-section lines by the tracking points originating from the tributary **3**

Tributary	Section	Distance [m]	Time [h]	
			min	max
3	K-K	806	66.0	99.6
	N-N	2506	139.2	184.0
	E-E	3881	153.6	198.4
	F-F	5112	166,4	211.2

Table 4

Average total distance and the time interval for reaching given cross-section lines by the tracking points originating from the tributary **4**

Tributary	Section	Distance [m]	Time [h]	
			min	max
4	G-G	448	34.0	43.0
	C-C	1620	46.0	48.5
	D-D	2971	59.4	70.8
	E-E	4317	69.6	79.8
	F-F	5548	86.7	94.1

It should be mentioned that for both of them the particle tracking paths form very thin beams. The same is true for most of the other side inflows (but it is certainly not true for paths starting from the Raba inflow). This is because of two effects. First – the side streams contribute quite a low fraction of the total flow in the lake; more than 95% of the inflowing water comes from Raba. It is the Raba originating current that

Table 5

Average total distance and the time interval for reaching given cross-section lines by the tracking points originating from the tributary **5**

Tributary	Section	Distance [m]	Time [h]	
			min	max
5	C-C	1582	29.4	34.8
	D-D	3282	59.8	85.2
	E-E	4283	78.0	93.0
	F-F	6627	111.6	165.6

Fig. 3. Tracking of pollutants entering the lake from the tributary **5**. The situation after 125 hours from the event of entering the lake by the pollutants.

shapes the flow picture in the lake. The tributaries' waters flow like they are carried at the sides of that main current. Following the Raba current can be best seen in the regions where the lake bows and the current follows suit. Second – as a high flood event is considered, the random dispersive movements are much slower than the collective ones and for such a state of the lake they can be neglected (Hachaj 2008).

3.3 Special cases

Tributaries **6** and **7** deserve special attention as for both of them the simulation predicts interesting phenomena. The tributary **6** after leaving its short southern "arm" of the lake enters a relatively shallow basin where the current velocity is low. (The main current flows north to it – in a deeper region.) This causes the virtual pollutant to spread over that basin with a number of the tracked particles crossing the **E-E** line three times (long path: H-I-E1-E2-E3-F in Table 6), while others turn left immediately after reaching the basin and cross that line only once (short path: H-I-E3a-Fa in Table 6.). This behavior – shown on Fig. 4 – causes a big diversity in travelled distances and obtained times. However, it should be pointed out that those times are very long: in fact, much longer than the state of the lake could be treated as steady. This tributary requires further investigation.

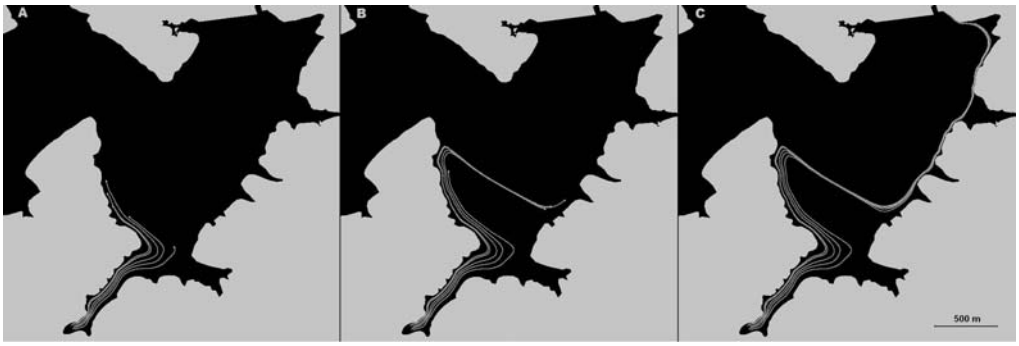

Fig. 4. Tracking of pollutants entering the lake from the tributary **6**. The panels show the situation after 150 hours (A), 225 hours (B) and 350 hours (C) from the event of entering the lake by the pollutants.

Table 6

Average total distance and the time interval for reaching given cross-section lines by the tracking points originating from the tributary **6**

Tributary	Section	Distance [m]	Time [h]	
			min	max
6	H-H	328	9.1	14.7
	I-I	854	52.5	76.3
	E-E1	1177	93.6	109.8
	E-E2	1470	99.0	167.4
	E-E3	3228	–	255.6
	F-F	5220	–	351.0
	E-E3a	2729	189.0	–
	F-Fa	5718	261.0	–

For the tributary **7** another interesting phenomenon can be observed: The main current passes quite closely to the eastern bank there. It makes a clockwise whirl appear in the small eastern basin the tributary **7** leads to. The virtual pollutant particles get caught by the whirl and revolve around for a long time being released to the main basin one after another on an irregular basis. This behavior is depicted on Fig. 5. For that tributary it makes no sense to make a distance/time table for the considered state of the lake. Instead, accumulation in the whirl can be assumed. The range of lake state dependant conditions for which such an effect is obtained will be one of the subjects of further analysis. Of course, observational verification of the simulations shown requires waiting for a high discharge event in the Dobczyce lake. For the comparison purposes the design flow values used in the examples above can be easily replaced with the ones measured in an actual natural event.

Fig. 5. Tracking of pollutants entering the lake from the tributary **7**. The situation after 120 hours from the event of entering the lake by the pollutants. Most of the tracking particles are caught by the clockwise whirl.

References

Hachaj, P.S. (2007a), Modeling of a two-dimensional velocity field for the water flow in the lake of Dobczyce, *Publs. Inst. Geophys. Pol. Acad. Sc.* **E-7 (401)**, 87-94.

Hachaj, P.S. (2007b), Modelowanie pola prędkości wody w zbiorniku dobczyckim – budowa siatki obliczeniowej i wstępne wyniki (Modeling of the velocity field in the Dobczyce lake – computational mesh construction and preliminary results), accepted for publication in *Czasopismo Techniczne. Seria Ś.*

Hachaj, P.S. (2008), Numerical modeling of pollution transport phenomena in the lake of Dobczyce, *Publs. Inst. Geophys. Pol. Acad. Sc*. (this issue).

Nachlik, E., G. Mazurkiewicz-Boroń, A. Bojarski, J. Banaś, W. Styka, K. Słysz, and S. Reizer (2006), *Studium Możliwości Zmiany Funkcji Zbiornika Dobczyckiego i Jego Zlewni z Uwzględnieniem Ochrony Czystości Wody w Zbiorniku* (Study on possibilities of function change of the Dobczyce Lake, including water purity protection), Kraków, 170 pp.

Accepted November 13, 2008

PUBLS. INST. GEOPHYS. POL. ACAD. SC., E-10 (406), 2008

Numerical Modelling of Pollution Transport Phenomena in the Lake of Dobczyce

Paweł S. HACHAJ

Institute of Water Engineering and Management
ul. Warszawska 24, 31-155 Kraków, Poland
e-mail: pawel.hachaj@iigw.pl

Abstract

This article describes a model designed for tracking the movement of a few kinds of pollutants in a wide range of environmental conditions (water level, total discharge, operational mode of the lake, presence or absence of wind) present in the Dobczyce lake. To solve the case, a finite element approach is used. Model theory and a sample result are both shown.

1. Introduction

Among many environmental disasters, toxins and other harmful substances transported by flowing water carry a significant threat towards all living beings, from plants through animals up to men who are exposed to their presence. We should do our best not to let any of those things to poison our waters, but at the same time we should be prepared to react when they do. We should be able to track them and remove or neutralize them as soon as possible.

The aim of this article is to present a numerical modelling tool designed for tracking the movement of a few kinds of pollutants in a wide range of environmental conditions (water level, total discharge, presence or absence of wind) present in the Dob-czyce retention lake. Model theory and sample results obtained for standard (non-flood) environmental conditions are both shown. The backbone for the model is the velocity field model for the lake of Dobczyce described briefly in (Hachaj 2007a) and in a more detailed way, but in Polish only, in (Hachaj 2007b). The following Sections 2 and 3 show the basic data of the lake and the numerical foundation of the model. For more detailed information about those topics please see the articles mentioned above.

2. The lake of Dobczyce

The Dobczyce lake is a retention reservoir placed at 60th kilometer of the Raba river. Table 1 sums up some basic data about that lake (Nachlik *et al*. 2006), while Fig. 1 shows the shape of the lake for minimal, nominal and maximal water levels.

Table 1

Dobczyce Lake – basic data

Parameter	Value
Total capacity	$14.5 \div 125 * 10^6$ m^3
Flooded area	$3.35 \div 10.65$ km^2
Total flow (possible range)	$1.8 \div 2717$ m^3/s
Range of surface level changes	15.9 m (256.7 ÷ 272.6 m a.s.l.)
Average depth (at average water level)	10.2 m

Fig. 1. The shape of the Dobczyce lake at different water levels: minimal (light grey), average (grey), and maximal (dark grey). The ❶ symbol shows the position of dam inlets while the ❷ symbol denotes the location of the water supply inlet. The double bold arrow indicates the main inflow (Raba), the single bold arrow indicates the biggest side inflow (Wolnica), while the thin arrows indicate a few of other inflows (minor creeks).

The main inflow into the lake is the Raba river. There are several creeks that also flow into this lake (out of which Wolnica is the most important one), but their contribution to the total flow is less than 5%. There is a number of outflows from the lake: bottom sluices at the base of the dam, an open spillway in the dam, a power plant sluice, and a water supply sluice.

3. Governing equations and the solving method

The equations used to model the flow of water in the considered lake are based on mass and momentum conservation concepts. They are reduced to two-dimensional

ones as the vertical movement can be neglected (see, e.g., Zienkiewicz and Taylor 2002, p. 219-223, 237-239). Thus, the vertical size of the considered medium is treated as a parameter the *x*, *y*-plane velocity is dependent on. The velocity components for both horizontal coordinates are then:

$$V_x = \frac{1}{H}\int_{z_0}^{z_s} v_x dz; \quad V_y = \frac{1}{H}\int_{z_0}^{z_s} v_y dz, \tag{1}$$

where: V_x, V_y = averaged (2D) velocity components in appropriate directions, H = water depth, z_0 = bed elevation, z_s = surface elevation, v_x, v_y = real (3D) horizontal velocity components in appropriate directions.

After the integration, the continuity (mass conservation) equation takes the following form:

$$\frac{\partial z_s}{\partial t} + \frac{\partial q_x}{\partial x} + \frac{\partial q_y}{\partial y} = \frac{q_m}{\rho}, \tag{2}$$

where: $q_m = \frac{dm_A}{dt}$ is the total mass flow rate per unit area (positive for inflow, negative for outflow), $q_x = V_x H$ = unit flow rate in the *x* direction, $q_y = V_y H$ = unit flow rate in the *y* direction, and ρ is the water density (considered constant).

Momentum transport equations for both horizontal directions are symmetrical to each other. The *x*-direction one is as follows:

$$\begin{aligned} &\frac{\partial q_x}{\partial t} + gH\frac{\partial z_0}{\partial x} + \frac{\partial}{\partial x}\left(\frac{q_x^2}{H} + \frac{gH^2}{2}\right) + \frac{\partial}{\partial y}\left(\frac{q_x q_y}{H}\right) + \\ &\qquad \frac{1}{\rho}\left(\tau_{bx} - \tau_{sx} - \frac{\partial}{\partial x}H\tau_{xx} - \frac{\partial}{\partial y}H\tau_{xy}\right) = 0, \end{aligned} \tag{3}$$

where: g = earth gravity, ρ = water density (considered constant), p_a = atmospheric pressure at the surface level, τ_{bx} = bed shear stress, *x* component, τ_{sx} = surface shear stress, *x* component (usually caused by wind), τ_{xx}, τ_{xy} = turbulence shear stresses acting in the *x* direction on planes perpendicular to the *x* and *y* directions, respectively.

For turbulent stresses the following formula is used:

$$\tau_{\phi\psi} = \rho\nu_t\left(\frac{\partial V_\phi}{\partial \psi} + \frac{\partial V_\psi}{\partial \phi}\right), \tag{4}$$

where φ and ψ represent any coordinate symbol, and:

$$\nu_t = 1\left[\frac{m}{s^2}\right] + 0.1\sqrt{\left(\frac{\partial V_x}{\partial x}\right)^2 + \left(\frac{\partial V_y}{\partial y}\right)^2 + \frac{1}{2}\left(\frac{\partial V_x}{\partial y} + \frac{\partial V_y}{\partial x}\right)^2}. \tag{5}$$

Figure 2 shows the vertical cross-section of the flowing water. The model is capable to calculate both the average velocity V_{av} and the surface velocity V_s. However, for windless (or, in general, small wind) conditions only one calculation is enough as the approximation $V_{av} \approx 0.75 \cdot V_s$ can well be used.

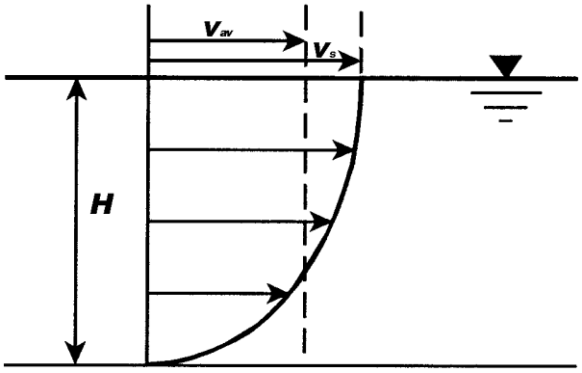

Fig. 2. Vertical cross-section of the velocity distribution.

In order to solve the model equations, the finite element method is used. The calculations are performed on a set of discrete meshes each consisting of quadrilaterals (wherever possible) and triangles. The procedure is supplemented by the method of weighted residuals to provide better convergence. To execute the calculations the "Depth-averaged Flow and Sediment Transport Model – FESWMS" program (Froehlich 2003), a part of the SMS package, is being used. The complete model consists of nine meshes designed each to carry out calculations for different range of the water surface level in the lake. As a result of numerical solving of the model equations, velocity maps are obtained. Those maps are in fact planar velocity fields (the velocity may be V_{av} or V_s depending on the needs), where each point of the lake has a velocity vector associated – a vector that depends on the position of the chosen point and on the state of the lake (water level, inflow and outflow values).

4. Considered types of pollutants

Regardless of their chemical or biological nature, the pollutants considered in this article can be divided into three categories:

- Surface-carried pollutants;
- Dissolved pollutants;
- Sediment pollutants.

For **surface-carried pollutants** (like various kinds of oils) the surface velocity should be used to track their propagation. Transport of such media is also quite susceptible to the wind conditions; if the wind is strong enough and the average water velocity is relatively small they may even move against the water current. On the other hand, their dispersion movement is limited when compared to the next category.

Dissolved pollutants move mainly with the average water current velocity. Yet as the bottom layers of water move much slower than the surface ones, the dispersive movement of such media may be significant. It should also be remembered that the layers cannot be considered as fixed physical structures but due to convective vertical movements they mix with each other. On the other hand, small or moderate wind influences spreading of such substances mostly by altering the average velocity.

The last category – **sediment pollutants** – becomes important in lakes like the considered one only during floods (very high total discharge) or very close the inflows to the lake – where and when the flow velocity is high enough to carry them. Most of the time the vast majority of the lake water moves much too slow to carry any sediment in an efficient way. Transport of such pollutants is not considered in this article (however it is still possible to calculate it within the model).

5. Competition of transport processes

Dissolved and surface-carried pollutants can be transported in two different processes: dispersive transport (where the chaotic movement is the main cause of the pollution spreading) and current transport (where the water current makes pollutants move). These two processes compete with each other. The whole lake can then be divided into three zones:

- Dispersive zone – containing all the regions where the chaotic dispersion is more significant than the collective movement caused by the current;
- Competitive zone – where both processes should be taken into account;
- Current zone – the regions where the water current velocity exceeds the velocity of random movements at least by an order of magnitude.

It should be pointed out that for the zones other than the current one the knowledge of the current velocity in any given point is not enough to track the pollutants. Random movements of their particles should be simulated using the standard dissipative transport equation:

$$\frac{\partial D}{\partial t} = k\nabla^2 D, \tag{6}$$

where D is the local density of the pollutant and k is a constant coefficient.

The average velocity of these chaotic movements of water particles in a lake is very hard to determine. It is surely higher than the molecular diffusion velocity measured in a laboratory-still water (which is of the order of magnitude of 1/20 mm/s). In a lake, every random blow of wind, every boat, or even a fish or a water bird may cause chaotic local flows of much more significant magnitudes than that. On the other hand one should be extremely careful when a model returns very small velocity values of the collective flow. Values significantly less than 1 mm/s would most probably be overestimated due to the static viscosity of water – the so called "Bingham plastic effect" (see e.g., Kovacs 1981, and references therein). Basing on both of these facts, the velocity limits for the three zones are now set as follows: $V > 0.5$ cm/s → current zone, 0.5 cm/s > $V > 0.5$ mm/s → competitive zone, $V < 0.5$ mm/s → dispersive zone. Those values need experimental verification and may be adjusted in future. Especially the scale of the Bingham effect for the Dobczyce lake will be the aim of future research. Up to now, static viscosity was considered primarily for flows in porous media or for capillary flows, and its significance for slow flows in lakes is not known very well.

The zones change their size and shape as functions of several external variables. Two of them are obvious; they are: water level z, determining the shape of the lake (and the depth in each place), and the total flow in the lake Q. But another important

circumstance to take into account is the "mode" of the water body. As the Dobczyce lake is a retention reservoir it can be either in steady state mode (inflow = outflow), in increasing volume mode (inflow > outflow, the water level rises), or in decreasing volume mode (inflow < outflow, the water level goes down). In the two latter cases additional competitive and current zones appear in shallow regions of a relatively flat bed where some areas are subsequently flooded (outgoing currents) or dried (incoming currents). It should be noted however that a major part of the banks of the Dobczyce lake is sloppy enough to neglect these processes for them during all the work of that water body. Sample ranges of these zones are shown on Fig. 3.

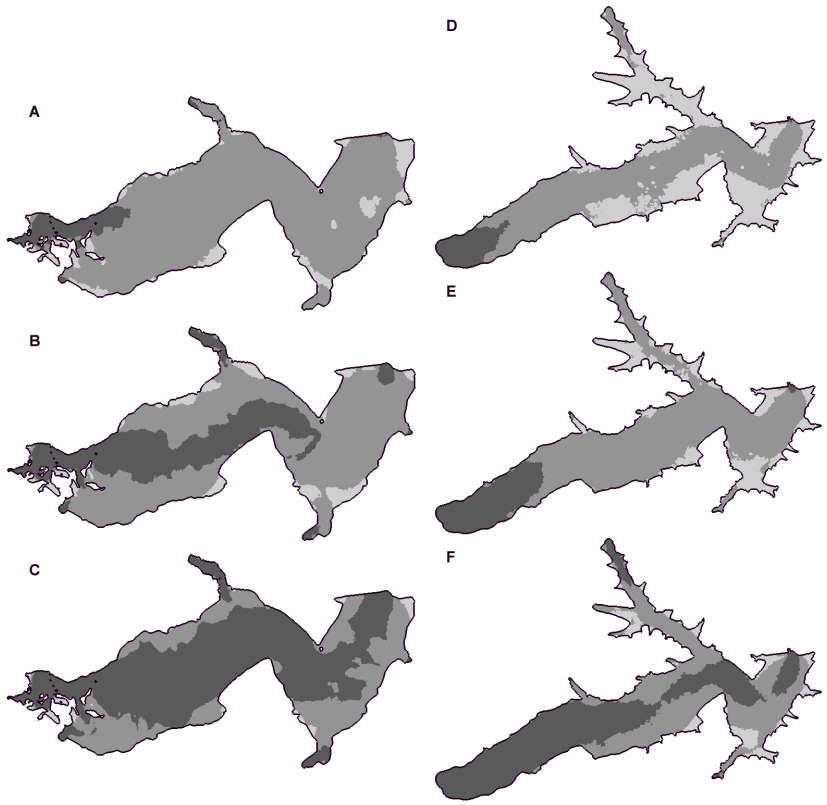

Fig. 3. The three types of transport zones: *dispersive* (light grey), *competitive* (grey), *and current* (dark grey) shown for different lake conditions: A, B, C – z = 260 m, Q = 12, 30, 50 m^3/s respectively; D, E, F – z = 272 m, Q = 12, 30, 50m^3/s, respectively. Please note that the scale is different for both columns (panels A, B and C are magnified for better clarity).

6. Modelling of pollution events

Apart from the ability to determine the pollution transport zones in the lake taken as a whole, the modelling tool is also capable to simulate actual pollution events either for risk management purposes or for forecasting the flow of contamination observed in reality. (It should be noted that the model is capable of providing answers in relatively short time thus it is possible to use it for real-time modelling of a given situation).

Example: Surface pollution originating from the Wolnica creek. Assumption: a patch of a surface-carried pollutant has been observed flowing into the lake from the stream of Wolnica. The lake is in the steady state, $z = 260$ m, $Q = 50$ m^3/s.

In this case the region of interest is almost entirely in the current zone. An appropriate method to simulate the contaminant movement is tracking the surface current lines that start by the inflow of Wolnica. This can be done by direct reading the tracking particles velocities from the map and moving them accordingly. Figure 4 shows subsequent stages of such simulation – starting from 1 hour from the event of entering the lake by the pollutant, ending at 20 hours from that event. For each frame the ends of the current lines denote the approximate position of the pollutant at the time shown in the upper right corner of the frame.

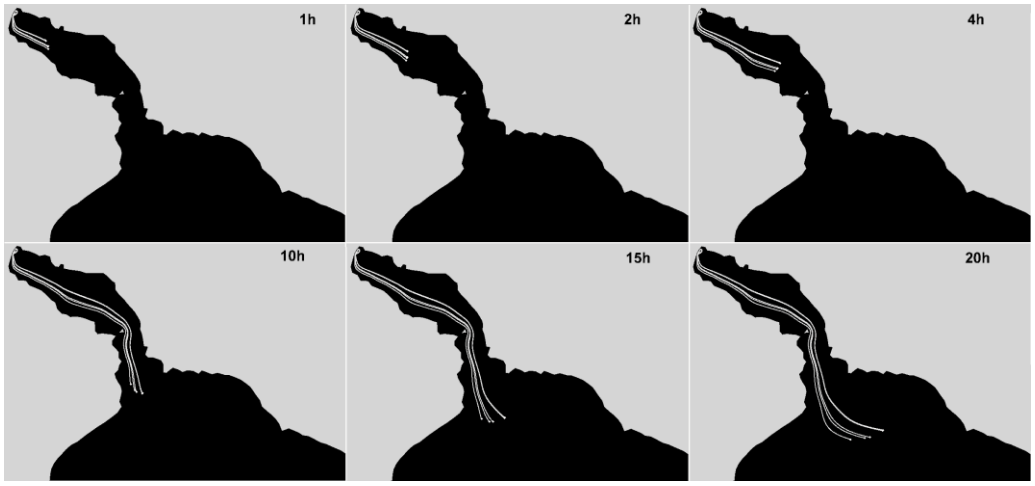

Fig. 4. Surface current line tracking for a simulation of pollution transport appearing at the Wolnica inflow. The timer starts when the pollutant reaches the lake, and it is shown for each frame in the upper right corner. Lake parameters: $z = 260$ m, $Q = 50$ m^3/s.

References

Froechlich, D.C. (2003), *Two-Dimensional Depth-Averaged Flow and Sediment Transport Model*, 207 pp.

Hachaj, P.S. (2007a), Modelling of a two-dimensional velocity field for the water flow in the lake of Dobczyce, *Publs. Inst. Geophys. Pol Acad. Sc.* **E-7 (401)**, 87-94.

Hachaj, P.S. (2007b), Modelowanie pola prędkości wody w zbiorniku dobczyckim – budowa siatki obliczeniowej i wstępne wyniki (Modelling of the velocity field in the Dobczyce lake – computational mesh construction and preliminary results), accepted for publication in *Czasopismo Techniczne. Seria Ś.*

Kovacs, G. (1981), *Seepage Hydraulics*, Budapest, 730 pp.

Nachlik, E., G. Mazurkiewicz-Boroń, A. Bojarski, J. Banaś, W. Styka, K. Słysz, and S. Reizer (2006), *Studium Możliwości Zmiany Funkcji Zbiornika Dobczyckiego i Jego Zlewni z Uwzględnieniem Ochrony Czystości Wody w Zbiorniku* (Study on possibilities of function change of the Dobczyce Lake, including water purity protection), Kraków, 170 pp.

Zienkiewicz, O.C., and R.L. Taylor (2002), A, *The Finite Element Method – Fluid Dynamics*, Oxford, 334 pp.

Accepted November 13, 2008

PUBLS. INST. GEOPHYS. POL. ACAD. SC., E-10 (406), 2008

Determination of the Range of Active Flow Zone in One-Dimensional Flow Models

Tomasz KAŁUŻA

Department of Hydraulic Engineering, Poznan University of Life Sciences
Piątkowska 94A, 60-649 Poznań, Poland
e-mail: kaltom@gmx.net

Abstract

This paper presents a method to calculate the active flow zone. The method assumes that the active part of the cross-section consists of the area which determines inbank capacity, and of the zone of interaction between the main channel and the floodplains. Using Pasche's method, the range of this zone has been determined for various vegetative clusters (trees and bushes) typical for river valleys.

1. Introduction

Natural, widespread floodplains are decisive for the transformation of flood and inundation waves. Their correct representation is both crucial and most difficult part of developing a one-dimensional flow model. The fundamental challenge is to determine the active cross-section area. Moreover, the range of active flow zone varies depending on the filling of high water channel. In Saint-Venant equations, the presence of widespread floodplains can be considered by splitting the river cross-section into the active cross-section Ac (flow-related) and the dead cross-section Ao, with the overall river cross-section being the sum of these two (Laks and Kałuża 2006). The active zone range can be determined using Pasche's (1984) method. Compared to other methods recommended by the German Association for Water Management, DVWK (1991), this method stands out by its good theoretical basis. It is also commonly used in practical engineering applications.

2. Materials and methods

Pasche assumed that the process of interaction slows the flow down in the main channel. Consequently, the depth-averaged flow velocity in the assumed dividing plane of the composite channel cross-section is v_T (Kubrak and Nachlik 2003).

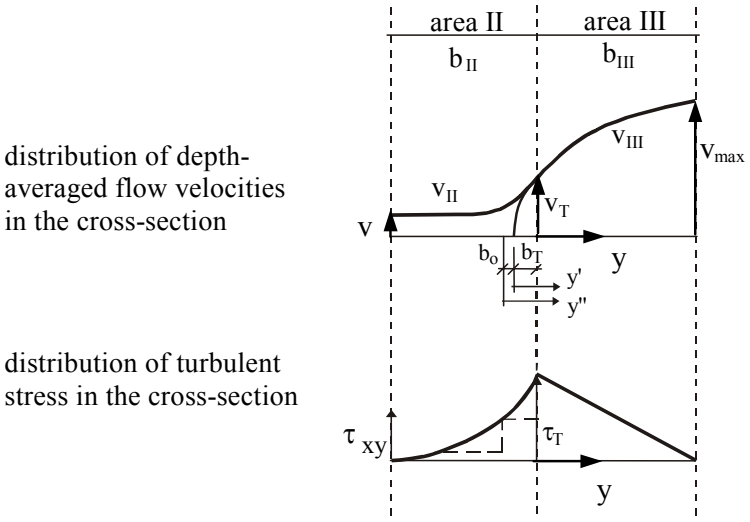

Fig. 1. Distribution of Reynold's velocity and stress in Pasche's method in compound cross-sections.

The assumption of variability of turbulent viscosity coefficient in the equation, according to Prandtl's assumption on the way of mixing, leads to linear variability of Reynold's stress over the channel width (Fig. 1) and logarithmic distribution of depth-averaged velocities in the channel:

$$\frac{v_{III}}{v_{*T}} = \frac{1}{\kappa} \ln \frac{y + b_T}{b_T} + C_T \quad \text{for} \quad 0 \le y \le b_{III} \tag{1}$$

where v_{III} is the velocity in area III [m/s], v_{*T} the dynamic velocity at the separation point between the main channel and the floodplain [m/s], κ is Karman's constant, b_T the distance from the hypothetic zero-velocity point to the origin of coordinates [m], and b_{III} is the width of area III [m].

By analysing the variation of depth-averaged velocity component in the direction of flow through the channel cross-section, Pasche marked off four hydrodynamic parts of this section: I – flow through the floodplain undisturbed by flow through the main channel, II – flow through the floodplain accelerated by flow through the main channel, III – flow through the main channel delayed by flow through the floodplain, IV – flow through the main channel undisturbed by flow through the floodplain. Tak-

ing into account the distribution of velocity one can assume that the active part of flow area consists of zones II and III. With zones III and IV (main channel) already delimited, the key difficulty is to determine the limits of zone II. Its range depends not only on water depth on floodplains, but first of all on the density of vegetation.

The origin of coordinates (y = 0) lies in the plane of separation. According to Pasche's original terminology, the integration constant C_T is called slip-velocity. This parameter is calculated from eq. (1) be setting the velocity over the area's edge to zero $v_{III}(y = 0) = v_T$:

$$C_T = \frac{v_T}{v_{*T}} \tag{2}$$

Next, Pasche considers the slip-velocity C_T as a function of Ω – a parameter which characterises the arrangement of trees in the channel cross-section by the spans a_x, a_y and the diameter d_p:

$$C_T = -3.27\, lg\,\Omega + 2.85 \tag{3}$$

$$\Omega = \left(0.07 \cdot \frac{a_{NL}}{a_x} \right)^{3.29} + \left(\frac{0.24 \cdot a_{NL}^{\,0.59} \left(C_W \cdot d_p \right)^{0.41}}{a_y} \right)^{0.95} \tag{4}$$

where a_{NL} denotes the length of Karman path resulting from flowing around a single tree:

$$a_{NL} = 128.87 \cdot d_p \cdot C_W \left(1 + \frac{g \cdot a_{NL} \cdot J}{0.5 \cdot v_T^2} \right)^{-2.143} \tag{5}$$

where J is the hydraulic gradient.

The drag coefficient C_W is determined for a single tree with an ideally two-dimensional flow. The value of C_W depends on the Reynold's number for high vegetation described by the relationship (Pasche 1984):

$$Re_p = \frac{v\, d_p}{\nu} \tag{6}$$

where v is the flow rate in the area with trees [m^3/s], d_p is the tree diameter [m], and ν is the coefficient of kinematic viscosity of water [m^2/s].

Pasche recommends to determine the width of interaction area from the equation:

$$b_{II} = \frac{c\, h_T}{\lambda_z \left(0.068 e^{0.56 C_T} - 0.056 \right)} \tag{7}$$

where λ_z is the coefficient of floodplain drag [-], h_T is the depth in the dividing plane, c = 1.0 for floodplains and c = 1.7 for slopes.

A detailed description of the computational procedure can also be found in a monograph edited by Kubrak and Nachlik (2003). The Pasche's method allows a fairly accurate assessment of the impact of density of vegetation in the floodplains on high water flow conditions. This refers both to the determination of floodplain drag coefficient, the value of C_T and the range of active zone. However, a detailed inventory of vegetative clusters is required. In practice, when analysing long river sections, a simplified classification of vegetation is often used, based on the study of aerial photographs, or on various types of thematic maps (e.g., maps of terrain cover). Naturally, this implies a certain classification of vegetation is used (e.g., dense forest, thin forest, dense bushes, thin bushes etc.). In this paper the values of C_T and the range of active zone b_{II} are studied for various types of typical vegetation clusters in the Warta river (Borysiak 1994). Apart from trees, two models of shrub structures are investigated: macro- and micro-structural. In the case of isolated shrubs occurring on a larger surface, the macro-structural model is used (diameter and span between shrubs are given), while in locations with wicker or other dense shrubs the micro-structural model, based on the study of diameter and span between individual shrub branches, is chosen.

3. Results and analysis

Using Pasche's method as presented in the previous section, computation of b_{II} and C_T was carried out for various diameters d_p and different span between individual plants a_x (it is assumed that $a_x = a_y$). Data typical for the Warta river section under study was assumed: depth h = 1.5 m, sand roughness for floodplains k_s = 0.15 m, hydraulic gradient J = 0.00017. For forested floodplains trunk diameter ranged from 0.1 to 0.4 m and the span between trunks from 0.7 to 6 m. C_T varied depending on trunk diameter (Fig. 2.) from 3.8 to 6.4 and from 3.8 to 4.7 for d_p = 0.1 m and d_p = 0.4 m, respectively. Given a fixed span between trunks a_x, C_T falls with the increase of diameter. At the same time, for a given diameter, C_T grows with the increase of span a_x. The dependence for the width b_{II} is similar (Fig. 2), the width increases as the span a_x rises and the diameter d_p falls. The minimum value obtained for b_{II} was 0.45 m for a_x = 1 m and d_p = 0.4 m, the maximum value was 52 m for a_x = 6 m and d_p = 0.1 m.

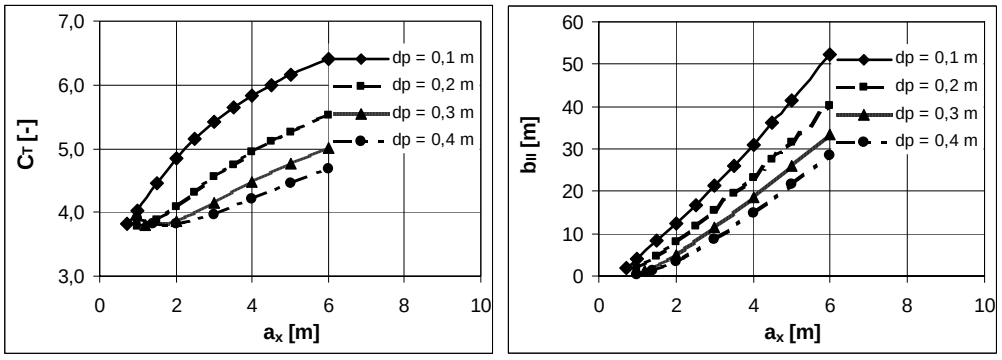

Fig. 2. C_T and width of b_{II} as a function of tree diameter and the span between trees.

In the case of shrub clusters with macro-structural parameters, i.e., given diameters from 1 to 3 m and distances between individual shrubs from 2 to 14 m, the value of C_T ranges from 3.9 to 4.2 m. Interestingly, for a fixed diameter the function describing the relationship between C_T and the span a_x has a distinct inflection point – namely the minimum value of C_T (Fig. 3). The study of b_{II} also revealed that similarly to trees the width of active zone grows as the diameter falls and as the span increases.

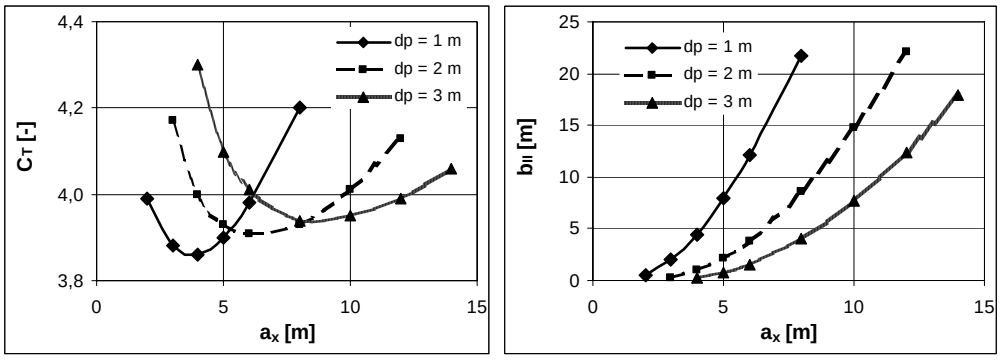

Fig. 3. C_T and width of b_{II} as a function of macro-structural parameters of shrubs.

For the case of micro-structure of shrubs the diameter of branches was assumed to vary from 0.005 to 0.02 m and the span between them from 0.05 to 0.3 m. In this case C_T ranges from 3.8 to 6.3. Given fixed span a_x, the value of C_T decreases with the increase of shrub branch diameter, and grows with the increase of span, given fixed diameter. Some departure from this rule was noted for d_p = 0.02 m, where an inflection point appeared for a_x = 0.1 m, similarly to the results for macro-structural parameters of shrubs. Results of the study of the interaction zone b_{II}, however, are similar to those for trees: the width grows as the diameter falls and the span between branches rises. In all the cases under study the interaction zone width did not exceed 3 m.

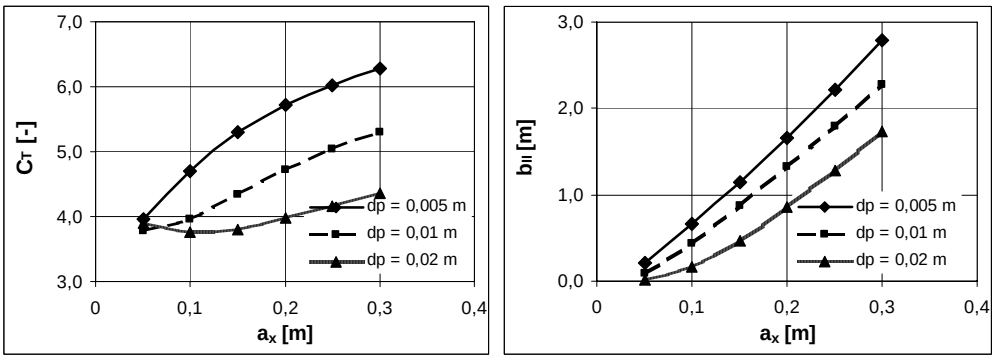

Fig. 4. C_T and width of b_{II} as a function of micro-structural parameters of shrubs.

The analyses of the width of interaction b_{II} as a function of plant parameters take into account the characteristics of vegetation density. This density appears in the well-known formula of Lindner (Pasche 1984) which describes λ_v – the friction factor of vegetation:

$$\lambda_V = \frac{4 \cdot h_p \cdot d_p \cdot c_{wR}}{a_x^2} \tag{8}$$

in the form of:

$$\varpi = \frac{d_p}{a_x^2} \tag{9}$$

Figure 5 shows typical dependences of the interaction zone width and C_T on the density of vegetation. Tree parameters and micro- and macro-structural parameters of shrubs have been selected. Figure 5 clearly shows the diversity of vegetative structures under analysis. Various density ranges translate to different types of relationships describing C_T and b_{II}. In the case of isolated bushes, a practically constant C_T equal approx. 4 can be assumed. However, for trees with density below 0.1 1/m, and for shrubs with density below 1 1/m, a steady increase of C_T can be seen. Different types of vegetation lead to different ranges of interference zone width, and consequently to different ranges of active zone. In the case of dense bushes it will amount to a little over 1 m, for isolated shrubs – up to approx. 10 m, and for trees – even over 100 m.

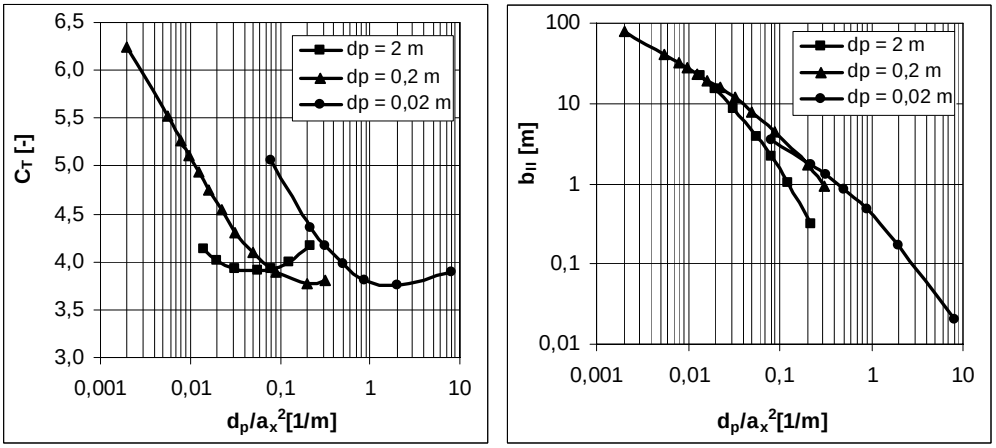

Fig. 5. Width of b_{II} and C_T as a function of vegetation density.

In order to confirm the significance of the influence of C_T on the interaction zone width, and thus on the change in the area of the active part of cross-section, computations carried out for the Warta river section comprising the Konińsko-Pyzderska valley, were used. To this end, the unsteady flow modelling system SPRUNER was used. The analyses covered two characteristic cross-sections of the river Warta, 346+000 and

358+450, for which computation of active surface as a function of C_T was carried out. The obtained results are shown in Figs. 6 and 7. The cross-section 346+000 (Fig. 6) located below the Konińsko-Pyzderska valley is compact and floodplains has no significant impact on the transformation of flood wave. The percentage of active zone area in the overall cross-section is considerably greater than in a cross-section with more complex shape (Fig. 7). With the decrease of slip coefficient for a given filling, the area of active zone increases, and for $C_T = 3$ coincides with the full cross-section at complete filling of channel (Fig. 6).

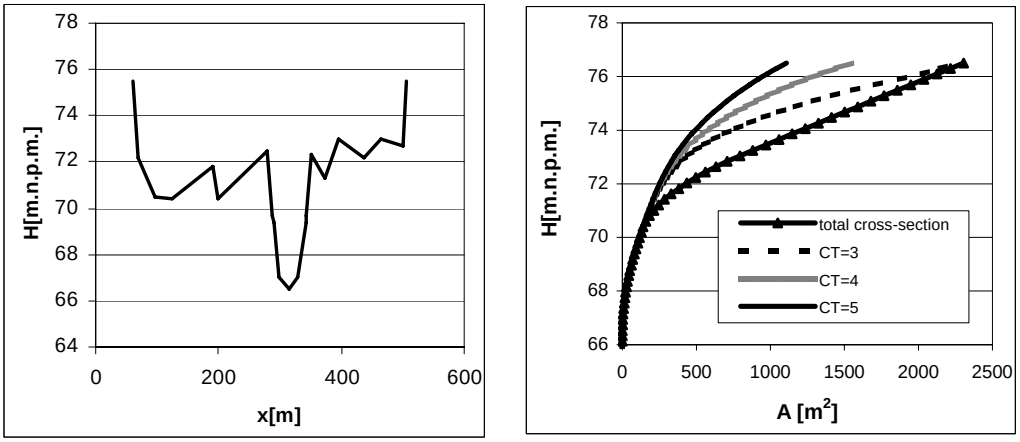

Fig. 6. The variation of the area of active part of Warta cross-section at km 346+000..

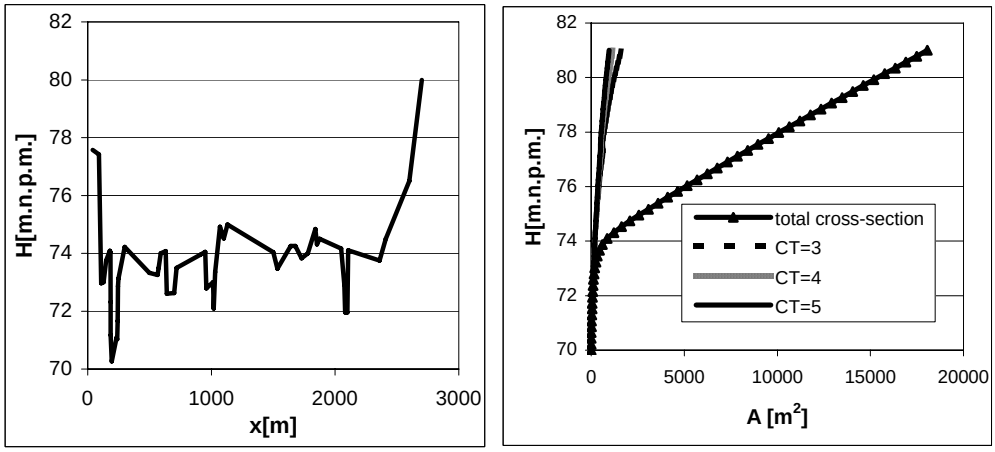

Fig. 7. The variation of the area of active part of Warta cross-section at km 358+450.

The cross-section 358+450, located in the Konińsko-Pyzderska valley, has natural, widespread floodplains, which are decisive for the transformation of flood wave. The percentage of active zone area in the overall cross-section is considerably smaller and even for the minimum value $C_T = 3$ does not coincide with full cross-section.

4. Summary and conclusions

The study of the method of determining the active flow zone led us to formulate the following remarks and observations:

- In the method of Pasche various vegetative clusters (trees and single or compact shrubs) shape the function of C_T and the range of interaction zone in different ways.
- For vegetation structures with diversified density three width ranges of b_{II} have been obtained: slightly over 1 m for dense bushes, up to approx. 10 m for isolated shrubs and over 100 m for trees.
- The described method of representing the active flow zone in one-dimensional models based on de Saint-Venant equations allows better representation of the transformation of flow conditions through widespread river floodplains. A correct assessment of vegetative structures and an appropriate determination of C_T are important.

Acknowledgments. The work was supported by grant of the Polish Ministry of Scientific Research and Information Technology, Grant No. N305 078 32/2740.

References

Borysiak, J. (1994), Struktura aluwialnej roślinności lądowej środkowego i dolnego biegu Warty, *Wydawnictwa Naukowe UAM, Poznań*.

DVWK (1991), Hydraulische Berechnung von Fließgewässern, DVWK – Merkblätter 220/1991, *Kommissionsvertrieb Verlag Paul Parey, Hamburg und Berlin*, in German.

Kubrak, J., and E. Nachlik (2003), Hydrauliczne podstawy obliczania przepustowości koryt rzecznych, *Wydawnictwo SGGW, Warszawa*.

Laks, I., and T. Kałuża (2006), Oddziaływanie doliny konińsko-pyzderskiej i polderu Golina na transformacje fal powodziowych rzeki Warty, *Zeszyty Naukowe Akademii Rolniczej we Wrocławiu*, nr **534**, 175-183.

Pasche, E. (1984), Turbulenzmechanismen in naturnahen Fließgewässern und die Möglichkeiten ihrer mathematischen Erfassung. *Mitt. Institut für Wasserbau und Wasserwirtschaft, RWTH Aachen*, Heft **52**, Aachen.

Wosiewicz, B., I. Laks, and Z. Sroka (1996), Computer system of flow simulation for the Warta River, *Prace Naukowe Instytutu Geotechniki i Hydromechaniki Politechniki Wrocławskiej, Seria Konferencje* **38**, Wrocław.

Accepted December 23, 2008

PUBLS. INST. GEOPHYS. POL. ACAD. SC., E-10 (406), 2008

Numerical Simulations of Storm Surge Disaster due to Typoon Maemi in Korea

Cha-kyum KIM[1] and Jong Tae LEE[2]

[1]Department of Civil Engineering, Gyeongnam Provincial Namhae College
195 Nambyun-ri, Namhae-up, Namhae-gun, Gyeongnam, 668-801, Korea
e-mail: kick@namhae.ac.kr

[2]Head of Urban Flood Disaster Management Research Center, Kyonggi University
Chungjung-ro, Seodaemoon-gu, Seoul, 120-702, Korea
e-mail: jtlee@kyonggi.ac.kr

Abstract

Three dimensional numerical simulations were carried out to calculate the storm surge and inundation area due to Typoon Maemi. The typoon landed on the southern coast of Korean Peninsula at 21 hr on 12 September 2003 with a central pressure of 950 hPa. It caused a terrific life damage with more than 130 people missing and dead and the property damage of about 5 billion US dollars. The residential and commercial area facing the Masan Bay located in the southern coast of Korea was heavily flooded and underground facilities suffered from the inundation by the storm surge. The simulated storm surge and the inundation area showed good agreement with field data.

1. Introduction

Typoon Maemi landed on the southern coast of Korea at 21 hr on 12 September 2003 with a central pressure and a progression speed of approximately 950 hPa and 45 km/h, respectively. The typoon caused an extremely high sea surface height, combined with astronomical high tide, severe storm surge and high waves. In Masan city facing Masan Bay, the residential and commercial area was flooded by the storm surge. It caused a terrific life damage with more than 130 people missing and dead and the property damage of about 5 billion US dollars. The maximum storm surge in Masan Port located in the southern coast of Korea was approximately 2.3 m. While Typoon Maemi was passing Masan Bay, the level of astronomical tide nearly reached the high water of a spring tide. A three dimensional numerical model was established to calculate the storm surge and inundation due to storm surge. A field survey of storm surge

traces in Masan city was carried out to evaluate the inundation water depth. Figure 1 shows the track of Typoon Maemi. Figures 2 and 3 show the air pressure and wind speed in Masan, Pusan and Yeosu, respectively.

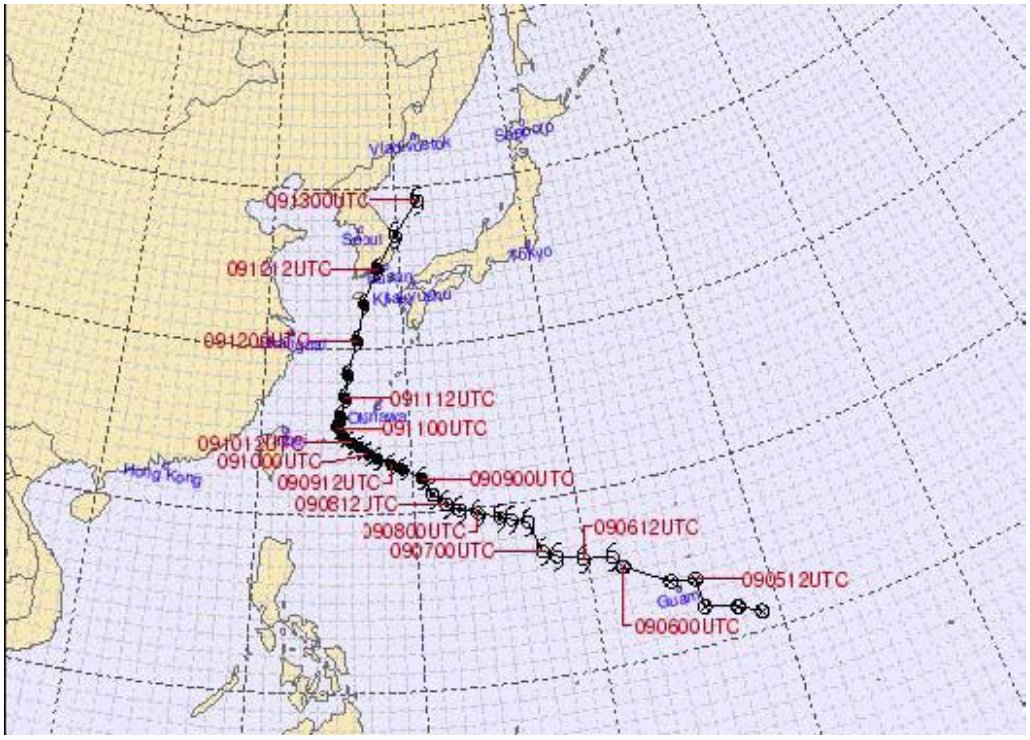

Fig. 1. Track of Typoon Maemi in September 2003.

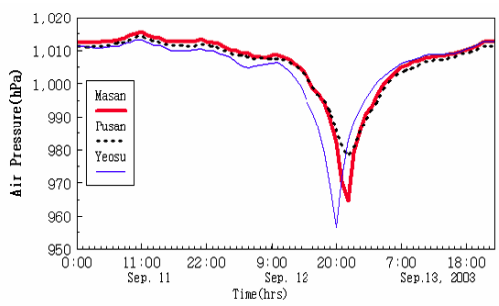

Fig. 2. Air pressure in Masan, Pusan and Yeosu.

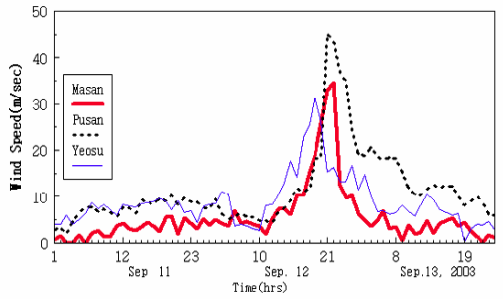

Fig. 3. Wind speed in Masan, Pusan and Yeosu.

2. Field survey

We measured the inundation trace in Masan city on September 18, 2003. Figure 4 shows the distribution of the inundation area obtained in the field survey. We deter-

mined the area by interviewing to witnesses and measuring the mud lines left on the some buildings.

According to some workers at the fishing wharf of Masan Port, the water level reached the level shown in Photo 1. The level was about 2 m higher than the maximum tide at Masan tide station near the wharf.

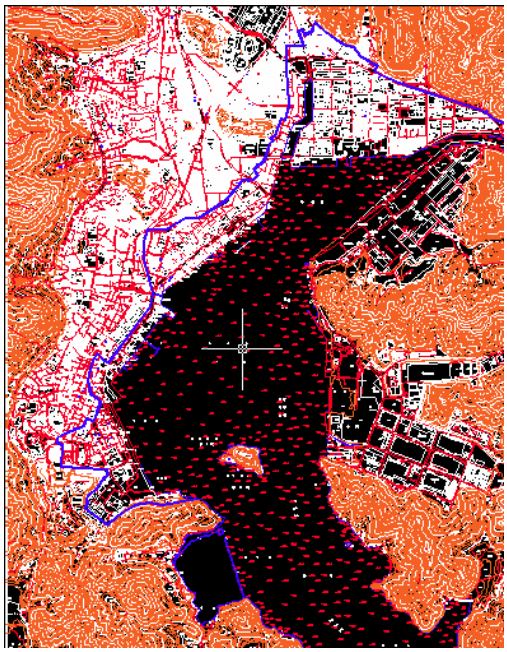

Fig. 4. Inundation area in Masan city (blue line: inundated area).

Photo 1. Water level according to witness at the fishing wharf of Masan Port.

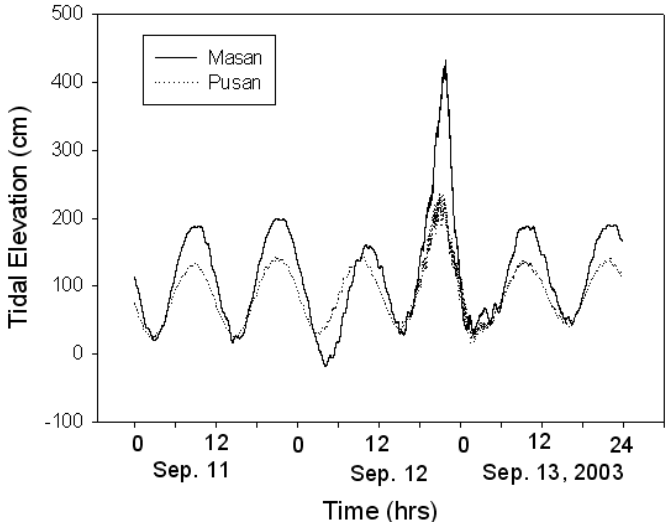

Fig. 5. Observed sea levels at Masan and Pusan Ports during Typoon Maemi.

Figure 5 shows the water level variations at the tide observatory station of Masan and Pusan Ports, which was based on the data provided by the National Oceanographic Research Institute, Korea. The water level in Masan Port indicates that the level reached approximately 4.3 m above the datum line, and the high tide and the storm surge occurred simultaneously. The astronomical tidal level was 2.0 m, and so the storm surge became 2.3 m.

3. Numerical simulation

Numerical experiments were carried out to simulate the storm surge and the inundation due to Typoon Maemi using a three-dimensional numerical storm surge model. The model was developed by the authors (Kim and Lee 2007) using an ADI (Alternating Direction Implicit) finite difference and layer-level hybrid scheme. Figure 6 shows the domain for the storm surge simulation at far field. The time step was 20 sec, and the horizontal grid size was 500 m. The area was discretized by 580×388 points in the horizontal and 4 layers over the depth, and the vertical grid size varied from 2 to 10 m. The domain (Masan Bay) for the inundation simulation at near field was given in Fig. 1. The time step was 3 sec, and the horizontal grid size was 30 m. The area was discretized by 200×280 points in the horizontal and 4 layers over the depth. Numerical experiments with and without combined M2, S2, K1 and O1 tidal constituents were conducted, where M2 and S2 are semidiurnal components by principal lunar and principal solar, respectively, and K1 and O1 are diurnal components by lunisolar and principal lunar, respectively.

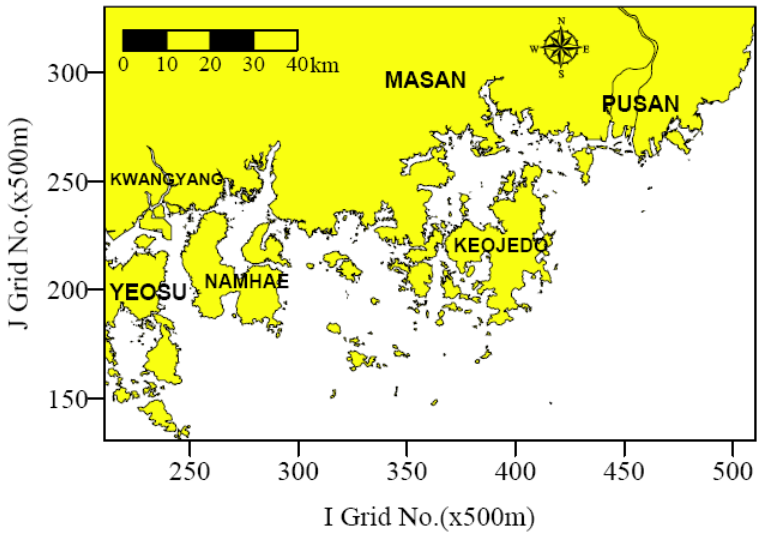

Fig. 6. Geography and simulation domain at far field.

The approximate highest high water (M2+S2+K1+O1) in Masan Bay is less than 1 m. The meteorological inputs (atmospheric pressure and wind stresses) for storm surge were calculated by a parametric typoon model, namely the Hydromet-Rankin

Vortex Model (Holland 1980, Bretschneider *et al*. 1984). The major inputs of the model are locations of typoon center, central atmospheric pressure and radius for maximum wind speed. The meteorological inputs at each hour interval were used in the storm surge model for each grid system. Wind drag coefficients were calculated with Wu (1982) formula. Storm surge height was defined by observed sea level minus predicted tidal level, where tidal elevations were predicted using 64 harmonic constituents based on 1 year record.

4. Model results

4.1 Storm surge hindcast

Figure 7 shows the comparison of the computed and observed storm surges at Masan Port. The computed maximum storm surge was 2.4 m, whereas the observed one was 2.3 m. The hindcasted storm surge was in agreement with the observed one, around its peak. It seems that the negative surge in the tide record was not related with the suction effect by air pressure depression and wind-drift effect of the typoon. The observed level was much lower than the computed level from 3 hr to 10 hr on 12 September 2003, but its reason is still unknown. Except for that, the computed tidal level agrees with the observed one.

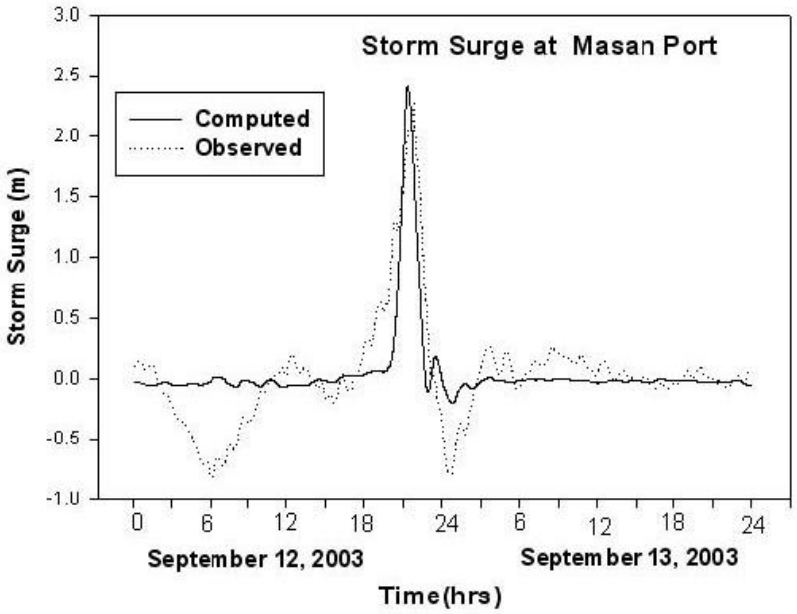

Fig. 7. Comparison of computed and observed storm surges at Masan Port.

4.2 Inundation simulation

Figures 8 and 9 show the observed and computed inundation areas in Masan city at 22 hr on 12 September 2003, respectively. The maximum inundation height reached 1.5 m at the wharf and 1 m or more at the reward city area. In fact, very clear inunda-

tion traces remained on the walls inside and outside of the buildings within 500 m from the wharf. The computed inundation area was in good agreement with the observed one.

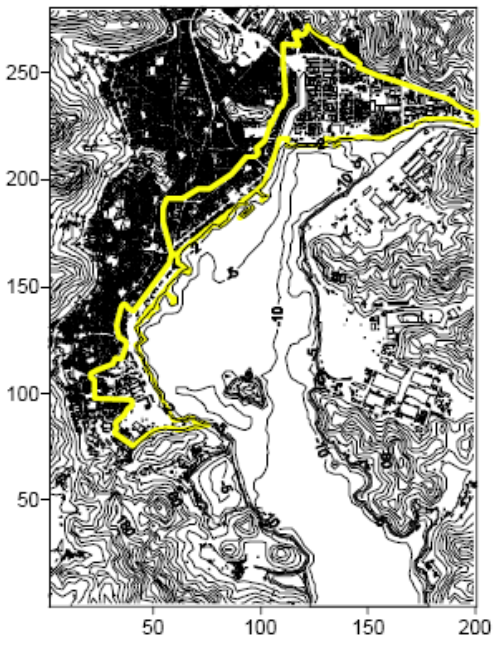

Fig. 8. Observed inundation area (yellow line).

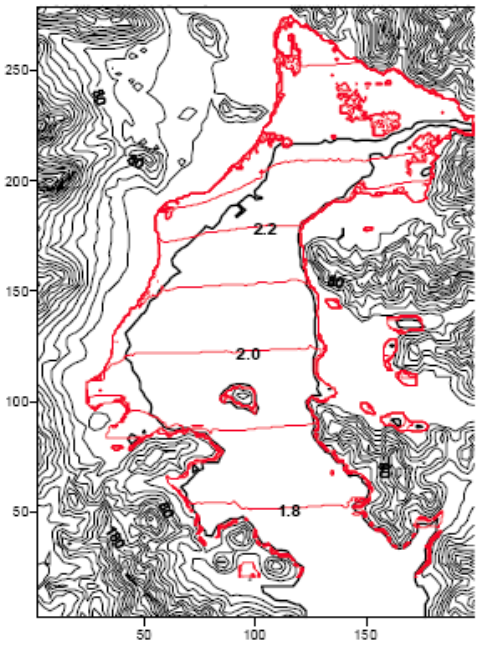

Fig. 9. Computed inundation area (red line).

5. Conclusion and discussion

The wind field of Typoon Maemi was hindcasted by the Hydromet-Rankin Vortex Model. The storm surge and the inundation area were simulated by the three-dimensional numerical model. Model results were sensitive to meteorological forces. The results showed that the storm surge and the inundation area obtained by the numerical model were in good agreement with the observed ones. It was confirmed that the storm surge exceeded 2 m in Masan Bay. The model may be an effective tool to understand the storm surge and inundation, and to prevent the disaster from a typoon. However, it is necessary to improve the numerical model to obtain a more accurate result, and to discuss on the storm surge and the inundation phenomena in more detail.

Acknowledgments. This study was supported by the 2003 Innovation Project for Construction Technology (03-SANHAKYOUN-C01-01) through the Urban Flood Disaster Management Research Center in KICTEP of MLTM KOREA.

References

Bretschneider, C.L., and J.M. Lo (1984), A Rankin vortex number as a guide to the selection of a model hurricane. **In:** *Proc. 19th ICCE*, 147-161.

Holland, G.J. (1980), An analytic model of the wind and pressure profiles in hurricanes, *Monthly Weather Review* **108**, 1212-1218.

Kim, C.-K., and J.T. Lee (2007), Storm surge hindcasting using a three dimensional numerical model. **In:** *Proc. 20th Annual Conference, PACON 2007*, A-29.

Wu, J. (1982), Wind-stress coefficients over sea surface from breeze to hurricane, *J. Geophys. Res.* **87**, 9704-9706.

Accepted November 13, 2008

PUBLS. INST. GEOPHYS. POL. ACAD. SC., E-10 (406), 2008

Random-Vortex Method for Free Surface Boundary Problem

Stanisław KOSTECKI and Wojciech RĘDOWICZ

Institute of Geotechnics and Hydrotechnics, Wrocław University of Technology
Wybrzeże Wyspiańskiego 27, 50-370 Wrocław, Poland
e-mails: stanislaw.kostecki@pwr.wroc.pl, wojciech.redowicz@pwr.wroc.pl

Abstract

In this paper the random-vortex method is applied to the two-dimensional flow of an incompressible viscous liquid. A formula for the boundary condition on the free surface and a formula for the no-slip and no-through boundary conditions are derived. The flow problem is solved using a fractional step algorithm. In the first step a velocity field is calculated from a vorticity advection equation. In the next steps the field is modified until it satisfies the boundary conditions. The condition on the free surface consists in the generation of a vortex sheet as a function of the free surface curvature and the liquid velocity components. The condition on the solid boundary is fulfilled by defining a vortex sheet on the boundary through a Fredholm equation of the 2nd kind and by calculating an additional potential velocity field. The diffusion of vorticity is determined by the random walk method. It is shown how the method works using as an example a stationary flat flow around a flap gate. The results of the calculations are compared with measurements performed on a flap gate model and good agreement is obtained.

1. Introduction

The free surface flow problem considered here concerns two media – a liquid and a gas – being in contact with each other. The problem is of considerable interest for studies of surface waves, gas bubble deformation, surface turbulence generation and for engineering calculations of the flow in an open trough and the flow around a hydrotechnic structure.

The free surface problem has been studied for several decades, but the interest in it has significantly grown in recent years. Batchelor (1967) presented a simple vorticity/free surface curvature dependence for the two-dimensional steady flow of an in-

compressible non-viscous liquid. Longuet (1998) provided a proof of the above solution. The mechanism of vorticity generation on a free surface in the two-dimensional system was presented by Lundgren and Koumoutsakos (1999) who proposed to calculate the vortex sheet on the free surface from the condition of consistency of pressure on this surface and to solve the vorticity diffusion equation with a boundary condition derived on the basis of the vorticity generated on the interface. The correlation between the deformation velocity tensor components and the vorticity components on liquid/gas interface, generalized to the 3-D system, was presented by Dopazo *et al*. (2000) who also derived an equation for the transport of the vorticity concentrated on the layer constituting the interface. Baker and Beale (2004) investigated the problem of the motion of the boundary separating two incompressible, non-viscous liquids, using the vortex blob method.

The present paper presents a mathematical description of the flat flow of an incompressible viscous liquid, expressed in terms of velocity and vorticity with a boundary condition on the free surface. The flow problem was solved by the random-vortex method. In order to show how the method works it was applied to a case of the flow around a weir flap gate.

2. Random-vortex method

The evolution of a vorticity field for the flow of an incompressible viscous liquid can be determined form the Navier-Stokes equation written in terms of vorticity and velocity as

$$\frac{\partial \omega}{\partial t} + \mathbf{u} \cdot \nabla \omega - \nu \nabla^2 \omega = 0, \qquad \mathbf{x} = [x_1, x_2], \qquad t > 0, \tag{1}$$

which expresses vorticity transport (in this form it is called the Helmholtz equation). Here velocity vector $\mathbf{u} = [u_1, u_2]$ and ν is a dynamic viscosity coefficient. Since for flat flows the vorticity vector is orthogonal to **u**, is treated as a scalar of the value $\omega = \partial u_2 / \partial x_1 - \partial u_1 / \partial x_2$.

Solution by the random (stochastic) vortex method consists in the decomposition of the vorticity transport (1) into two stages: advection and diffusion, written as:

– for advection (in a Lagrangian frame)

$$\frac{\mathrm{d}\,\omega\big(\mathbf{X}(\boldsymbol{\alpha},t),t\big)}{\mathrm{d}\,t} = 0 \tag{2}$$

$$\frac{d\mathbf{X}(\boldsymbol{\alpha},t)}{dt} = \mathbf{u}\big(\mathbf{X}(\boldsymbol{\alpha},t),t\big) \tag{3}$$

– for diffusion

$$\frac{\partial \omega(\mathbf{x},t)}{\partial t} - \nu \nabla^2 \omega(\mathbf{x},t) = 0 \tag{4}$$

where: $\mathbf{X}(\boldsymbol{\alpha},t)$ and $\boldsymbol{\alpha}=(\alpha_1,\alpha_2)=\mathbf{X}(\boldsymbol{\alpha},t)\big|_{t=0}$ stand for, respectively, the trajectory and initial position of a liquid particle (a vorticity carrier). According to relation (2), vorticity is preserved along the trajectory of the particle

$$\omega\big(\mathbf{X}(\boldsymbol{\alpha},t),t\big)=\omega_0(\boldsymbol{\alpha}) \tag{5}$$

The velocity field is recovered from the vorticity field on the basis of the generalized Biot-Savart law (Majda and Bertozzi, 2002)

$$\mathbf{u}(\mathbf{x},t)=\int_{\mathbb{R}^2}\mathbf{K}\big(\mathbf{x}-\mathbf{X}(\boldsymbol{\alpha},t)\big)\omega\big(\mathbf{X}(\boldsymbol{\alpha},t),t\big)d\mathbf{X}(\boldsymbol{\alpha},t)\,, \tag{6}$$

where $\mathbf{K}(\mathbf{x})=\dfrac{1}{2\pi}\left(-\dfrac{x_2}{|\mathbf{x}|^2},\dfrac{x_1}{|\mathbf{x}|^2}\right)$, $\quad |\mathbf{x}|=\sqrt{x_1{}^2+x_2{}^2}$.

By combining equations (3), (5) and (6) one gets the following integrodifferential relation for the particle trajectory

$$\frac{d\mathbf{X}(\boldsymbol{\alpha},t)}{dt}=\int_{\mathbb{R}^2}\mathbf{K}\big(\mathbf{X}(\boldsymbol{\alpha},t)-\mathbf{X}(\boldsymbol{\alpha}',t)\big)\omega_0(\boldsymbol{\alpha}')d\mathbf{X}(\boldsymbol{\alpha}',t)\,, \tag{7}$$

In the vortex method one searches for approximate solution (7) by discretizing the vorticity field in the flow region and mollifying singular kernel $\mathbf{K}(\mathbf{x})$. The discretization consists in replacing the continuous field with a finite set of vortex particles. The approximate trajectory of the particle at the initial instant at $\boldsymbol{\alpha}_i$ shall be denoted as $\mathbf{X}^h(\boldsymbol{\alpha}_i,t)=\mathbf{X}_i^h(t)$.

The kernel can be mollified through a convolution with mollifying function $\mathbf{K}_\varepsilon(\mathbf{x})=\big(\mathbf{K}*f_\varepsilon\big)(\mathbf{x})$ in the general form: $f_\varepsilon(\mathbf{x})=\varepsilon^{-2}\cdot f(\varepsilon^{-1}\mathbf{x})$, $\varepsilon>0$, where ε is a cut radius (a scaling parameter). Basic function $f(\mathbf{x})$, called a cut function, is assumed to be smooth and axially symmetric, with a limited (or rapidly decreasing to zero in infinity) carrier, and fulfilling specific conditions ensuring the convergence and stability of the method (Majda and Bertozzi 2002). Integrodifferential relation (7) after flow region discretization and kernel approximation becomes the following system of ordinary differential equations:

$$\frac{d\mathbf{X}_i^{h,\varepsilon}(t)}{dt}=\sum_{j\in\Lambda}\mathbf{K}_\varepsilon\left(\mathbf{X}_i^{h,\varepsilon}(t)-\mathbf{X}_j^{h,\varepsilon}(t)\right)\omega_0(\alpha_j)h^2,\ \ i,j\in\Lambda=Z^2\,. \tag{8}$$

In the viscous splitting algorithm, vorticity particles are advanced with the velocity of local advection in the first substep. In the second substep, diffusion acts on the particles, changing the vorticity field.

Since it exploits the consistency between the diffusion equation solution and the description of the Brownian movement of particles (vorticity carriers), the diffusion problem in the random vortex method is solved by the random walk method. This means that the particles are subject to random displacement $\boldsymbol{\eta}(t)=\big(\eta_1(t),\,\eta_2(t)\big)$,

which is determined from a normal (Gaussian) distribution with the expected value equal to zero and variance $2t\nu$ (Chorin 1973, Kostecki 2007).

The evolution of vorticity, consisting in the displacement of vortex particles through advection and diffusion, is analyzed in discrete time steps and it can be calculated by, for example, the Euler method

$$\widehat{\mathbf{X}}_i^{h,\varepsilon}(t+\Delta t) = \mathbf{X}_i^{h,\varepsilon}(t) + \Delta t \mathbf{u}_i^{h,\varepsilon}(t) + \boldsymbol{\eta}(t) \tag{9}$$

where $\mathbf{u}_i^{h,\varepsilon}(t) = \sum_{j\in\Lambda} \mathbf{K}_\varepsilon\left(\mathbf{X}_i^{h,\varepsilon}(t) - \mathbf{X}_j^{h,\varepsilon}(t)\right)\Gamma_{0j}$ and $\Gamma_{0j} = \omega_0(\alpha_j)h^2$ is a vortex particle circulation. On the basis of the calculated trajectories the velocity field, the vorticity field and the stream function can be recovered from the following relations:

$$\mathbf{u}^{h,\varepsilon}(\mathbf{x},t) = \sum_{j\in\Lambda} \mathbf{K}_\varepsilon\left(\mathbf{x} - \mathbf{X}_j^{h,\varepsilon}(\boldsymbol{\alpha}_j,t)\right)\Gamma_{0j} \tag{10}$$

$$\omega^{h,\varepsilon}(\mathbf{x},t) = \sum_{j\in\Lambda} f_\varepsilon\left(\mathbf{x} - \mathbf{X}_j^{h,\varepsilon}(\boldsymbol{\alpha}_j,t)\right)\Gamma_{0j}, \tag{11}$$

$$\psi^{h,\varepsilon}(\mathbf{x},t) = \sum_{j\in\Lambda} G_\varepsilon\left(\mathbf{x} - \mathbf{X}_j^{h,\varepsilon}(t)\right)\Gamma_{0j} \tag{12}$$

where $G_\varepsilon(\mathbf{x}) = (G * f_\varepsilon)(\mathbf{x})$, $G(\mathbf{x}) = -(2\pi)^{-1}\ln|\mathbf{x}|$. The above equations describe the flow in the whole plane in which particles can move freely. In most engineering problems there is a problem of the boundary on which specific conditions must be fulfilled.

3. Boundary conditions

Let us consider a flat flow in region *D* confined by boundary *S*. The boundary consists of the following segments:

- a solid boundary on which the velocity of the liquid is equal to that of the boundary,
- an inlet with a prescribed velocity distribution,
- an outlet with a prescribed direction of velocity vectors,
- the free surface of water, on which the friction force is assumed to be equal to zero.
- The above conditions are briefly discussed with regard to their application to the vortex method in the subsections below.

3.1 Conditions for solid boundary, inlet and outlet

Two conditions, no-through-flow and no-slip-flow, should be considered for an impervious solid boundary. A method consisting in determining a potential velocity field which after superposition with the vortex velocity field fulfils the condition of disappearance of the liquid velocity component normal to the boundary is employed to satisfy the former condition. The potential velocity field can be expressed by a gradient

from the velocity potential function, which means that the rotation of the field disappears and the field does not change the vorticity of the flow region.

It is best to represent the solution of the potential flow problem with the Dirichlet boundary condition by a potential stream function which satisfies the Laplace equation.

$$\nabla^2 \psi_p(\mathbf{x},t) = 0, \qquad \psi_p(\mathbf{x},t) \in D, \qquad t \geq 0, \quad \mathbf{x} \in \mathbb{R}^2 \tag{13}$$

$$\psi_p(\mathbf{x},t) = \psi_b(\mathbf{x},t) - \psi_\omega(\mathbf{x},t), \qquad \mathbf{x} \in S \tag{14}$$

where ψ_ω is the vortex stream function whose approximation is given by relation (12). Stream function ψ_b values on the boundary are known and, for example, for the channel bottom and the free surface they amount, respectively, to $\psi_b = 0$ $\psi_b = Q$, where Q is the volume flow rate. At the channel inlet, if the velocity profile is known, ψ_b can be calculated by integrating the normal velocity component along the boundary segment constituting the inlet. The part of boundary S between points A and B on which one can assume a Neumann condition according to which the velocity vectors are normal to the boundary, constitutes the outlet.

$$\frac{\partial \psi_p(\mathbf{x},t)}{\partial n} = 0, \qquad \mathbf{x} \in \widehat{AB} \tag{15}$$

Problem (3)-(15) is solved here by the boundary element method.

The no-slip-flow condition follows from the generation of friction forces between the liquid and the solid boundary whereby the velocity of the boundary and that of the liquid are consistent in the direction tangent $\hat{\mathbf{t}}$ to the boundary. The condition can be expressed by the relation:

$$\left(\mathbf{u}_\omega(\mathbf{x},t) + \mathbf{u}_p(\mathbf{x},t) - \mathbf{U}_b(\mathbf{x},t)\right) \cdot \hat{\mathbf{t}} = 0, \qquad \mathbf{x} \in S \tag{16}$$

where: $\mathbf{u}_\omega$ = the vector of the vortex velocity from equation (10), $\mathbf{u}_p = \nabla \psi_p$ = the potential velocity, $\mathbf{U}_b$ = the velocity of the boundary; $\mathbf{U}_b = 0$ when the boundary is stationary (e.g., the channel bottom) and $\mathbf{U}_b \neq 0$ for a moving boundary (e.g., a hydrotechnical gate).

Friction produces a torque on the liquid particles adhering to the boundary whereby vorticity is generated on the latter. In the present calculations this phenomenon is modelled by vortex sheet $\gamma(\mathbf{x})$ forming on the solid boundary. After its generation the vortex sheet was discretized to vortex particles:

$$\Gamma_i = -\int_{ds_i} \gamma(\mathbf{x}) \cdot dS, \qquad \mathbf{x} \in S \tag{17}$$

where ds_i are the lengths of the elementary segments into which the boundary is divided, in which the sheets are turned into vortex particles. As a result of this operation, vortex particles are generated in the centres of the segments in each time step, compensating the jump of the tangent velocity component on the solid boundary.

The intensity of vortex sheet $\gamma(\mathbf{x})$ can be determined by solving the Fredholm integral equation of the 2nd kind derived by the author (Kostecki 2008):

$$\pm\gamma(\boldsymbol{\xi}) = -2\left(\mathbf{u}_{\omega} + \mathbf{u}_{p} - \mathbf{U}_{b}\right)(\boldsymbol{\xi})\cdot\hat{\mathbf{t}}(\boldsymbol{\xi}) + \frac{1}{\pi}\int_{S}\gamma(\mathbf{x})\frac{\partial \ln|\mathbf{x}-\boldsymbol{\xi}|}{\partial\hat{\mathbf{n}}(\boldsymbol{\xi})}dS(\mathbf{x}),\ \mathbf{x},\boldsymbol{\xi}\in S \tag{18}$$

where: $\hat{\mathbf{n}}(\boldsymbol{\xi})$ and $\hat{\mathbf{t}}(\boldsymbol{\xi})$ are unit vectors, respectively, normal and tangent to the boundary at point $\boldsymbol{\xi}$. The sign on the left side of the equation is positive when the vector normal to the boundary is directed outwards the flow region.

3.2 Free surface boundary condition

The free surface constitutes a boundary between the two fluids, on which the velocities of the two fluids' particles are equal (Fig. 1a). Hence, neglecting the surface tension, one can assume that the stresses on the two sides of the sheet are at equilibrium. For an incompressible Newtonian fluid the stresses on surface element *ds* with normal vector $\hat{\mathbf{n}}$ are given by the relation:

$$\tau_{\mathbf{n}} = \mathbf{T}\cdot\hat{\mathbf{n}} = \left(-p\mathbf{I} + 2\mu\mathbf{D}\right)\cdot\hat{\mathbf{n}} \tag{19}$$

where: $\mathbf{T}$ is the stress tensor, p pressure, μ the dynamic viscosity coefficient, and $\mathbf{D}$ the strain-rate tensor.

Assuming that the density and viscosity of fluid 2 (gas) are low in comparison to those of liquid 1, the stresses in fluid 2 can be neglected. Then the equation of equilibrium of shear stress on the free surface is described by the relation (Lundgren and Koumoutsakos 1999)

$$\hat{\mathbf{t}}\cdot\mathbf{D}\cdot\hat{\mathbf{n}} = \hat{\mathbf{t}}\cdot\left(\nabla\mathbf{u} + \nabla\mathbf{u}^{T}\right)\cdot\hat{\mathbf{n}} = \hat{\mathbf{t}}\cdot\nabla\mathbf{u}\cdot\hat{\mathbf{n}} + \hat{\mathbf{n}}\cdot\nabla\mathbf{u}\cdot\hat{\mathbf{t}} = 0 \tag{20}$$

For vorticity in the flat flow the following relations hold:

$$\omega = \hat{\mathbf{n}}\cdot\left(\nabla\mathbf{u} - \nabla\mathbf{u}^{T}\right)\cdot\hat{\mathbf{t}} = \hat{\mathbf{n}}\cdot\nabla\mathbf{u}\cdot\hat{\mathbf{t}} - \hat{\mathbf{t}}\cdot\nabla\mathbf{u}\cdot\hat{\mathbf{n}} \tag{21}$$

Combining (20) and (21) one gets

$$\omega = -2\hat{\mathbf{t}}\cdot\nabla\mathbf{u}\cdot\hat{\mathbf{n}} \tag{22}$$

Since $\hat{\mathbf{t}}\cdot\nabla\mathbf{u} = \dfrac{\partial\mathbf{u}}{\partial s}$ and $\dfrac{\partial(\mathbf{u}\cdot\hat{\mathbf{n}})}{\partial s} = \mathbf{u}\cdot\dfrac{\partial\hat{\mathbf{n}}}{\partial s} + \hat{\mathbf{n}}\cdot\dfrac{\partial\mathbf{u}}{\partial s}$, relation (22) can be written as

$$\omega = -2\frac{\partial(\mathbf{u}\cdot\hat{\mathbf{n}})}{\partial s} + 2\mathbf{u}\cdot\hat{\mathbf{t}}\kappa \tag{23}$$

where $\kappa = \dfrac{\partial\hat{\mathbf{n}}}{\partial s}$ is the curvature of surface $S(\mathbf{x},t)$.

The physical sense of equality (23) is that vorticity on the free surface will be generated depending on the doubled change of the normal velocity component of the

free surface of water and the doubled tangent velocity component multiplied by the curvature of this surface. Assuming that the vorticity is concentrated on the free surface, which is considered to be a very thin layer (Fig. 1b), the intensity of the vortex sheet can be calculated as follows

$$\gamma(\mathbf{x},t) = \lim_{dx_2 \to 0} \omega(\mathbf{x},t) \cdot dx_2 \tag{24}$$

In the present paper, vortex sheet intensity $\gamma(\mathbf{x},t)$ is discretized using vortex particles with circulation Γ_i according to relation (17). The particles are located in the centres of segments ds_i.

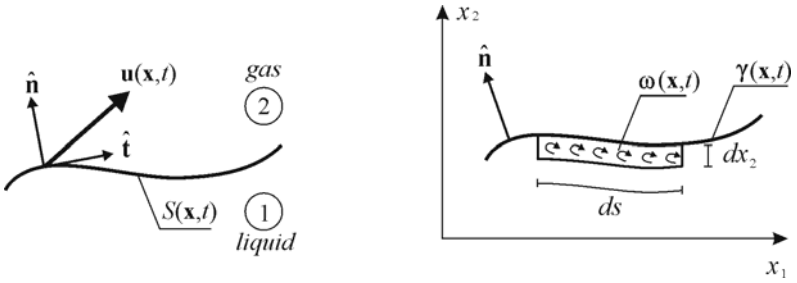

Fig. 1. (a) Sketch of the interface; (b) Schematic of vortex sheet intensity determination.

In the next time steps the vortex particles generated on the solid boundary and on the free surface are displaced through advection and diffusion whereby the evolution of a vorticity field is modelled. According to the method's algorithm, the particles which as a result of the displacement cross the boundaries of the region of the flow are eliminated from the calculations.

4. Exemplary calculations of flow over flap gate

The performance of the vortex method with the free water surface boundary condition was checked for a flow through a model of a flap gate for which also experimental studies were carried out. The dimensions of the physical model are shown in Fig. 2a. Calculations were done in a dimensionless system, assuming all the distances to be normalized to outlet depth $h_w = 0.192$ and mean inlet velocity $\mathbf{u}_0 = [0.521, 0]$; hence Reynolds number Re = 10^5. Also time was normalized relative to $h_w / |\mathbf{u}_0|$.

The vortex method calculations were done assuming: the length of the boundary segments for determining vortex sheet intensity h = 0.026, the cut radius for the mollifying function $\varepsilon = h^{0.95} = 0.0312$, time step dt = 0.025, the number of time steps for each simulation kt = 500, and a velocity distribution averaging time of 2.5.

The flap gate was assumed to be stationary ($\mathbf{U}_b = 0$) and vortices were generated on the solid boundary due to only discontinuities of tangent velocity in the direction perpendicular to the solid boundary. Also the flow was assumed to be stationary; hence $\mathbf{u} \cdot \hat{\mathbf{n}} = 0$ on the free surface (cf. eq. 23) and vortices were generated due to only

the free surface curvature. The shape of the free surface was measured on the model and then approximated by 5th degree polynomial $y(x)$; the latter was used to determine the curvature (Fig. 2b).

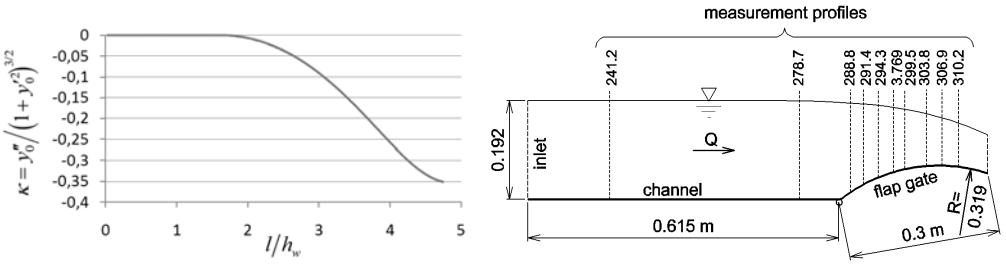

Fig. 2. (a) Curvature of free surface of water; (b) channel and flap gate dimensions.

The calculation results in the form of visualization of the evolution of vortex particles and an averaged velocity field distribution are shown in Figs. 3a and 3b, respectively.

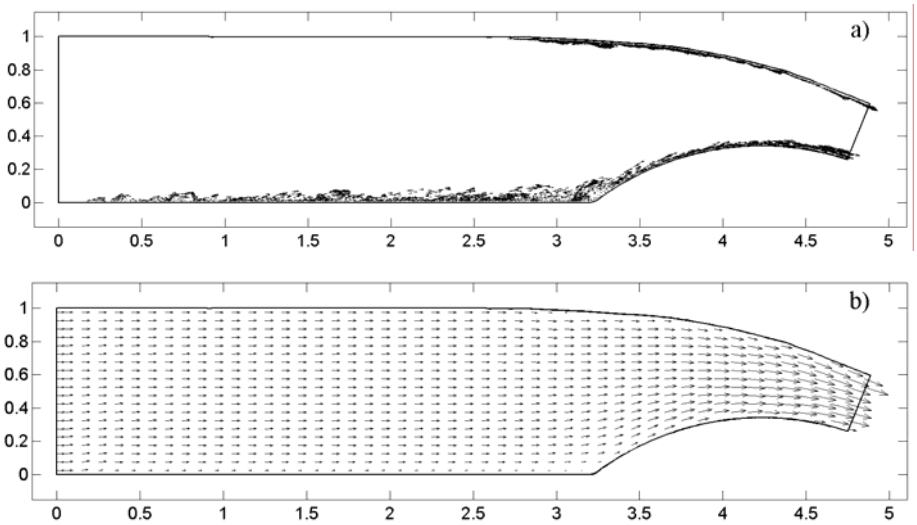

Fig. 3. Simulation result, Re = 100000 at kt = 500 for Δt = 0.1 and N = 4049: (a) vortex particle distribution; (b) averaged velocity field.

5. Model tests

Tests were carried out on the physical flap model in order to determine the velocity distribution in selected hydrometric verticals in the inlet channel and over the flap. The investigations were conducted in a hydraulic laboratory in a 6.0×0.7×0.15 m glass measuring flume for unit flow q_w = 0.1 m^3/s and Re = 10^5. The dam stage model (Fig. 4) consists of a channel with gradient So = 0.002 ensuring gentle water inflow, a 0.3 m high dam heel, a flap gate and an outlet. Upstream of the flap gate the flow is

calmed by a stilling screen. Flap gate curvature radius R = 0.3193 m and arc chord length a = 0.30 m. The flap gate support structure allows one to adjust the flap gate position from −10° to 50°.

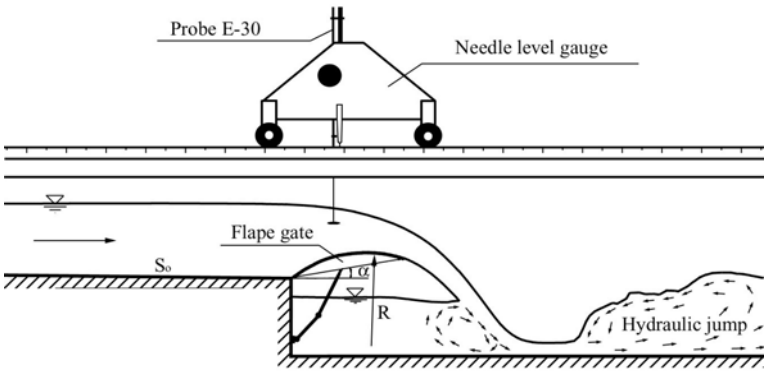

Fig. 4. Sketch of water velocity measurement setup.

The water flow rate was measured with an accuracy below 1% using a Thomson overflow. Water levels upstream and over the flap were measured with an accuracy of 0.0001 m using a needle level gauge. In order to keep an even pressure (equal to the atmospheric pressure) in the space under the flap, the required quantity of air (Q_a) was supplied. The pressure under the flap was measured by means of a PE350 pressure gauge capable of measuring pressure difference with an accuracy of 0.1 hPa.

6. Tests results and comparison with calculations

The measurements were performed for the flap tilted at angle α = 10° and water flow Q = 0.015 m^3/s. After the water flow conditions became steady, water elevations upstream and over the flap were measured. On this basis an empirical equation describing the water level depression curve above the flap gate edge was formulated. The equation was needed for numerical calculations.

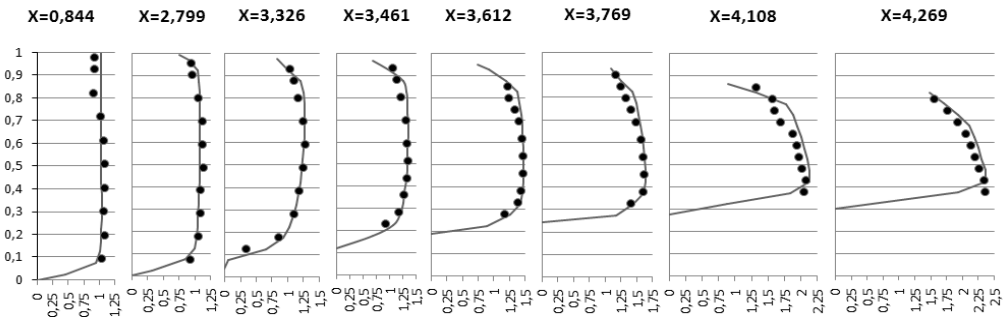

Fig. 5. Comparison of distributions of horizontal velocity components: ~ calculations and • measurements.

Table 1

Comparison of calculated and measured velocity profiles

Profile $x = 2.799$					Profile $x = 4.269$				
Depth [m]	V_m [-]	V_c [-]	Error [%]	Sd [-]	Depth [m]	V_m [-]	V_c [-]	Error [%]	Sd [-]
0.0174	0.9594	1.0445	–8.87	0.0383	0.0052	1.5489	1.6048	–3.61	0.1708
0.0374	1.0434	1.0737	–2.91	0.0422	0.0152	1.7575	1.8383	–4.60	0.2015
0.0574	1.1102	1.0800	2.72	0.0383	0.0252	1.9119	2.0466	–7.04	0.0710
0.0774	1.1213	1.0787	3.80	0.0422	0.0352	2.0468	2.1557	–5.32	0.0326
0.0974	1.1244	1.0721	4.65	0.0403	0.0452	2.1181	2.2216	–4.88	0.0326
0.1174	1.0900	1.0615	2.61	0.0364	0.0552	2.1926	2.2852	–4.22	0.0249
0.1374	1.0799	1.0473	3.02	0.0307	0.0652	2.2609	2.3413	–3.56	0.0172
0.1574	1.0420	1.0254	1.60	0.0364	0.0752	2.3366	2.3554	–0.80	0.0230
0.1774	0.9243	0.8328	9.89	0.0710	0.0852	2.3559	1.9644	16.6	0.0422

The horizontal water velocity components were measured in eleven hydrometric verticals in the channel axis. In each vertical, measurements were carried out at ten levels uniformly spaced along the height, by means of the PE30 probe. The measurements were performed for 30 s in a time step of 0.1 s and then mean velocities and standard deviations in the particular points were calculated. The measurement results for the dimensionless quantities in the selected verticals are shown in Table 1 which also includes the calculated horizontal velocity components and the percentage difference between them. Velocity distributions for several verticals are compared in Fig. 5.

7. Discussion

Certain conclusions emerge from the analysis of the water flow conditions and the measurement results. As the stream approaches the flap edge, a gentle depression forms, which is associated with the increase in the mean velocities in the particular verticals. Also the velocity distribution along the height changes. In the inlet channel the maximum velocities in the vertical occur in its upper and middle part, but in the stream over the flap the shape of the velocity profile changes and the maximum water velocity vectors occur near the flap's surface.

The velocity distributions calculated and measured along the inlet channel segment are consistent and the differences do not exceed 5%. The exception are the values near the free surface and the bottom. This divergence can be due to the influence of the geometry of the probe's ellipsoidal disk (30 mm in diameter and 10 mm high) and its location. According to the principle of measurement with this instrument the minimum distance of the probe from the bottom's surface should be 0.02 m, whereas the extreme measurements were made at a distance of 0.01 m. Because of the location of the probe in the vicinity of the free surface, its head is not fully submerged, which significantly affects the accuracy of the measurement. The fact that the results are loaded with significant errors is confirmed by the clearly higher standard errors of the discussed measurement results (Table 1).

8. Conclusions

The random vortex method was applied to solve the problem of the flat flow of an incompressible viscous liquid with a free surface condition. Attention was focused on the mathematical formulation of boundary conditions leading to the determination of the intensity of the vortex sheet forming along the edges. The intensity of the vortex sheet on the solid boundary, where the tangent velocity component is discontinuous, was determined from the Fredholm equation. The strategy presented by Lundgren (1999), consisting in the assumption of the zero-shear-stress condition, was applied to the free surface. For stationary motion this strategy leads to the determination of vorticity as a doubled product of the tangent velocity and the free surface curvature. In this study the vorticity was transformed to vortex sheet intensity. Then the vortex sheet intensity was discretized to a circulation of particles (vorticity carriers) from the evolution of which one can determine the velocity field, the vorticity field and the stream function.

It was demonstrated how the method works using as an example the flow around a flap gate model. The results were compared with the results of physical model tests. A comparison of the velocity distributions shows that the vortex method simulates well the flow with the proposed boundary conditions on the free surface. Slight differences in the shape of the compared velocity profiles are probably due to the type of instrument used to measure velocity.

In the authors' opinion this research should be continued, especially due to the fact that no studies dealing with the application of the vortex method to the flow of a liquid with a free surface have been found in the literature on the subject. The authors intend to improve the accuracy of the measurements by carrying out the investigations on a model with larger geometric dimensions or by changing the instrument used to measure the velocity in the surface and bottom zones.

References

Baker, G.R., and J.T. Beale (2004), Vortex blob methods applied to interfacial motion, *J. Comp. Phys*. **197**, 233-258.

Batchelor, G.K. (1967), *An Introduction to Fluid Dynamic*, Cambridge University Press, London.

Chorin, A.J. (1973), Numerical study of slightly viscous flow, *J. Fluid Mech*. **57**, 785-796.

Dopazo, C., A. Lozano, and F. Barreras (2000), Vorticity constraints on a fluid/fluid interface, *Phys. Fluids* **12**, 1928-1931.

Kostecki, S. (2007), Deterministic and Stochastic Vortex Method for Two-Dimensional Vorticity Transport Equation, *Publs. Inst. Geophys. Pol. Acad. Sc.* **E-7 (401)**, 119-127.

Kostecki, S. (2008), Numerical modeling of flow through moving water-control gates by vortex method. Part I – problem formulation, *Arch. Civ. Mech. Eng*. vol. **VIII**, no. 3.

Longuet-Higgins, M.S. (1998), Vorticity and curvature at a free surface, *J. Fluid Mech*. **356**, 149-153.

Lundgren, T., and P. Koumoutsakos (1999), On the generation of vorticity at a free surface, *J. Fluid Mech*. **382**, 351-366.

Majda, A.J., and A.L. Bertozzi (2002), *Vorticity and Incompressible Flow*. Cambridge University Press, Cambridge.

Accepted November 13, 2008

PUBLS. INST. GEOPHYS. POL. ACAD. SC., E-10 (406), 2008

Modelling of River Network with Widespread Floodplain Valleys

Ireneusz LAKS

Department of Theory of Construction and Agricultural Building Engineering
University of Live Sciences in Poznań
Piątkowska 94, 61-452 Poznań, Poland
e-mail: ilaks@up.poznan.pl

Abstract

One-dimensional models of unsteady flow provide a good representation of flow transformation as long as the conditions of flow are close to the assumptions of 1D motion, i.e., there is one predominant flow direction which coincides with river longitudinal gradient. However, this assumption is too simplistic when a lengthy river section with widespread floodplain valleys is being modelled. When developing a numerical model of river hydrodynamics, correct representation of flow transformation through these water-course elements is the most important, but also the most challenging part. Motion of liquids in floodplains may not be regarded as one-dimensional (particularly in the initial phase of filling the valley with water and in the closing phase, when water returns to the main channel). Representation of these would require 2D models. One of the methods used to represent spatial motion of water on floodplains in 1D unsteady flow models is to split the river cross-section into its active and inactive zones. The fundamental difficulty is to determine the range of active cross-section. Pasche's method is one of possible techniques applicable for this purpose.

1. Introduction

Since the possibility arose of applying numerical methods to differential equations describing the motion of free surface liquids, numerous specialist works have dealt with modelling of unsteady flows in open channel networks. This refers in particular to the well known numerical models based on de Saint-Venant equations (Abbott 1991, Cunge 1989). These models provide a good representation of flow transformation provided that there is no great discrepancy between flow conditions and the assumptions of one-dimensional motion, i.e., there is one predominant flow direction

which coincides with river longitudinal slope (Maidment 1992), and the transversal and vertical components are negligible. This criterion, together with correct data describing channel geometry, drag, flow balance and its time-dependant distribution, allows the researcher to obtain reliable results useful in design, water management and flood protection(Wosiewicz 1996).

However, the assumption required in one-dimensional models, i.e., that of one prevailing flow direction, is too simplistic when modelling a lengthy river section with widespread floodplain valleys. Natural, vegetated and widespread floodplains are decisive for the transformation of flow though a watercourse for flood waves. Motion of liquids in floodplains may not be regarded as a one-dimensional phenomenon (particularly in the initial phase of filling the valley with water and in the closing phase, when water returns to the main channel) and a comprehensive representation of these would require two-dimensional models. Despite considerable progress, practical applicability of such models for long river sections is still unrealistic, which is chiefly due to the cost of reliable measurement data required for the model.

One-dimensional models of unsteady flow are therefore only a tool for analysis and forecasting of flood wave transformations for long river sections and river networks. Nevertheless, they must take into account the spatial character of motion, which is achieved by extra parameters ensuring better representation of real flow conditions in widespread floodplain valleys.

2. Equations describing one-dimensional unsteady motion of liquids in open channels

One of the methods to represent the spatial character of motion in floodplains in one-dimensional unsteady flow models is to split the river cross-section into the active cross-section A_c (flow-related) and the inactive (dead) zones A_o, with the overall river cross-section being the sum of these two: $A = A_c + A_o$.

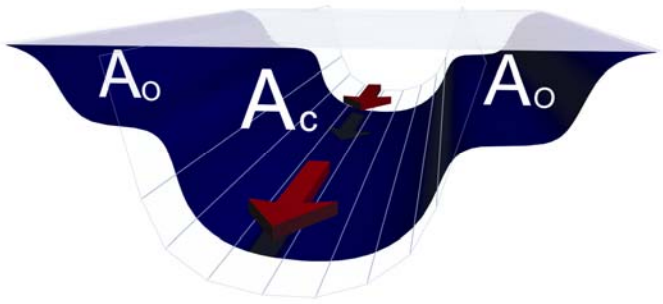

Fig. 1. Computational division of river cross-section into its active (A_c) and dead (A_o) component.

The mass conservation equation, in which all of the cross-section is considered, looks as follows (Maidment 1992):

$$\frac{\partial Q}{\partial x} + \frac{\partial (A_C + A_O)}{\partial t} = q. \tag{1}$$

The momentum equation (2) takes into account only the active part, hence the total cross-section area is substituted with the active cross-section area:

$$\frac{\partial Q}{\partial t} + \frac{\partial (\beta Q^2 / A_C)}{\partial x} + gA_C \left(\frac{\partial h}{\partial x} + Sf + S_{ec} \right) + W = 0, \tag{2}$$

where Q – flow rate [m^3/s], h – water table ordinate [m], x – cross-section position coordinate [m], t – time [s], g – acceleration due to gravity [m/s^2], q – unitary lateral inflow on the length of the watercourse [m^3/s/m], β – momentum coefficient [-], S_f – hydraulic gradient [-], S_{ec} – term representing the loss due to the cross-section getting narrower or wider [-], $W = qQ/A_c$ – term representing the unitary lateral inflow in the equation of motion [m^3/s^2].

3. Determining the range of active cross-section

The key difficulty is to determine the range of the active cross-section zone. One of the methods to do it is that of Pasche (1984), used in the unsteady flow modelling system SPRUNER (Wosiewicz 1996). It is assumed that the active part of cross-section consists of the area which determines inbank capacity and of the b_{II} zone (Fig. 2.) of interaction between the main channel and floodplains, calculated according to the formula (Laks 2005):

$$b_{II} = \frac{R_{hz}^{\frac{4}{3}}}{8\, g\, n_z^2\, (0.068 e^{0.56 C_T} - 0.056)} \tag{3}$$

where R_{hz} – hydraulic radius of floodplain [m], n_z – floodplain roughness coefficient, C_T – slip-velocity in Pasche's method [-].

Further details on the method to determine the range of the b_{II} zone can be found in (Laks and Kałuża 2005, Laks and Wosiewicz 1997).

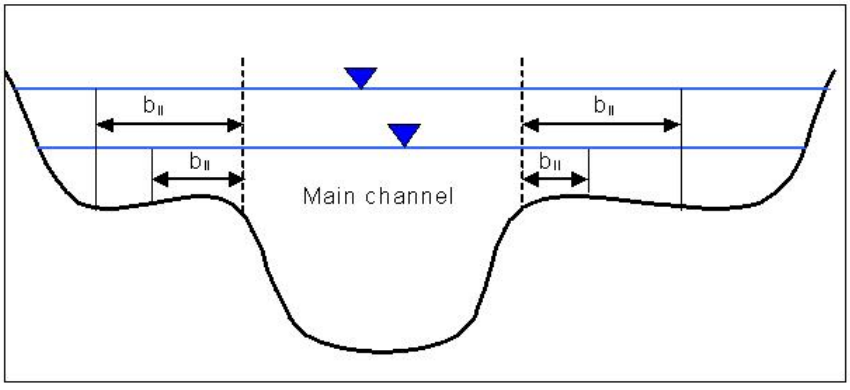

Fig. 2. Determining the range of active cross-section.

4. Computer implementation

The above assumptions on the range of active flow zone have been implemented in the unsteady flow modelling system SPRUNER (Wosiewicz 1996), developed at the Faculty of Land Reclamation and Environmental Engineering at the University of Life Sciences in Poznań.

The system determines the active flow zone according to the following scheme:

- for water levels below the inbank capacity, the active zone and the overall cross-section coincide,
- for water levels exceeding the inbank capacity, for each tabulated water level ordinate the range of active zone is calculated according to formula (3) for both the left and the right banks,
- given the range of active zone, the surface area $A_c(h)$ is calculated, together with all other parameters required for numerical solving of de Saint-Venant equations.

Each cross-section corresponds to two sets of data, separately for the active part and for the entire flow area. The system also stores the values of C_T calculated from Eq. (3) for each cross-section, separately for the left and the right floodplain. This parameter is considered a model-specific constant, the value of which can be determined in the process of calibration the model to the real situation.

5. Analysis of the size of active flow zone for selected cross-sections of the Warta river

The size of the active part of the cross-section (as a function of water depth) has been analysed for three characteristic river cross-sections of the Warta river (Figs. 3 and 4). It has been assumed that C_T is 5.0.

The cross-section 350+100 (Fig. 3), located in the region of Koninsko-Pyzderska valley, is characterized by widespread floodplains which are decisive for the transformation of flood waves. The width of floodplain valley is 3150 m, the width of the main channel is 70 m. For this cross-section, the active zone area does not exceed 14% of the overall cross-section area.

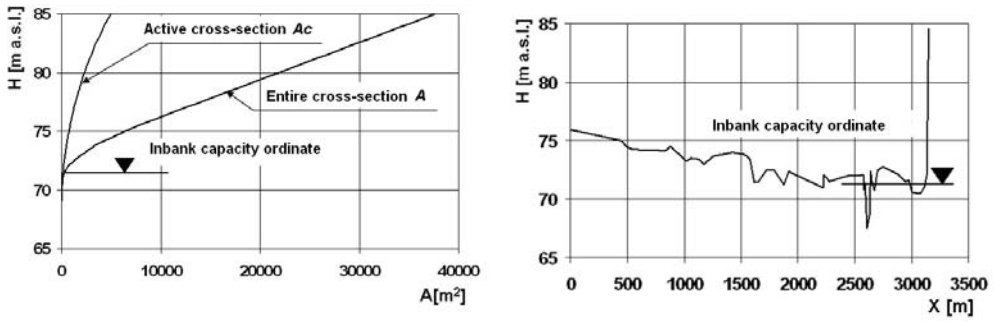

Fig. 3. Computational cross-section of the Warta river at km 350+100. Surface area of the active cross-section and the entire cross-section

For some cross-sections and a specific water level, the total surface area of the cross-section may be equal to that of the active zone, which is shown in the example given in Fig. 4. This means that the valley is filled to such a depth for which also in the floodplains there is one predominant direction of flow coinciding with that of the longitudinal gradient of the watercourse.

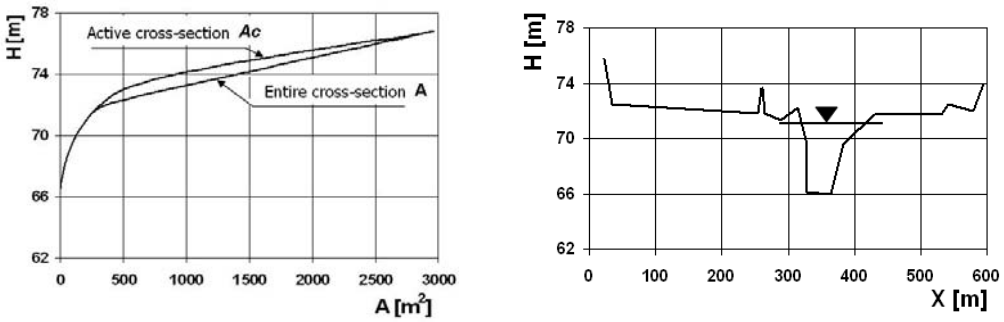

Fig. 4. Computational cross-section of the Warta river at km 348+000. Surface area of the active cross-section and of the entire cross-section.

For the same cross-section (km 348+000), the change in the percentage of active area in the entire cross-section area is presented as a function of water table level (Fig. 5). This plot describes the two principal work-phases of floodplains. In phase one, the valley is being filled up, hence the share of the active zone falls. In the floodplains the momentum is not transferred in the direction of the longitudinal axis of the watercourse (transversal and local gradients prevail). Phase two refers to the moment when the filling is sufficient for the active zone share to start rising again. Local or transversal gradients are no longer decisive for the direction of flow in the floodplains. The floodplain valley increasingly transfers momentum in the direction consistent with the dominant flow direction, until in all the cross-section, the water flows through the entire cross-section in the direction parallel to the longitudinal axis. This description is clearly very simplistic, but it shows how the spatial character of motion in the floodplains can be included into one-dimensional models.

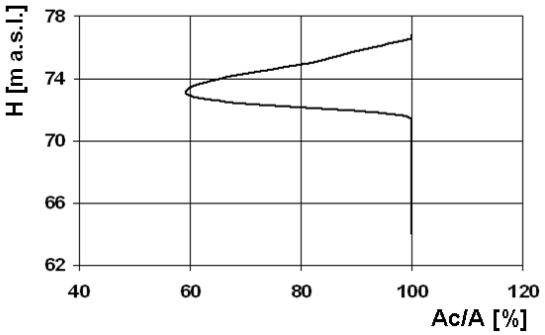

Fig. 5. Computational cross-section of the Warta river at km 348+000. Percentage of active cross-section in the entire cross-section as a function of water level.

The presented examples of computational cross-sections of the Warta river show that the range of the active flow zone may be calibrated with considerable impact on computational results. For widespread floodplain valleys the key calibration parameter is not the roughness coefficient but C_T from formula (3). It is this parameter that will be decisive for the size of active zone. Consequently, it will define the influence of floodplains on flow transformation.

6. Calculation of flow transformation for the 1997 flood wave on the Warta river section from the Jeziorsko reservoir to Oborniki

In order to verify the methodology described above, a one-dimensional model was developed of a 180 km section of the Warta river between cross-sections km 384+150 (lower dam post at the Jeziorsko reservoir) and km 206+300 (IMGW gauging station in Oborniki).

The model comprised 244 computational sections, 221 cross-sections, 27 bridges, 4 by-pass channels (in Koło, Konin, Śrem and Poznań), 2 embankment weirs, and one riverside reservoir (the Golina polder). Two tributaries – Prosna and Ner – were taken into account. Calculations were carried out for two variants: with and without the active zone. The model was also calibrated. Results are shown in Fig. 6.

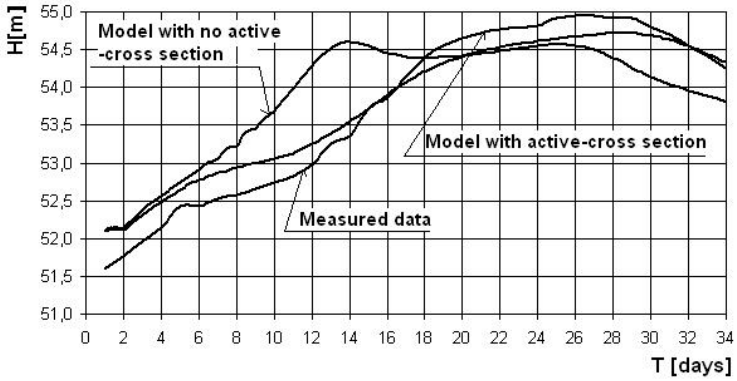

Fig. 6. Comparison of calculated and measured hydrographs at the gauging station in Poznań.

For the variant with no separated active flow there is no sufficient agreement between measured and calculated results. This refers to the wave shape, time of maximum discharge and the discrepancies between levels at individual points of the hydrograph. In the variant in which a separate active flow zone is considered, the input wave is considerably transformed and its shape is in good agreement with measurements. Calculated time of maximum levels and discharges coincides with the time determined based on measurements. Discrepancies between measured and calculated results occur in the values of water table ordinates. However, it should be stressed that the procedure of calibration was very simplistic and consisted of merely three „predictor-corrector" steps. More sophisticated model identification methods, e.g., optimisation methods using gradient solution search algorithms, might lead to better agreement of calculated and measured results.

7. Conclusions

The schemes described in this paper, developed for the representation of widespread floodplain valleys, introduce new parameters into one-dimensional unsteady flow models based on de Saint-Venant equations. These parameters require calibrating in the process of calibrating the model to the real situation. In practice, for each simulation in which a flood wave is analysed a parameter must be chosen (in the above scheme C_T) which determines the range of active zone and its water level-dependant behaviour. In this way, no out of range roughness coefficient values are introduced into the model, which, in fact, indicates that either the physical background of the model is inadequate or the data describing the watercourse geometrics is uncertain, although geometry is generally considered reliable.

References

Abbott, M.A., K. Havnø, and S. Lindberg (1991), The forth generation of numerical modelling in hydraulics, *J. Hydraul. Res*. **29**, 5, 581-600.

Cunge, J.A. (1989), *Recent Developments in River Modelling, Proc. Int. Conf. Hydraulic and Environmental Modeling of Coastal*, Estarine and River Water, Bradford, England.

Laks, I., and T. Kałuża (2005), Implementacja Aktywnej Strefy Przepływu w Komputerowym Systemie Modelowania Przepływu Nieustalonego SPRUNER, *Gospodarka Wodna, Zeszyt nr 1*, 2005.

Laks, I., and B.J. Wosiewicz (1997), Uwzględnienie oddziaływania polderów w jednowymiarowych modelach transformacji przepływu. *Roczniki Akademii Rolniczej w Poznaniu, Melioracje i Inżynieria Środowiska* **19**, 159-167.

Maidment, D.R. (ed.) (1992), *Handbook of Hydrology*, McGRAW-HILL INC, New York.

Pasche, E. (1984), *Turbulenzmechanismen in naturnahen Fließgewässern und die Möglichkeiten ihrer mathematischen Erfassung*. Mitt. Institut für Wasserbau und Wasserwirtschaft, RWTH Aachen, Heft 52.

Wosiewicz, B., I. Laks, and Z. Sroka (1996), Computer system of flow simulation for the Warta river, *Prace Naukowe Instytutu Geotechniki i Hydromechaniki Politechniki Wrocławskiej, seria Konferencje* **38**, Wrocław.

Accepted December 10, 2008

PUBLS. INST. GEOPHYS. POL. ACAD. SC., E-10 (406), 2008

Hydraulic Problems during 2001 Flood in Gdańsk

Wojciech MAJEWSKI

Institute of Meteorology and Water Management
Podleśna 61, 01-673 Warszawa, Poland
e-mail: wojciech.majewski@imgw.pl

Abstract

Floods in urban areas cause considerable economic and social losses. Measures for the mitigation of flood consequences are usually limited by existing city infrastructure. The city of Gdańsk is situated within a complicated system of rivers and channels called Gdańsk Water Node (GWN). The critical point of the GWN is the Radunia Channel, 13.5 km long. The main reason of the urban flash flood was intensive precipitation which appeared on 9 July 2001. The paper presents reasons, run and consequences of the flood, hydrological analysis, field measurements, formulation of 1D mathematical model of GWN, based on MIKE 11, various hydraulic calculations, including proposals of new hydraulic solutions.

1. Introduction

Gdańsk is an important Polish harbour situated on the southern coast of the Baltic Sea in the lowland area, at the mouth of the Vistula River. It is large industrial, scientific and cultural centre with 460 thousand inhabitants and its area is 262 km^2. It is the capital of the Pomeranian province. Therefore, any flood in this city results in considerable damages and losses. Flash flood, which invaded Gdańsk in 2001 was a very specific flood, different from others, which depend on high discharge in the river, which flows through the city.

Floods become recently more frequent than before and bring severe consequences. It is estimated that about 37% of economic losses caused by natural disasters are due to floods. There are many publications concerning floods and mitigation of their effects. The third International Symposium on Flood Defence, which was held in 2005 in Nijmegen, was a very important event concerning all aspects of flood defence and management. An important aspect is the fact of changing general approach from previous flood protection to flood management.

Gdańsk is situated in the Vistula delta, which was in the past and is at present endangered by various types of flooding (Fig. 1). In the XIXth century and earlier, the main hazard of flooding was due to ice jams, which formed on the Gdańsk Vistula, the western arm of Vistula (Jasińska and Majewski 2004). The turning point in the solution of flood problems was the construction of a new outlet of the Vistula River to the sea in 1895, called the Przekop Wisły. The river arm, Gdańsk Vistula was cut-off at Przegalina by means of a navigation lock, and thus the Dead Vistula was created (Jasińska 2002). Now the Gdańsk region has a very complicated system of rivers and channels. The urban flash flood, which invaded Gdańsk in 2001 came from the moraine hills situated on the west of the city. In recent years the city expansion went in this direction. This resulted in considerable decrease of retention capacity. Engineering organizations were warning city authorities about a possible flood coming from this direction in case of intensive precipitation.

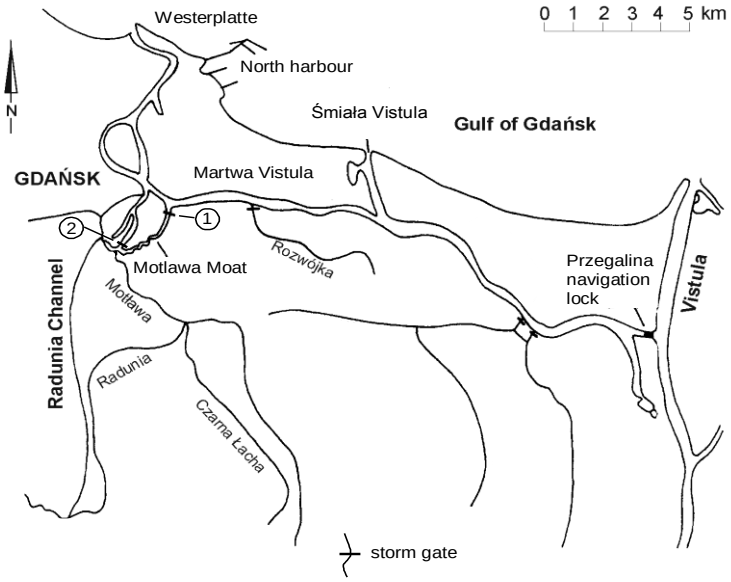

Fig. 1. Gdańsk Water Node (scheme).

The aim of the paper is to present hydraulic and hydrological situation of Gdańsk, sudden intensive rainstorm and its consequences in the form of flood, formulation of the mathematical unsteady flow model, and hydraulic calculations for various new technical solutions. The main emphasis is on hydraulic aspects.

2. Gdańsk Water Node

Gdańsk region has a very complicated system of rivers and channels (Fig. 1), which is called Gdańsk Water Node (GWN). The main rivers are Vistula and Dead Vistula. The terrains along these rivers are protected by flood dykes. Dead Vistula has several tributaries and channels, which at the discharge point are equipped with storm gates.

To prevent the inflow of salty waters into rivers and streams storm gates close automatically when water level in the Dead Vistula is higher than in the tributaries. Baltic Sea is practically tideless; however, winds blowing from the sea may result in the increase of water level up to 1.5 m above mean water level in the Gulf of Gdańsk.

There are two smaller but also very important rivers in GWN: Motława and Radunia. Motława River flows along Gdańsk Żuławy and discharges into Dead Vistula forming several branches within the city. One of them is Opływ Motławy, which was a defensive moat of Gdańsk in ancient times. Now it forms a flood retention reservoir. There are two main storm gates separating inland part of GWN from the Dead Vistula.

Radunia River flows towards Gdańsk from the moraine hills. It has important slope and mountain character, which results in large variation of discharge. In the XIVth century an artificial channel, called Radunia Channel (RCh), was constructed to supply water to the city of Gdańsk. It branches from the Radunia River in the vicinity of Pruszcz Gdański. It runs at the foot of moraine hills. The length of the Radunia Channel is 13.5 km and its catchment, totally on the left hand side, amounts to 55 km^2. There are 7 small natural streams and several outlets from storm drainage networks, which discharge into RCh. Their discharge in normal conditions does not exceed 1 m^3/s. The total volume of the Radunia Channel is estimated as about 0.3 mln. m^3. The bottom width of the channel is around 8 m and has an almost rectangular cross-section. The average slope of the channel is 0.5‰, its conveyance at maximum depth of 2.7 m was estimated at about 20 m^3/s. The RCh has an embankment on the right-hand side, which runs parallel to the main road and railway line leading to Gdańsk from the south. This embankment has the crest width from 3 to 5 m and height of 4 to 5 m. The inner slope of the channel is in many places protected by means of concrete slabs supported on sheet piles. The area along the right bank of the RCh is occupied by the old urban part of Gdańsk lying in a depression. RCh discharges into Motława River. It has also additional outflow to Motława Moat.

3. Precipitation regime

Precipitation in Gdańsk is highly non-uniform in space and time. During last years there were frequent intensive rainstorms, which usually covered only a small area. The average annual precipitation in Gdańsk is about 600 mm and the July average is 68 mm. In recent years it was observed that the maximum daily precipitation occurred in July. On 9 July 2001 over a period of 4 hours the whole catchment of the RCh received 80 mm of precipitation. The amount of precipitation on 9 July was 120 mm.

4. Flood run and its consequences

The flood in Gdańsk in July 2001 was a typical urban flash flood and was caused by intensive rainfall. It was the first serious natural flood in the Gdańsk region since the construction of the Wisła Przekop (Vistula River Direct Channel) in 1895.

Dramatic situation was caused by the fact that flooding started within a very short time from the beginning of rainfall. It may be regarded that water which fell in the form of precipitation on the catchment of RCh formed a surface run-off, which

moved down the slope of moraine hills. Part of water was collected in the streams discharging into RCh, and part of water entered the storm drainage system. All water found finally the way to RCh, which could not accommodate such important discharge.

As the result of intensive precipitation over the catchment of RCh, the inflow of water to the channel was estimated as 100 m^3/s during 4 hours in comparison to the channel conveyance 20 m^3/s. As the result of this inflow the embankment of the RCh was breached in 5 places, which resulted in flooding of the area of the city situated in the depression on the right side of the channel and the main road. This resulted in destruction of the main road and railway line in several places (Fig. 2).

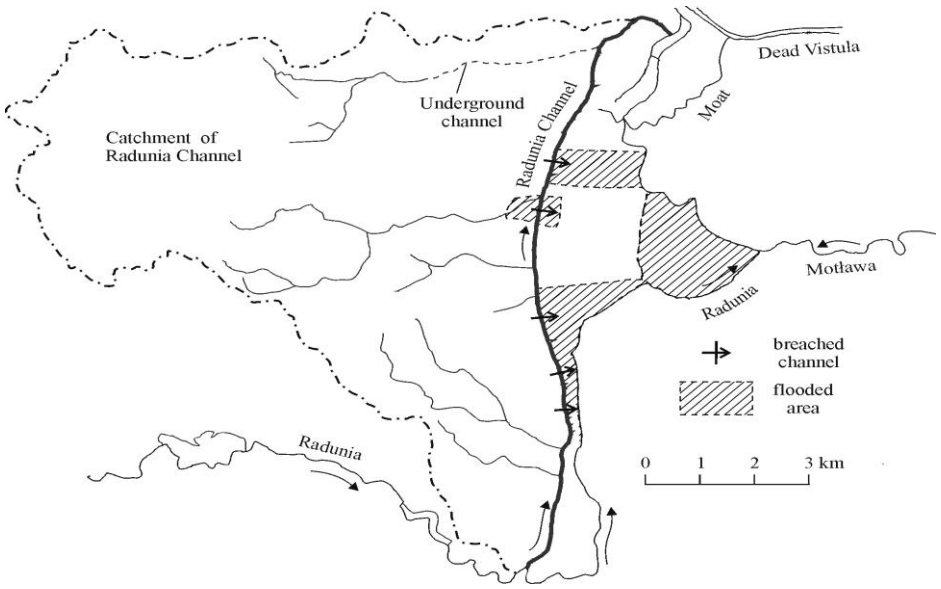

Fig. 2. Breached RCh and flooded areas.

Also two main roads approaching Gdańsk from the west turned into torrential rivers. Gdańsk main railway station was flooded, which caused one week's break in traffic. In other part of the city the main embankment of the small reservoir on the Strzyża Stream was breached, which resulted in a severe flood along the street and flooding of the crossing on the main road between Gdańsk and Gdynia.

Losses in the city infrastructure caused by flood were very high and estimated at about 50 mln. USD. More than 300 families were affected by the flood (damaged houses, loss of property). It was necessary to rescue people and their property from complete damage and destruction. Basements of numerous houses were flooded and required draining and drying. About 5000 people received special calamity status, which affords social assistance.

5. Flood Protection Project

After the flood of 2001, the Regional Board of Water Management in Gdańsk decided to undertake steps to improve flood protection in the Gdańsk area in the future, espe-

cially in the region of GWN (Majewski *et al*. 2003, 2004) in case of a similar rainstorm. The analysis of the existing spatial situation of the city indicates, however, that the present infrastructure does not allow any major change in the network of channels in the Gdańsk area. The main tasks of the project were defined as follows:

- field measurements of all rivers and channels forming GWN (cross-sections and longitudinal profiles),
- hydrologic analysis of rivers and streams together with water level changes in the sea,
- development of 1D unsteady flow model of the whole system of rivers and channels including hydraulic structures,
- analysis of possible new hydraulic structures to mitigate flood situation in GWN in case of a rainstorm similar to that in July 2001 (retention reservoirs, improvement of flow conveyance of rivers and channels, improvement of flood dykes, additional discharges from RCh),
- calculations for various possible solutions of flood protection,
- analysis of results and proposal of technical solutions.

Field measurements of river and channel cross-sections and longitudinal profiles were necessary to update existing data. More than 250 cross-sections were measured. They formed the basis for the mathematical model. Hydrologic analysis of discharge probability in all rivers and channels was necessary as initial conditions for hydraulic calculations. Possible coincidence of high water elevations in the Gulf of Gdańsk, and thus in Dead Vistula, together with high discharges in the rivers of GWN were analyzed.

1D unsteady flow model of the whole GWN was developed, including all hydraulic structures, e.g., weirs, bridges, culvers and storm gates. This model was based on MIKE 11 HD. An important task was the assessment of Manning roughness coefficient. This was done on the basis of field inspection. No data were available for the verification of values of roughness coefficients.

6. Hydraulic calculations

Hydraulic calculations included the following parts:

- discharge from the catchment to RCh,
- conveyance of RCh including all discharges from the catchment,
- conveyance of Radunia and Motława Rivers including natural flows and additional discharges from RCh,
- operation of storm gates situated at the outflow from Motława Moat.

A special part of the model was the catchment of RCh. This catchment was divided into subcatchments of the streams and areas between them. Inflows to the RCh were determined by means of empirical formulas taking into account proposed 18 artificial retention reservoirs. Finally, the lateral inflow to RCh and its longitudinal distribution was determined. On the basis of these data, discharge along the length of

the RCh was determined. Increase of discharge in the RCh was not possible because of channel construction. In some places, the calculated discharge exceeded channel conveyance and the only solution was the construction of 4 controlled side outflows to Radunia or Motława Rivers.

The calculations of the conveyance of Radunia and Motława Rivers were carried out for the discharge of 1% probability, estimated from hydrologic analysis. These calculations indicated that in some places existing flood dykes are too low and need heightening. Sample calculation of discharge changes along the Radunia River and water levels along its run are shown in Fig. 3.

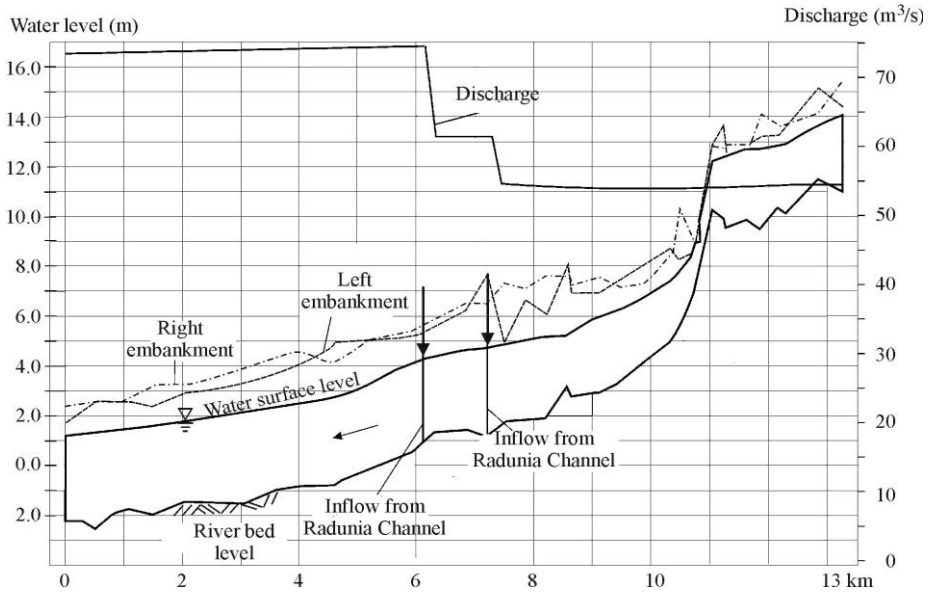

Fig. 3. Water level and discharge along Radunia River.

Water inflow from the moraine hills to the Martwa (Dead) Vistula cumulates in the River Motława, which before flowing into Gdańsk, forms the reservoir (Motława Moat). Its surface area is about 20 ha, which afford the additional storage of about 200 000 m^3 of water. Motława Moat is connected with Martwa Vistula by means of two storm gates, which close automatically when the water level in the Martwa Vistula is higher than that on the landward side. There are six storm gates altogether, however, the most important are the storm gates on the Motława Moat.

The first inflow to the Motława Moat is in the form of a side discharge from the Radunia Channel. Its maximum capacity is 12 m^3/s. The next tributary is the River Motława, which collects waters from the River Radunia and other rivers. Maximum discharge of the River Motława at the inflow to Motława Moat is estimated at 90 m^3/s. This discharge changes with time. Hydrologic analysis provides the discharges of all inflows according to the probability of their appearance.

Hypothetic storm surges in Martwa Vistula were assumed for various probabilities from p = 0.3% to p = 10%. The average water elevation in the Martwa Vistula is

about 0.40 m a.s.l. The maximum water elevation for a storm surge of the probability p = 0.3% is 1.5 m and the time of reaching the maximum water elevation is about 16 hours.

The 1D mathematical model includes also the flow through storm gates. Inflow hydrogram to the Motława Moat is assumed together with the hydrogram of water elevations in the Martwa Vistula, which constitutes the lower boundary condition. In the beginning, the same water level in the Motława Moat and in the Martwa Vistula is assumed. As a result of calculations we obtain a change in water levels in the Motława Moat compared with those on the Martwa Vistula. This indicates when storm gates close and then open again. Example calculation for discharge Q = 12 m^3/s and storm surge of p = 0.3% is shown in Fig. 4.

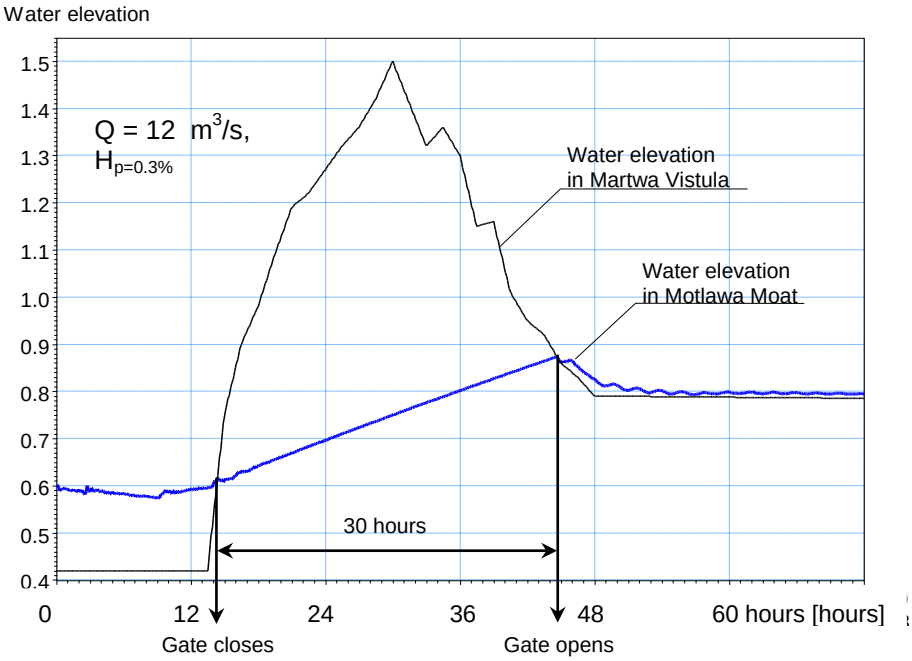

Fig. 4. Water elevations in Martwa (Dead) Vistula and Motława Moat.

7. Conclusions

- The existing spatial situation of the city of Gdańsk indicates the difficulty in carrying out any general change in the network of channels in GWN. The Radunia Channel is of great importance for possible floods caused by intensive precipitation in the city of Gdańsk. It was found that there is no possibility of significantly increasing the conveyance of the channel. Moreover, Radunia Channel is a technology monument and change of its construction or layout requires acceptance from the Gdańsk Architect's Office.
- In order to decrease the inflow to the Radunia Channel in case of intensive precipitation it was decided, on the basis of hydraulic calculations, to con-

struct 18 small reservoirs on all streams discharging to the RCh and install 4 control outflows from the Radunia Channel to the Radunia and Motława Rivers. In addition, 2 flood polders were proposed for extreme situations (Fig. 5). The proposed constructions are expensive and it will take several years to put them into operation.

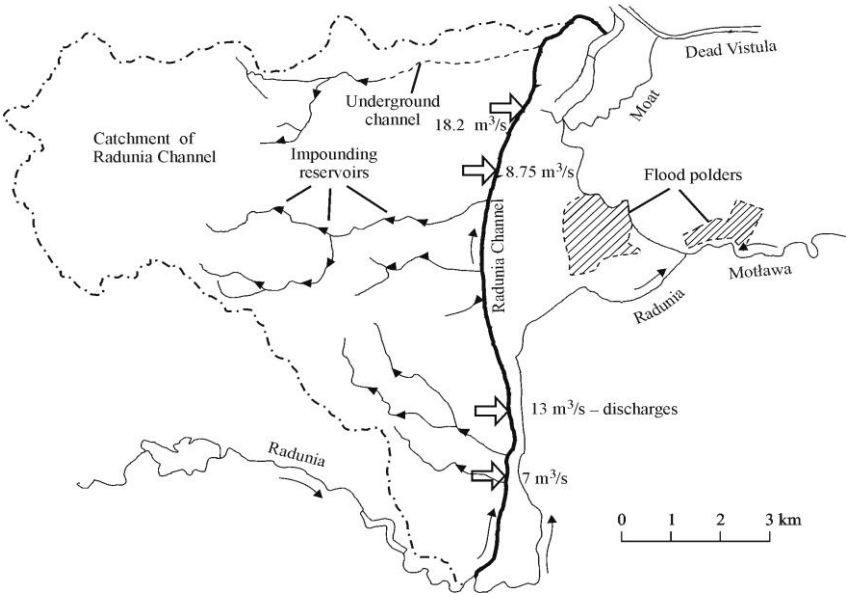

Fig. 5. Proposed technical solutions in GWN.

- The storm gates Brama Żuławska and Kamienna Grodza play a very important role in the GWN. Depending on water levels in Martwa Vistula caused by storm surges and the inflow to Motława Moat, two situations are possible: Closure of the gates and impoundment of Motława Moat and Motława River upstream. In the second case, storm surge does not result in closing of the storm gates, but only increased water levels in Motława Moat. In this case the discharge is through both storm gates and its intensity depends on the difference in water elevation on both sides of them.
- It was also proposed to install automatic precipitation and water level gauges net in the GWN to create, together with meteorological radar, a flood warning system.
- One social conclusion is of great importance. People and local authorities quickly forget about the flood and disaster caused by the inundation.

References

Floods, From Defence to Management 2005, *3rd International Symposium on Flood Defence*, Nijmegen, Symposium Proceedings, Taylor and Francis.

Jasińska, E. (2002), Hydrology and hydrodynamics of Martwa Vistula and Vistula Przekop (in Polish), *Publication of the Institute of Hydro-Engineering.*

Jasińska, E., and W. Majewski (2004), Flood problems in the city of Gdańsk, *Proceedings Defra Flood and Coastal Management Conference.*

Majewski, W. (2002), Flood in Gdańsk in July 2001, *Proceedings Conference Integrated Disaster Risk Management, IIASA Laxenburg, Austria.*

Majewski, W., *et al*. (2003, 2004), *The model of water distribution in the Gdańsk Water Node for flood protection in the Martwa Vistula catchment*, Institute of Hydro-Engineering Gdańsk (unpublished internal report, in Polish).

MIKE 11, *Hydrodynamic Module*, DHI Water and Environment.

POWÓDŹ 1997, *Scientific and technical Forum*, Proceedings Institute of Meteorology and Water Management Warsaw (in Polish).

Accepted November 13, 2008

PUBLS. INST. GEOPHYS. POL. ACAD. SC., E-10 (406), 2008

Extreme Mixing Events in Rivers

Russell MANSON[1] and Steve WALLIS[2]

[1] The Richard Stockton College of New Jersey, School of Natural Sciences and Mathematics,
PO Box 195, Pomona, New Jersey, 08240,USA
e mail: russell.manson@stockton.edu

[2] Heriot-Watt University, School of the Built Environment,
Riccarton, Edinburgh, EH14 4AS, UK
e mail: s.g.wallis@hw.ac.uk

Abstract

Although much effort has been expended on quantifying dispersion in simple channels, much less work has focused on compound channels, particularly for over-bank flows. Following an earlier study of a hypothetical compound channel, this paper provides further evidence for the significantly different flow dependence of dispersion coefficients for in-bank and over-bank conditions. The study is based on a natural cross-section of the River Severn, UK, and uses the same method as the earlier work, by combining the Shiono-Knight hydraulic model with the Fischer flow structure integral. The results show that dispersion coefficients are typically two orders of magnitude larger during over-bank flows compared to in-bank flows. Importantly, the maximum dispersion does not occur under the maximum flow. Instead, the maximum dispersion occurs when the flood plain inundation reaches the far edge of the flood plain.

1. Introduction

At the reach scale, mixing in rivers is usually dominated by longitudinal dispersion. There are numerous methods for estimating the associated dispersion coefficient ranging from in-situ tracer studies to theoretical analyses of the relevant transport processes, however in the majority of practical applications to pollution incidents or to water quality problems workers rely on empirical equations that enable dispersion to be quantified from bulk flow hydraulic parameters (Wallis and Manson 2004). For in-bank flows in simple channels this empirical approach is often successful, but for higher flows when adjacent floodplains are inundated the authors have previously suggested that existing empirical equations are of little or no use (Manson and Wallis

2004). This earlier study concerned a hypothetical, two-stage trapezoidal channel with symmetrical flood plains on both sides of the main channel. In contrast, in the current paper dispersion coefficients are evaluated for a cross-section of a natural compound channel, which can be expected to give a more realistic view of longitudinal dispersion during over-bank conditions than the previous study. The same method as before is used, but the results are presented differently and a novel idea is explored that examines the frequency distribution of the dispersion coefficient.

2. Analysis

Longitudinal mixing in rivers occurs due to the interaction of several physical processes, principally differential longitudinal advection, cross-sectional mixing and transient storage. In the following, transient storage is ignored: thus the analysis is not valid for channels that contain significant areas of either short-term or long-term transient storage (due to, for example, re-circulations in dead zones and/or interactions with the hyporheic zone, respectively). Applying conventional shear flow mixing theory (Fischer, 1967; Rutherford, 1994), therefore, in which the transverse profile of longitudinal velocity interacts with the transverse mixing, a theoretical expression for the dispersion coefficient is given by the following flow structure triple integral:

$$D = -\frac{1}{A}\int_0^W hu \int_0^y \frac{1}{\varepsilon h} \int_0^y hu \, dydydy \,, \tag{1}$$

where D is the dispersion coefficient, A is the cross-sectional flow area, h is the flow depth, u is the velocity deviation, ε is the transverse mixing coefficient, W is the top flow width and y is the transverse co-ordinate direction. The quantities h, u and ε all vary with y and, therefore, take local depth-average values. The velocity, u, is given by the difference between the local depth-averaged longitudinal velocity and the cross-sectional average longitudinal velocity, and ε is given by the product Ehu_*, where E is the non-dimensional transverse mixing coefficient (usually assumed to be independent of y) and u_* is the local shear velocity. The way in which ε is evaluated implies that transverse mixing occurs due to turbulent diffusion. Although the effects of secondary flows on the mixing are not directly included, their presence could, in principle, be accounted for by increasing the value of E used. Clearly, D can be evaluated for any cross-section if the transverse profiles of u and u_* can be calculated from the transverse profile of depth, a method for which is described below.

Steady, two-dimensional depth-average flow along a prismatic channel may be described by the Shiono-Knight model (SKM), which is derived from a momentum conservation approach (Shiono and Knight 1991). The following equation is a simplified version of the SKM, in which secondary flows are ignored:

$$\rho g S h = \tau_b \cos\theta - \frac{d}{dy}(h\tau_{yx}) \,, \tag{2}$$

where ρ is the fluid density, g is the acceleration due to gravity, S is the longitudinal channel slope, τ_b is the local longitudinal bed shear stress, θ is the local transverse bed

slope and τ_{yx} is the local depth-average shear stress caused by transverse turbulent momentum exchange. Equation (2) applies at all transverse locations and describes a local balance between the component of fluid weight down the longitudinal slope and the resisting longitudinal stresses on horizontal and vertical planes. τ_b can be expressed using a local application of Manning's resistance equation, in which the hydraulic radius is replaced by the local flow depth, giving:

$$\tau_b = \frac{\rho g u^2 n^2}{h^{1/3}}, \tag{3}$$

where n is the local Manning resistance coefficient. τ_{yx} can be expressed using the eddy-viscosity concept, namely:

$$\tau_{yx} = \rho \lambda h u_* \frac{du}{dy}, \tag{4}$$

where λ is the non-dimensional eddy viscosity (usually assumed to be independent of y). Combining Eqs. (2)-(4) gives:

$$Sh = \frac{u^2 n^2 \cos\theta}{h^{1/3}} - \frac{1}{g}\frac{d}{dy}\left(\lambda h^2 u_* \frac{du}{dy}\right). \tag{5}$$

Once u_* is expressed in terms of u using the Manning equation, Eq. (5) can be solved using a numerical method. Finally, with all the ingredients now being available, Eq. (1) can be used to evaluate D using numerical integration, e.g. see French (1986).

3. Application and results

The method described above was used to calculate dispersion coefficients for the river cross-section shown in Fig. 1, which is based on a natural cross-section of the River Severn, UK, described in Carling *et al* (2002). Results were obtained for a wide range of stages in order to investigate the dispersion coefficient behaviour for both in-bank and over-bank flows. Two hydraulic scenarios were considered by undertaking computations for two values of λ. Taking $\lambda = 0.6$ employed all terms in Eq. (2), while taking $\lambda = 0$ employed a simplified hydraulic model, in which the transverse exchange of momentum was ignored, i.e. the velocity profile was determined only by the local depth and bed resistance. In both cases, the longitudinal bed slope was taken as 0.0001, and Manning's n for the main channel was calibrated as 0.035 (for the $\lambda = 0.6$ case), giving a bank-full flow of about 70 m^3/s, which is of the same magnitude as that

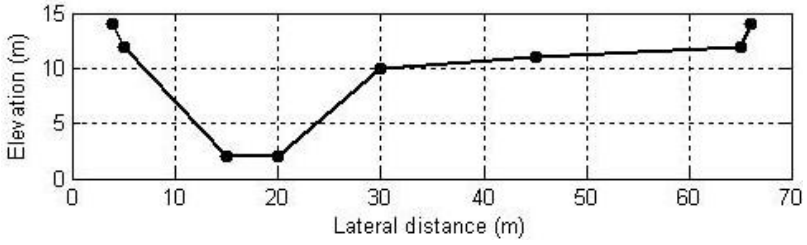

Fig. 1. Channel cross-sectional profile.

given by Carling *et al*. (2002), namely approximately 100 m^3/s. The floodplain Manning's *n* was taken as 0.050 reflecting it consisting of closely grazed pasture.

The model was set up in order to produce hydraulic results that were representative of a real river cross-section. However, there is a lot of uncertainty over some of the input data, and so it is not expected that the model would necessarily predict accurately the hydraulic conditions for the particular cross-section used. For example, λ tends to be a catch-all parameter that allows for the exclusion of secondary flows and three-dimensional effects from the hydraulic model. Hence its value of 0.6 is somewhat larger than if transverse momentum exchange were due only to turbulence, but is consistent with the values discussed in Shiono and Knight (1991). Despite such issues, the main features of the hydraulics and, importantly, their variation over the width can be expected to be captured.

The results enabled the relationships between stage, flow and dispersion coefficient to be found. For example, Fig. 2 shows how the dispersion coefficient varied with stage, using a logarithmic scale in order to better expose both the in-bank and the over-bank results. A novel way of portraying the dispersion coefficients, as a cumulative frequency distribution, was also explored. To do this the flow was assumed to follow a log-normal frequency distribution with mean and standard deviation of approximately 70 m^3/s and 15 m^3/s, respectively. The mean value was based on the one in two year flow corresponding to the bank-full condition (Carpenter *et al*. 1999), but the choice of standard deviation was arbitrary. The dispersion coefficient frequency distribution was then found by randomly sampling flows from the flow frequency distribution, computing the corresponding dispersion coefficient from the dispersion coefficient-flow relationship found earlier and constructing the frequency distribution of the resulting dispersion coefficients. Flow frequency and dispersion coefficient cumulative frequency distributions are shown in Figs. 3 and 4.

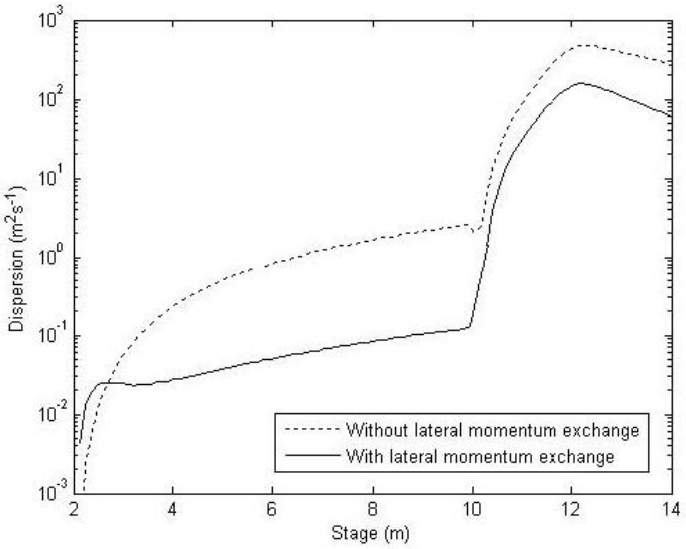

Fig. 2. Variation of dispersion coefficient with stage.

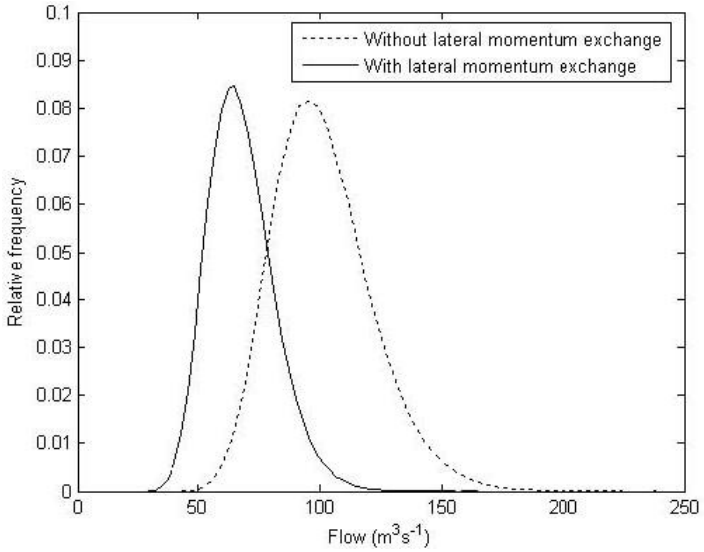

Fig. 3. Flow frequency distributions.

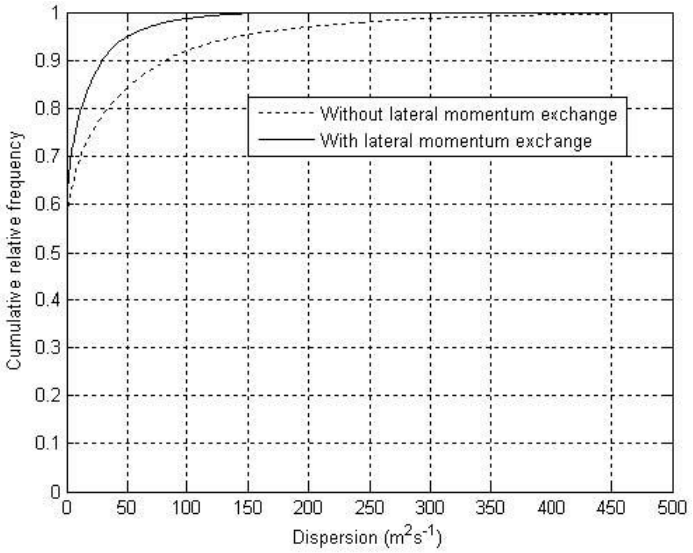

Fig. 4. Cumulative frequency distributions.

4. Discussion

Figure 2 shows that the dispersion coefficient increases slowly with stage and takes small values (typically < 1 m^2/s) for in-bank flows (stage < 10 m), but increases rapidly towards the order of 1000 m^2/s once the bank full flow is exceeded. A maximum value is reached when the stage equals the elevation of the far edge of the floodplain (12 m), and at even higher stages the dispersion coefficient reduces. These trends are consistent with the earlier results for a hypothetical channel given in Manson and Wallis (2004), and show that maximum longitudinal mixing conditions do not occur dur-

ing the highest flows. Instead, they occur at a lower flow, when the shear flow dispersion mechanism encapsulated by Eq. (1) achieves its maximum potential. This occurs when the transverse velocity gradients are largest and coincides with the floodplain inundation reaching the far edge of the floodplain.

The effect of ignoring the transverse exchange of momentum in the hydraulic model leads to an over-estimation of the flow, which is consistent with larger velocity magnitudes being predicted (as a result of the removal of one of the momentum dissipation terms). This trend is apparent from the comparison of the flow frequency distributions shown in Fig. 3. The main effect of omitting this process on the dispersion coefficient is to increase values, particularly for the in-bank case, see Fig. 2. This occurs purely through the effect of changing λ in the hydraulic model, because in all the dispersion coefficient computations using Eq. (1), E was fixed at 0.6. Since it is usually assumed that the physical mechanisms responsible for mixing momentum and mass are the same, it may not appear to be very logical to take $\lambda = 0$ and $E = 0.6$. However, whereas taking E to be zero is clearly of no benefit (yielding infinite dispersion coefficients), taking λ to be zero has some potential use. For example, it would enable close comparison with some pioneering work in dispersion coefficient prediction by, e.g., Jain (1976) and Deng *et al*. (2002), and it would help investigate the sensitivity of the results to the complexity of the hydraulic model. In this regard, if it were found that computed dispersion coefficients were insensitive to the transverse exchange of momentum, this term could be dropped, which would allow a much simpler calculation procedure. Clearly, the results in Fig. 2 suggest that this is not the case.

Both sets of dispersion coefficients peak (during over-bank flow) at extremely large values in comparison to those normally found in rivers of the size of the case study (Rutherford 1994). Although the peak values are smaller than in the authors' earlier study (Manson and Wallis 2004) they are uncomfortably large. Nevertheless, until field measurements of dispersion coefficients are undertaken in such over-bank flows, these predictions, and their implications, cannot be ignored. Of course, explicitly including the effects of secondary flows, both on the flow structure and on the transverse mixing may lead to more realistic (i.e. smaller) values being predicted. The former would tend to reduce transverse velocity gradients, while the latter would augment the transverse mixing: both of these would reduce the dispersion coefficient. On the other hand the value of λ would, logically, need to be reduced, so it is too early to speculate on the overall effect. However, it is doubtful that it would change the contrast between the in-bank and over-bank behaviour of the dispersion coefficient.

Figure 4 shows the cumulative probability distribution for the dispersion coefficient, which is a novel and useful way of portraying such information, from which the probability that an observed value is less than a target value is easily deduced. For example, when the transverse momentum transfer is included the probabilities that the dispersion coefficient is less than 50, 25, 10 and 5 m^2s^{-1} are approximately 0.95, 0.90, 0.80 and 0.70, respectively. Clearly, although large or very large dispersion coefficients are predicted for most over-bank flows they do not occur often because the corresponding flows are relatively rare. For example, when the transverse momentum transfer is included, maximum dispersion occurs under flows of about 150 m^3/s, which are considerably rarer than the bankfull flow of about 70 m^3/s, see Fig. 3.

5. Conclusions

The study has confirmed the general behaviour of dispersion coefficients in relation to in-bank and over-bank flows found in the previous analysis of a hypothetical compound channel. These new results for a real compound channel strengthen the case that during over-bank flows dispersion coefficients can reach values that are one or two orders of magnitudes larger than typical in-bank values. The maximum values occur when the flood plain inundation reaches its far edge: under such conditions the dispersive potential of the transverse gradient of longitudinal velocity is highest. It is of particular note that the maximum mixing conditions do not coincide with the maximum flow rate. There are significant differences between the results from the two hydraulic models studied, which suggests that the transverse exchange of momentum should not be ignored. Indeed, increasing the complexity of the hydraulic model even further to explicitly include the effect of secondary flows would appear to be an important issue for further work. Consideration of the frequency distribution of the dispersion coefficient is a novel idea that has the potential to enhance the interpretation of mixing events in rivers. For example, in the current case although some very large dispersion coefficients are predicted, they are only rarely encountered.

References

Carling, P.A., Z.X. Cao, M.J. Holland, D.A. Ervine, and K. Babaeyan-Koopaei (2002), Turbulent flow across a natural compound channel, *Water Resour. Res.* **38**, 12, doi: 10.1029/2001WR000902.

Carpenter, T.M., T.A. Sperfslage, K.P. Georgakakos, T. Sweeney, and D.L. Fread (1999), National threshold runoff estimation utilizing GIS in support of operational flash flood warning systems, *J. Hydrol.* **224**, 1-2, 21-44.

Deng, Z.-Q., V.P. Singh, and L. Bengtsson (2001), Longitudinal dispersion coefficient in straight rivers, *J. Hydraul. Eng. ASCE* **127**, 11, 919-927.

Fischer, H.B. (1967), The mechanics of dispersion in natural streams, *J. Hydraul. Div. ASCE*, **93**, HY6, 187-215.

French, R.H. (1986), *Open-Channel Hydraulics*, McGraw-Hill, 706 pp.

Jain S.C. (1976), Longitudinal dispersion coefficients for streams, *J. Environ. Eng. Div*. ASCE **102**, EE2, 465-474.

Manson, J.R., and S.G. Wallis (2004), Fluvial mixing during floods, *Geophys. Res. Lett*. **31**, L14502, doi:10.1029/2004GL020452.

Rutherford, J.C. (1994), *River Mixing*, Wiley, 347 pp.

Shiono, K., and D.W. Knight (1991), Turbulent open-channel flows with variable depth across the cross-section, *J. Fluid Mech*. **222**, 617-646.

Wallis, S.G., and J.R. Manson (2004), Methods for predicting dispersion coefficients in rivers, Proceedings of the Institution of Civil Engineers, *Water Management* **157**, WM3, 131-141.

Accepted November 13, 2008

PUBLS. INST. GEOPHYS. POL. ACAD. SC., E-10 (406), 2008

Simulation Approach Used for the Second *L*-Moment Derivation of the Inverse Gaussian Distribution

Iwona MARKIEWICZ and Witold G. STRUPCZEWSKI

Institute of Geophysics Polish Academy of Sciences
Ks. Janusza 64, 01-452 Warszawa, Poland
e-mails: iwonamar@igf.edu.pl, wgs@igf.edu.pl

Abstract

Maximum Likelihood (ML) estimate of upper quantiles looses its optimal properties if a wrong distribution is assumed in the ML procedure. Since its estimates base on the main probability mass, the alternative estimation techniques yielding estimates more dependent on upper tail elements of a sample are of interest in flood frequency analysis (FFA). Several systems of describing the shape of probability distribution have been developed and used for matching the assumed distribution to the data. One of them is the system basing on the linear moments. The *L*-moment estimates have highly desirable properties, like small bias and no algebraic bound of *L*-moment estimate ratios. It is shown how to use the *L*-moment system for probability distribution description if the analytical formulas of the linear moments have not been derived. The inverse Gaussian distribution serves as an example.

1. Introduction

The flood frequency analysis (FFA) comes down to the estimation of upper quantiles of peak flows probability distribution obtained from annual (or partial duration) series, while an assumed distribution function has a character of statistical hypothesis. Several systems of describing the shape of probability distribution can be alternatively used in FFA. All of them contain the location measure, then the dispersion measure, the skewness, the kurtosis etc. In FFA the role of skewness in distribution choice is especially important. Since two-parameter distributions are recommended for at-site FFA (e.g. Cunnane 1989), the role of dispersion becomes significant as for two-parameter distributions the skewness is expressed just by a dimensionless dispersion measure. Hence, the accuracy of the dispersion measure estimate is particularly important.

The most commonly used system of probability distribution description is one basing on the conventional moments. Hence the dispersion measure of this system, i.e., the standard deviation (SD), is the most popular measure of dispersion. With the development of probability weighted moments and then *L*-moments as an alternative system for describing shapes of probability distributions (Greenwood *et al*. 1979, Landwehr *et al*. 1979, Hosking 1990), the second *L*-moment, previously known under Gini's statistics (Gini 1912), has become a popular dispersion measure.

In the paper some properties of the second *L*-moment and the standard deviation will be compared in respect to flood frequency modelling. Moreover, the simulation approach will be used for the second *L*-moment derivation of the inverse Gaussian distribution.

2. The second *L*-moment superiority over the standard deviation

Several dispersion measures can be alternatively used in FFA. Among them there are both the standard deviation (σ) and the second *L*-moment (λ_2), presented in Table 1 with their sampling estimators for *N*-element sample.

Table 1

Dispersion measures for population and sample

Dispersion measure	Population	Sample
Standard deviation	$\sigma = \left[\int_{-\infty}^{+\infty} (x-\mu)^2 \, dF(x) \right]^{1/2}$	$s = \left[\frac{1}{N} \sum_{i=1}^{N} \left(x_i - \overline{x} \right)^2 \right]^{1/2}$
Second *L*-moment	$\lambda_2 = \int_{-\infty}^{+\infty} 2(x-\mu) F(x) \, dF(x)$	$l_2 = \frac{1}{N} \sum_{i=1}^{N} \frac{(2i-N-1)}{(N-1)} x_{i:N}$

To get dimensionless dispersion measures, the coefficients of variation are used, i.e., $C_V = \sigma/\mu$ for classical system and $LC_V = \tau = \lambda_2/\lambda_1$ for linear system, where $\mu = \lambda_1$ is the mean of population.

The attractiveness of *L*-moments comes from the fact that estimators of linear moments, in contrast with conventional moments, have very small bias in moderate and large samples. Moreover, the sampling *L*-moment ratios are not algebraically bounded. For instance, the estimate of the *L*-coefficient of variation $L\hat{C}_V$ does not have the algebraic bound dependent on the sample size and for a distribution that takes only positive values $L\hat{C}_V \in (0, 1)$ (Hosking and Wallis 1997), whereas the sampling estimator of the coefficient of variation C_V has an algebraic upper bound. For a set of $N \geq 2$ non-negative values x_i, not all equal, $\hat{C}_V$ cannot exceed $(N-1)^{1/2}$ (e.g., Kendall and Stuart 1969, p. 54).

The second *L*-moment exists when the first moment of population exists, as it needs a convergence of the integral with the linearly related random variable. Whereas for the standard deviation existence the second moment must be finite, as under

integral the second power of random variable is used. The property of existence is essential especially when the heavy-tailed distributions are used, since these distributions have their conventional moments only in limited range of shape parameter.

An important practical problem is an assessment of the vulnerability of the estimate of maximum flow distribution in respect to the largest sample elements. In FFA the robustness of an estimation method to largest elements of a sample is regarded as a desirable property by those who consider the chosen model as the true one and upper sample elements as of poor quality, and an unwelcome property by those who think that the assumed simple model cannot reproduce the true distribution in a whole range of variability and accept the quality of upper sample elements. The robustness depends on the estimation method as well as on the statistics using for describing of the probability distribution form. The λ_2 estimate (Table 1) is linear function of sampling data, while for the standard deviation the second power of data is used. Therefore, SD gives generally greater weight to the extreme tails of the distribution than does the second *L*-moment. So the sample SD is more affected by extreme observations and outliers than is the sample second linear moment (Markiewicz *et al*. 2006, p. 401-402)

Concluding, the foregoing properties of the dispersion measures in the *L*-moment system of describing the shape of probability distribution, i.e. small bias of estimators, no algebraic bound of estimator ratios, existence when the mean of population exists, robustness to outliers, show that the λ_2 is highly competitive dispersion measure. The estimation method based on the linear moments is recommended to use in flood frequency modelling (e.g. Robson and Reed 1999).

3. Probability distributions used in FFA

The probability functions used in flood frequency analysis should not be upper bounded and negative skew (e.g. Rao and Hamed 2000). Since the hydrological samples are usually of relatively small size, to estimate reliably and efficiently many parameters (Landwehr *et al*. 1980), both two-and three-parameter distributions are used. Since two-parameter distributions are recommended for at-site FFA (e.g. Cunnane, 1989) and the *L*-moments system is attractive for flood frequency modelling, the distributions like log-Gumbel, log-logistic, log-normal, Weibull, Gamma and Gumbel are mostly used. The log-Gumbel and log-logistic are the heavy-tailed distributions, which are highly recommended by many researchers of extreme events for peak flows modelling. They have conventional moments only in a certain range of shape parameter values and the range decreases with a moment order. The attractive for FFA distributions which do not have derived *L*-moments, like the inverse Gaussian or the inverse gamma, are precluded if the *L*-moments techniques are going to be used. However, the set of alternative distributions can be extended for the distributions without having derived the population *L*-moments if a simulation approach is used to asses them. The methodology is shown for the inverse Gaussian distribution.

3.1 Inverse Gaussian distribution

The inverse Gaussian distribution, known in hydrology mainly under the name “the convective diffusion distribution” (Strupczewski *et al*. 2002) and being equivalent to the two-parameter Halphen type A distribution (Perreault *et al*. 1999), has the form:

$$f(x) = \frac{\alpha}{\sqrt{\pi x^3}} \exp\left[-\left(\alpha - \frac{\beta}{\alpha} x \right)^2 \Big/ x \right], \tag{1}$$

where $\alpha > 0$ and $\beta > 0$ are scale and shape parameters, respectively, and $x > 0$.

Both the cumulative distribution function (cdf) $F(x)$ and the quantile x_F have no explicit analytical form and the basic definitions of the foregoing statistics involving the pdf integration should be used. Similarly, the linear moments have not been derived so far.

The mean of the inverse Gaussian is expressed by:

$$\mu = \alpha^2 / \beta \tag{2}$$

and the standard deviation is:

$$\sigma = \alpha^2 \left(2\beta^3 \right)^{-1/2}. \tag{3}$$

So the conventional variation coefficient has the form:

$$C_V = \left(2\beta \right)^{-1/2}. \tag{4}$$

4. The second *L*-moment derivation

Since any variation coefficient is a function only of the shape parameter, (see Eq. 1), the population relation between the shape parameter and the LC_V is of interest. First, 50.000-element samples from inverse Gaussian distribution with the mean equal to one and C_V varying from zero to 1.5 have been generated and the $L\hat{C}_V$ value has been calculated from the particular samples. The *L*-moments ratio estimates have very small biases even in moderate samples (Hosking and Wallis 1997, p. 28). This authorizes us to consider the LC_V estimates got for $N = 50.000$ sample as the population values, i.e., $L\hat{C}_V \approx LC_V$. Following this way, the set of pairs (C_V, LC_V) is created and shown in Fig. 1. The range of variation coefficient variability, i.e., $C_V \in (0, 1.5)$ is wide enough since referring to the real data, for 36 series of annual peak flows of Polish rivers and each of them containing at least 85 years long measurements, the mean value of $\hat{C}_V$ equals 0.634 and its standard deviation is 0.135. At the same time, the average $L\hat{C}_V$ is 0.328 with its SD = 0.065. Since the shape parameter β is related to C_V by Eq. (4), the relation LC_V *versus* β and its inverse can be obtained in this way. For instance, for $C_V = 0.3$ which corresponds to $\beta = 5.556$, value of LC_V obtained from simulation equals 0.165.

The relation presented in Fig. 1 is approximated by applying the polynomial least squares fitting procedure (e.g. Krysicki *et al*. 1999). It means that function *f* which defines a relation between two sets of points, x_i and y_i for $i = 1, \ldots, M$, has *m*-th degree polynomial form, where $m \leq M$. The polynomial coefficients a_i for $i = 0, \ldots, m$ are derived by the least squares procedure and the fitting accuracy is expressed by coefficient of determination (R):

$$R = \left\{ 1 - \sum_{i=1}^{M} \left[y_i - f\left(x_i; a_0, a_1, \ldots, a_m\right) \right]^2 \Big/ \sum_{i=1}^{M} \left[y_i - \bar{y} \right]^2 \right\}^{1/2} . \tag{5}$$

The R value varies from zero to one. The coefficient of determination equal one indicates that function f is ideally fitted to the given sets of points.

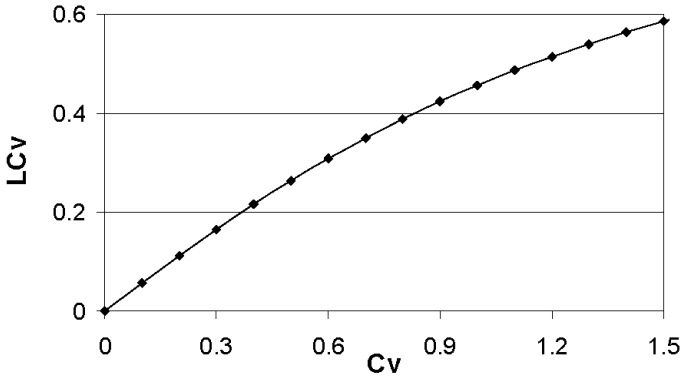

Fig. 1. Relation LC_V *versus* C_V for inverse Gaussian distribution.

The relation between LC_V and C_V (Fig. 1) is pretty well approximated by the second degree polynomial, i.e., $y = -0.1258x^2 + 0.5823x$, where variable x refers to the C_V and y refers to the LC_V and $M = 16$, has a determination coefficient $R = 0.9998$. The foregoing assessment is already sufficient in regard to an application. The third degree polynomial $y = 0.0153x^3 - 0.1654x^2 + 0.6054x$ has the coefficient of determination equal to 0.9999, while its value one is reached for the fourth degree polynomial $y = 0.0157x^4 - 0.0419x^3 - 0.102x^2 + 0.5849x$. Finally, substituting the shape parameter β from Eq. (4) in place of C_V one can obtain the relation LC_V *versus* β. Then the inverse relation, i.e. $\beta = g(LC_V)$ can be approximated from the simulation data set $(\beta_i, LC_{V_i}; i = 1, ..., M)$.

4.1 The methodology confirmation

The credibility of the methodology presented in the paper has been investigated for the gamma and the log-Gumbel distributions. The estimates $L\hat{C}_V$ obtained from simulated large sample of the foregoing distributions have been compared with the population LC_V values, since both the gamma and the log-Gumbel distributions have an explicit analytical form of LC_V. The experiment has been carried out for 10.000-element samples generated from both pdfs for various population C_V values and its results are presented in Table 2. For completeness the estimate $\hat{C}_V$, i.e. the simulation assessment of C_V is shown as well. Note a high quality of approximation of the linear variation coefficient, even in the case of the heavy-tailed log-Gumbel distribution. The log-Gumbel gives considerably inferior evaluation for the conventional variation coefficient C_V, which is related to large bias for the conventional moment estimates in case of high distribution skewness (see Section 2).

Table 2

Large sample estimates of C_V and LC_V

$N = 10000$	gamma			log-Gumbel		
C_V	$\hat{C}_V$	LC_V	$L\hat{C}_V$	$\hat{C}_V$	LC_V	$L\hat{C}_V$
0.2	0.200	0.112	0.112	0.201	0.100	0.100
0.6	0.600	0.324	0.325	0.595	0.241	0.240
1.0	1.008	0.500	0.502	0.924	0.315	0.320
2.0	2.010	0.763	0.761	1.339	0.380	0.380

5. Conclusions

The linear moments system of describing the shape of probability distribution has several desirable properties in respect to flood frequency modelling. Among them there are very small biases of *L*-moments even in moderate samples. However, for some distributions an explicit analytical form of the *L*-moments has not been derived, which precludes using the *L*-moments method for them. Taking advantage from a small bias of the *L*-moments estimates, the simulation experiments can be used to derive the population *L*-moments. This is shown for the inverse Gaussian distribution. The second degree polynomial gives sufficiently good approximation of the relation $LC_V = h(C_V)$, which enables to obtain the relation between the LC_V and the shape parameter β and vice versa. A comparison of LC_V obtained from the simulation approach and from the analytical formula for distributions having the explicit *L*-moments, confirms the validity and a high accuracy of methodology presented in the paper.

Acknowledgements. This work was supported by the Polish Ministry of Science and Higher Education both under the Grant 2P04D05729 entitled “Enhancement of statistical methods and techniques of flood events modelling” and under the Grant N525 001 32/0013 entitled “The mean deviation used in flood frequency analysis”.

References

Cunnane, C. (1989), *Statistical distributions for flood frequency analysis,* Operational Hydrology Report No.33, World Meteorological Organization, Geneva.

Gini, C. (1912), Variabiltà e Mutabilità, contributo allo studio delle distribuzioni e relazioni statistiche, *Studi Economico-Giuridici dell’ Univ. di Cagliari*, **3**, part 2, 1-158.

Greenwood, J.A., J.M. Landwehr, N.C. Matalas, and J.R. Wallis (1979), Probability weighted moments: definition and relation to parameters of several distributions expressible in reverse form, *Water Resour. Res.* **15**, 1049-54.

Hosking, J.R.M. (1990), *L*-moments: Analysis and estimation of distributions using linear combination of order statistics, *J. Royal Statist. Soc.*, Series B, **52** (1), 105-124.

Hosking, J.R.M., and J.R. Wallis (1997), *Regional frequency analysis. An approach based on L-moment,* Cambridge University Press.

Kendall, M.G., and A. Stuart (1969), *The advanced theory of statistics. Vol. 1. Distribution theory*, Charles Griffin & Company Limited, London.

Krysicki, W., J. Bartos, W. Dyczka, K. Królikowska, and M. Wasilewski (1999), *Rachunek prawdopodobieństwa i statystyka matematyczna w zadaniach. II. Statystyka matematyczna*, 4th ed., PWN, Warsaw.

Landwehr, J.M., N.C. Matalas, and J.R. Wallis (1980), Quantile estimation with more or less floodlike distributions, *Water Resour. Res.*, **16** (3), 547-555.

Markiewicz, I., W.G. Strupczewski, K. Kochanek, and V.P. Singh (2006), Relationships between three dispersion measures used in flood frequency analysis, *Stochastic Environmental Research and Risk Assessment* **20**, 391-405, DOI: 10.1007/s00477-006-0033-x.

Perreault, L., B. Bobee, and P.F. Rasmussen (1999), Halphen distribution system. I: Mathematical and statistical properties and II: Parameter and quantile estimation, *J. Hydrologic Eng.,* ASCE, **4 (3)**, 189-199 and 200-208.

Rao, A.R., and K.H. Hamed (2000), *Flood frequency analysis*. CPC Press LLC.

Robson, A., and D. Reed (1999), *Flood Estimation Handbook. Volume 3: Statistical procedures for flood frequency estimation,* Institute of Hydrology, Wallingford, Oxfordshire, UK.

Strupczewski, W.G., S. Węglarczyk, and V.P. Singh (2002), Physics of flood frequency analysis. I: Linear convective diffusion wave model, *Acta Geophys. Pol.* **50** (3), 433-455.

Accepted November 13, 2008

PUBLS. INST. GEOPHYS. POL. ACAD. SC., E-10 (406), 2008

Sediment Transport in the Middle Odra River. Verification of Ackers-White's Formulae with Reference to Big Flows

Zygmunt MEYER and Adam KRUPIŃSKI

Technical University of Szczecin, Department of Geotechnical Engineering
Al. Piastów 50, 71-310 Szczecin, Poland
e-mails: meyer@ps.pl, krupina@ps.pl

Abstract

The paper presents a method of sediment calculation for a compound river cross-section. An essential point for each calculation of sediment is to keep it in relation to the water flow condition. In the paper, a method is shown in which the verification of sediment calculation can be based upon well-defined Chezy constant.

1. Introduction

Sediment transport in rivers has been a research subject for many years. In spite of the fact that the literature concerning this problem is very rich, mechanism of this phenomenon is still subject to study. In the literature there are many formulae which make the sediment transport rate dependent on both the composition of transported material and elements of water motion. These are mainly empirical formulae to be verified by experimental tests and the range of their application is restricted. Pluta (2003) has presented a comparison of the results of calculations by different methods for Odra River. Ackers-White's formulae (Ackers and White 1975) have found a wide application among many formulae which allow to calculate sediment transport rate in the rivers with movable alluvial bottom. This results from the fact that they include elements of water motion, which are well described in the literature, as, e.g., the flow pattern. This allows to introduce an additional element (Coufal 1993) to the sediment transport rate, such as wind action on the water surface or influence of river junction upon the sediment sorting (Krupiński 2001).

At the Department of Geotechnical Engineering of the Technical University in Szczecin, many tests have been made to analyse application possibilities of Ackers-White's formulae for the Lower and Middle Odra River (Meyer *et al*. 1998, 1997, Meyer and Coufal 2007).

The tests results confirm the possibility of this method's application for calculating the sediment transport rate, however the accuracy of these calculations varies. Analysis of the Ackers-White's procedure allows us to find which calculation elements have the biggest impact on the results' distribution. The calculations show that the parameter which defines the beginning of grain movement in the formula of sediment transport rate has a very big influence on the calculation results. The estimation of this parameter's correctness in the Ackers-White's method is carried out in the present paper. Calculation of sediment transport rate in the river during flood, when inundation areas are filled by flowing water, is still a problem. These issues make the subject of the present elaboration.

2. Phenomenon analysis

2.1 The Ackers-White's method

The Ackers-White's method (Ackers and White 1975) assumes that the content of sediment which was taken from the bottom is known as the sieve curve $\{p_i; D_i\}$, and also the water depth H and river slope I are known. On such a basis it is possible to calculate the average velocity

$$\upsilon_o = \frac{Q}{B \cdot H} = \frac{q}{H} \tag{1}$$

and the shear velocity

$$u_* = \sqrt{gHI}\ . \tag{2}$$

The dimensionless diameter is calculated for each fraction D_i

$$D_{gr}^{(i)} = D_i \left[\frac{g(S-1)}{\nu^2} \right]^{1/3}, \tag{3}$$

where ν is the kinematic coefficient of water viscosity, while S is the density ratio (sediment grains material to water). The following parameters are calculated on the grounds of D_{gr}

$$\left.\begin{aligned} n &= 1 - 0.56 \cdot \log D_{gr} \\ A &= \frac{0.23}{\sqrt{D_{gr}}} + 0{,}14 \\ m &= \frac{9.66}{D_{gr}} + 1{,}34 \\ \log C &= 2.86 \log D_{gr} - (\log D_{gr})^2 - 3.53 \end{aligned}\right\} \tag{4}$$

Further, the following parameters are calculated:

- grain mobility F_{gr}

$$F_{gr} = \left[\frac{\upsilon_o}{\sqrt{gD}\ (\text{S-1})} \cdot \frac{1}{\sqrt{32}\ \log \frac{\alpha \text{H}}{\text{D}}} \right] \cdot \left[\frac{u_*}{\upsilon_o} \cdot \sqrt{32}\ \log \frac{\alpha \text{H}}{\text{D}} \right]^{\eta}, \tag{5}$$

– function of sediment transport G_{gr} according to the formula

$$G_{gr} = C \left[\frac{F_{gr}}{A} - 1 \right]^m, \tag{6}$$

– value of dimensionless parameter X of sediment movement:

$$X = \frac{S \cdot D}{H} \cdot G_{gr} \left(\frac{\upsilon_o}{u_*} \right)^n, \tag{7}$$

– and sediment transport rate ω:

$$\omega = \rho g Q \cdot X\ . \tag{8}$$

Calculation of sediment transport rate, for which bottom samples are taken and a sieve curve $\{D_i, p_i\}$ is prepared, is carried out separately for each fraction, and a weighted average is calculated afterwards. It is necessary to underline that this method takes into consideration both the bed load and the suspended sediment.

We get

$$\omega = \sum_{i=1}^{N} p_i \cdot w(D_i)\ . \tag{9}$$

Ackers and White (1975) emphasise clearly that this method should not be applied to the cohesive sediment (with small diameter), such as dusts and loams, because the calculations result in unrealistic, large quantities of sediment, and that is why the sieving curve should be "cut off" from the lower side (Pluta 2003), limiting it to sands and gravels.

2.2 Verifying procedure by the Ackers-White's method in case of big flows

It is assumed that during field measurement the samples were taken from three different places in the river cross-section: from the river midstream and from the flood areas. The obtained hydraulic and geometrical values are shown in Fig. 1.

On the grounds of Fig. 1 the basic relationships can be written as:

$$Q = H_1 B_1 \cdot \upsilon_{o1} + H_2 B_2 \cdot \upsilon_{o2} + H_3 B_3 \cdot \upsilon_{o3} \tag{10}$$

and

$$\omega = \omega_1 + \omega_2 + \omega_3\,, \tag{11}$$

where

$$\omega_1 = \sum_{i=1} \left[p_i^{(1)} \cdot \omega\left(D_i^{(1)} \right) \right], \tag{12}$$

$$\omega_2 = \sum_{i=1}\left[p_i^{(2)} \cdot \omega\left(D_i^{(2)}\right)\right], \tag{13}$$

$$\omega_3 = \sum_{i=1}\left[p_i^{(3)} \cdot \omega\left(D_i^{(3)}\right)\right]. \tag{14}$$

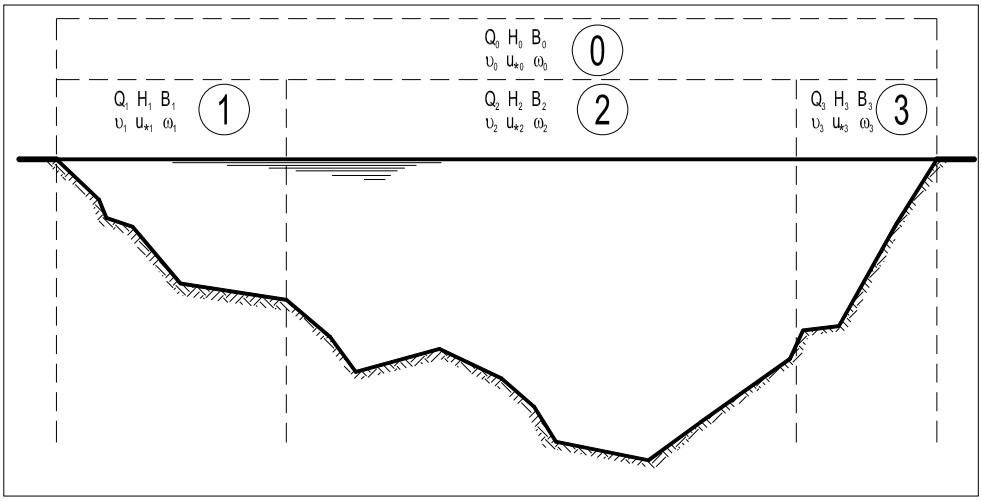

Fig. 1. River cross-section and sampling sites.

Moreover, the sediment continuity equation is fulfilled in the range of the successive fractions in the river. We have

$$\omega(D_i) \cdot p_i^{(0)} = \omega_1(D_i) \cdot p_i^{(1)} + \omega_2(D_i) \cdot p_i^{(2)} + \omega_3(D_i) \cdot p_i^{3}. \tag{15}$$

Relationship (15) allows to obtain the so-called resultant sieving curve in the cross-section where the samples were taken from three different places. It is

$$p_i^{(0)} = \frac{\sum_{j=1}^{3}\left[\omega_j(D_i) \cdot p_i^{(j)} \right]}{\omega_0(D_i^{(0)})}. \tag{16}$$

As far as the sieve curve is concerned it is known that the total sum of the successive fractions' content must make 100%. So we have:

$$\sum_{i=1}^{i=N} p_i^{(0)} = 1. \tag{17}$$

It is an additional equation, which enables calculating one additional unknown value. The shear velocity to average velocity ratio is presumed as both the additional unknown value and the parameter for optimization

$$\frac{u_*}{\upsilon_o} = \xi. \tag{18}$$

Then the formula of grain mobility (5) is obtained in the following form

$$F_{gr} = F_{gr}(\xi) = \left[\frac{\upsilon_o}{\sqrt{gD}\ (\text{S-1})} \cdot \frac{1}{\sqrt{32}\ \log\frac{\alpha \text{H}}{\text{D}}} \right] \cdot \left[\xi \cdot \sqrt{32}\ \log\frac{\alpha \text{H}}{\text{D}} \right]^n . \tag{19}$$

Afterwards, the parameter ξ appears in other terms of this procedure and we get

$$G_{gr} = f(\xi); \quad X = X(\xi) = \frac{S \cdot D}{H} \cdot G_{gr}(\xi) \cdot \left(\frac{1}{\xi} \right)^n \quad \text{and} \quad \omega = \omega(\xi) \tag{20}$$

$$\omega_1 = \omega(\xi) \quad \text{and} \quad \omega_2(\xi); \quad \omega_3(\xi).$$

The optimisation still requires ξ to be made dependent on the velocity.

On the grounds of the Chezy formula it is possible to write down (for $I_2 = I_3$)

$$\upsilon_{30} = \upsilon_{20} \cdot \left(\frac{H_3}{H_2} \right)^{2/3} \cdot \frac{n_3}{n_2} \tag{21}$$

and

$$\upsilon_{10} = \upsilon_{20} \cdot \left(\frac{H_1}{H_2} \right)^{2/3} \cdot \frac{n_1}{n_2} . \tag{22}$$

In order to simplify calculations, *n* = *const* is assumed in the first approximation. After substituting it to formula (10), we get

$$\upsilon_{20} = \frac{Q}{\left(\frac{H_1}{H_2} \right)^{2/3} \cdot B_1 H_1 + B_2 H_2 + \left(\frac{H_3}{H_2} \right)^{2/3} \cdot B_3 H_3} . \tag{23}$$

The following relationships result from the shear-stress velocity formula

$$u_{1*} = u_{2*} \left(\frac{H_1}{H_2} \right)^{1/2} \tag{24}$$

and

$$u_{3*} = u_{2*} \left(\frac{H_3}{H_2} \right)^{1/2} . \tag{25}$$

If the parameter ξ from formula (18) is substituted to the above equations, the searched shear-stress velocity to average velocity ratio will be obtained for each of three parts of riverbed cross-section. We have

$$\frac{u_{2*}}{\upsilon_{20}} = \xi \tag{26}$$

and

$$\frac{u_{1*}}{\upsilon_{10}} = \xi\left(\frac{H_2}{H_1}\right)^{1/6}, \tag{27}$$

$$\frac{u_{3*}}{\upsilon_{30}} = \xi\left(\frac{H_2}{H_3}\right)^{1/6}. \tag{28}$$

Finally, we obtain relationships that each component of the sediment transport rate, ω_1; ω_2; $\omega_3 = f(\xi)$, and the entire sediment transport rate $\omega = f(\xi)$ are also functions of ξ.

2.3 Calculation results of sediment transport rate's parameters

On the grounds of the presented procedure it is possible (assuming the value ξ in the beginning) to calculate a joined sediment transport rate for three parts of the river bed cross-section, and then the principle of "one" (Eq. 17) is checked. There is one such a value ξ, that verifies this formula. It is possible to check how the joint sediment transport rate changes downstream, because the sediment samples were taken in six different cross-sections on the ca. 20-km-long section. For the steady motion there is another equation verifying the calculation

$$\frac{d\omega}{dx} = 0. \tag{29}$$

This equation was used to optimize the second parameter. There is a term $\frac{\alpha H}{D}$ in formula (20) for F_{gr}; the parameter α = 12.3 is assumed. Verification was made to check which parameter α makes the sum of standard deviation of sediment transport rate the smallest. The calculation results are presented in Table 1.

Table 1

Optimisation of parameter α

km	calculations for the assumed values α :																			
	15.0		12.3		10.0		7.0		**5.0**		**4.0**		3.0		2.0		1.0		0.5	
	ξ	ω_0	ξ	ω_0	ξ	ω_0	ξ	ω_0	ξ	ω_0	ξ	ω_0	ξ	ω_0	ξ	ω_0	ξ	ω_1	ξ	ω_2
594	*0.022*	*0.010*	*0.022*	*0.010*	*0.021*	*0.010*	*0.021*	*0.010*	*0.025*	*0.399*	*0.025*	*0.394*	*0.030*	*1.907*	*0.027*	*1.627*	*0.032*	*5.520*	*0.027*	*5.761*
598	*0.033*	*2.702*	*0.031*	*2.345*	*0.029*	*2.028*	*0.027*	*1.568*	*0.022*	*0.630*	*0.021*	*0.532*	*0.026*	*2.549*	*0.028*	*4.780*	*0.023*	*4.376*	*0.019*	*4.999*
604	*0.075*	*1.184*	*0.073*	*1.157*	*0.072*	*1.131*	*0.068*	*1.087*	*0.065*	*1.047*	*0.063*	*1.024*	*0.061*	*0.995*	*0.057*	*0.958*	*0.051*	*0.903*	*0.087*	*8.649*
608	*0.041*	*0.161*	*0.040*	*0.147*	*0.039*	*0.133*	*0.038*	*0.112*	*0.050*	*1.306*	*0.035*	*0.082*	*0.033*	*0.069*	*0.031*	*0.054*	*0.038*	*0.778*	*0.025*	*0.025*
609	*0.039*	*0.611*	*0.038*	*0.588*	*0.037*	*0.567*	*0.036*	*0.531*	*0.034*	*0.502*	*0.033*	*0.486*	*0.032*	*0.471*	*0.031*	*0.458*	*0.038*	*3.221*	*0.107*	*74.28*
614	*0.054*	*0.168*	*0.052*	*0.154*	*0.051*	*0.140*	*0.049*	*0.118*	*0.047*	*0.099*	*0.045*	*0.087*	*0.043*	*0.073*	*0.041*	*0.055*	*0.037*	*0.032*	*0.046*	*0.820*
$\omega_{śr}$	0.9		0.7		0.7		0.7		0.6		0.5		1.2		1.6		3.0		18.7	
δ^2	4.7		4.0		3.1		2.0		1.0		**0.64**		5.4		16.5		26.2		4214.9	
$\delta^2/\omega_{śr}$	5.4		7.4		6.9		4.7		**2.8**		2.5		3.8		6.7		3.0		12.0	

In column one "km" denotes location along the river. As a result, α_{opt} = 4.3 is obtained and this value is different from α = 12.3. The parameter ξ was the second element that was verified. On the grounds of the Chezy equation it is known that

$$\xi = \frac{u_*}{\upsilon_o} = \frac{\sqrt{g}}{C}. \tag{30}$$

Hence

$$C = \frac{\sqrt{g}}{\xi}. \tag{31}$$

This means that in each cross section it is possible to control the constant value C for the Chezy equation. This constant value is recognized for the Middle and Lower Odra River. It turns out that if the value A is assumed according to formula (4), the obtained values of C will not be realistic. Therefore, different values of A are presumed for calculations according to the relationship

$$A_1 = A \cdot \varepsilon . \tag{32}$$

The calculation results are shown in Table 2.

Table 2

Optimisation of parameter C

for α=12.3																				
	1.1A			1.2A			1.3A			1.4A			1.5A			1.6A			1.7A		
km	ω_0	ξ	$C_{wg\ Chezy}$	ω_1	ξ	$C_{wg\ Chezy}$	ω_2	ξ	$C_{wg\ Chezy}$	ω_2	ξ	$C_{wg\ Chezy}$	ω_2	ξ	$C_{wg\ Chezy}$	ω_3	ξ	$C_{wg\ Chezy}$	ω_3	ξ	$C_{wg\ Chezy}$
594	0.488	0.035	***89***	0.564	0.043	***73***	0.652	0.052	***61***	0.762	0.062	***51***	0.861	0.072	***44***	0.93	0.084	***37***	1.007	0.097	***32***
598	3.06	0.041	***76***	5.337	0.058	***54***	8.422	0.079	***40***	12.44	0.105	***30***	17.99	0.138	***23***	21.27	0.170	***18***	25.12	0.212	***15***
604	1.22	0.092	***34***	1.30	0.113	***28***	1.39	0.136	***23***	1.51	0.161	***19***	1.66	0.189	***17***	1.75	0.220	***14***	1.85	0.254	***12***
608	0.21	0.051	***62***	0.29	0.062	***51***	0.37	0.075	***42***	0.45	0.089	***35***	0.55	0.105	***30***	0.61	0.122	***26***	0.68	0.140	***22***
609	0.67	0.048	***66***	0.78	0.058	***54***	0.90	0.070	***45***	1.05	0.083	***38***	1.18	0.097	***32***	1.28	0.113	***28***	1.39	0.130	***24***
614	0.22	0.066	***48***	0.29	0.081	***39***	0.37	0.097	***32***	0.45	0.116	***27***	0.55	0.136	***23***	0.61	0.158	***20***	0.68	0.183	***17***
average	0.978		62.47	1.426		49.73	2.016		40.42	2.778		33.37	3.797		28.01	0.145		23.86	0.169		20.5
δ^2	5.9		1919	19.1		1170	50.0		796	112.7		576	242.6		445	0.0		337	0.0		266

In column one, "km" denotes location along the river. It appears that in order to obtain the constant value C in the Chezy formula as it results from the flow conditions in the successive six cross-sections, parameter A must change. In every cross-section these changes were made depending on characteristic features of the sieve curve for the current material, assuming the statistic parameters:

$$D_o = \sum \left(p_i \cdot D_i \right) \tag{33}$$

and average values

- average standard deviation

$$\delta = \sqrt{\sum \left[p_i \left(D_i - D_o \right)^2 \right]}, \tag{34}$$

- and skewness of sieve curve

$$\vartheta = \sqrt[3]{\sum \left[p_i \left(D_i - D_o \right)^3 \right]}. \tag{35}$$

The empirical formula to calculate the value of ε was obtained on this way in the following form

$$\varepsilon = -0.123\ \mathrm{D_o} - 1.875 \cdot \delta + 2.052 \cdot \vartheta . \tag{36}$$

The optimisation results for formula (36) are presented in Table 3.

Table 3

Optimisation of parameter ε

for α=12,3 flow parameters					sieve curve parameter			calculated
km	ω_0	H_0	ξ	C_{Chezy}	D_0	δ	ϑ	n_s
594	0.996	1.720	0.087	**36.00**	1.21	1.80	2.50	0.0304
598	9.722	1.730	0.087	**35.84**	1.13	1.55	2.14	0.0306
604	1.197	2.010	0.086	**36.42**	0.98	0.98	1.51	0.0308
608	0.435	1.920	0.086	**36.40**	0.82	1.19	1.89	0.0306
609	1.083	1.870	0.087	**36.00**	0.72	0.93	1.47	0.0308
614	0.321	2.050	0.087	**36.02**	0.64	0.75	1.32	0.0313

In column one, "km" denotes location along the river. While making Tables 2 and 3 it was assumed that α = 12.3 as Ackers suggests. It results not only from the fact that the formulae were verified on the grounds of the field measurements for these relationships by many authors, but also that there is preserved a possibility to compare presented calculation results with other parameters. Moreover, the calculations show that such a variable value of coefficient α has a very little influence upon the sediment transport rate w that is calculated for ξ_{opt}.

3. Conclusions

The paper presents the verification of Ackers-White's formulae for calculation of sediment transport rate under the conditions of the Middle Odra River and big flows, when the inundation areas are flooded.

The analyses were carried out with the help of optimisation of parameter ξ, which describes the ratio of the obtained velocity to the average velocity in the selected river cross-section.

The verification consisted in comparing the constant value C in the Chezy formula resulting from the river water flow to the constant value that was calculated on the grounds of the optimal parameter ξ from the Ackers-White's method.

The verification indicates that the formula needs to be replaced by the constant value A, which defines the beginning of grain motion in the river. This constant value was made dependent on the parameters of sieving curve, reaching a good accuracy. Meyer and Coufal (2007) did similarly determining a representative grain diameter in dependence on the statistic parameters of sieve curve.

The verification allowed also to optimize the parameter α, which appears informula (20) for the grain mobility. Using the constant stream of the sediment transport rate along the river, it is possible to define that $\alpha_{opt} = 4.6$ and this is a different value from what was assumed both by Ackers and in the literature, i.e. $\alpha = 12.3$. Due to the fact that this change does not affect the verification results, concerning the constant value C in the Chezy formula it is suggested to preserve $\alpha = 12.3$ in calculations.

The program of further researches includes:

- field measurements in other places of the Middle and Lower Odra River in order to gain materials for verification, especially for big flows;
- verification of Ackers-White's method for different sections and for changeable flows in the Odra River;
- searching for more universal relationships defining parameters A, α and bottom roughness for longer river sections and big flows.

4. Notations

A – parameter of grain movement in the Ackers-White's method,
B – riverbed width,
C – constant value in the Chezy formula,
D_o – average grain diameter of bottom sediment,
D_{gr} – dimensionless parameter defining sediment size,
F_{gr} – mobility parameter,
g – acceleration due to gravity,
G_{gr} – dimensionless parameter of sediment transport rate,
H – river depth,
I – river slope,
n – roughness coefficient by Manning,
$\{p_i, D_i\}$ – set of values of sieve curve,
u_* – shear velocity,
υ_o – average flow velocities,
ω – sediment stream,
X – dimensionless sediment transport rate,
x – horizontal co-ordinate of the assumed system of coordinates,
α – constant value in the average velocity formulae,
ε – function of change of parameter A,
ξ – shear velocity ratio, to average velocity.

Note: lower indices denote sediment fractions; upper indices (Eqs. 12 to 16) denote the number of riverbed cross-section part.

References

Ackers, P., and W.R. White (1975), Sediment transport, new approach and analysis, *J. Hydraul. Div. ASCE*, **99**, HY 11.

Meyer, Z., R. Coufal, and R. Kotiasz (1998), Influence of the sediment transport on the steady water flow in the river, *3rd International Conference Hydro-Science and Engineering, ICH'' 98* – Cottbus.

Sawicki, I.M. (1998), *Flows with Free Water Surface*, Wydawnictwo Naukowe PWN, Warszawa.

Pluta, M. (2003), Applicability of Sediment Transport Formulae for Odra River. *XI seminarium naukowe z cyklu Regionalne Problemy Ochrony Środowiska w Ujściu Odry.* Szczecin-Ystad-Świnoujście.

Meyer, Z., R. Coufal, and A. Roszak (1997), Division of Sediment Stream in River Bifurcation during Flood at Widuchowa Weir in lower Odra River. *XVII Ogólnopolska Szkoła Hydrauliki*, wrzesień 1997.

Coufal, R. (1993), Wind Shear Stress Affected Sediment. *Proceedings of the Advances of Hydro-Science and Engineering*. Part B, pp.1749-1754, S. Wang (ed.), The University of Mississippi.

Krupiński, A. (2001), *Sediment Sortation Influence on Bottom Changes in River Junction at Kostrzyn*, Praca doktorska. Szczecin 2001.

Meyer, Z., and R. Coufal (2007), Determination of Sediment Transport Characteristic Diameter for the Odra River Section. *XXVII International School of Hydraulics Hydraulic and Environmental Hydraulics*, Hucisko 18-21 Sept. 2007.

Accepted December 10, 2008

PUBLS. INST. GEOPHYS. POL. ACAD. SC., E-10 (406), 2008

Uncertainty in the Relationship Between Flow and Parameters in Models of Pollutant Transport

Marzena OSUCH[1], Renata J. ROMANOWICZ[1], and Steve WALLIS[2]

[1]Institute of Geophysics Polish Academy of Sciences
Ks. Janusza 64, 01-452 Warsaw, Poland
e-mails: marz@igf.edu.pl, renatar@igf.edu.pl

[2]Heriot-Watt University
Riccarton, Edinburgh, EH14 4AS, UK
e-mail: s.g.wallis@hw.ac.uk

Abstract

A fluorescent dye-tracer study is usually performed under steady-state flow conditions. However, the model parameters, estimated using the tracer data, depend on the discharges. This paper investigates the uncertainty of the relationship between discharges and parameters of a transient storage and an aggregated dead zone model. We apply a Bayesian statistical approach to derive the cumulative distribution of a range of model parameters conditioned on discharges. The set of tracer data consists of eighteen tracer concentration profiles taken at two cross-sections from the Murray Burn, a stream flowing through the Heriot-Watt University Campus at Riccarton in Edinburgh.

1. Introduction

The transport downstream of a conservative pollutant can be described by the Advection-Dispersion Equation (ADE) introduced by Taylor (1953). Bencala and Walters (1983) further extended the ADE approach by introducing the transient storage (TS) model that includes solute trapping in dead zones. Estimation of model parameters is the basis of the successful application of that model in presenting pollutant transfer in rivers and streams. Due to the complexity of the processes involved, a widely accepted method to understand the fate of solutes in streams is to perform a tracer study,

in which a known mass of usually conservative solute is released into the stream. An examination of concentration profiles of the artificially released dye at cross-sections downstream and fitting appropriate models constitute the means to estimate a number of model parameters, including longitudinal dispersion. The process of transport of pollutant depends on the flow conditions and in particular on the discharge. The nature of that dependence is complex and usually is derived from a number of tracer experiments (e.g., Deng *et al*. 2002, Harvey and Wagner 2000).

As an alternative to the transient storage model, the Aggregated Dead Zone (ADZ) model was introduced by Beer and Young (1983). The ADZ model is identified and the parameters are estimated from the collected time series data using system identification techniques (Young 1984). The method is stochastic and the model parameters, including the residence time of the tracer transport process, have the form of random variables, thus allowing for derivation of their dependence on flow in a stochastic form. However, the ADZ model parameters also depend on discharge, as was shown by Wallis *et al*. (1989), Young and Wallis (1994) and Young and Lees (1993).

Smith *et al*. (2006) presented an estimation of ADZ model parameters dependent on discharge within a Bayesian framework thus allowing the errors and predictive uncertainty to be taken into account. The parameters were conditioned on surrogate data derived from water quality measurements. Unfortunately the predictions were not very promising, despite using very elaborate methods, including a full treatment of uncertainties and application of the Monte Carlo Markov Chain sampling from the posterior distribution of parameters.

The aim of this study is the estimation of uncertainty involved in the conditioning of both transport models on flow using a simpler, though less formal, approach. As the TS model is purely deterministic and the ADZ model is stochastic in nature, different approaches are required to estimate the uncertainty in the dependence of their parameters on flow. The Generalised Likelihood Uncertainty Estimation (GLUE) approach developed by Beven and Binley (1992) is suitable for the deterministic models and is therefore applied to the TS model. The method consists of applying Monte Carlo sampling of parameter space and undertaking multiple runs of a deterministic transient storage model. In the present paper we follow the form of the GLUE approach described by Romanowicz *et al*. (2000), where Bayesian conditioning was applied to a Gaussian air pollution model. The relationship between model parameters and flow has the form of a nonlinear regression model based on multiple random realizations of the deterministic transport model. The parameterization of that relationship and introducing it into the TS model allow for the conditioning of parameter estimates and as a result, also model predictions, on the whole set of available observations. In the case of the ADZ model, the approach is based on Monte Carlo sampling of ADZ model parameters taking into account heteroscedastic variance of the observations and estimates of the covariance of the model parameters obtained during model calibration stage.

2. Description of the experiments

Both approaches are illustrated using eighteen tracer experiments performed on the Murray Burn in Edinburgh, UK, under different flow conditions. The experiments were described by Wallis and Manson (2005) and Piotrowski *et al*. (2007). The set of data consists of eighteen tracer experiments taken from two cross-sections from the Murray Burn, a stream flowing through the Heriot-Watt University Campus at Ricarton in Edinburgh. The studied reach is 0.5 km long and the stream is of the order of 3 m wide. The experiments consisted of gulp injection of a known amount of Rhodamine WT dye. The measurements of tracer concentrations at 4 cross-sections below the point of injection were performed using a calibrated Turner Design fluorometer. We concentrate on the first two cross-sections only in order to eliminate differences in channel geometry and the variability of the other conditions influencing pollutant transport.

3. Distributed transient storage model

The transport of a conservative soluble pollutant along a uniform channel is usually described by the well-known Advection-Dispersion Equation. The One-dimensional Transport with Inflow and Storage model (OTIS) introduced by Bencala and Walters (1983) was applied in this study. The OTIS model is formed by writing mass balance equations for two conceptual areas: the stream channel and the storage zone. The exchange of solute mass between the stream channel and the storage zone is modelled as a first-order mass transfer process. Conservation of mass for the stream channel and storage zone yields (Bencala and Walters 1983, Runkel and Broshears 1991):

$$\frac{\partial C}{\partial t} = -\frac{Q\partial C}{A\partial x} + \frac{1}{A}\frac{\partial}{\partial x}\left(AD\frac{\partial C}{\partial x} \right) + \alpha\left(C_S - C \right) \tag{1}$$

$$\frac{dC_S}{dt} = \alpha\frac{A}{A_S}\left(C - C_S \right) \tag{2}$$

where: C is the solute concentration in the stream [g/m^3], t is time [s], Q – the flow discharge [m^3/s], A – the main channel cross-sectional area [m^2], x – the distance downstream [m], D – the coefficient of longitudinal dispersion [m^2/s], C_S – the concentration in the storage zone [g/m^3], α – the exchange coefficient [1/s], and A_S is the storage zone cross-sectional area [m^2].

Since it is not possible to estimate solute transport parameters reliably from hydraulic variables and channel characteristics, application of the transient storage model (1-2) requires the estimation of model parameters based on data from tracer experiments including measurements of discharge. Estimation of model parameters, namely D, A, A_S and α, was performed by minimizing the residuals between the simulated and observed concentrations. A general least squares objective function and Nealder-Mead minimization algorithm were used in this study. The results of the estimation

procedure are presented in the Table 1, they are analogous to those obtained by Wallis and Manson (2005) for a similar model but a different numerical scheme.

Table 1

Parameters of transient storage models

Experiment	Q [m^3/s]	D [m^2/s]	A [m^2]	A_S [m^2]	α [1/s]
2	0.0680	0.606	3.45E-01	8.80E-05	2.51E-03
4	0.0436	0.494	2.78E-01	1.16E-04	2.71E-03
5	0.0475	0.449	2.95E-01	1.20E-04	2.93E-03
6	0.1285	1.210	4.65E-01	6.98E-05	5.83E-01
7	0.1342	1.020	4.49E-01	6.44E-05	7.03E-01
8	0.0459	0.402	2.84E-01	9.35E-05	5.97E-01
9	0.0353	0.550	2.40E-01	1.15E-04	3.69E-03
10	0.0563	0.624	3.09E-01	1.06E-04	3.32E-01
15	0.0495	0.618	2.78E-01	1.29E-04	4.15E-03
16	0.0156	0.328	1.82E-01	1.20E-04	2.79E-01
17	0.0139	0.412	1.63E-01	1.15E-04	3.37E-01
18	0.0330	0.541	2.56E-01	9.68E-05	2.98E-01
20	0.2610	3.010	5.90E-01	3.60E-05	8.50E-03
21	0.1621	0.922	4.80E-01	4.53E-05	1.46E-02
22	0.2575	2.420	6.18E-01	3.00E-05	1.69E-02
23	0.0621	0.529	3.47E-01	1.55E-04	3.73E-03
24	0.5354	2.980	9.66E-01	5.90E-06	1.06E-02
26	0.9524	4.290	1.05E+00	5.28E-06	6.86E-03

The differences between optimal parameter values result mainly from differences in hydraulic conditions between the experiments. The relationship obtained between optimal model parameters and flow is shown in Fig. 1.

Only the exchange coefficient α does not show a well defined relationship with flow. The other parameters show a relationship that can be easily parameterised using, for example, a power law function (Wallis *et al*. 1989). In Fig. 1 we present such a parameterisation together with 0.95 confidence bounds for the fit. The OTIS model is deterministic and therefore the parameterisation does not take into account any uncertainty related to the model structure and observations.

4. Application of uncertainty analysis to conditioning the dispersion estimates on flow

In this section we investigate the application of the GLUE technique to assess the influence of flow values on four OTIS parameters (the longitudinal dispersion (D),

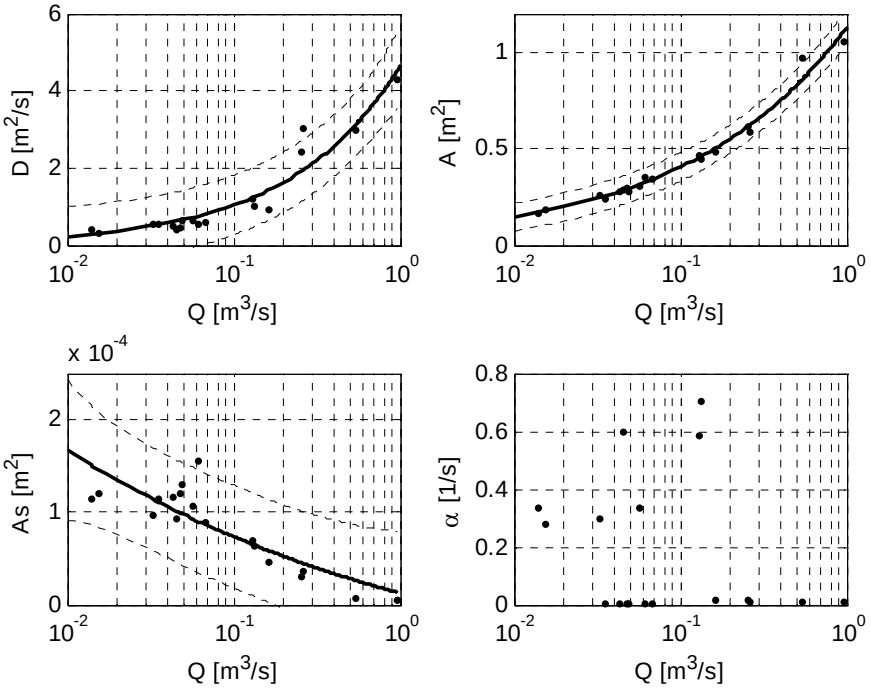

Fig. 1. Graphical relationship between optimised model parameters and flow (black dots); power law fit, excluding α, is shown by black lines.

the main channel area (A), the storage zone area (A_S) and the exchange coefficient (α)). The basic assumption of this methodology (Beven and Binley 1992) is that in the case of over-parameterized environmental models, a unique solution of the inverse problem is not possible due to a lack of data (an interactive discussion of this topic is presented by Pappenberger *et al*. (2007)). There can be many different parameter sets which provide reasonable results. Therefore, calibration should consist of the estimation of the multidimensional distribution of model parameters conditioned on observations. For such an analysis the Bayesian formula is used:

$$f(\mathbf{X}|\mathbf{z}) = \frac{f_0(\mathbf{X})L(\mathbf{z}|\mathbf{X})}{L(\mathbf{z})} \tag{3}$$

where $\mathbf{z}$ is the vector of observed concentrations, $\mathbf{X}$ is the parameter vector, $f(\mathbf{X}|\mathbf{z})$ is the posterior distribution (probability density) of the parameters conditioned on the observations $\mathbf{z}$, $f_0(\mathbf{X})$ is the prior probability density of the parameters, $L(\mathbf{z})$ is a scaling factor, $L(\mathbf{z}|\mathbf{X})$ represents the likelihood measure based on the relationship between $\mathbf{z}$ and $\mathbf{X}$.

In this study tracer concentrations at the second cross-section were used as the observation vector $\mathbf{z}$; four analyzed OTIS model parameters were used as the parame-

ter vector **X**. Furthermore, it was assumed that the likelihood measure is proportional to the Gaussian distribution function (Romanowicz and Beven 2006):

$$L(\mathbf{z}|\mathbf{X}) \approx e^{(\mathbf{z}-Y(\mathbf{X}))^2/\sigma^2} \tag{4}$$

where **z** is vector of the observed tracer concentration, Y is a vector of simulated concentration and σ^2 denotes the mean error variance determining the width of the distribution function. It is important to note that in the GLUE methodology a subjective choice of the distribution width is allowed. On the basis of posterior likelihood values, the distribution of simulated tracer concentrations can be evaluated.

The model parameter space is sampled using the Monte Carlo method. The prior distribution $f_0(\mathbf{X})$ of parameters is introduced at this stage. During the analysis set up we followed the methodology outlined in Romanowicz *et al*. (2000), describing the estimation of uncertainty of a Gaussian air pollution model predictions. The model parameters were sampled uniformly within the ranges chosen following the results of optimisation of the OTIS model, with the mean equal to the optimum values. In that way we incorporated the information obtained from the deterministic solution whilst allowing for the uncertainty of the model structure and observations. The resulting posterior cumulative distributions of all four model parameters and flow for 3 experiments with different values of observed flow are shown in Fig. 2.

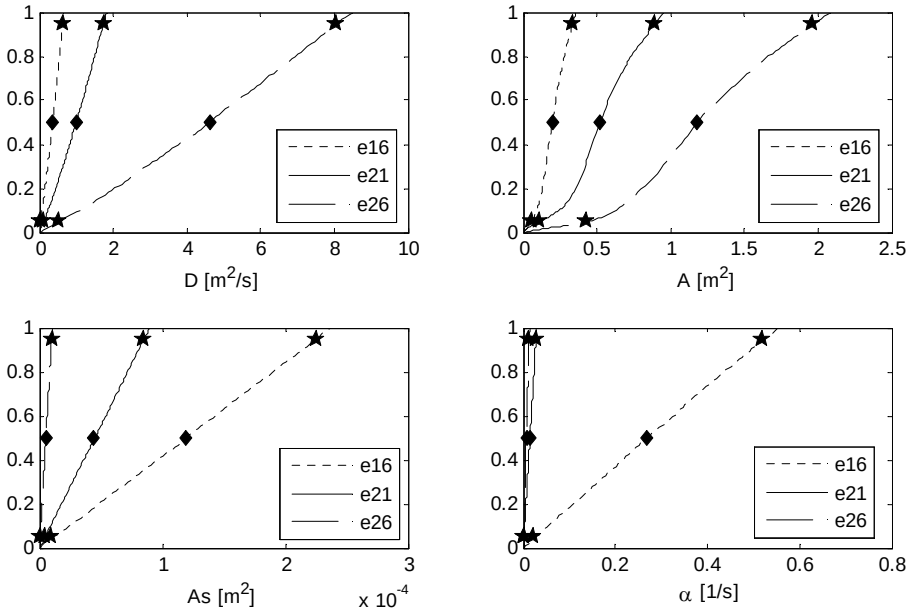

Fig. 2. Comparison of posteriori cdf for parameters for experiment 16 (dotted line), 21 (solid line) and 26 (dashed line) with observed flow equal to 0.0156, 0.1621, 0.9524 [m^3/s] respectively, stars denote the upper and the lower 0.95 confidence bounds.

The posterior cumulative distribution functions (cdfs) for the parameters can be used to derive the error bounds for the parameters. Figure 3 presents the relationship derived between four model parameters (D, A, A_S and α) and flow, with 0.95 confidence bounds being an equivalent to the relationship shown in Fig. 1, but taking into account the model and observation uncertainty. The uncertainty of the relationship for D and A increases with flow magnitude, which was not shown by the deterministic analysis. However, this might be a result of sampling from wider parameter ranges for larger flow magnitudes. The posterior cdfs show the influence of conditioning on observations only for high values of flow (experiment 26) for D and A. This result suggests that the choice of prior distribution might influence the results and further research is required to test different priors. The transient storage parameters A_S and α require some additional discussion. The analysis of tracer experiments performed by Wallis and Manson (2005) indicates that the processes of transient storage were negligible for the river reach under consideration. The estimated transient storage cross-sectional area is very small (of the order of 10^4), showing a well defined dependence on flow, though the cross sectional area decreases further with the increase of flow. However, the relationship between exchange coefficient α and flow is not well defined showing a threshold-type dependence thus indicating that there is no enough information on the transient storage processes within the tracer experiment data. The estimated relationship between OTIS model parameters and flow can be used to interpolate/extrapolate the parameter values for flow values not used in the calibration stage.

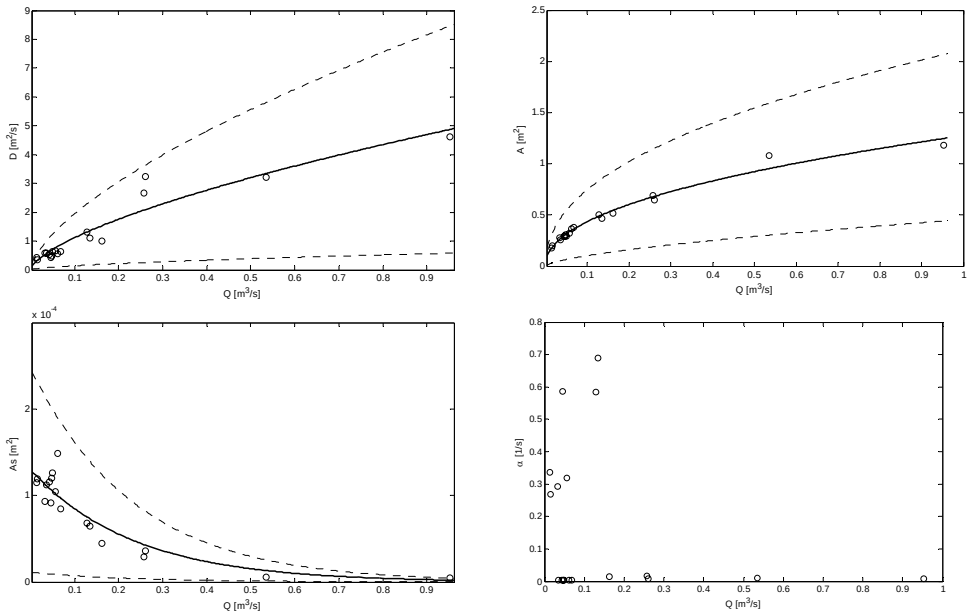

Fig. 3. Relationship between OTIS parameters and flow with 0.95 confidence bounds derived from the MC analysis of the model conditioned on tracer experiments.

5. The ADZ model

As an alternative to the transient storage model described by means of partial differential equations (1-2), a data-based mechanistic approach was introduced (Beer and Young 1983, Beven and Young 1998, Wallis 1989, Young and Lee, 1993). In this approach a so-called aggregated dead zone (lumped) model is identified and the parameters are estimated from the observed time series data using system identification techniques (Young 1984). In the ADZ model the change of solute concentration in a river reach is described as:

$$Cout_k = \frac{B(z^{-1})}{A(z^{-1})} Cin_{k-\delta}, \qquad Cobs_k = Cout_k + \xi_k \tag{5}$$

where $Cout_k$ is the concentration at the upstream end of the river reach at time k, Cin_k is the estimated concentration at the downstream end of the river reach, $Cobs_k$ is the measured concentration at the downstream end of the river reach, z^{-1} is the backshift operator, δ is the advection time delay, A and B are polynomials of the backshift operator of the order m and n respectively, and ξ_k represents the combined effect of all stochastic inputs to the system, including measurement noise. A and B are given by:

$$B(z^{-1}) = b_0 + b_1 z^{-1} + b_2 z^{-2} + \ldots + b_m z^{-m} \tag{6}$$

$$A(z^{-1}) = 1 + a_1 z^{-1} + a_2 z^{-2} + \ldots + a_n z^{-n} \tag{7}$$

The order of the ADZ model describing the transport of solute in the river reach is described by the triad [n, m, δ] and is determined in a statistical time series analysis technique using the recursive-iterative simplified, refined, instrumental variable (SRIV) method (Young 1984) available in the Captain Toolbox developed at the University of Lancaster. Identification of model structure and estimation of parameters of the transfer functions models were conducted independently for every experiment.

In order to account for the observation error varying with the value of flow, Monte Carlo analysis was performed with flow values following the heteroscedastic distribution and STF model parameters derived for each generated value of flow. Additionally, in the inner loop, also the STF model parameters were sampled randomly following the distribution estimated by the RIV routine. The resulting sample was used to derive the estimates of residence time and steady state gain for the STF model. Figures 4 and 5 show the relationship between ADZ model parameters (a_1, b_0) and flow together with 0.95 confidence bounds, obtained from the MC analysis. Similarly as in the case of OTIS analysis, there is evident increase of uncertainty of the relationship for large flow values.

The derived mean travel times, being the sum of residence time (derived from a_1) and advective delay, also depend on flow (Fig. 6). The increase in the uncertainty of that relationship with flow is much smaller than the parameter uncertainty due to relatively small uncertainty in estimated advective delay, which is an order of magni-

tude larger than the residence times. However, that result may be caused by too certain predictions of advective delay, as only heteroscedasticity of observations was taken into account. This indicates the need for further investigation using continuous type transfer function models.

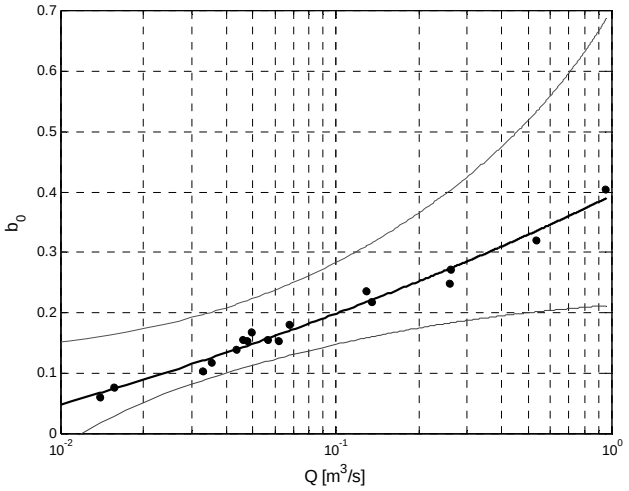

Fig. 4. Relationship between discharge and b_0 (parameter of first order ADZ model) with 0.95 confidence bounds marked as gray lines.

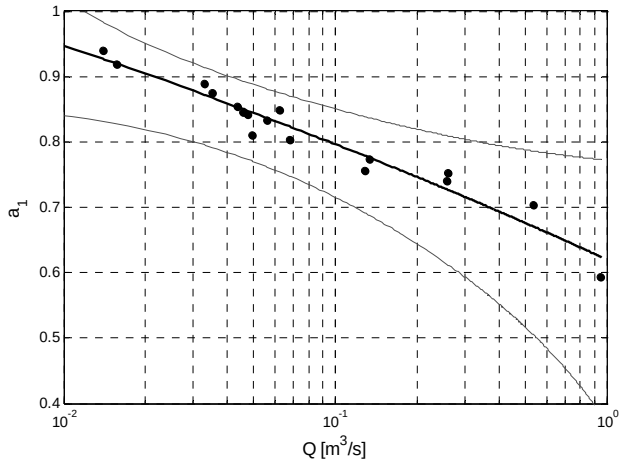

Fig. 5. Relationship between discharge and a_1 (parameter of first order ADZ model) with 0.95 confidence bounds marked as gray lines.

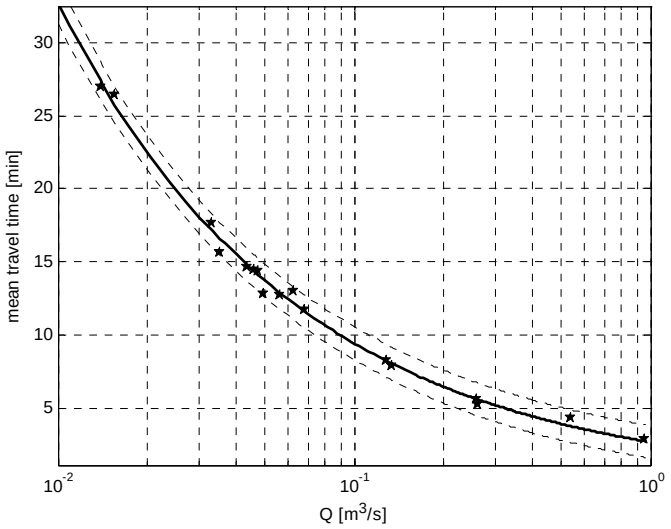

Fig. 6. Relationship between mean travel time and discharge with 0.95 confidence bounds.

The application of the ADZ model to flow values differing from those used during the calibration of the parameter dependence on flow requires interpolation/extrapolation of the ADZ model parameters, together with the estimated variance following the relationships obtained.

6. Conclusions

We have presented an analysis of the uncertainty of the relationship between solute transport model parameters and flow magnitude for both a deterministic, mechanistic model (OTIS) and a stochastic ADZ model based on the tracer experiment data from a reach of the Murray Burn, UK. The GLUE procedure was used to estimate the uncertainty in the relationship between OTIS model parameters and flow related to the parameter and observational uncertainty. The derivation of a dependence of the stochastic ADZ model parameters on flow was performed applying MC sampling of the ADZ model parameters, following the distribution obtained from the SRIV procedure and taking into account the heteroscedastisity of errors of observed concentrations. The estimated uncertainty in the dependence of both OTIS model and ADZ model parameters on flow shows large increases with flow values. This indicates that smaller time steps for tracer sampling should be used for larger flows. However, in the case of the STF model, that increase of uncertainty in parameter values does not influence much the estimated mean travel time uncertainty.

In a continuation of this work, in the validation stage of the TS model, the estimated mean value and variance of the parameterized relationship for each parameter are used within the MC setup to derive OTIS model predictions for different values of flow than those used in the calibration stage. Work is also underway on the introduc-

tion of nonlinear parameterisation of ADZ model parameters directly into the model structure and on the use of continuous time transfer function models.

Acknowledgments. We would like to thank to anonymous reviewer for comments, which helped to greatly improve this paper.

References

Beer, T., and P.C. Young (1983), Longitudinal dispersion in natural streams, *J. Environ. Eng.* **109**, 1049-1067.

Bencala, K.E., and R.A. Walters (1983), Simulation of solute transport in a mountain pool-and-riffle stream: a transient storage model, *Water Resour. Res*. **19**, 3, 718-724.

Beven, K.J., and A. Binley (1992), The future of distributed models: model calibration and uncertainty prediction, *Hydrol. Process*. **6**, 279-298.

Beven, K.J., and P.C. Young (1998), An aggregated mixing zone model of solute transport through porous media, *J. Contaminant Hydrology* **3**, 129-143.

Deng, Z.Q., L. Bengtsson, V.P. Singh, and D.D. Adrian (2002), Longitudinal dispersion coefficient in single-channel streams, *J. Hydraul. Eng*. **128**, 901-916.

Harvey, J.W., B.J. Wagner, and K.E. Bencala (1996), Evaluating the reliability of the stream tracer approach to characterize streamsubsurface water exchange, *Water Resour. Res*. **32**, 8, 2441-2451.

Pappenberger, F., K.J. Beven, K. Frodsham, R.J. Romanowicz, and P. Matgen (2007), Grasping the unavoidable subjectivity in calibration of flood inundation models: A vulnerability weighted approach, *J. Hydrol*. **333**, 2-4, 275-287.

Piotrowski, A., S.G. Wallis, J.J. Napiórkowski, and P.M. Rowiński (2007), Evaluation of 1-D tracer concentration profile in a small river by means of Multi-Layer Perceptron Neural Networks, *Hydrology and Earth System Sciences* **11**, 6, 1883-1896.

Richardson, K., and P.A. Carling (2006), The hydraulics of a straight bedrock channel: Insights from solute dispersion studies, *Geomorph*. **82**, 98-125.

Romanowicz, R.J., H. Higson, and I. Teasdale (2000), Bayesian Uncertainty Estimation Methodology applied to air pollution modelling, *Environmetrics* **11**, 351-371.

Romanowicz, R.J., and K.J. Beven (2006), Comments on Generalised Likelihood Uncertainty Estimation, Reliability Engineering and System Safety, DOI: 10.1016/j.ress.2005.11.030.

Runkel, R.L., and R.E. Broshears (1991), *One dimensional transport with inflow and storage (OTIS): A solute transport model for small streams*. Tech. Rep. 91-01, Center for Adv. Decision Support for Water and Environ. Syst., Univ. of Colorado, Boulder.

Smith, P., K. Beven, J. Tawn, S., Blazkova, and L. Merta (2006), Discharge-dependent pollutant dispersion in rivers: Estimation of aggregated dead zone parameters with surrogate data, *Water Resour. Res*. **42**, W04412, doi:10.1029/2005WR004008

Taylor, G.I. (1954), *The dispersion of matter in turbulent flow through a pipe*, Proceedings of the Royal Society, A223, 446-468.

Young, P.C. (1984), *Recursive Estimation and Time Series Analysis*, Springer-Verlag, Berlin.

Young, P.C., and M. Lees (1993), *The Active Mixing Volume: A new concept on Modelling Environmental Systems*. **In:** Statistics for the Environment, John Wiley & Sons, Chichester, 3-44.

Young, P.C., and S.G. Wallis (1994), *Solute transport and dispersion in channels*. **In:** K. Beven and M.J. Kirkby Channel (eds.), Network Hydrology, John Wiley & Sons Ltd.

Wallis, S.G., P.C. Young, and K.J. Beven (1989), *Experimental investigation of the aggregated dead zone model for longitudinal solute transport inn stream channels*, Proceedings of the Institution of Civil Engineers, 87, 1–22.

Wallis, S.G. (1994), *Simulation of Solute Transport in Open Channel Flow*. **In:** Mixing and Transport in the Environment, John Wiley & Sons, Chichester, 89-111.

Wallis, S., and R. Manson (2005), Modelling solute transport in a small stream using DISCUS, *Acta Geophys. Pol*. **53**, 4, 501-515.

Wallis, S., A. Piotrowski, P.M. Rowiński, and J.J. Napiórkowski (2007), *Prediction of dispersion coefficients in a small stream using artificial neural networks*, Proceedings 32nd Congress of IAHR, July, 1-6 2007, Harmonizing the Demands of Art and Nature in Hydraulics, paper 175.

Accepted December 23, 2008

PUBLS. INST. GEOPHYS. POL. ACAD. SC., E-10 (406), 2008

Developments in Floodplain Inundation Modelling

Gareth PENDER, Sylvain NÉELZ, and Yang LIU

School of the Built Environment, Heriot Watt University, Edinburgh, UK,
e-mail:g.pender@hw.ac.uk

Abstract

The advantage of using 2D hydrodynamic models to predict floodplain inundation is that they provide estimates of the velocity field in addition to estimates of flood inundation extent and depth. However, velocity predictions require topographic features on the floodplain to be accurately represented within the solution grid of the numerical model. For a typical developed floodplain this requires a grid resolution of between 2 to 5 m. Floodplain models using this level of resolution are relatively demanding of computer resources and it can take days to simulate a typical 12 hour flood event using a standard dual processor PC. An important issue facing the modeller is therefore, can the floodplain velocity field be predicted to an acceptable level of accuracy using less computer resources. The following presents an initial assessment of two possible methods for achieving this.

Firstly, results from Coarse Grid Models (CGM) at grid resolutions of 10 m and 50 m are compared against benchmark results from a Fine Grid Model (FGM) with a 2 m grid resolution using statistics based on the timing of inundation throughout the modelled domain. Methods for improving the coarse grid predictions using simulations from a limited number of fine grid simulations are presented and illustrated by application to a case study site.

Secondly, the study investigates replicating water level and velocity predictions using a non-linear *v*-Support Vector Regression (*v*-SVR) model. This is an integration of *v*-SVR with CGM predictions using a small number of FGM runs to train *v*-SVR. The simulated results suggest that the proposed method is able to achieve good predictive results (water level and velocity) as well as provide considerable savings in computer time.

Key words: flooding, modelling, velocity.

1. Introduction

Until relatively recently, most flood modelling in the UK was undertaken using 1D modelling methods. However, the increasing availability of remotely sensed digital elevation models of both rural and urban floodplains has resulted in an increased interest in the use of 2D modelling, or in some cases hybrid techniques where a 1D model for the river channel is linked to a 2D model of the floodplain. Such models provide detailed insight into the hydrodynamics of floodplain inundation. However, the time required to run a relatively modest 2D model using standard office computing facilities can be significant.

The paper reports on the compromise between model grid resolution and runtime necessary to ensure 2D predictions can be made using typical desk top computing facilities. Further it reviews the potential of improving Coarse Grid Model (CGM) results using a relatively small number of Fine Grid Model (FGM) predictions and a non-linear *v*-Support Vector Regression (*v*-SVR) model trained on a limited number of FGM predictions. The inclusion of sub-grid scale blockage in relatively coarse grid models and improving coarse grid model results using fine grid model results are discussed.

2. Representation of sub-grid scale blockage

Case study site

The study site is a ~5 km^2 area of lowlands along the banks of the Thames Estuary in England. It is generally very flat, with most areas lying at only 1 m above Datum. A 1 m (resolution) LiDAR Digital Terrain Model (filtered to remove vegetation and building features) provided the underlying topography used in the study. This DTM was further processed to remove "false blockages" such as bridges, and to fill in areas of missing data. In addition, exact building locations and geometries were extracted from Ordnance Survey (the mapping agency for Great Britain) Mastermap® data.

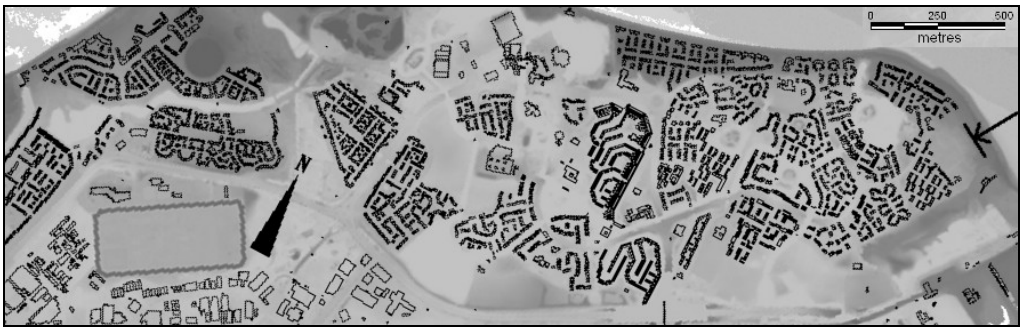

Fig. 1. Map of the floodplain.

Model construction

An inflow hydrograph was used as an upstream boundary condition at the location indicated by the arrow in Fig. 1. The shape of the hydrograph is similar to what could be expected for tidally driven inundation through a breached embankment. Inflow lasts for a few hours and ends as the tide recedes. Three grid resolutions were used (2, 10 and 50 m), and simulations were repeated with four different hydrographs of similar shapes, but characterised by a different value of the peak discharge, see Fig. 2.

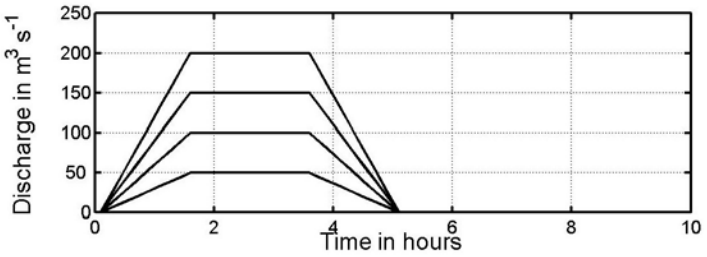

Fig. 2. Inflow hydrographs used in the study.

Fine grid model (FGM)

Ground elevations at computational nodes were extracted from the underlying DTM. In contrast with some previous studies (Néelz and Pender 2006), buildings were not reinstated into the DTM. Instead, the blockage effect that they exert on the flow was taken into account through the use of a very high Manning's *n* value of 0.5 in computational cells found to coincide with buildings. This ensured that the flow velocities were reduced to near-zero values inside these cells. A value of Manning's *n* of 0.035 was used uniformly in the rest of the domain.

Coarse grid model (CGM)

In the CGMs (resolutions 10 m and 50 m), node elevations were extracted from the DTM as in the FGM. However, as buildings only partially filled cells roughness values were assigned according to:

$$n = 0.035 + \left(0.075556 \cdot (k-1) + 0.16\right) \cdot p / 100 \qquad (1)$$

where p is the percentage of cell surface area occupied by buildings, and k is an integer. Ten simulations were run with k = 1, ..., 10, so that k was the "calibration" parameter on which the agreement between FGM and CGM results depended, see Néelz and Pender (2007).

Optimising CGM predictions

The purpose of the modelling exercise is therefore to optimise the value of k (for 10 m and 50 m grid models) to minimise the differences between CGMs and the

FGM across the output points in solution domain identified in Fig. 3. Differences between models were measured using the lag time T for predicted values to reach a predetermined value of water depth H or hazard coefficient (defined as $H = d.(v + 0.5)$, in which v is the flow velocity). An optimum value of k was considered to have been identified when the mean of the differences T was zero and the standard deviation Σ of the differences was a minimum.

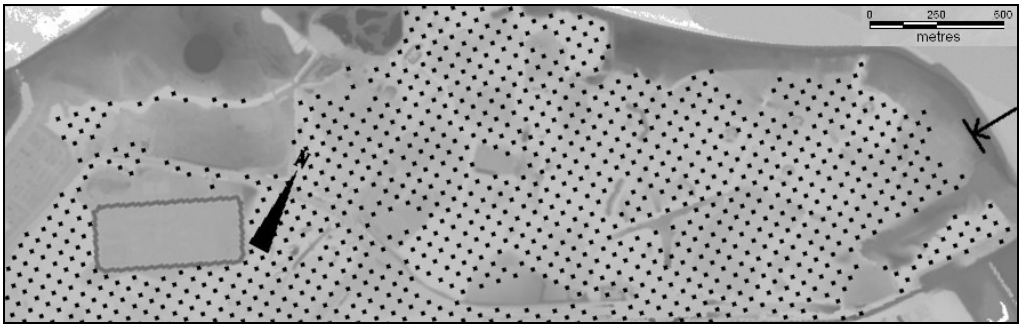

Fig. 3. Output points.

Néelz and Pender (2007) reported that an optimised value of k (within the interval 4-6) is clearly identifiable (Fig. 4) for the 10 m CGM. This varies only to a limited extent with the magnitude of the flood discharge. Results from the 50 m CGM lead to similar conclusions, with optimised values of k being found in the same range.

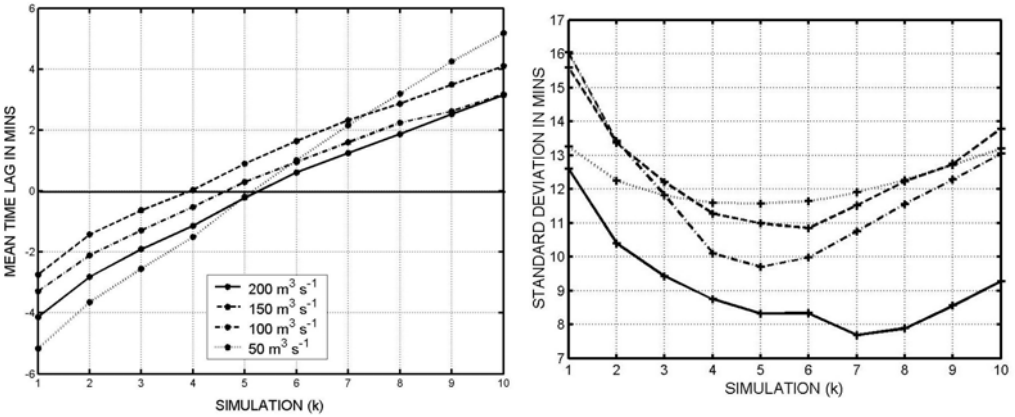

Fig. 4. Plots of (left) T vs. k and (right) Σ vs. k for the 10 m CGM, using arrival times based on water depth, also showing the dependency on the choice of threshold depth.

3. Improving CGM predictions

As previously discussed, the main advantage of utilising 2D hydrodynamic models is to obtain detailed prediction of the velocity field as the flood propagates across the

floodplain. This is important as velocity is a key component of flood hazard. The aim of the research was therefore to investigate improving CGM estimates of velocity using a limited number of FGM predictions (preferably no more than two) for each potential breach location. To investigate the potential of the method, further analysis of the results from the Thamesmead study was undertaken using the data from the output points shown in Fig. 3.

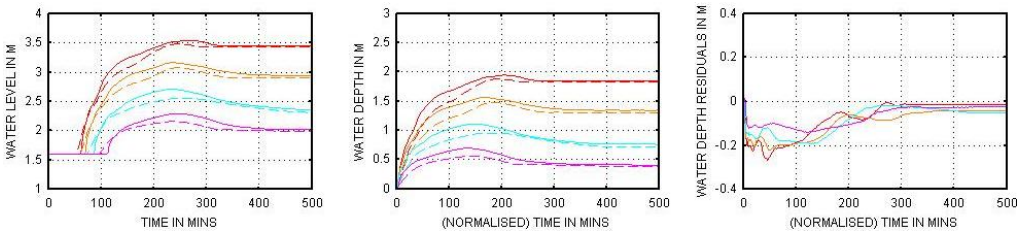

Fig. 5. Reparameterisation of the time series (left) to the arrival time of the flood wave (centre). Solid lines: CGM results. Dashed lines: FGM results. The colours represent different values of q.

Prediction improvement technique

The technique progresses by:

1. Obtaining FGM and CGM predictions for high and low values of peak inflow through the breach location, here values of 100 m^3/s and 500 m^3/s are used.
2. As the time series of water level predictions include a discontinuity at the elapsed arrival time of the flood wave (Fig. 5, left), it is necessary to normalise the arrival times by subtracting the arrival from the elapsed time at all points (Fig. 5, centre).
3. Residual differences between FGM and CGM predictions at each output point are then calculated.
4. Other CGM simulations are undertaken for a different value of peak inflow (in the example presented here 50 m^3/s, 200 m^3/s and 350 m^3/s); these predictions are then adjusted using linear interpolation or extrapolation of the residual values to bring them closer to the predictions that would be made from a FGM with this boundary condition.
5. The time lag is then reinstated into the prediction by reversing step 2.

Prediction using v-SV regression model

The Support Vector Machine (SVM) technique uses a kernel function that maps the nonlinear input data to a higher dimensional hyperspace (Schölkopf *et al*. 2000). One commonly used kernel function is the Gaussian Radial Basis Function (RBF), kernel $k(x_1, x_2) = \exp(-\lambda\|x - y\|^2)$. Through this mapping into a higher dimensional space, the training data can be approximated to a linear function. Schölkopf *et al*. (2000) use

a parameter ν to control the number of support vectors in the ν-Support Vector Regression (ν-SVR) and also present an improved algorithm using the parameter ε to the ε-Support Vector Regression. The primary reason for our adoption of *v*-SVR as the basic approximating tool in our study is its proven capabilities as function approximation tool from a given data set and its short time for training.

The strategy of using coarse grid model outputs as training samples and fine grid model outputs as targets for the *v*-SVR is presented below:

1. **Initialise:** Select n and T, where n = total number of sampling points using fine and coarse grid models, and T = total time for the simulation.
2. **Generate training samples:** Run the fine and coarse grid models with the number of p different inflow hydrographs. Compute the initial training samples size $s = n \times p$.
3. **Construct predictive model:** Use s training samples to train *v*-SVR.
4. **Predict fine grid model outputs:** Run the CGM with a new inflow hydrograph and assign predictive values (water depth and velocity) to each grid using the nonlinear *v*-SVR.

The step-by-step procedure shows that the algorithm is simple and straightforward.

Improvement of predictions from interpolation in FGM results

Figures 6 and 7 give an illustration of what can be achieved for time series predictions of water level and flows at two locations on the floodplain. The CGM predictions (light blue) have been corrected (red) to bring them closer to those of a FGM using the same boundary condition. Similar promising improvements are made at many other locations.

However, a number of limitations of the approach were also apparent as many results suffered from (a) over- or under-correction for at least a part of the time domain, or (b) arrival time prediction errors. The most important limitation occurred at locations where flooding was shallow or nonexistent for the training run $q = 100$ m^3/s. Also, residuals during the first minutes of the inundation process were often excessively dependent on q, as differences in the way topography is represented in the FGM and the CGM affect shallow flows only (and therefore have consequences for low values of q that last longer than for high values of q). This can cause noisy predictions of velocity during the rising limb of the flood, see Fig. 7 (left), and can also lead to substantial errors in the arrival time predictions. In addition, the approach did not take into account how temporal characteristics of flood fronts varied depending on q. An example is shown in Fig. 7 (right), where prediction inaccuracies for $q = 200$ m^3/s and $q = 350$ m^3/s between the times 150 and 300 min may be due to this. Predictions for $q = 50$ m^3/s were very inaccurate at all locations where inundation was very shallow, see Fig. 7 (left). Finally, it should be mentioned that the prediction of velocity was often made more difficult by the presence of oscillations (either physical or numerical) in the results from the training runs.

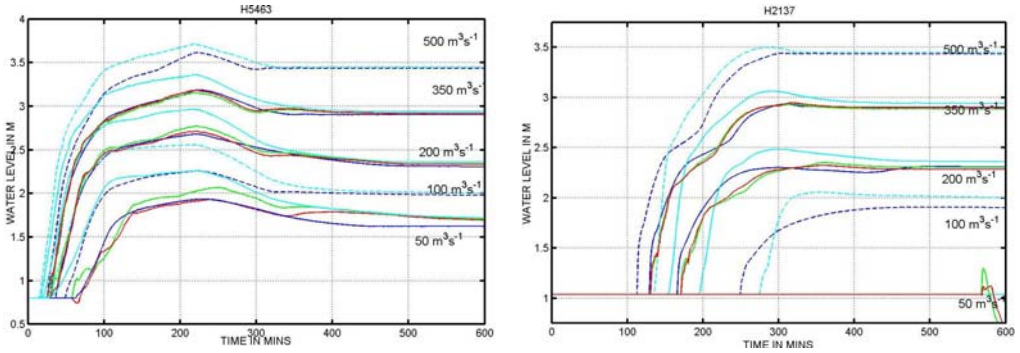

Fig. 6. Prediction of water level at 2 locations on the floodplain. Training runs based on q = 100 m^3/s and q = 500 m^3/s. Methods used: linear interpolation/extrapolation of residuals (red); averaging of residuals (green). Light blue: CGM results. Dark blue: FGM results. Dashed lines: training runs.

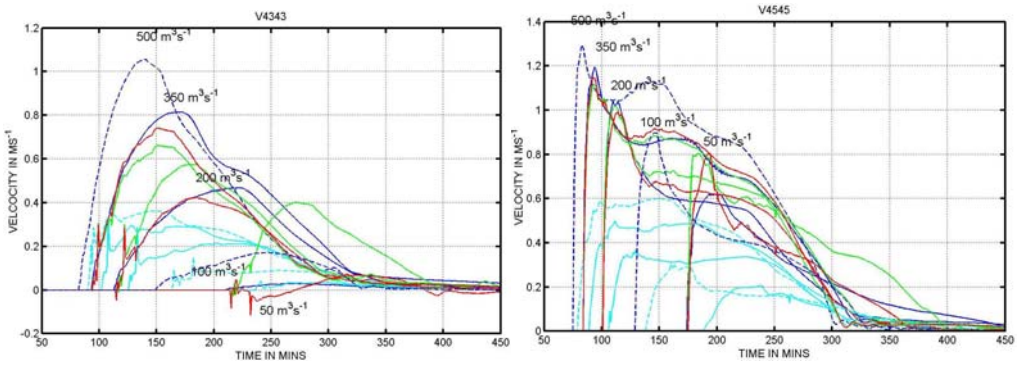

Fig. 7. Prediction of velocity at 2 locations on the floodplain. Training runs based on q = 100 m^3/s and q = 500 m^3/s. See previous figure caption for colour codes.

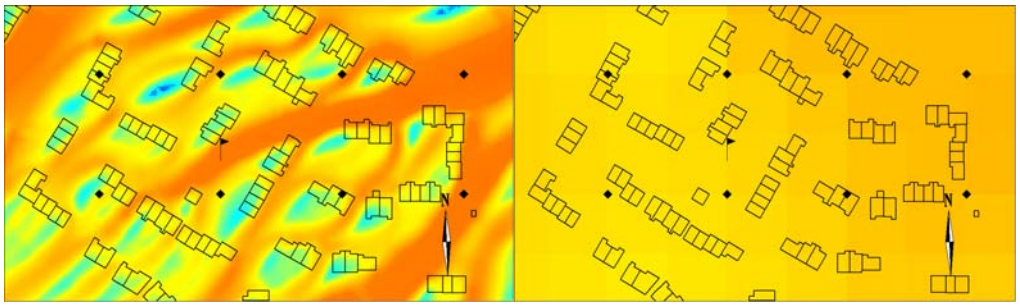

Fig. 8. Peak velocity field predicted by the 2 m FGM (left) and the 50 m CGM (right), for q = 200 m^3/s. The black dots are the computation nodes of the 50 m model. The flag indicates the location where the approach is tested.

Improving spatial prediction of velocity

In addition to improving predictions of water levels and velocities at the computational grid points of the coarse grid model, the approach can also be used to improve the spatial resolution of CGM model results. Predictions at any location on the floodplain can be obtained by spatial interpolation from grid node predictions, and can subsequently be improved using an estimation of residuals. The inherent "blurring" effect obtained in the CGM predictions is illustrated by Fig. 8, which clearly shows that major flow routes through the urban environment are not adequately modelled using the 50 m model and that very significant benefits may be gained from using the results from training runs of the 2 m models.

Water level and velocity prediction using a nonlinear v-SV regression model

Five simulations were used for training and one (q = 500 m^3/s) for testing. For the T = 10 hours simulation, every half hour data were used for v-SVR (n = 20). The number of input patterns of v-SV regression is equal to 3 (water level/velocity, time and discharge on the inflow hydrograph), the number of training samples can be calculated by $5 \times 20 = 100$ and the number of test samples can be calculated by $1 \times 20 = 20$. The Gaussian Radial Basis Function (RBF) kernel was used in the experiments. Figures 9 and 10 show the graphical results produced by v-SVR, CGM and FGM for two random locations on the floodplain. The evaluated performance statistics is shown in Table 1 and 2. From Table 1 and 2, it can be seen that the performance of v-SVR is much better than CGM with respect to the RMSE and the results of FGM and v-SVR are very close in most cases. From Figs. 9 and 10, there is very little separation between FGM and v-SVR indicating a good match between simulated

Table 1

Performance statistics using v-SVR and CGM for water level prediction

Grid Location (index)	RMSE between CGM and FGM	RMSE between v-SVR and FGM
682	1.6858	0
2000	0.0624	0.3501

Table 2

Performance statistics using v-SVR and CGM for velocity prediction

Grid Location (index)	RMSE between CGM and FGM	RMSE between v-SVR and FGM
682	0.028	0
2000	0.1	0.0307

and observed values using *v*-SVR and FGM. For the location shown in Fig. 10 (a), the water level prediction is not as good as the CGM because the simulated water level obtained from the CGM is already very close to FGM prediction. More training samples are needed to provide a more accurate prediction result for this location. In our experiment, only 5 simulations were used for training.

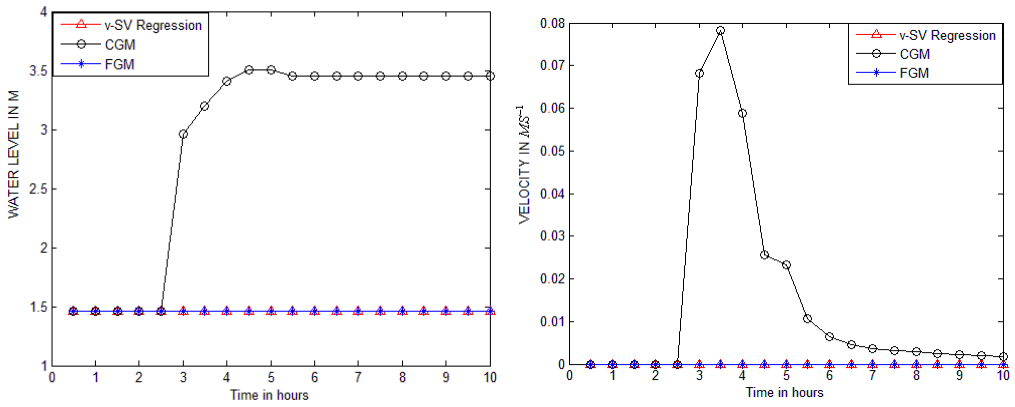

Fig. 9. Predictions of water level and velocity at the first random location on the floodplain. Simulation run (q = 500 m^3/s) was used for testing.

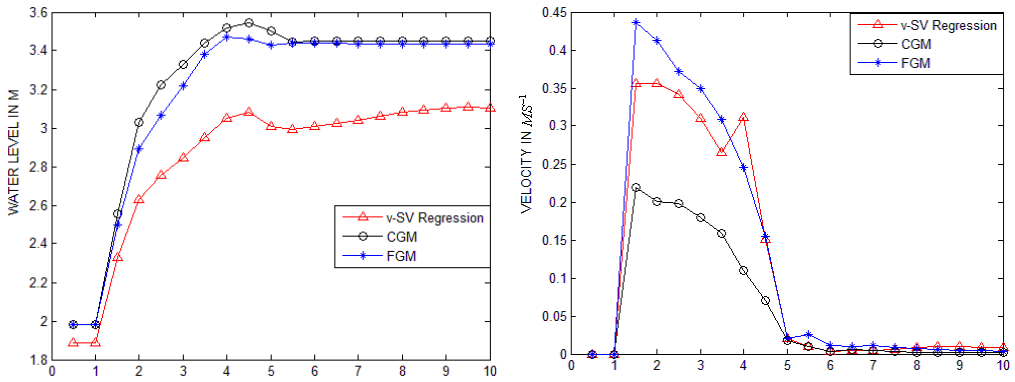

Fig. 10. Predictions of water level and velocity at the second random location on the floodplain. Simulation run (q = 500 m^3/s) was used for testing.

4. Conclusions

1. CGM predictions of water depth and velocity can be improved to obtain predictions closer to those which would be obtained from a FGM by correcting the CGM results using residual differences between two FGM and CGM training runs.

2. It is found that if a full 2D hydrodynamic CGM is used, it is very likely that the full 2D CGM will predict the results inaccurately due to low resolution data. Therefore, it is essential that the CGM be used together with FGM runs or a *v*-SVR technique to improve the predictions. Here the kernel method was used to map the data into feature space corresponding to the kernel and then to undertake linear regression. When a limited number of FGM runs is available, these can be used to improve the performance of a CGM. The proposed methods have been applied to the model construction for Thamesmead site. The experiments showed that by using *v*-SVR, it achieved a sufficiently accurate water level and velocity predictions comparable to the results obtained using the FGM.

Acknowledgements. The research reported in this paper was conducted as part of the Flood Risk Management Research Consortium. The FRMRC is supported by grant GR/S76304 from the Engineering and Physical Sciences Research Council, in partnership with the Natural Environment Research Council, the DEFRA/EA Joint Research Programme on Flood and Coastal Defence, UKWIR, the Scottish Executive and the Rivers Agency (Northern Ireland). This financial support is gratefully acknowledged. The authors are also grateful to the Environment Agency for England and Wales, Infoterra and Halcrow Group Ltd. for providing the LiDAR data, to WBM Australia for the use of their TUFLOW software, and Ordnance Survey for providing Mastermap® data.

References

Bates, P.D., and A.P.J. De Roo (2000), A simple raster-based model for flood inundation simulation, *J. Hydrol.* **236**, 54-77.

Chow, V.T. (1998), *Open Channel Hydraulics*, McGraw-Hill Education.

Cobby, D.M., D.C. Mason, M.S. Horritt, and P.D. Bates (2003), Two-dimensional hydraulic flood modelling using a finite-element mesh decomposed according to vegetation and topographic features derived from airborne scanning laser altimetry, *Hydrol. Process.* **17**, 10, 1979-2000.

Gomes Pereira, L.M., and R.J. Wicherson (1999), Suitability of laser data for deriving geographical information. A case study in the context of management of fluvial zones, *ISPRS Journal of Photogrammetry and Remote Sensing* **54**, 105-114.

Marks, K., and P.D. Bates (2000), Integration of high-resolution topographic data with floodplain flow models. *Hydrol. Process.* **14**, 11, 2109-2122.

Néelz, S., and G. Pender (2007), "Parameterisation of Square Grid Hydrodynamic Models of Inundation in the Urban Area", *Proc. XXXII IAHR Congress, 1st to 6th July 2007, Venice, Italy*, on CD.

Néelz, S.P.F., and G. Pender (2006), "The influence of errors in digital terrain models on flood flow routes". **In:** R. Ferreira, E. Alves, J. Leal, and A. Cardoso (eds.), *River Flow 2006*, vol. 2, pp. 1955-1962, Taylor Francis.

Schölkopf, B., A. Smola, R. Williamson, and P. Bartlett (2000), New Support Vector Algorithms, *Neural Computation* **12**, 1207-1245.

Stelling, G.S. (1984), On the construction of computational methods for shallow water flow problems, *Rijkswaterstaat Communications*, No 35/1984. The Hague, Netherlands.

Syme, W.J. (1991), Dynamically Linked Two-Dimensional/One-Dimensional Hydrodynamic Modelling Program for Rivers, Estuaries & Coastal Waters, *M. Eng. Sc.* (*Research*) *Thesis*, Dept. of Civil Engineering, The University of Queensland, Australia.

Accepted December 23, 2008

PUBLS. INST. GEOPHYS. POL. ACAD. SC., E-10 (406), 2008

Stochastic Transfer Function Simulator of a 1-D Flow Routing

Renata J. ROMANOWICZ, Adam KICZKO, and Jarosław J. NAPIÓRKOWSKI

Institute of Geophysics Polish Academy of Sciences
Ks. Janusza 64, 01-452 Warszawa, Poland
e-mail: renatar@igf.edu.pl

Abstract

The paper presents an application of a Stochastic Transfer Function (STF) approach and a State Dependent Parameter (SDP) transformation of model variables to the combined reservoir management and flow routing problem on the Upper Narew River, NE Poland. The management objective is to reach required flow conditions in the reaches of an ecologically valuable river. A 1-D distributed flow routing model was designed for the study. However, both optimisation methods and reservoir management analysis require numerous model realizations which are computationally very expensive. A much more efficient solution consists of the application of a simplified STF simulator of river flow, which is calibrated on historical data and distributed model realizations for the parts of the river where the observations are not available. The model is stochastic, enabling derivation of prediction uncertainty in a straightforward manner. The obtained optimal control policy is tested on a fully distributed model.

1. Introduction

River floods are commonly considered as natural phenomena with threats to life and health and loss of property. However, in some situations they have a positive impact, helping to preserve the natural features of a particular region. Due to their natural character and high water content, floodplains are commonly areas of rich biodiversity. Equally, valuable fluvial ecosystems can be destroyed by shortages of water in critical periods of high-water demand (vegetation growth). It is the task of hydrologists to assess the short and medium-term inputs to, and retention of, water eco-systems in vulnerable areas and to devise methods to regulate those inputs. This is the case in the Narew catchment, north-east Poland, in the area within the boundaries of the Narew National Park (NNP), where spring floods not only cause no material damage but bring positive effects in preserving the natural qualities of the region.

To maintain the required status of riverine wetlands with fluvial-glacial feed, it may be necessary to retain, during the river's vegetation growth period, not only higher than minimum flows according to a hydro-biological criterion, but also to keep or introduce a flood impulse. The concept of flood impulse was introduced by Junk *et al*. (1989) for tropical rivers and was further developed by Tocker *et al*. (2000) for rivers situated in intermediate climate zones. The concept was followed by Kiczko *et al*. (2007), where the problem of reservoir management was studied. The aim was an analysis of the possibility of reaching the ecologically desirable conditions in the Narew National Park wetlands through reservoir management. River flow was described using a distributed 1-D model. Derivation of the optimal time and length of the releases from the reservoir was based on the optimisation of the entire system including the river and the reservoir (Dysarz and Napiórkowski 2002), using the Differential Evolution Algorithm (Storn and Price 1995). The optimisation algorithm requires multiple 1-D model evaluations and therefore the computation time is a limiting factor of the procedure (Dysarz and Napiórkowski 2003).

In order to facilitate the computations, a lumped parameter simulator of a distributed flow routing is introduced in the multiobjective optimisation of a water management system consisting of a lowland river and a storage reservoir. The developed simulator applies the Stochastic Transfer Function (STF) approach together with a nonlinear transformation of variables. The model is calibrated on historical data and on distributed model realizations for the parts of the river where the observations are not available. The model is stochastic, enabling derivation of prediction uncertainty in a straightforward manner; therefore, it is suitable for scenario analysis of the water management system under uncertain climatic conditions. Estimated probability of water levels at the cross-sections along the river enables the derivation of probability maps of inundation at different times of the year.

2. Methodology

Consider a 1-D numerical model with the river geometry described by n cross-sections. This kind of approach is used in many popular 1-D flow routing models (ISIS, HEC-RAS, UNET, MIKE 11). The methodology we apply here is based on the application of a lumped discrete-time STF model combined with the nonlinear State Dependent Parameter (SDP) type transformation to simulate flow routing along the river instead of a distributed 1-D model. Experience gained by Romanowicz *et al*. (2004, 2006), and Beven *et al*. (2008), indicated that STF models are compatible with distributed model predictions at cross-sections where observations are available. The interpolation of water levels at cross-sections between the measurement sites can be obtained when STF simulators are calibrated on the distributed model simulations at these cross-sections.

As 1-D model applies spatial discretisation based on cross-sections along the river and the floodplains, the simulator can also apply that type of spatial discretisation, but it can be made coarser than in a distributed model, depending on the application.

When water levels are used as the STF model variable, we can use the nonlinear transformation of water levels upstream (model input) in order to separate linear dy-

namics from the nonlinear flow routing process (Young *et al*. 2006, Romanowicz *et al.* 2007, Romanowicz *et al*. 2008). The resulting simulator takes the form of the so-called Hammerstein type model (Fig. 1A). However, when flow is used as the model variable, the STF model cannot be accompanied by a nonlinear transformation of the input, as this type of model would not be able to keep the mass balance for the steady state solution. In that case the simulator consists of a system of linear STF models. The nonlinear flow-water level transformation used to evaluate water levels at each cross-section applies a rating curve-type conversion, which does not influence the flow routing module (Fig. 1B).

Figures 1A and 1B illustrate both schemes for a single sub-reach between two cross-sections of a distributed UNET model. In Fig. 1A, $h_{i,k}$ denotes water level upstream at discrete time period k, $h_{n,k}$ denotes the water level downstream at cross-section n, $f_{i,n}(.)$ denotes a nonlinear transformation between input and output (Romanowicz *et al*. 2008).

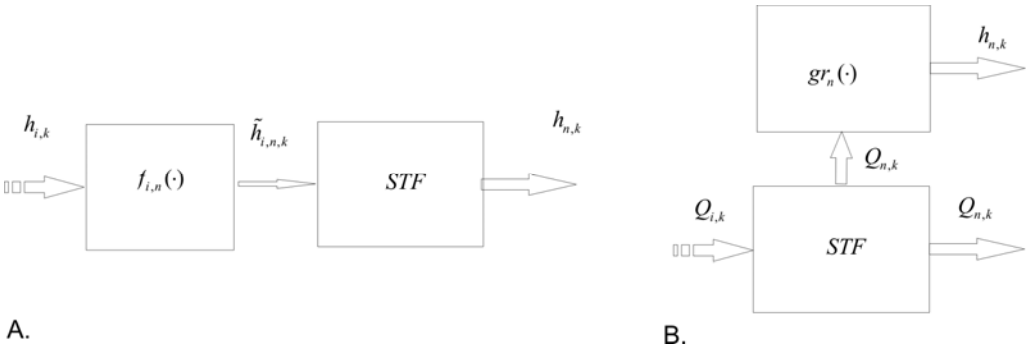

Fig. 1. (A) The scheme of a nonlinear Hammerstein type STF simulator of one sub-reach of a 1-D flood routing model (a sub-reach without tributaries); (B) The scheme of a linear STF model for flow with a nonlinear conversion for the water levels.

In Fig. 1B, $Q_{i,k}$ denotes discrete flow upstream, $Q_{n,k}$ denotes flow value downstream and $gr_n(.)$ denotes the "rating curve" type transformation for the 1-D model variables. At the reach scale, the discrete-time STF (Young 1984) describes the process dynamics.

The model structure identification and estimation of parameters is performed using MATLAB optimisation routine together with a Simplified Refined Instrumental Variable (SRIV) routine from Captain toolbox (www.lancaster.ac.uk). The STF model error is assumed to account for all the uncertainty at the output of the system that is associated with the inputs affecting the model, including measurement noise, unmeasured inputs, and uncertainties associated with the model structure.

The choice of the type of STF model input determines the simulator structure. In the first approach, flow (water level) at the cross-sections upstream of each sub-reach of a numerical 1-D model is used as an input variable. In this case, the model of the entire river reach consists of n serially connected modules shown in Fig. 1A or 1B, depending on the choice of routing variables. The output from the sub-reach upstream is used here as an input to the downstream sub-reach. The other approach consists of

building an independent Single Input Single Output (SISO) or Multiple Input Single Output (MISO) model for each cross-section, using the available observed inputs upstream (flows or water levels) and simulated by the 1-D model flows or water levels at a cross-section as an output. In the second approach, each cross-section of the 1-D model is modelled as an independent input-output system using the modules A or B from the Fig. 1, depending on the choice of routing variable. In the case where lateral inflow is present, the multi-input model is required for the *i*th cross-section. Therefore the required river reach is modelled by the set of those SISO (or MISO) transfer functions. In the following step of the procedure, the flows obtained from the simulator are transformed into water levels. That nonlinear transformation, derived using the State Dependent Parameter (SDP) method (Young *et al*. 2001) from 1-D model simulations for each cross-section, is subsequently parameterised using radial basis functions (Buhmann 2003). We shall call this approach a parallel simulator to distinguish it from the sequential scheme. This approach should give smaller prediction errors due to the lack of propagation of the error. However, when differences between the cross-sections are large, modelling errors would occur due to smaller correlation between the sites.

3. River Narew study: parallel STF simulator

The study reach is about 110 km long. It starts at the Siemianówka reservoir and goes down over the lowland, agricultural area and Narew National Park (NNP) enclosing valuable wetland ecosystems, as shown in Fig. 2. In recent years both a reduction in mean flows and shorter flooding periods have resulted in a serious threat to the rich wetland ecosystems situated along the river in NNP. These undesirable changes were caused by changes in local climate, manifested as recent mild winters and a reduction in annual rainfall that have resulted in reduced groundwater resources.

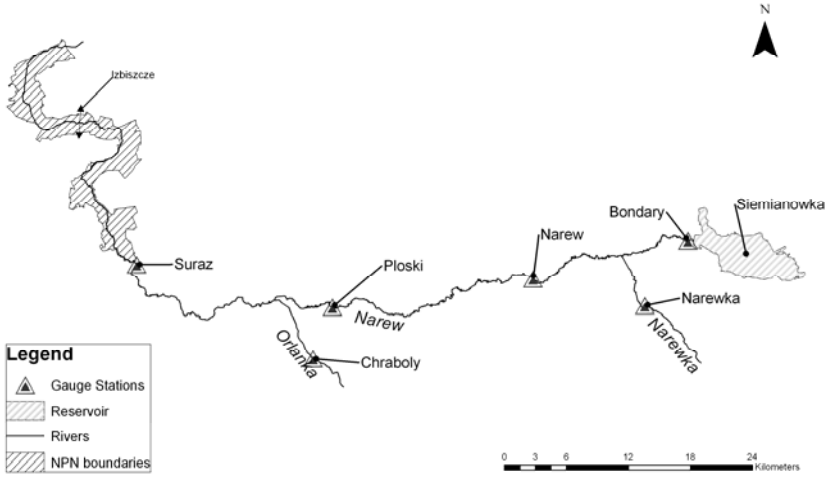

Fig. 2. Upper Narew Valley showing the study area, stage gauging stations are shown as triangles, shaded crossed area on the right denotes the reservoir and crossed area on the left denotes the marshland.

The UNET (Barkau 1993) 1-D model was chosen here due to its short run times. This code is a numerical implementation of a Saint Venant equation. In the UNET model, the river reach is represented by 57 cross-sections at about 2 km intervals obtained from a terrain survey. The model was calibrated by adjusting the Manning coefficients separately for the channel and left- and right-floodplains and water surface slope was used as a downstream boundary condition. Observations of daily water levels are available at Bondary, Narew, Ploski and Suraż on the River Narew and Narewka and Orlanka on its two tributaries. To keep a reasonable size of parameter dimensions, it was assumed that roughness coefficients do not change spatially between the gauges. The calibration period is 23.07.1981 – 28.08.1982 and the validation was performed for the period 27.08.1982 – 23.07.1983. Channel and floodplain (left and right) roughness coefficients for four reaches between gauging stations and downstream cross-section were used as model parameters. Optimization was carried out using the Differential Evolution (DE) algorithm (Storn and Price 1995). Verification gave a good fit with a mean standard deviation less than 0.14 m for each gauging station.

In flood forecasting and inundation modelling we are interested in water level predictions rather than flows. However, an analysis of the UNET model results indicated that flow at each cross-section can be described by a linear dynamic relationship, while the level-level relationship is highly nonlinear. Simulated water levels at each cross-section can be derived from flow–water level nonlinear relationships, specific for each cross-section, for most of the cross-sections apart from one, situated near the first tributary. Therefore, it was decided to use flows rather than water levels to build the simulator. A preliminary analysis indicated also that use of a parallel model structure is more suitable for the present application than the sequential.

Only daily observations of water levels are available from the gauging stations along the studied Narew reach. As shown in Romanowicz and Osuch (2008), daily time step does not allow for the adequate modelling of influence of tributaries on the wave celerity variation downstream Suraż. As the 1-D model output has a flexible discretisation time (e.g., 1 hour), in this application a 1-D model serves both as spatial and temporal interpolator of the observations.

STF models were obtained for hourly flows simulated by UNET at 9 cross-sections along the River Narew within the NNP region, between Suraż and Izbiszcze, with observed flows at Bondary, Narewka and Orlanka as input variables. All the models have 1st order dynamics. The obtained goodness of fit criterion R_T^2 for the validation stage (1982-1983) varies between 99.33% and 99.99%. The validation results for Suraż indicate that the UNET model has nearly linear input-output relationships for flows, i.e., it has linear dynamics.

Figure 3 presents the rating curve for Suraż and water level–flow relationship obtained from UNET simulations at that cross-section shown with dotted black line. The nonparametric relationship was parameterised using Radial Basis functions (Buhmann 2003), but any other suitable parameterisation may be used. The resulting water levels at Suraż were obtained using the MISO STF model with observed flows at Bondary, Narewka and Orlanka as input variables and radial basis transformation. Figure 4 presents estimated water levels at Suraż (continuous line) together with 0.95 confi-

dence bounds shown as shaded area together with observed water levels shown by dots and UNET model simulations shown by stars.

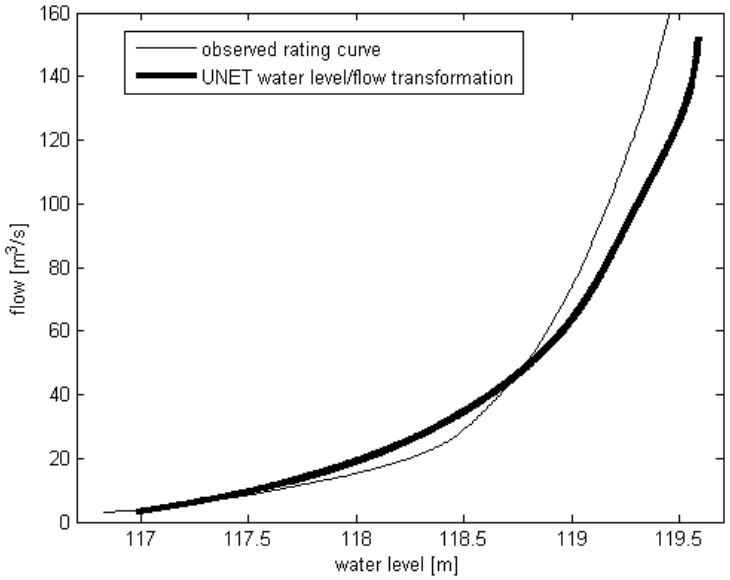

Fig. 3. Observed rating curve for Suraż (thin line) and UNET level/flow relationship (thick line).

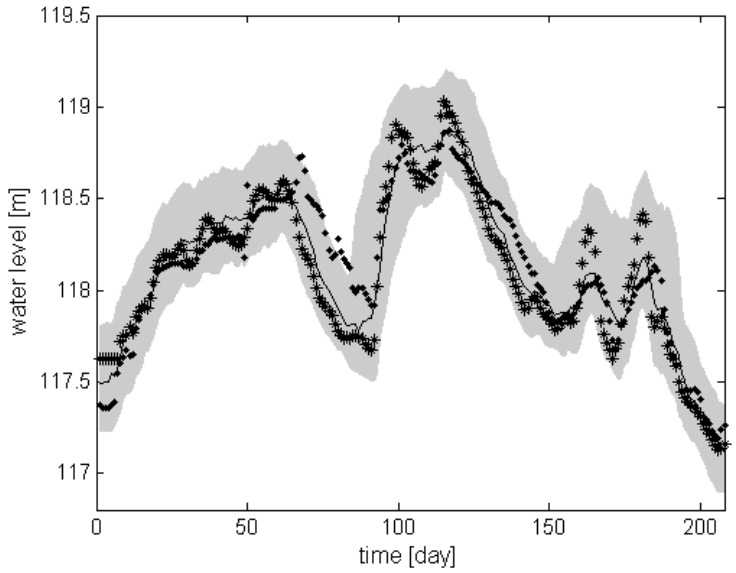

Fig. 4. Validation of the STF simulator for the cross-section at Suraż; dots denote observations, stars denote UNET simulations and continuous line denotes the simulator estimates with 0.95 confidence bounds shown by shaded area.

4. Application of a simulator in reservoir management

In this application we use discharges from the Siemianówka reservoir as control variables. The optimisation criteria described in Kiczko *et al*. (2008) are chosen to combine reservoir management and ecological requirements posed by the wetland ecosystems along the river floodplains. Optimization of discharges from Siemianówka reservoir (control stage) was performed using historical discharges at the Bondary gauging station before the time when the reservoir was built to test the ability of improving water conditions by introducing the discharges from the reservoir. The reservoir is described using a simple discrete balance equation. Initial reservoir storage was set to the recommended value for a chosen control period by the reservoir management policy. Reservoir outflows are represented as a sum of rectangular pulses

$$Q_{out}(t) = Q_{base} + \sum_{j=1}^{NP} P_j\left(t, t_j, dt_j, q_j\right) \tag{1}$$

where Q_{base} is the minimum flow (a minimum allowed discharge from the reservoir), t_j is the time middle point of j-th pulse, dt_j is the pulse duration time, q_j is the discharge and NP is the number of considered pulses, and $P_j(.)$ is the rectangular pulse discharge.

Values of the middle time of the pulse, pulse duration time and the pulse height were used as control variables describing reservoir discharges. Ten pulses were applied (NP = 10); therefore, there were 30 control variables.

In the study by Kiczko *et al*. (2008), three different management scenarios were analysed. In the present paper we report the results for only one scenario, from the period 0.5.10.1982 – 13.07.1983, in order to test the performance of the simulator. The optimisation problem was solved using DE Algorithm with the simulator used for flow routing. Figure 5 presents a comparison of water levels at Suraż simulated using

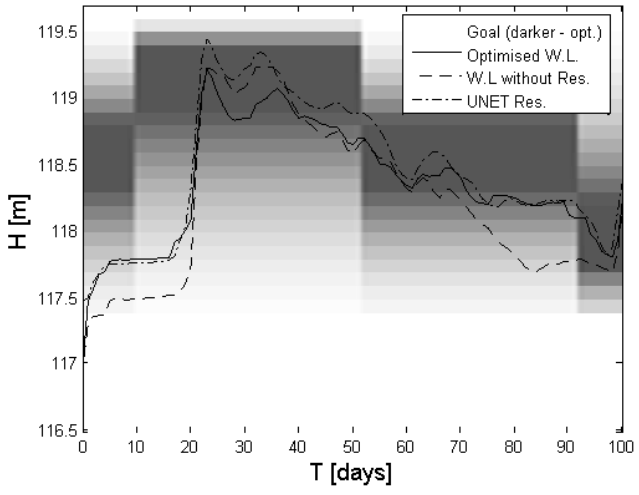

Fig. 5. Water levels (W.L.) at Suraż; historical observed marked with a dashed line, optimised marked with a continuous line; UNET simulations marked with a dash-dotted line.

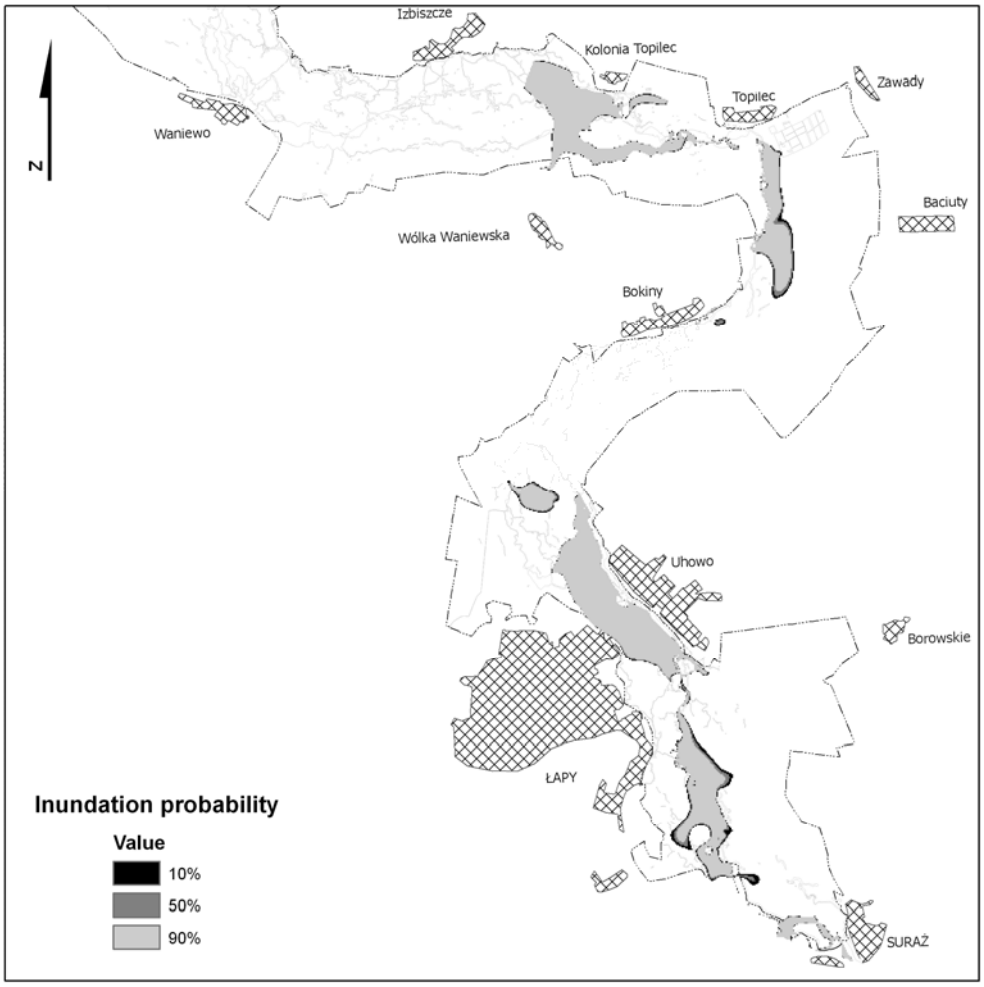

Fig. 6. Low water levels probability map at the NNP area between Suraż and Izbiszcze.

UNET with results obtained using the simulator when the optimised discharges from the reservoir are applied. Also shown are the observed historical water levels at Suraż. The dark shaded area presents the values of the optimum criterion applied in order to fulfill ecological goals (the darkest shade represents the best value of the criterion).

As mentioned before, the simulator predictions are given together with the uncertainty bounds. In this study we additionally apply Monte Carlo sampling to estimate the influence of parameters and observations uncertainty as well as uncertainty related to the nonlinear transformation of flows into water levels. The quantiles of predictions are used to derive the maps of probability of inundation at high and/or low water levels as shown in Fig. 6 for inundation predictions at low water levels for the region of NNP between Suraż and Izbiszcze. Comparison of these maps with ecologically desired water conditions along the River Narew reach within the Narew National Park may serve as an indicator of water management outcome.

5. Conclusions

We have demonstrated that the 1-D flow routing can be successfully approximated using a system of lumped STF models (so-called simulator). The simulator structure depends on the choice of the routing variable (water levels or flows) and on the choice of input variables (sequential or parallel system). In the case of UNET model, a choiceof flows as the routing variable and a parallel structure gives superior results. The simulator was applied within the optimisation routine to derive the best reservoir discharge scheme from the point of view of joint ecological and economic criteria. Further work is required to extend this approach towards the modelling of the uncertainty of predictions related to the uncertainty of the distributed model parameters. At present only observation and simulator parameters uncertainty were taken into account during the estimation of the simulator predictions uncertainty. The uncertainty of model predictions is used to derive the probability maps of inundation extent within the ecologically valuable reach of the River Narew.

Acknowledgements. This work was partly supported by Scientific Network "Geoinformation Systems" funded by the Polish Ministry of Science and Higher Education.

References

Barkau, R.L. (1993), UNET, one-dimensional flow through a full network of open channels, user's manual version 2.1. Publication CPD-66, U.S. Army Corps of Engineers, Davis, CA, Hydrologic Engineering Center.

Beven, K.J., P.C. Young, D. Leedal, and R.J. Romanowicz (2008), Computationally efficient flood water level prediction (with uncertainty), to appear in the Proceedings of Flood Risk Conference, Oxford, UK, September, 2008.

Buhmann, M.D. (2003), *Radial Basis Functions: Theory and Implementations*. Cambridge University, Cambridge.

Dysarz, T., and J.J. Napiórkowski (2002), Global optimisation method for determination of reservoir decision rules during flood. **In:** *5th ICHE, Warsaw, Poland, CD Proceedings*, p. Track F, PDF 153.

Dysarz, T., and J.J. Napiórkowski (2003), Computer-based analysis and design of control mechanisms for flood operation in multireservoir systems. **In:** J.J. Napiórkowski (ed.), *Modelling and Control of Floods*, Publs. Inst. Geophys. Pol. Acad. Sc., E-3 (365), 83-96.

Junk, W.J., P.B. Bayley, and R.E. Sparks (1989), The flood pulse concept in river floodplain systems. **In:** D.P. Dodge (ed.), *Large River*; Proc. Intern. Sym. Journal of Canadian Fisheries and Aquatic Sciences, 11, 106-107.

Kiczko, A., R.J. Romanowicz, and J.J. Napiórkowski (2007), A study of flow conditions aimed at preserving valuable wetland areas in the Upper Narew Valley using GSA-GLUE methodology. **In:** *Proceedings 21st International Conference on Informatics for Environmental Protection, September 12-14, 2007*, Warsaw, Poland, Shaker Verlag, 175-183.

Kiczko, A., A. Piotrowski, J.J. Napiorkowski, and R.J. Romanowicz (2008), Integration of reservoir management and flow routing model: Upper Narew case study, *Publs. Inst. Geophys. Pol. Acad. Sc*. **E-9** (405), 41-55.

Romanowicz, R.J., P.C. Young, and K.J. Beven (2004), Data assimilation in the identification of flood inundation models: derivation of on-line multi-step ahead predictions of flows. **In:** B. Webb, N. Arnell, C. Onf, N. MacIntyre, R. Gurney, and C. Kirby (eds.), *Proceedings of the BHS international conference: hydrology, science and practice for the 21st century*, London, July 2004, 348-53.

Romanowicz, R.J., P.C. Young, and K.J. Beven (2006), Data assimilation and adaptive forecasting of water levels in the river Severn catchment, United Kingdom, *Water Resour. Res.* **42**, W06407, DOI: 10.1029/2005WR004373.

Romanowicz, R.J., A. Kiczko, and F. Pappenberger (2007), A state dependent nonlinear approach to flood forecasting, *Publs. Inst. Geophys. Pol. Acad. Sc*. **E-7** (401), 223-230.

Romanowicz, R.J., P.C. Young, K.J. Beven, and F. Pappenberger (2008), A data based mechanistic approach to nonlinear flood routing and adaptive flood level forecasting, *Advances in Water Resour.* **31**, 8, 1048-1056, DOI: 10.1016/j.advwatres.2008.04.015.

Romanowicz, R.J., and M. Osuch (2008), An integrated data based mechanistic lowland catchment model for the Upper Narew, *Publs. Inst. Geophys. Pol. Acad. Sc*. **E-9** (405), 57-74.

Storn, R., and K.V. Price (1995), Differential Evolution – a simple and efficient adaptive scheme for global optimization over continuous spaces. *Technical Report TR-95-012*, International Computer Sciences Institute, Berkeley, CA, USA.

Tockner, K., F. Malard, and J.V. Ward (2000), An extension of the flood pulse concept, *Hydrological Processes* **14**, 16-17, 2861-2883.

Young, P.C. (1984), *Recursive Estimation and Time Series Analysis*, Berlin: Springer-Verlag.

Young, P.C., P. McKenna, and J. Bruun (2001), Identification of non-linear stochastic systems by state dependent parameter estimation, *International Journal of Control* **74**, 18, 1837-1857, DOI: 10.1080/00207170110089824.

Young, P.C., R.J. Romanowicz, and K.J. Beven (2006), Updating Algorithms in Flood Forecasting, Flood Risk Management Research Consortium, *Report UR5*, www.floodrisk.org.uk.

Accepted November 13, 2008

PUBLS. INST. GEOPHYS. POL. ACAD. SC., E-10 (406), 2008

On the Rationale of Seasonal Approach to Flood Frequency Analysis

Witold G. STRUPCZEWSKI and Krzysztof KOCHANEK

Institute of Geophysics Polish Academy of Sciences
Ks. Janusza 64, 01-452 Warszawa, Poland
e-mails: wgs@igf.edu.pl, kochanek@igf.edu.pl

Abstract

The annual peak-flow series of Polish rivers are mixtures of summer and winter flows. The seasonal series are believed to be more homogeneous than the annual series in respect of the distribution. Consequently, a seasonal maxima approach to the stationary flood frequency analysis (FFA) has been introduced by the Polish Hydrological Service. The FFA is performed for the winter and summer peaks separately and the time-dependent annual peak flow quantiles are computed by an union formula of two independent events. Assuming that the seasonal maxima follow the Gumbel distribution, the sampling properties of an annual maxima (AM) quantile estimate got by using the seasonal maxima are examined and compared with those got from the annual maxima (AM) samples. The asymptotic variance and bias of ML-estimate of the upper quantiles are compared with sampling experiment assessment.

1. Introduction

Floods in Poland transpire both in summer and winter. The majority of floods in Poland are caused either by heavy rains (summer floods) or by thaws (winter floods). Although summer floods dominate in southern part of Poland and winter in the northern part, many annual peak flow series are a mixture of summer and winter peak flows. Their ratio changes along the river course. The method of combining the distributions of the seasonal maxima (SM) for the annual maxima (AM) distributions has been introduced to FFA in the Polish Hydrological Service (e.g., Ozga-Zielinska *et al*. 1999, 2007, Kruszewski 2001). The method attracted much attention in the literature (e.g., Waylen and Woo 1982, Lamberti and Pilati 1985, Buishand and Demaré 1990) mainly focused on the monthly precipitation maxima. The seasonal maxima are assumed to be independent and the probability of annual maximum value is derived

from the union of independent events. Buishand and Demaré (1990) in their fundamental study derived asymptotic expressions for the bias and variance of quantile estimates obtained by fitting the Gumbel distribution to the maxima in *m*-separate seasons. Introduced by Strupczewski (1965) to FFA in Poland, the SM approach was soon dislodged by the POT method (Strupczewski 1967) which in fact due to too rigorous assumptions has never been widely used in Poland. The main problems of upper quantile estimation are model misspecification (i.e. model error), a sample non-representative for population and the number of parameters to be estimated from the observation data (i.e. sampling error). Following Buishand and Demaré (1990) and other publications on seasonal maxima, it is assumed here that summer and winter seasonal maxima follow the Gumbel distribution. Expressions for the asymptotic variance and bias of the ML quantile estimate from both the SM and AM approaches are given. The results from these expressions are presented for a situation of non-seasonal variation and compared with estimates got by sampling experiments.

2. Preliminaries

The seasonal maxima (SM) approach is based on the union of two independent events. If the winter and summer peaks are subject to the cumulative distribution function (cdf) $F_1(x; \boldsymbol{\theta}_1) = P_1(X_1 \le x; \boldsymbol{\theta}_1)$ and $F_2(x; \boldsymbol{\theta}_2) = P_2(X_2 \le x; \boldsymbol{\theta}_2)$ with the parameter vectors $\boldsymbol{\theta}_1$ and $\boldsymbol{\theta}_2$, respectively, then from the union of these two independent events one gets the cdf of annual peak flows $[X = \max(X_1, X_2)]$ as

$$F(X \le x; \boldsymbol{\theta} = \boldsymbol{\theta}_1, \boldsymbol{\theta}_2) = F_1(X_1 \le x; \boldsymbol{\theta}_1) \cdot F_2(X_2 \le x; \boldsymbol{\theta}_2). \tag{1}$$

The pdf of the X-variable is got by differentiating Eq. (1) with respect to x:

$$f(x; \boldsymbol{\theta} = \boldsymbol{\theta}_1, \boldsymbol{\theta}_2) = F_2(x; \boldsymbol{\theta}_2) \cdot f_1(x; \boldsymbol{\theta}_1) + F_1(x; \boldsymbol{\theta}_1) \cdot f_2(x; \boldsymbol{\theta}_2), \tag{2}$$

where $f_i(x; \boldsymbol{\theta}_i) = dF_i(x; \boldsymbol{\theta}_i)/dx$.

In the SM approach, the parameters $\boldsymbol{\theta}_1$ and $\boldsymbol{\theta}_2$ are estimated separately from winter peaks series ($X_{1,1}, X_{1,2}, \ldots, X_{1,N}$), and summer peaks series ($X_{2,1}, X_{2,2}, \ldots, X_{2,N}$), respectively. In the AM approach, the parameters $\boldsymbol{\theta} = (\boldsymbol{\theta}_1, \boldsymbol{\theta}_2)$ are estimated from the F distributed sample of annual peak flows ($X_1, X_2, \ldots, X_N$). The ML method is used here for the purpose. Having estimated the parameters $\boldsymbol{\theta}$, quantile estimates can be computed from Eq. (1). If the function

$$\hat{x}(F) = \phi(F; \hat{\boldsymbol{\theta}}) \tag{3}$$

does not exist in explicit form, an iterative technique must be applied to obtain $\hat{x}(F)$ for given values of the parameters $\boldsymbol{\theta}$ and the probability of non-exceedance F. In the SM approach, the asymptotic covariance matrix of the estimators of the parameter vectors $\hat{\boldsymbol{\theta}}_1$ and $\hat{\boldsymbol{\theta}}_2$ is obtained separately for the both vectors by the inversion of the respective Fisher information matrix (Fisher 1921), while applying the AM approach for the both vectors simultaneously. The asymptotic variance of the $x(F)$ estimator, i.e., $\mathrm{var}^{SM}\{\hat{x}(F)\}$ and $\mathrm{var}^{AM}\{\hat{x}(F)\}$, can be obtained by the first-order Taylor series expansion of Eq. (3) about the point $\boldsymbol{\theta}$.

One can find from Eq. (1) that any two of three distribution functions define the third one. For example, for given F_1 and F_2 distributions with parameter number pn_1 and pn_2, respectively, the F will have $pn = pn_1 + pn_2$ parameters. If the F and F_1 are given functions, the F_2 will be ($pn_2 = pn + pn_1$)-parameter function. Obviously the number of parameters to be estimated from a sample adverse affects accuracy of quantile estimates.

To unify the three functions in respect to the number of parameters one has to assume that seasonal distributions do not differ in respect to parameter numbers ($pn_1 = pn_2$) and moreover that the population values of parameters are the same for these two distributions. Note that the F_1 and F_2 can differ in form and their parameters can have a different meaning. Then from each of the samples, i.e. ($X_{1,1}$, $X_{1,2}$, …, $X_{1,N}$), ($X_{2,1}$, $X_{2,2}$, …, $X_{2,N}$) and (X_1, X_2, …, X_N), the same number of parameters will be estimated. It is intended to equalize the chance of the both approaches in regard to accuracy of the AM quantile estimates.

Note that the SM approach does not reduce the size of the sample upon which parameter estimates are made and it makes use of additional information on flood behaviour. Therefore, using the SM approach one can expect a gain in the accuracy of annual maxima estimation if compared with the annual maxima (AM) approach. The probability that the seasonal peak X_2 is the annual peak X is defined by

$$P(X = X_2) = P(X_2 \geq X_1) = \int_0^\infty f_2(x) \cdot F_1(x) \cdot dx \,. \tag{4}$$

More can be achieved if the peaks of both seasons equally contribute to the AM distribution, i.e., $P(X = X_2) \approx 0.5$. Equation (4) can serve in testing the fit of the SM model (Eq. 1) to the data. It is illustrated in Appendix A taking the exponential distribution.

3. Gumbel as seasonal distributions

Cdfs of seasonal maxima distributions are assumed to be of Gumbel form

$$F_i(x) = \exp\left[-e^{-\left(\frac{x-\beta_i}{\alpha_i}\right)}\right] \qquad i = 1, 2 \,. \tag{5}$$

Hence the annual maxima cdf (1) take the form

$$F(x) = \exp\left[-e^{-\left(\frac{z-\beta_1}{\alpha_1}\right)}\right] \exp\left[-e^{-\left(\frac{z-\beta_2}{\alpha_2}\right)}\right]. \tag{6}$$

The quantile $x(F)$ is given here in an implicit form

$$x(F) = \phi(F; \alpha_1, \beta_1, \alpha_2, \beta_2) \,. \tag{7}$$

Using the SM model, the parameters (α_1, β_1) and(α_2, β_2) are estimated by the ML method from ($X_{1,1}$, $X_{1,2}$, …, $X_{1,N}$), ($X_{2,1}$, $X_{2,2}$, …, $X_{2,N}$) samples, separately. It leads to the quantile estimate

$$\hat{x}^{SM}(F) = \phi\left(F; \hat{\alpha}_1^{SM}, \hat{\beta}_1^{SM}, \hat{\alpha}_2^{SM}, \hat{\beta}_2^{SM}\right). \tag{8}$$

Asymptotic formula for the variance and the bias of quantile estimators (8) are given by Eqs. (B.14) and (C.1-6) in Appendices B and C, respectively. To be close to the practice, the case of the same number of parameters for seasonal and annual distributions is considered here. It is done by assuming no seasonal variation in parameter values: $\alpha_1 = \alpha_2 = \alpha$; $\beta_1 = \beta_2 = \beta$. In this case, the variance and bias do not depend on the location parameter β (see Eqs. (B.17) and (C.7)). Then the annual maxima have a Gumbel distribution with parameters $\beta' = \beta + \ln 2$ and α:

$$F^{AM}(x) = \exp\left[-2e^{-\left(\frac{x-\beta}{\alpha}\right)}\right] = \exp\left[-e^{-\left(\frac{x-\beta'}{\alpha}\right)}\right], \tag{9}$$

hence

$$x^{AM}(F) = \beta' - \alpha \ln(-\ln F) = \beta - \alpha \ln\left(-\ln\sqrt{F}\right). \tag{10}$$

Fitting a Gumbel distribution directly to the annual maxima leads to the ML-estimate

$$\hat{x}^{AM}(F) = \hat{\beta}'^{AM} - \hat{\alpha}^{AM} \ln(-\ln F). \tag{10a}$$

which has the asymptotic variance and bias given by Eqs. (B.19) and (C.9) (Phien 1987), respectively.

The two quantile estimates of the AM $\hat{x}^{SM}(F)$ and $\hat{x}^{AM}(F)$ can be compared by the asymptotic variance ratio which for no seasonal variation has the form (Fig. 1):

$$Q(F) = \frac{\mathrm{var}^{SM}\{\hat{x}(F)\}}{\mathrm{var}^{AM}\{\hat{x}(F)\}} = \frac{0.8786 + 0.6784\,y(F) + 0.3040\,y^2(F)}{1.1087 + 0.5140 \cdot y(F) + 0.6079 \cdot y^2(F)}, \tag{11}$$

where

$$y(F) = -\ln(-\ln F). \tag{12}$$

Note that $Q(F)$ does not depend on α and β in this case.

Application of the SM approach leads here to a considerable reduction of variance of the AM quantile estimate, which increases with the probability F.

As far as bias of quantile estimates is concerned, little reduction of the absolute value of bias for the SM model is observed and, moreover, the biases of large quantiles of both models differ in sign (Fig. 2).

4. Sampling experiment

Equations (11) and (C.7a, C.9) are based on asymptotic expressions which need not be appropriate for small N. To investigate their usefulness a Monte Carlo sampling experiments for the SM and AM methods have been performed. The maximum likelihood method has been applied to estimate the upper quantiles. Then, averaged over 20,000 Monte Carlo loops, the bias and variance of the selected upper quantiles were calcu-

lated. The calculations were carried out for Gumbel pseudo-random samples with sizes of $N = 20$ and $N = 50$. It is important to note that values of parameters α and β were the same for generated summer and winter samples.

The comparison of the theoretical and sampling reduction of the upper quantiles variance (Fig. 1) revealed that the asymptotic theory should not be applied for hydrological sample size, due to the relatively large discrepancy, especially for higher quantiles.

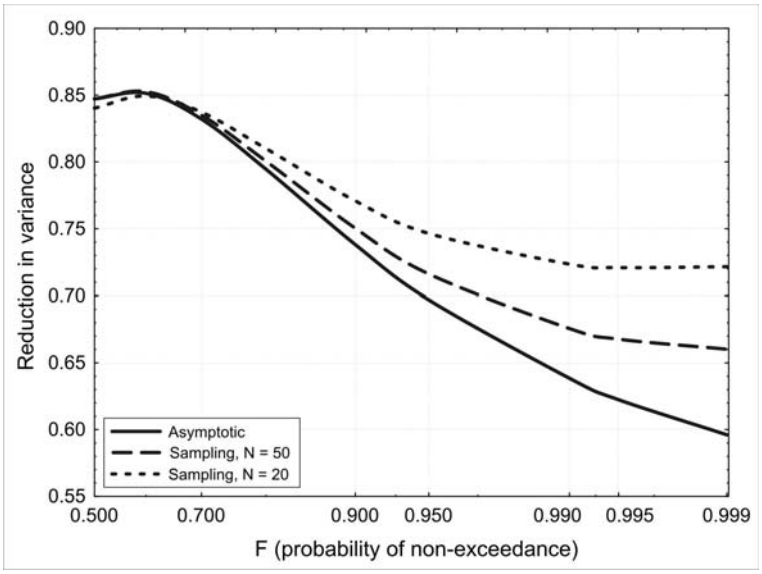

Fig. 1. Reduction of variance of ML-quantile estimates got by SM model.

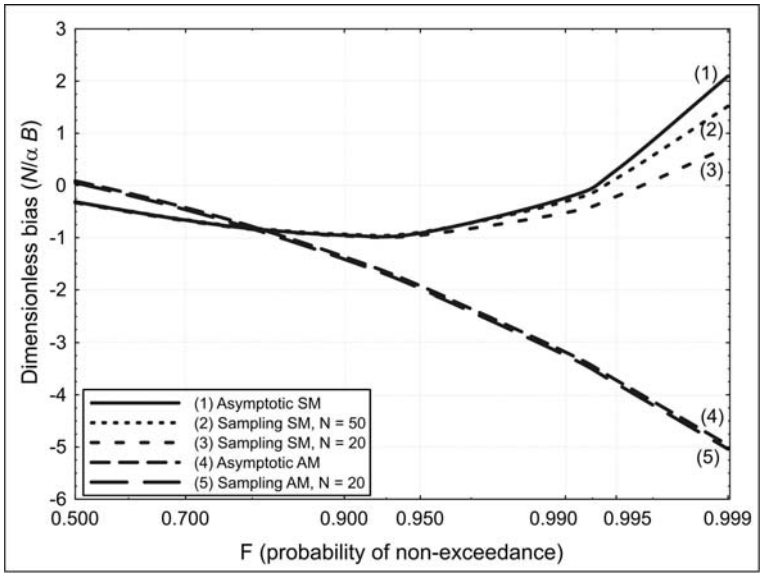

Fig. 2. Dimensionless ML biases for the AM and SM models and various sample sizes.

As far as bias is concerned, to enable the comparison to asymptotic results, the dimensionless sampling bias was calculated by relation to the value of α parameter and sample size (N):

$$DB\{\hat{x}(F)\} = \frac{N}{\alpha} B\{\hat{x}(F)\} . \tag{13}$$

The dimensionless sampling bias both for the SM and AM methods correspond relatively well with the asympthotic results (Fig. 2). This is so, even though the sampling sizes are small. It is worth noting that the seasonal approach (SM) produces smaller bias (in terms of absolute values) than the annual approach. Characteristic is also, that the AM approach always produces negative bias, whereas the SM is negative only for lower quantiles (up to ca. $F > 0.995$).

5. Conclusions

If the underlying assumptions are fulfilled, the SM approach to the AM distribution estimation is highly competitive to that based on the AM samples. Therefore, the problem with its implementation in the FFA lies in possible misspecification of seasonal models and correctness of the assumption of independence of winter and summer peak flows.

Acknowledgements. This work was partly supported by the Polish Ministry of Science and Informatics under the Grant 2 P04D 057 29 entitled 'Enhancement of statistical methods and techniques of flood events modelling'.

Appendix A

Verification of the Independence Assumption

The pdf of the ratio $W = X_1/X_2$ of the winter to summer peak flows ($f_W(w)$) can be derived from the seasonal peak flows pdfs, i.e., $f_1(x_1)$ and $f_2(x_2)$, providing Eq. (1) holds. To do it, the distribution of functions of two-dimensional random variables (W, X_2) (e.g., Kaczmarek 1977) should be derived first:

$$f(w, x_2) = f_1(w \cdot x_2) \cdot f_2(x_2) \cdot |J| , \tag{A.1}$$

where J is the determinant of the form

$$J = \begin{vmatrix} \partial x_1/\partial w & \partial x_1/\partial x_2 \\ \partial x_2/\partial w & \partial x_2/\partial x_2 \end{vmatrix} = \begin{vmatrix} x_2 & w \\ 0 & 1 \end{vmatrix} = x_2 .$$

Hence

$$f(w, x_2) = f_1(w \cdot x_2) \cdot f_2(x_2) \cdot x_2 . \tag{A.2}$$

The pdf of the W variable is the marginal distribution of the two-dimensional variate (W, X_2):

$$f_w(w) = \int_0^{\infty} f(w, x_2)\, dx_2 \tag{A.3}$$

and

$$\text{cdf}\, F_w(w) = \int_0^{\infty} f_w(w)\, dw\,. \tag{A.4}$$

Note that an arbitrary moment $\alpha_k(w)$ may be calculated from

$$\alpha_k(w) = \int_{-\infty}^{\infty}\int_{-\infty}^{\infty} (x_1/x_2)^k f(x_1, x_2)\, dx_1\, dx_2 = \int_{-\infty}^{\infty} x_1^k f_1(x_1)\, dx_1 \cdot \int_{-\infty}^{\infty} x_2^{-k} f_2(x_2)\, dx_2\,, \tag{A.5}$$

i.e., without having to find the density function (A.3).

The probability that the summer peak flow (X_2) is annual peak flow (X) is obtained from Eq. (A.4) substituting $w = 1$. It is equivalent to Eq. (4) as

$$\begin{aligned} F_w(1) &= \int_0^1 f_w(w)\, dw = \int_0^1\int_0^{\infty} f(w, x_2)\, dx_2 dw = \int_0^1\int_0^{\infty} f_1(w\cdot x_2)\, f_2(x_2)\, x_2\, dx_2 dw = \\ &= \int_0^{\infty} f_2(x_2)\left[\int_0^1 f_1(w\cdot x_2)\cdot x_2\, dw\right] dx_2 = \int_0^{\infty} f_2(x_2)\cdot F_1(x_2)\, dx_2\,. \end{aligned} \tag{A.6}$$

Denoting by $p = P(x = x_2)$ the probability of success brings us to the binomial distribution, i.e., to the discrete probability distribution of the number of successes in a sequence of N independent yes/no experiments, each of which yields success with probability p. Its probability mass function (pmf) is defined by

$$f(k; N, p) = \binom{N}{p} p^k (1-p)^{N-k} \tag{A.7}$$

and the mean value, i.e., the expected number of summer maxima in the N-element annual maxima series

$$\hat{N}_{x=x_2} = E\left[N(x = x_2)\right] = N\cdot\hat{p}\,. \tag{A.8}$$

Comparing the estimate $\hat{N}_{x=x_2}$ with the observed number of years $N_{x=x_2}$ one can assess an overall fit of the model, i.e., the chosen distribution functions together with the independency assumption, to the data $((X_{1,j}, X_{2,j}); j = 1, 2, \ldots, N)$. If $N_{x=x_2} < \hat{N}_{x=x_2}$; the interest is in evaluating the probability of getting from the N-element sample the value $\eta \le N_{x=x_2}$. It can be expressed in terms of the cumulative distribution function (cdf)) as the regularized incomplete beta function:

$$\Pr\left(\eta \le N_{x=x_2}\right) = F\left(N_{x=x_2}; N, \hat{p}\right) = I_{1-\hat{p}}\left(N - N_{x=x_2}, N_{x=x_2} + 1\right). \tag{A.9}$$

In the opposite case, i.e., if $N_{x=x_2} > \hat{N}_{x=x_2}$, one has to assess the probability of exceedance the observed $N_{x=x_2}$ value:

$$\Pr\left(\eta > N_{x=x_2}\right) = 1 - F\left(N_{x=x_2}; N, \hat{p}\right) = 1 - I_{1-\hat{p}}\left(N - N_{x=x_2}, N_{x=x_2} + 1\right). \qquad \text{(A.10)}$$

Example:

As an example, consider the exponential distributions with lower bound zero both for winter and summer peak flows:

$$\text{pdf } f_i(x) = \frac{1}{\alpha_i}\exp(-x/\alpha_i) \quad \text{and} \quad \text{cdf } F_i(x) = 1 - \exp(-x/\alpha_i); \quad i = 1, 2. \qquad \text{(A.11)}$$

Then Eq. (A.2) takes the form:

$$f(w, x_2) = \frac{x_2}{\alpha_1\alpha_2}\exp\left[-\left(\frac{w}{\alpha_1} + \frac{1}{\alpha_2}\right)x_2\right] \qquad \text{(A.12)}$$

and pdf of the variable W (Eq. A.3)

$$f_w(w) = \frac{1}{\alpha_1\alpha_2}\int_0^\infty x_2 \exp\left[-\left(\frac{w\alpha_2 + \alpha_1}{\alpha_1\alpha_2}\right)x_2\right]dx_2 = \frac{\alpha_1\alpha_2}{(w\alpha_2 + \alpha_1)^2} = \frac{(\alpha_1/\alpha_2)}{(w + (\alpha_1/\alpha_2))^2} \qquad \text{(A.13)}$$

while the cdf

$$F_w(w) = 1 - \frac{\alpha_1}{w\alpha_2 + \alpha_1} = \frac{w\alpha_2}{w\alpha_2 + \alpha_1} = \frac{w}{w + (\alpha_1/\alpha_2)} \qquad \text{(A.14)}$$

and

$$F_w(1) = \frac{\alpha_2}{\alpha_2 + \alpha_1} = \frac{1}{1 + (\alpha_1/\alpha_2)}. \qquad \text{(A.15)}$$

Note that the moments (A.5) of the pdf (A.13) do not exist for any (α_1/α_2) value. Substituting Eq. (A.11) into Eq. (4) we come to (A.15)

$$P(X = X_2) = \int_0^\infty \frac{1}{\alpha_2}\exp\left(-\frac{x}{\alpha_2}\right)\cdot\left(1 - \exp\left(-\frac{x}{\alpha_1}\right)\right)\cdot dx = \frac{\alpha_2}{\alpha_1 + \alpha_2}. \qquad \text{(A.16)}$$

For $\alpha_1 = \alpha_2 = \alpha$ $P(X = X_2) = 1/2$, while for $\alpha_1 = 2\alpha_2 = \alpha$ $P(X = X_2) = 1/3$.

Appendix B

Asymptotic Formula for the Variance of Quantile Estimators for Gumbel as Seasonal Distribution

SM approach

Taking Gumbel (Eq. 5) as a seasonal distribution, the following formula defines approximate asymptotic variance of quantile estimate got by SM approach

$$\mathrm{var}^{SM}\{\hat{x}(F)\} \approx$$

$$\approx \sum_{i=1}^{2}\left\{\left(\frac{\partial\hat{x}(F)}{\partial\hat{\beta}_i}\right)^2 \mathrm{var}(\hat{\beta}_i)+\left(\frac{\partial\hat{x}(F)}{\partial\hat{\alpha}_i}\right)^2 \mathrm{var}(\hat{\alpha}_i)+2\frac{\partial\hat{x}(F)}{\partial\hat{\beta}_i}\frac{\partial\hat{x}(F)}{\partial\hat{\alpha}_i}\,\mathrm{cov}(\hat{\beta}_i,\hat{\alpha}_i)\right\}, \quad \text{(B.1)}$$

where in the case of ML estimation (Phien 1987)

$$\mathrm{var}(\hat{\alpha}_i)=0.6079\,\alpha_i^2/N,\quad \mathrm{var}(\hat{\beta}_i)=1.1087\,\alpha_i^2/N,\quad \mathrm{cov}(\hat{\alpha}_i,\hat{\beta}_i)=0.2570\,\alpha_i^2/N. \quad \text{(B.2)}$$

The first order partial derivatives of $\hat{x}(F)$ with respect to the parameter estimates are required to obtain an expression for $\mathrm{var}^{SM}\{x(F)\}$. Since the function (7) does not exist in an explicit form, but the cdf (6) does, the derivatives can be obtained by the method of implicit partial differentiation. Let us define the function $h(\bullet)$ as

$$h\left(\phi(\boldsymbol{\theta}),\boldsymbol{\theta}\right)=F_1\left(x_F,\boldsymbol{\theta}_1\right)\cdot F_2\left(x_F,\boldsymbol{\theta}_2\right)-F=0\,, \quad \text{(B.3)}$$

where $x_F=\phi(\boldsymbol{\theta})$ (see Eq. (3)). Differentiating of (B.3) with respect to θ yields

$$\frac{\partial h}{\partial\theta}+\frac{\partial h}{\partial x_F}\frac{\partial\phi}{\partial\theta}=0. \quad \text{(B.4)}$$

Because the derivatives of h can be obtained directly from (B.3), (B.4) readily gives

$$\frac{\partial\phi}{\partial\theta}\equiv\frac{\partial x_F}{\partial\theta}=-\frac{\partial h/\partial\theta}{\partial h/\partial x}\,. \quad \text{(B.5)}$$

For Gumbel as seasonal distribution, Eq. (B.3) takes the form

$$h\left(\phi(\boldsymbol{\theta}),\boldsymbol{\theta}\right)=\prod_{j=1}^{2}\exp(-\hat{\alpha}_j A_j)-F=0 \quad \text{(B.6)}$$

where

$$A_j=\hat{\alpha}_j^{-1}\exp\left[-\{\hat{x}(F)-\hat{\beta}_j\}/\hat{\alpha}_j\right] \quad \text{(B.7)}$$

or denoting

$$\hat{z}_j(F)=\{\hat{x}(F)-\hat{\beta}_j\}/\hat{\alpha}_j\,, \quad \text{(B.8)}$$

$$A_j=\hat{\alpha}_j^{-1}\exp\left[-\hat{z}_j(F)\right]. \quad \text{(B.7a)}$$

Then

$$\frac{\partial h}{\partial \hat{x}} = \left(A_1 + A_2\right) \exp\left(-\hat{\alpha}_1 A_1 - \hat{\alpha}_2 A_2\right) \tag{B.9}$$

$$\frac{\partial h}{\partial \hat{\beta}_i} = -A_i \exp\left(-\hat{\alpha}_1 A_1 - \hat{\alpha}_2 A_2\right) \tag{B.10}$$

hence

$$\frac{\partial \hat{x}(F)}{\partial \hat{\beta}_i} = -\frac{\partial h / \partial \hat{\beta}_i}{\partial h / \partial x} = \frac{A_i}{A_i + A_2}. \tag{B.11}$$

Proceeding similarly, one gets

$$\frac{\partial h}{\partial \hat{\alpha}_i} = -\frac{\hat{x} - \hat{\beta}_i}{\hat{\alpha}_i} A_i \exp\left(-\hat{\alpha}_1 A_1 - \hat{\alpha}_2 A_2\right) = -\hat{z}_i(F)\, A_i \exp\left(-\hat{\alpha}_1 A_1 - \hat{\alpha}_2 A_2\right) \tag{B.12}$$

hence

$$\frac{\partial \hat{x}(F)}{\partial \hat{\alpha}_i} = -\frac{\partial h / \partial \hat{\alpha}_i}{\partial h / \partial x} = \hat{z}_i(F) \frac{A_i}{A_1 + A_2} = \hat{z}_i(F) \frac{\partial \hat{x}(F)}{\partial \hat{\beta}_i}. \tag{B.13}$$

Substituting of (B.2), (B.11) and (B.13) into Eq. (B.1) leads to:

$$\mathrm{var}^{SM}\left\{\hat{x}(F)\right\} \approx \frac{1}{N} \sum_{i=1}^{2} \left(\frac{\hat{\alpha}_i A_i}{A_1 + A_2} \right)^2 \left[1.1087 + 0.5140\, \hat{z}_i(F) + 0.6079\, \hat{z}_i^2(F)\right]. \tag{B.14}$$

For the case of no seasonal variation, i.e., $\alpha_1 = \alpha_2 = \alpha$, $\beta_1 = \beta_2 = \beta$ and from Eq. (10),

$$z_i(F) = z(F) = \frac{x - \beta}{\alpha} = -\ln\left(-\ln\sqrt{F}\right),$$

we get

$$\frac{\partial \hat{x}(F)}{\partial \hat{\beta}_i} = \frac{1}{2} \tag{B.15}$$

while

$$\frac{\partial \hat{x}(F)}{\partial \hat{\alpha}_i} = \frac{\hat{z}(F)}{2} = -0.5 \cdot \ln\left(-\ln\sqrt{F}\right) \tag{B.16}$$

and Eq. (B.14) is reduced to

$$\mathrm{var}^{SM}\left\{\hat{x}(F)\right\} \approx \frac{\alpha^2}{N}\left(0.5544 + 0.2570 z(F) + 0.3040 z^2(F)\right) \tag{B.17}$$

or alternatively substituting into (B.17) $z(F) = \ln 2 + y(F)$, where $y(F) = -\ln(-\ln F)$

$$\mathrm{var}^{SM}\left\{\hat{x}(F)\right\} \approx \frac{\alpha^2}{N}\left(0.8786 + 0.6784 y(F) + 0.3040 y^2(F)\right). \tag{B.17a}$$

AM approach

Asymptotic variance of ML quantile estimators of Gumbel

For the ML estimator of $x(F)$ got from Gumbel distributed AM samples, i.e., $\hat{x}^{AM}(F) = \hat{\beta}' - \hat{\alpha}\ln(-\ln F)$, the expression for asymptotic variance takes the form

$$\mathrm{var}^{AM}\left\{\hat{x}(F)\right\} \approx$$

$$\approx \left(\frac{\partial \hat{x}(F)}{\partial \hat{\beta}'}\right)^2 \mathrm{var}(\hat{\beta}') + \left(\frac{\partial \hat{x}(F)}{\partial \hat{\alpha}}\right)^2 \mathrm{var}(\hat{\alpha}) + 2\frac{\partial \hat{x}(F)}{\partial \hat{\beta}'}\frac{\partial \hat{x}(F)}{\partial \hat{\alpha}}\mathrm{cov}(\hat{\beta}', \hat{\alpha}). \qquad \text{(B.18)}$$

Substituting into it

$$\frac{\partial \hat{x}(F)}{\partial \hat{\alpha}} = -\ln(-\ln F) = y(F)$$

$$\frac{\partial \hat{x}(F)}{\partial \hat{\beta}'} = 1$$

and Eq. (B.2), we get for the AM approach

$$\mathrm{var}\left(\hat{x}_F^{AM}\right) = \frac{\alpha^2}{N}\left(1.1087 + 0.5140 \cdot y(F) + 0.6079 \cdot y^2(F)\right). \qquad \text{(B.19)}$$

Appendix C

Asymptotic Formula for the Bias of Quantile Estimators for Gumbel as Seasonal Distribution

SM approach

Taking Gumbel as seasonal distribution the following formula defines approximate asymptotic bias of quantile estimate

$$B^{SM}\left\{\hat{x}(F)\right\} \approx \sum_{i=1}^{2}\left\{\frac{\partial \hat{x}(F)}{\partial \hat{\beta}_i}B(\hat{\beta}_i) + \frac{\partial \hat{x}(F)}{\partial \hat{\alpha}_i}B(\hat{\alpha}_i) + \right.$$

$$\left. + \frac{1}{2}\frac{\partial^2 \hat{x}(F)}{\partial \hat{\beta}_i^2}\mathrm{var}(\hat{\beta}_i) + \frac{1}{2}\frac{\partial^2 \hat{x}(F)}{\partial \hat{\alpha}_i^2}\mathrm{var}(\hat{\alpha}_i) + \frac{\partial^2 \hat{x}(F)}{\partial \hat{\alpha}_i^2 \partial \hat{\beta}_i^2}\mathrm{cov}(\hat{\alpha}_i, \hat{\beta}_i)\right\} \qquad \text{(C.1)}$$

where, in the case of ML estimation (Hosking 1985)

$$B(\hat{\beta}_i) \approx 0.370\ \hat{\alpha}_i/N, \qquad B(\hat{\alpha}_i) \approx -0.772\ \hat{\alpha}_i/N, \qquad \text{(C.2)}$$

while $\mathrm{var}(\hat{\alpha}_i)$, $\mathrm{var}(\hat{\beta}_i)$ and $\mathrm{cov}(\hat{\alpha}_i, \hat{\beta}_i)$ are given by Eq. (B.2). First and second order partial derivatives of $\hat{x}(F)$ with respect to the parameter estimates are needed to obtain an expression for bias of $\hat{x}(F)$ (Eq. (C.1)). Differentiating the first order partial derivatives (Eqs. (B.11) and (B.13)) with respect to parameter estimates $\hat{\alpha}_i$ and $\hat{\beta}_i$ one gets (Buishand and Demaré 1990):

$$\frac{\partial^2 \hat{x}(F)}{\partial \hat{\beta}_i^2} = \left(\frac{A_1/\hat{\alpha}_1 + A_2/\hat{\alpha}_2}{A_1 + A_2} - \frac{2}{\hat{\alpha}_i} \right) \left(\frac{\partial \hat{x}(F)}{\partial \hat{\beta}_i} \right)^2 + \frac{1}{\hat{\alpha}_i} \frac{\partial \hat{x}(F)}{\partial \hat{\beta}_i}, \tag{C.3}$$

$$\frac{\partial^2 \hat{x}(F)}{\partial \hat{\beta}_i \, \partial \hat{\alpha}_i} = \hat{z}_i(F) \frac{\partial^2 \hat{x}(F)}{\partial \hat{\beta}_i^2} + \frac{\partial \hat{x}(F)}{\partial \hat{\beta}_i} \left\{ \frac{\partial \hat{x}(F)}{\partial \hat{\beta}_i} - 1 \right\} \Big/ \hat{\alpha}_i \,, \tag{C.4}$$

$$\frac{\partial^2 \hat{x}(F)}{\partial \hat{\alpha}_i^2} = \hat{z}_i(F) \frac{\partial^2 \hat{x}(F)}{\partial \hat{\beta}_i \, \partial \hat{\alpha}_i} + \frac{\partial \hat{x}(F)}{\partial \hat{\alpha}_i} \left\{ \frac{\partial \hat{x}(F)}{\partial \hat{\beta}_i} - 1 \right\} \Big/ \hat{\alpha}_i \,. \tag{C.5}$$

In the situation of no seasonal variation:

$$\frac{\partial^2 \hat{x}(F)}{\partial \hat{\beta}_i^2} = \frac{1}{4\alpha}, \qquad \frac{\partial^2 \hat{x}(F)}{\partial \hat{\beta}_i \, \partial \hat{\alpha}_i} = \frac{z(F) - 1}{4\alpha}, \qquad \frac{\partial^2 \hat{x}(F)}{\partial \hat{\alpha}_i^2} = \frac{z(F)[z(F) - 2]}{4\alpha}, \tag{C.6}$$

where $z(F) = \ln 2 + y(F)$, while $y(F) = -\ln(-\ln F)$. The expression for the bias of $\hat{x}(F)$ then becomes

$$B^{SM}\left\{\hat{x}(F)\right\} = \frac{\alpha}{N}\left(0.519 - 0.948 \cdot z(F) + 0.152 \cdot z^2(F)\right), \tag{C.7}$$

or expressing $z(F)$ by $y(F)$

$$B^{SM}\left\{\hat{x}(F)\right\} = \frac{\alpha}{N}\left(0.0726 - 0.7373 \cdot y(F) + 0.152 \cdot y^2(F)\right). \tag{C.7a}$$

AM approach
Asymptotic bias of ML quantile estimators of Gumbel

For the ML estimator of $x(F)$ got from AM samples, i.e., $\hat{x}^{AM}(F) = \hat{\beta}' - \hat{\alpha}\ln(-\ln F)$, the expression for asymptotic bias takes the form

$$B^{AM}\left\{\hat{x}(F)\right\} = \frac{\partial \hat{x}(F)}{\partial \hat{\beta}'} B(\hat{\beta}') + \frac{\partial \hat{x}(F)}{\partial \hat{\alpha}} B(\hat{\alpha}). \tag{C.8}$$

Substituting into it (C.2) and the derivatives of $\hat{x}^{AM}(F)$ in respect to parameter estimates $\hat{\beta}'$ and $\hat{\alpha}'$, one gets

$$B^{AM}\left\{\hat{x}(F)\right\} = \frac{\alpha}{N}\left(0.370 - 0.772 \cdot y(F)\right). \tag{C.9}$$

References

Buishand, T.A., and G.R. Demaré (1990), Estimation of the annual maximum distribution from samples of maxima in separate seasons, *Stochastic Hydrol. Hydraul.* **109**, 1-9.

Fisher, R.A. (1921), On the mathematical foundations of theoretical statistics, *Philos. Trans. R. Soc. Ser*. A **222**, 309-368.

Hosking, J.R.M. (1985), A correction for the bias of maximum likelihood estimators of Gumbel parameters – comment, *J. Hydrol.* **78,** 393-396.

Kaczmarek, Z. (1977), *Statistical Methods in Hydrology and Meteorology*, US Dep. of Commerce, Warsaw.

Kruszewski, A. (2001), Program QMAXP Wersja 1.40, Institute of Meteorology and Water Management, Poland.

Lamberti, P., and S. Pilati (1985), Probability distributions of annual maxima of seasonal hydrological\variables, *Hydrol. Sc. J.* **1, 3**, 111-135.

Ozga-Zielińska, M., J. Brzeziński, and B. Ozga-Zieliński (1999), Computation regulations of maximum annual flow discharge with given probability of exceedance for hydrologic design. Long observational series (in Polish), *Materiały badawcze. Seria: Hydrologia i Oceanologia*, vol. **27**, IMGW, Warsaw.

Ozga-Zielińska, M., J. Brzeziński, and B. Ozga-Zieliński (2007), Probability estimation of probability of annual extremal flow discharges from inhomogeneous series. Alternative method (in Polish), *Gospodarka Wodna* **5**, 191-196.

Phien, H.N. (1987), A review of methods of parameter estimation for the extreme value type-I distribution, *J. Hydrol.* **90**, 251-268.

Strupczewski, W. (1965), High water frequency (in Polish), *Przegl. Geofiz*. X(XVIII), **1**, 83-93.

Strupczewski, W. (1967), Determination of the probability distribution of maximum discharges on basis of all observed floods, *Publ. IAHS*, **3**, 41-49.

Waylen, P., and M.K. Woo (1982), Prediction of annual floods generated by mixed processes, *Water Resour. Res.* **18**, 1283-1286.

Accepted December 8, 2008.

PUBLS. INST. GEOPHYS. POL. ACAD. SC., E-10 (406), 2008

Evaluation of the Nida River Main Current Below the Perpendicular Flood Channel Outlet

Andrzej STRUŻYŃSKI and Maciej WYRĘBEK

Department of Water Engineering
Al. Mickiewicza 24/28, 30-059 Kraków, Poland
e-mails: rmstruzy@cyf-kr.edu.pl; m.wyrebek@gmail.com

Abstract

The development of computational techniques increases the number of easy-to-use software designed for creating mathematical models, including the free CCHE2D software. This encouraged the authors to produce a computer model of a river section influenced by a projected channel outlet conducting water from a small reservoir. A few discharge configurations were tested to verify the potential of the inflowing stream and the jets created in the Nida River. Velocity distribution of water flowing into the Nida River during annual average flow conditions was measured.

1. Introduction

The paper evaluates flow disturbance below the flood channel outlet in the Nida River. At the moment, the river flows in a regulated, artificial channel. One of the cut-off meander loops in Pińczów has been transformed into an artificial lake. The existing outlet capacity is too low, which results in an improper flow regime in the reservoir. Proposed additional pipe projected at the shortest distance to the Nida River would increase water exchange in the reservoir. This will improve water quality, which is an important factor for local habitats including rare species of molluscs and for local people as long as the reservoir is used for recreation purposes. Flow disturbance model after the introduction of an additional duct was developed with the help of the CCHE2D software.

2. The goal of the study and methodology

Unlike the existing outlet from the reservoir which conducts water to the cut-off meander loop and mostly supplies the wetlands, the additional outlet would channel

water directly to the river. The presented calculations were conducted in order to estimate the Nida River hydraulic balance and bed stability after the creation of a shortened outlet from the reservoir. For that purpose, the river flow disturbance as well as the velocity and distribution of the stream in the Nida River channel were modeled. Calculations were performed with the help of the CCHE2D software. The modeled flow distance was 450 meters.

3. The study object

The Nida River

The Nida River in the Pińczów cross-section flows in its lower run, which starts from the Mierzawa River outlet (Fig. 1). The basin area in the cross-section of Pinczów equals 3358 km^2. Characteristic discharge parameters are as follows: $Q_{1\%} = 450$ m^3 s^{-1} and $Q_{50\%} = 150$ m^3 s^{-1}. The discharges in the river channel were as presented below: summer average flow of 8 m^3 s^{-1}, bank flow of 40 m^3 s^{-1}, and spring flood flow of 70 m^3 s^{-1}. The width of the trapezoidal channel is 40 m. In the summer, average water depth is 0.5 meters, while water velocity equals 0.5 m s^{-1}. Flow capacity measured in spring and summer 2007 varied from 6 to 9 m^3 s^{-1}. The measured average bottom sand diameter is 0.6 mm and the slope of the river bottom equals 0.61‰ (Bartnik *et al*. 2004).

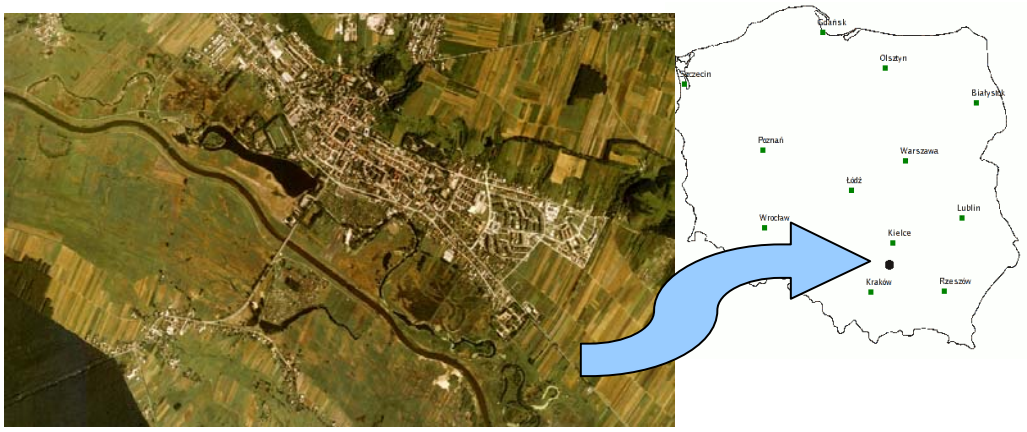

Fig. 1. Location of the study area.

Bed forms created on sand shoals can be also found in the river. In the cross-section there are often deep zones and shallow waters (Fig. 2). In the modeled section of the Nida River, the shallow water zone has been stabilized near convex banks.

According to Hjulström's results (Wołoszyn *et al*. 1974), sedimentation processes appear in this section for velocities lower than 0.05 m s^{-1}. For velocities up to 0.2 m s^{-1}, balanced transportation can be found, and after this speed is exceeded, bed erosion processes appear. Critical drag stresses for sand fraction between 0.4 and 1 mm vary from 2.45 to 2.95 N m^{-2} Wołoszyn *et al.* 1974. The Ashley measurement

results (Radecki-Pawlik 2006) define the maximum flow velocity for stable bed, when bed forms are created in the Nida River; it is defined in the range from 1.1 to 1.3 m s^{-1} (Fig. 3).

Fig. 2. The reservoir and the Nida River with visible bedforms (photo: Aeroklub Pińczowski). A – proposed channel, B – existing channel.

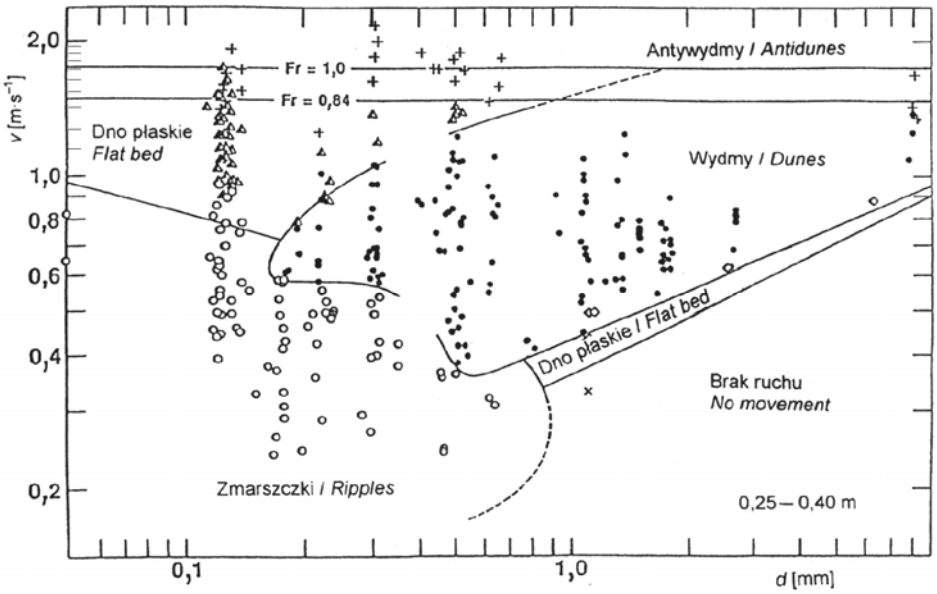

Fig. 3. River bed forms formation conditions depending on the mean flow velocity after Ashley (Radecki-Pawlik 2006).

The reservoir

The reservoir area equals 10 ha and its maximum depth exceeds 1.5 m. Water outflow system conductivity reaches 170 $l s^{-1}$ for the normal water level, which is too low since as a result water is stored in the reservoir for 8 days instead of the required 4-5 days (Strużyński 2007a). As far as the costs of the restoration are concerned, the goal can be achieved after building an additional channel which would increase normal flow through the reservoir as well as increase the safety of surrounding areas during floods. Flow discharge in this balancing duct will reach from 150 $l s^{-1}$ to 450 $l s^{-1}$ during normal water level and 750 $l s^{-1}$ during flood (Strużyński 2007b). The slope of the channel would be 4‰.

4. Modeling methodology

Finite element method

The CCHE is an analysis system for two-dimensional, unsteady, turbulent river flow, sediment transport, and water quality evaluation (Zhang 2006).

The continuity equation:

$$\frac{\partial Z}{\partial t}+\frac{\partial (hu)}{\partial x}+\frac{\partial (hv)}{\partial y}=0. \tag{1}$$

The momentum equations:

$$\frac{\partial u}{\partial t}+u\frac{\partial u}{\partial x}+v\frac{\partial u}{\partial y}=-g\frac{\partial Z}{\partial x}+\frac{1}{h}\left[\frac{\partial (h\tau_{xx})}{\partial x}+\frac{\partial (h\tau_{xy})}{\partial y}\right]-\frac{\tau_{bx}}{\rho h}+f_{Cor}v, \tag{2}$$

$$\frac{\partial v}{\partial t}+u\frac{\partial v}{\partial x}+v\frac{\partial v}{\partial y}=-g\frac{\partial Z}{\partial y}+\frac{1}{h}\left[\frac{\partial (h\tau_{yx})}{\partial x}+\frac{\partial (h\tau_{yy})}{\partial y}\right]-\frac{\tau_{by}}{\rho h}+f_{Cor}u, \tag{3}$$

where u and v are the depth-integrated velocity components in the x and y directions, respectively; g is the gravitational acceleration; Z is the water surface elevation; ρ is water density; h is the local water depth; f_{Cor} is the Coriolis parameter; τ_{xx}, τ_{xy}, τ_{yx} and τ_{yy} are the depth integrated Reynolds stresses; and τ_{bx} and τ_{by} are shear stresses on the bed surface.

In the equations presented above, the Reynolds stresses have approximate values based on Boussinesq's assumption:

$$\tau_{xx}=2\nu_t\frac{\partial u}{\partial x},$$

$$\tau_{xy}=\tau_{yx}=\nu_t\left(\frac{\partial u}{\partial y}+\frac{\partial v}{\partial x}\right), \tag{4}$$

$$\tau_{yy} = 2\nu_t \frac{\partial v}{\partial y}.$$

The CCHE2D model adopts two zero-equation eddy viscosity models. The first one is the depth-integrated parabolic model, in which the eddy viscosity ν_t is calculated by the following formula:

$$\nu_t = \frac{A_{xy}}{6} \kappa U^* h, \tag{5}$$

where A_{xy} is an adjustable coefficient of eddy viscosity, K is the von Karman constant, and U^* is the shear velocity.

The second eddy viscosity model is the depth-integrated mixing length model,

$$\nu_t = \bar{l}^2 \sqrt{2\left(\frac{\partial u}{\partial x}\right)^2 + 2\left(\frac{\partial v}{\partial x}\right)^2 + \left(\frac{\partial u}{\partial x} + \frac{\partial v}{\partial x}\right)^2 + \left(\frac{\partial \bar{U}}{\partial z}\right)^2},$$

$$\bar{l} = \frac{1}{h}\int \kappa z \sqrt{\left(1 - \frac{z}{h}\right)} dz = \kappa h \int_0^1 \lambda \sqrt{1-\lambda}\, d\lambda \approx\sim 0.267 \kappa h, \tag{6}$$

$$\frac{\partial \bar{U}}{\partial z} = C_m \frac{U^*}{\kappa h},$$

where C_m is the coefficient with a value of 2.34375 so that the equation of depth-integrated parabolic model will cover the equation of depth-integrated mixing length in the case of a uniform flow in which all the horizontal velocity gradients vanish.

5. Generating the mesh and running the model

The mesh was generated with the help of the CCHE2D Mesh Generator on the basis of bathymetry measurements conducted in June 2007 and the satellite image taken in 2004 (Strużyński 2007b, Bartnik *et al*. 2004). The main parameters of the mesh are presented in Table 1.

The bed elevation model, mesh at the outlet, and the outlet boundary condition were defined through the rating curve (Fig. 4).

In CCHE2D there are three turbulence models available: the parabolic eddy viscosity model, the mixing length model and the k-e model (Zhang 2006). In the runs performed the mixing length model was used with Method 1 of time iteration. During stabilization of the modeled flow, Method 2 was used. There is no strict description of how many iterations *per* one step are performed. Within Method 1, a ‘small’ number of iterations per time step is done, and while Method 2 is chosen the solver CCHE2D performs a ‘bigger’ number of iterations.

The 3-meter long mouth of this duct was modeled as a steep (3.7%) spillway.

Table 1

Parameters of the generated mesh and performed modeling

Model parameters	
River section length [m]	450
Channel length [m]	100
River/channel width [m]	45/2
Max. river depth [m]	1.5
Average mesh density [m]	1
No. of cells	17760
No. of inlets/outlets	2/1
No. of steps per run	3600
Time step [s]	0.1–1

The Manning roughness coefficient in riverbed was defined as 0.025. The CCHE2D software cannot simulate flows in pipes, so a transformation to the flow with similar condition in a concrete channel was made. Roughness value of 0.0175 was chosen for the trapezoidal channel to reflect flow depth and velocity in the substituted pipe.

This paper presents preliminary results of modeling. Water flow calculations were conducted including, e.g., velocity, shear stresses and the Froude number. The modeled flow in the system was initially developed for low flow conditions ($Q = 8$ $m^3 s^{-1}$) with very low discharge in the channel ($Q = 0.01$ $m^3 s^{-1}$). The stabilization time was 16 minutes. Every case was developed after 7200 steps. The model was stable for about 1 hour of simulation for all performed cases with the exception of case 4 (see Table 2) in which outflow velocity from the channel was continuously increasing until it reached the speed of over 2.5 m s^{-1} in the 10-meter radius surrounding the channel mouth. In this case, the Chezy formula was used to choose the best modeling step.

6. Results and discussion

Velocity measurements and modeling

The presented plot of iso-velocity lines (Fig. 5) is created for yearly average flow conditions ($Q = 8$ $m^3 s^{-1}$). The presented velocity distribution was measured in situ in the cross-section localized 100 meters upstream from the outlet of the proposed channel. Bed geometry and velocities reflect hydrodynamic conditions shown on Figs. 2 and 3. Bed elevation of the model created in CCHE2D was more generalized when compared to the investigated cross-section. However, velocity distribution gathered from the model reflects the in situ measurements. In sections localized downstream to the channel outlet, the influence of the flowing stream predictably moderates the main discharge.

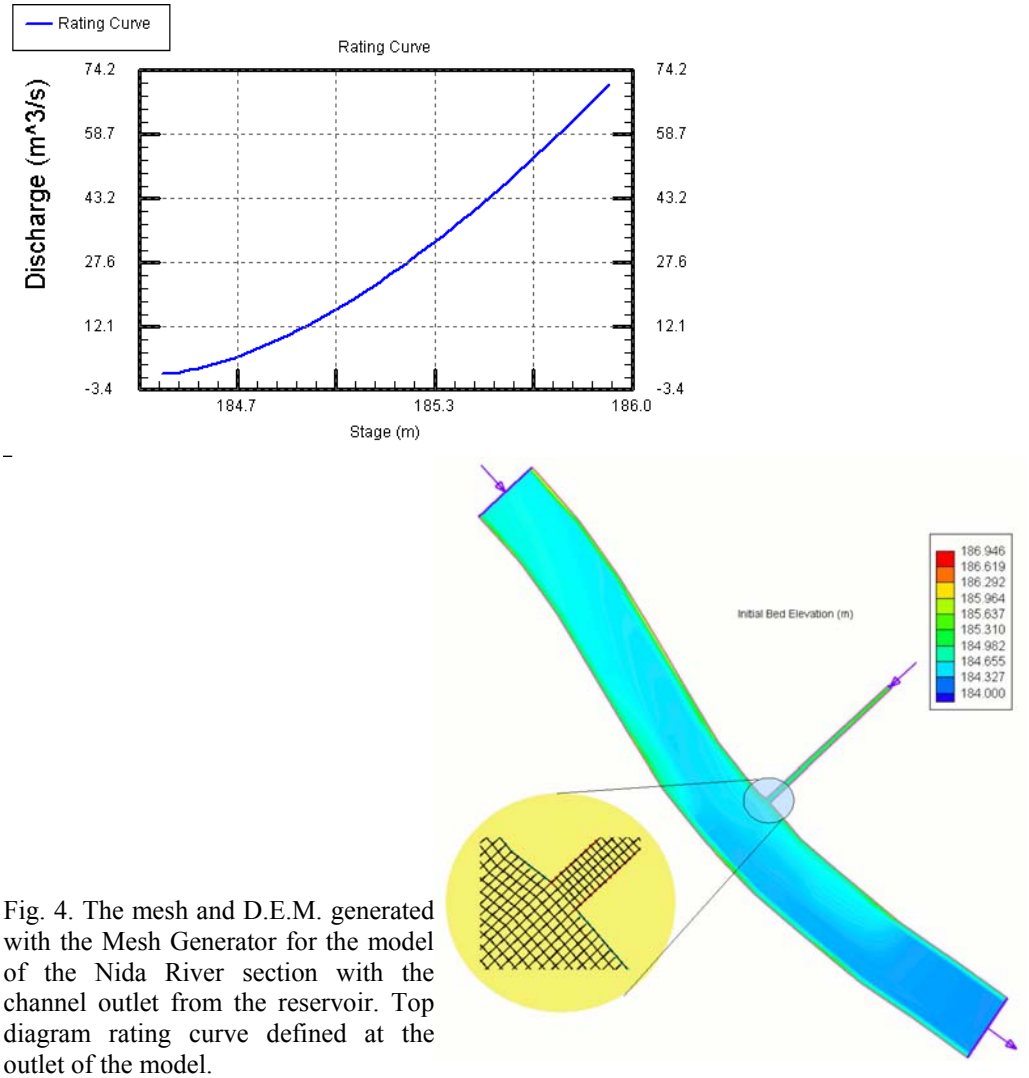

Fig. 4. The mesh and D.E.M. generated with the Mesh Generator for the model of the Nida River section with the channel outlet from the reservoir. Top diagram rating curve defined at the outlet of the model.

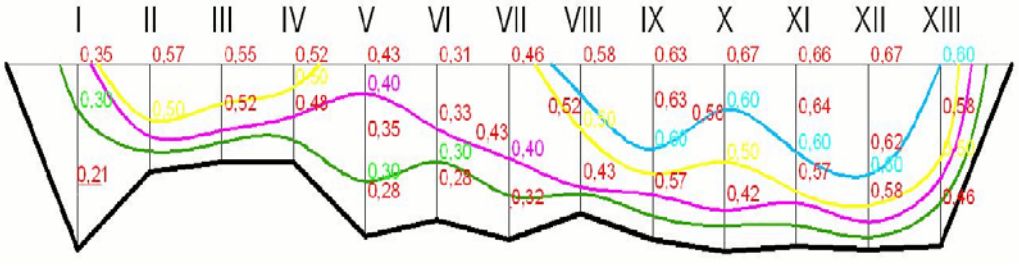

Fig. 5. Measured velocity points and isotachs plotted in the Nida River cross-section in Pińczów.

The jet stream created by the current from the channel divides the main flow into three zones. The jet itself creates a 'tail', the shadow zone near the left bank, and the narrowed cross-section with condensed flow (Fig. 6).

(a) $Q_{ch} = 0.15$ m^3 s^{-1} – case 1,

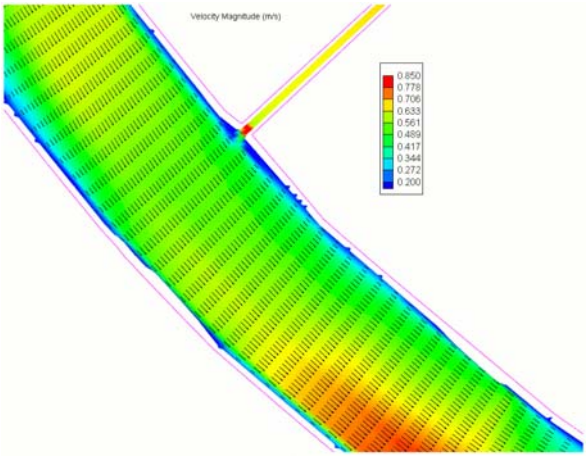

(b) $Q_{ch} = 0.45$ m^3 s^{-1} – case 2 (see Table 2).

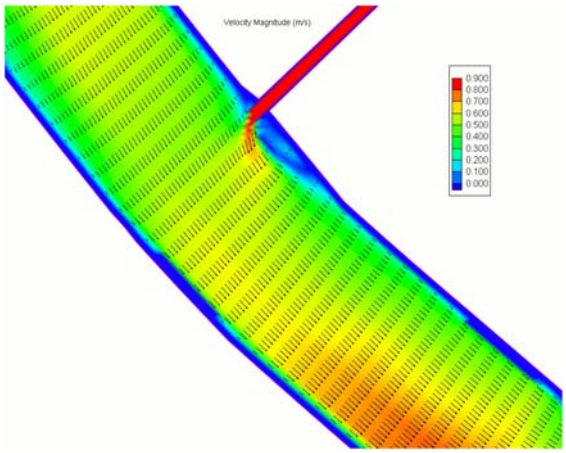

Fig. 6. Main stream moderation by the outflow of water from the side channel during flow $Q = 8$ m^3 s^{-1}.

Interpretation of CCHE2D results

The border of the shadow zone was defined as a zone of relatively high velocity gradient appearing between the inner region (shadow zone) and the tail. The main parameters of the tail and shadow zone in the model were measured for the performed runs. As long as the localization of the channel outlet can disturb the main flow, the maximum velocity and shear stress values were searched in the model for separate cases. The main results of 5 cases of modeling have been gathered in Table 2. In the

channel, first four models were run under free flow water conditions and in the last case a backwater flow from the river was simulated.

As shown in Table 2, the length of shadow zone increases proportionally to the river flow and the width grows with the increase of discharge in the channel. While the backwater appears in the channel, the velocity of outflowing water decreases, which reduces the influence of the channel on the main stream during flood flow. Under the flow parameters combined in case 4, the shadow zone reaches the highest range and the shear stresses exceed 16 N m^{-2}. In spite of the biggest stresses found in the river in case 5 (9.5 N m^{-2}), the most intensive influence of the perpendicular channel on the Nida River flow can appear when the water from the channel freely flows through the mount.

Table 2

The results gathered from CCHE2D modeling and the Chezy equation

Discharge Q m^3 s^{-1} river/channel	Case 1 8/0.15	Case 2 8/0.45	Case 3 8/0.75	Case 4 40/0.75	Case 5 70/0.75 ***
Average river flow depth in the upstream sections [m]*	0.34	0.34	0.34	0.9	1.26
Stream average velocity in the river/channel [m s^{-1}]*	0.53/0.64	0.53/1.10	0.53/1.32	1.00/1.32	1.24/1.32
Maximum stream velocity in the tail formed downstream the channel outlet [m s^{-1}]**	0.54	0.6	1.15	1.6	0.3
Maximum value of shear stresses in the river upstream/in the tail [N m^{-2}]**	3.6/2.0	3.6/3.7	3.6/10	5.5 / 16	9.5/0.2
The width/length of the shadow zone [m]**	5/12	6/16.5	8.5/25	8/86	3.5/23

*by using the Chezy equation, **data from the CCHE2D, ***backwater flow conditions in the channel.

These conditions (cases 1-4) are more reasonable for the gravitationally drained reservoir but can intensify bed erosion processes in the riverbed as long as the critical dragging forces, which equal 2.7 N m^{-2} for the moderate-size sand fractions covering bottom, are exceeded.

Following Wołoszyn (1974), for cases 1 to 3, permissible average velocity equals 0.42 m s^{-1}; for the case 4 flow, velocity can reach 0.49 m s^{-1}, and in case 5 it can reach 0.52 m s^{-1}. It can be stated after Hjulstrom (Wołoszyn *et al*. 1974) that erosion processes would appear in all cases; however, the results of more extensive Ashley measurement results (Radecki-Pawlik 2006) indicate that for cases 1 and 2 dunes or ripples would appear; for case 3, dunes or flat bed; and only in cases 4 and 5, massive

transportation and flat bed would appear. The range of velocities found in Fig. 3 (1.1 to 1.3 m s^{-1}) indicates that conditions of flat bed formation can start exceeding the shear stresses in the range from 6 to 7.8 N m^{-2}. Destroyed balance of bed load transportation leads to erosion processes and is potentially dangerous for bed stability, especially in the zones of rapid flow tail created by channel activity. Massive transportation disturbs hydro-morphological balance during almost every spring flood in the sections of the Nida River near Pińczów in the vicinity of a local airfield and below the bridge on the national road (Bartnik *et al*. 2004). There is a concept of river renaturation, which would improve bed stability and decrease flood hazard. As long as the river is regulated, flood protection of areas localized in the neighborhood of the reservoir will not be effectively performed. The tail simulated in case 4 does not reach the pillars of the road bridge localized 120 meters below the channel mouth.

7. Conclusions

The results of the modeling performed in cases 1 and 2 confirmed the possibility of using the proposed conduct during low flow conditions in the river and the reservoir. The results calculated in case 3 indicate that flow from the channel would overcome parameters of bed stability. The income of 0.75 m^3 s^{-1} from reservoir would cause local bed degradation processes in the Nida River even in low flow conditions. This means that in the regulated river, massive transportation of bed material takes place if the flow is higher than annual average. As shown in case 4, the conduct should not be used in high flow conditions appearing in the river. In case 5, we have to deal with backwater in the conduct. The drown outlet will increase flow resistance in the pipe (in the CCHE2D modeled as a channel). Additionally, the difference of water levels in the reservoir and in the river will decrease, which will affect the discharge in the pipe. These two processes would decrease the risk of using the conduct in flood conditions in the Nida River.

The results of case 4 are the most unfavorable. Due to the appearance of free flow conditions in the pipe (checked with the use of the Darcy-Weisbach equation), flood flushing and water refreshing operations necessary for improving the good state of the reservoir would not be possible or should be carried out with special care. From another point of view, this additional outlet is to be localized on the convex bank, where the bar is located, so it would be possible to perform short-term outflows of the required $Q = 0.75$ m^3 s^{-1}, whose influence would be easily supplemented within the natural processes of aggradation of bed material. This can be described in detail after simulating bed movement in the model, which can be done with CCHE2D.

The results of the CCHE2D model with the created mesh are reasonable for all the examined cases. The stability of the modeled flow in the Nida River and the channel conducting water from the reservoir was high. In case 4, however, proper results had to be searched in the history file. The decision was made on the basis of the Chezy formula calculations. The problem of model instability was not solved in the conducted modeling session. The results taken from the created mesh should be verified on a new mesh of higher density close to the outlet of the channel.

References

Bartnik, W., S. Deńko, A. Strużynski, and T. Zając (2004), *Renaturyzacja obszaru zlewni Nidy – Koncepcja opracowana dla potrzeb ochrony zasobów przyrodniczych w związku z planami realizacji programu „NATURA 2000”* (*Renaturation of the Nida River basin – The concept of nature protection on the basis of “Nature 2000” program*), Drukrol s.c., Kraków, pp. 183 (in Polish).

Strużyński, A. (2007a), *Koncepcja poprawy warunków użytkowania zalewu pińczowskiego (...), Ekspertyza wykonana na zamówienie Urzędu Miejskiego w Pińczowie* (*The concept of the Pińczowski reservoir improvement, an expertise conducted for the municipality of Pińczów*), manuscript (in Polish).

Strużyński, A. (2007b), *Optymalizacja eksploatacji zalewu pińczowskiego w celu zmniejszenia jego zamulenia* (*The rebuilding of outflow system in the Pińczowski reservoir and its optimal exploitation for the reduction of alluviation processes*), Infrastruktura i Ekologia Terenów Wiejskich, Komisja Technicznej Infrastruktury Wsi PAN/o Kraków, No 4/2, p. 179-188 (in Polish with English summary).

Radecki-Pawlik, A. (2006), *Wybrane zagadnienia kształtowania się form korytowych potoku górskiego i form dennych rzeki nizinnej* (*Selected aspects regarding the formation of mountain stream bars and lowland river dunes*), Zesz. Nauk. AR Kraków, rozprawy, No 281, pp. 142 (in Polish with English summary).

Wołoszyn, J., W. Czamara, R. Eliasiewicz, and J. Krężel (1974), *Regulacja rzek i potoków* (*River and stream training*), AWR Wrocław (in Polish).

Zhang, Y. (2006), *CCHE-GUI – Graphical Users Interface for NCCHE Model User's Manual – Version 3.0*, National Center for Computational Hydroscience and Engineering, School of Engineering, The University of Mississippi, MS 38677, portable document, http://ncche.olemiss.edu, pp. 158.

Accepted November 13, 2008

PUBLS. INST. GEOPHYS. POL. ACAD. SC., E-10 (406), 2008

Influence of Vegetated Floodplains on Compound Channels Discharge Capacity in 1D Modelling

Dorota SWIATEK

University of Life Sciences – SGGW
Nowoursynowska 159, 02-786 Warszawa, Poland
e-mail: dorotams@levis.sggw.pl

Abstract

Three different types of models were applied to compare an impact of floodplain treatment in 1D modelling on compound channels discharge capacity and retention volume of vegetated floodplains. The tested models are based on 1D St Venant equations with the Darcy-Weisbach friction law. A traditional way in which floodplains in 1D modelling are considered storage areas was compared to a model with conveyance of vegetated floodplain and a model with lateral shear stress between the channel and floodplain section, proposed in the Pasche approach. The models were applied to a steady flow in a 50 km long double trapezoidal channel, and differences in rating curves, retention volume of vegetated floodplains, and discharge distribution in a cross-section, were found between the models.

1. Introduction

Designing of compound channels, as well as projects of environmental flood management require in many cases estimating discharge capacities of compound channels and retention volume of vegetated floodplains. One dimensional hydrodynamic models are widely applied for solving these problems. This type of models is based on the assumptions of 1D flow, with the most relevant believing that the water level and discharge vary only in the longitudinal direction. Flow processes in channels with local flood berm vegetation between the main channel and floodplains are very complex.

When water overflowing the main channel and overbank flow occurs, processes, such as interaction between the main channel and floodplain flows, significant variation of resistance parameters with depth and flow regimes, distribution of boundary shear stresses and effects of vegetation on retarding flow (Knight 2001), will be considered. A traditional way to deal with floodplains in 1D modelling is considering floop-

lains retention areas with zero longitudinal velocities. In a one-dimensional model, floodplains geometry is accounted for in only one of Saint Venant's equations – a continuity equation, and the momentum equation reduces that to hydraulic parameters within the main channel geometry (Cunge *et al*. 1980). In another simplified approach widely used in solving river flow, cross-section conveyance is solved as the sum of conveyance of the main channel and left and right floodplain, and water level calculated for the cross-section is considered constant across the cross-section. A zero shear stress assumption is made for a vertical division between a channel and floodplain section. Although these methods are attractive in their simplicity, they ignore secondary effects due to the interaction between high velocities in the main channel and low velocities on the floodplain, and in consequence, overestimation of discharge capacity (Ackers 1993). Presently one-dimensional methods for water level calculation have been developed which take into account a lateral shear stress between the main channel and vegetated floodplain (e.g., Pasche 1984, Nuding 1998) and are capable of considering a momentum transfer between the main channel and the floodplain.

2. Developed models

Three different types of models were applied to compare an impact of floodplain treatment in 1D modelling on compound channels discharge capacity and retention volume of vegetated floodplains. Water levels, discharge distribution between the main channel and floodplain, as well as retention volume were compared for the following models:

- model DW_FA_P: Vegetated floodplain and St Venant equations with the Pasche's method for description of a momentum transfer between the main channel and floodplain (Swiatek 2007),
- model DW_FA: Vegetated floodplain and St Venant equations with a zero lateral shear stress between the channel and a floodplain section,
- model DW_FIN: St Venant equations with floodplains as storage areas.

Both models, DW_FA_P and DW_FA, enable accounting for flow resistance resulting from vegetation covering a compound channel with floodplain in unsteady flow calculations. Moreover, the DW_FA_P allows to consider a momentum exchange between the main channel and floodplains, proposed in the Pasche approach (Pasche 1984). In the DW_FIN model it is only possible to take into account flow resistance caused by the main channel vegetation. The floodplain is considered only a storage area with zero velocities, and thus will not contribute to the overall momentum flux in a cross section.

A basis for calculations in the three models is the friction law of Darcy-Weisbach and the conveyance factor *K*, expressed as

$$K = A\left(\frac{8gR}{\lambda}\right)^{1/2}, \tag{1}$$

where: A = cross area of flow; g = gravitational acceleration; R = hydraulic radius; λ = friction factor.

Flow resistance in parts of channel sections overgrown with vegetation depends on both vegetation and bed roughness and is calculated as a sum of channel bed λ_s and submerged vegetation λ_v friction factors (Indlekofer 1981). Friction factors for high vegetation λ_v were the aim of investigations by Kaiser (1984), Lindner (1982) and Pasche (1984), and are computed according to the concept issued by these authors. The lateral shear stress between the main channel and vegetated floodplain is taken into account in the model DW_FA_P. In this model, a compound river cross section is divided into sections with vertical imaginary walls between the main channel and neighbouring floodplains. The heights of these boundaries are taken into consideration in calculations of the wetted perimeter of the main channel, and separate Darcy-Weisbach friction factors are estimated for these imaginary walls. According to Pasche (1984), a friction factor of the boundary depends mainly on relationships of a plant diameter and distances between individual plants, and the contributing width of the floodplain that has influence on the interaction process. This process decreases the discharge in the main channel and increases the discharge on the floodplain.

The total conveyance (Eq. 1) for a compound cross section in models DW_FA_P and DW_FA is obtained by summing the subdivision conveyances of the channel and floodplains. The total conveyance K is introduced to the St Vetnant equations.

3. Results

In order to compare a compound channel discharge capacity and retention volume of vegetated floodplains, three models were applied to a steady flow in a double trapezoidal channel. The channel length was L = 50 km and bottom slope J = 0.0005. A compound river cross-section was stable and its geometry and growth of vegetation as presented in Fig. 1. The left floodplain was 60 m wide and covered with shrubs of d_p = 1.0 m of diameter and an average distance between individual shrubs of $a_x = a_y$ = 2.5 m. A part of the left channel slopes was covered with low vegetation of roughness k_s = 0.5 m. The bottom of the main channel was covered with small and medium-grain sand of roughness k_s = 0.05 m. The right channel slopes were covered with low vegetation of roughness k_s = 0.09 m. The right floodplain was 60 m wide and planted with shrubs and trees of an average diameter of d_p = 0.04 m, and average spacing $a_x = a_y$ = 0.3 m. The floodplains roughness was 0.10 m.

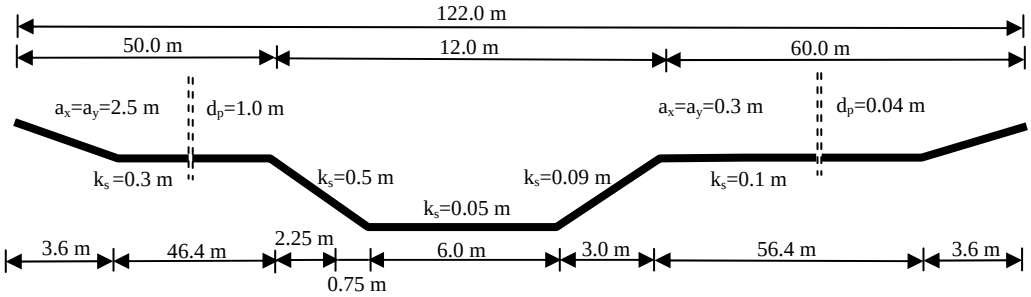

Fig. 1. A sketch of a compound cross-section.

A numerical mesh with a constant space step Δx = 1000 m and 51 nodes was used. Simulations for a steady flow were performed for different values of discharge ranging from 2 m^3/s to 35 m^3/s, and then rating curves were elaborated for the tested models (Fig. 2).

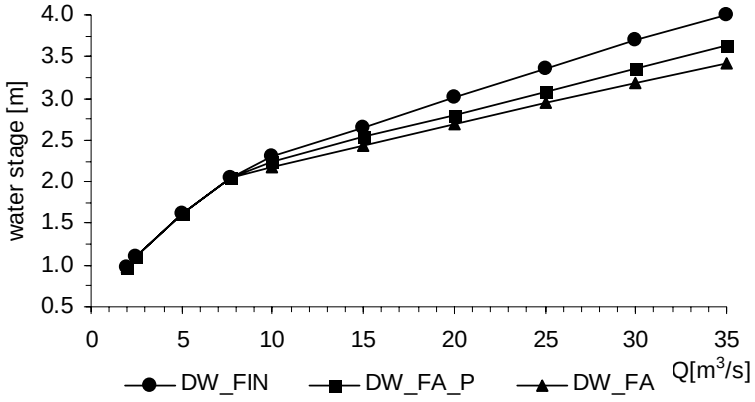

Fig. 2. Rating curves for tested models.

In model DW_FIN, water level at discharge of 35 m^3/s was about 0.57 m and 0.36 m higher than in models DW_FA and DW_FA_P (Fig. 2). It is so because in model DW_FIN only the main channel transports all the water in the longitudinal direction. The lateral shear stress assumed in model DW_FA_P causes the water level to be 0.21 m higher than in model DW_FA. The differences in water levels vary from 0.06 m at discharge of 10 m^3/s to 0.21 m at 35 m^3/s. The water depth on floodplains varies from 0.24 m to 1.64 m for the studied range of discharges (model DW_FA_P). The ratio of differences in water levels in models DW_FA_P and DW_FA as referred to water depths on floodplains shows that for low water levels on floodplains, the lateral stress played a significant role. In Fig. 3, retention volume of floodplains is shown for the tested models. In model DW_FIN, the maximum retention volume is about 19% higher than in model DW_FA_P, and 31% higher than in model DW_FA (Table 1).

Table 1

Percentage variability of retention volume of floodplains
in models DW_FA_P and DW_FA in relation to model DW_FIN

Q $[m^3/s]$	$V_{DW\_FA\_P}/V_{DW\_FIN}$ %	V_{DW_FA}/V_{DW_FIN} %
10	72	25.
15	92	64
20	74	65
25	77	66
30	79	68
35	81	69

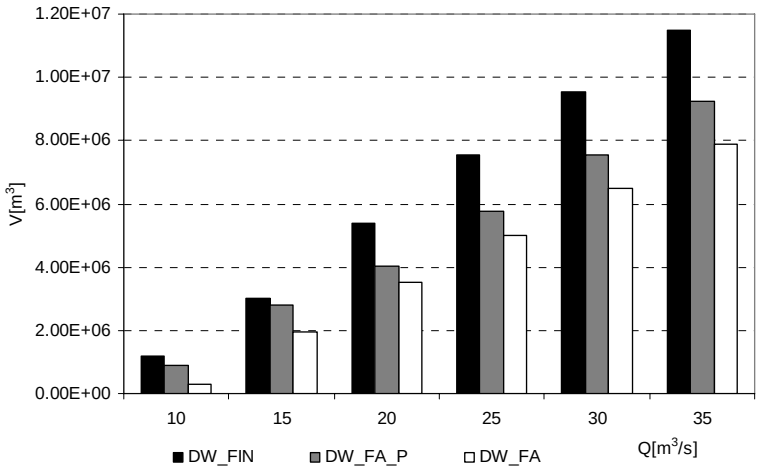

Fig. 3. Retention volume of floodplains calculated in tested models.

Models DW_FA_P and DW_FA allow to take into account longitudinal velocities on floodplains. Calculated discharges for the main river channel and left and right floodplains are shown in Figs. 4-6. At the total discharge of 35 m^3/s, in model DW_FA_P over 31% of this value, was transported on the floodplains and in model DW_FA – about 26% (Table 2). Highest differences (Table 2) are at low water levels on floodplains. This is due to the fact that the impact of resistance of the vegetated floodplain is lower than that of the lateral shear stress.

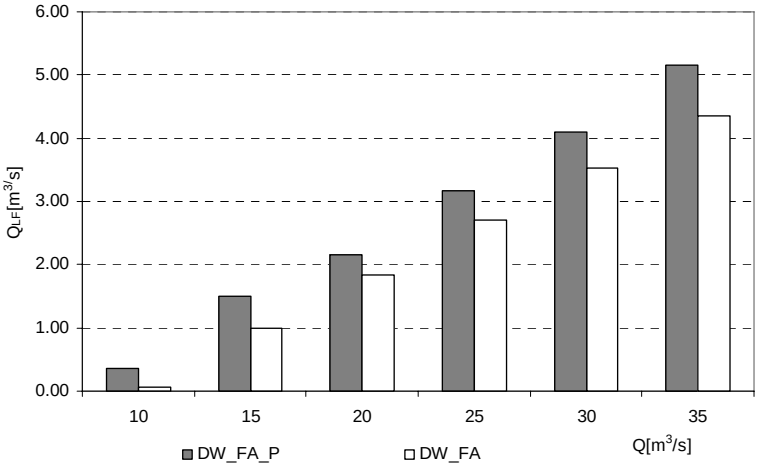

Fig. 4. Discharges Q_{lf} in the left floodplain calculated in models DW_FA_P and DW_FA.

4. Conclusions

A traditional model in which floodplains are considered to be the only storage areas significantly overestimates a discharge capacity in relation to a model with conveyance of vegetated floodplain, and model with lateral shear stress between the channel and

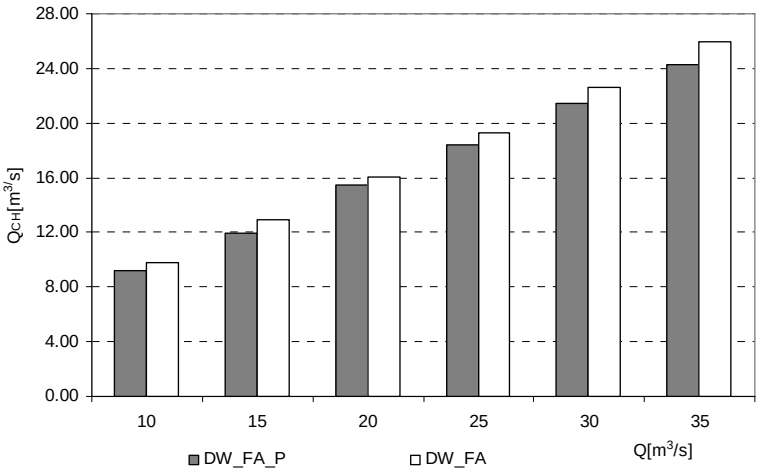

Fig. 5. Discharges Q_{CH} in the main chanel calculated in models DW_FA_P and DW_FA.

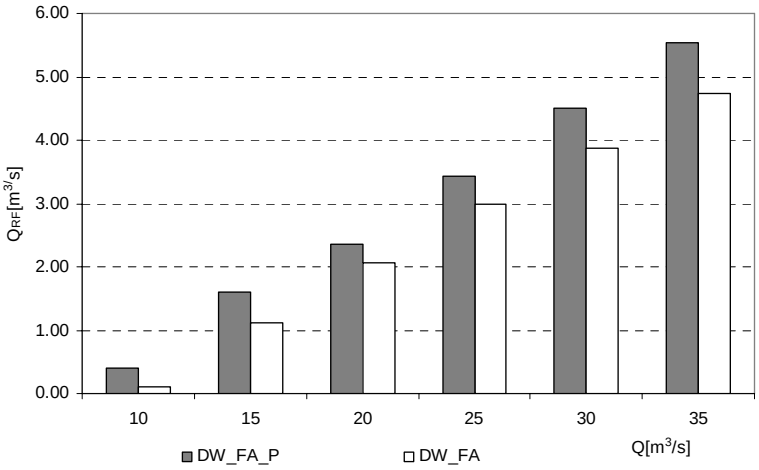

Fig. 6. Discharges Q_{RF} in the right floodplain calculated in models DW_FA_P and DW_FA.

Table 2

Percentages of discharge on the floodplains and in the main channel in models DW_FA_P (Q_P) and DW_FA (Q_F)

Q [m^3/s]	Q_P$_{CH}$ /Q$_{TOT}$ %	Q_P$_{LRF}$ /Q$_{TOT}$ %	Q_F$_{CH}$ /Q$_{TOT}$ %	Q_F$_{LRF}$ /Q$_{TOT}$ %
10	92	8	98	02
15	79	21	86	14
20	78	22	81	19
25	74	26	77	23
30	71	29	75	25
35	69	31	74	26

the floodplain. Percentage differences in water depth for a studied example in which floodplain is covered with shrubs and trees achieve 40% and 22%, respectively, at high water levels on floodplains. In the model with vegetated floodplain conveyance and lateral shear stress between the channel and floodplain, the water depth on floodplains is about 15% higher than in the model in which only vegetated floodplain conveyance is considered. The differences in water levels and discharge distribution in the floodplains in these two models depend on, which factor, the lateral stress or the effects of vegetal resistance of high plants, played a more significant role.

Contrary to the traditional approach where floodplains are considered storage areas, models with floodplain conveyance compute velocities, discharges, and friction factors for each specified part according to the type of vegetation in floodplains and the main channel. They may be used to estimate a new water surface level for renaturalized rivers, especially for flood conditions, as well as, to ensure suitable conditions for habitat diversity in projects of environmental flood management. They are an appropriate tool to estimate floodplain vegetation influence on flow conditions.

Acknowledgments. Author wishes to acknowledge the financial support offered by Warsaw University of Life Sciences – SGGW for the research project 504-10-05260011.

References

Ackers, P. (1993), Flow formulate for straight two-stage channels, *J. Hydraul. Res*. **31**, 4, 509-531.

Cunge, J.A., F.M. Holly, and A. Verwey (1980), *Practical Aspect of Computational River Hydraulics*, Boston, 420 pp.

Indlekofer, H. (1981), *Überlagerung von Rauhigkeitseinflüssen beim Abfluß in offenen Gerinnen*. Mitt. Institut für Wasserbau und Wasserwirtschaft, RWTH Aachen, Heft 37, 105-145.

Kaiser, W. (1984), Fließwiderstandsverhalten in Gerinnen mit durchströmten Ufergehölzzonen. *Thesis presented for the degree of Doctor in Applied Sciences TH Darmstadt*.

Knight, D.W., and J.D. Demetriou (1983), Flood plain and main channel flow interaction. Journal of Hydraulic Engineering 122 (10), 583-586.ISSN 0733-Lindner K., 1982: *Der Strömungswiderstand von Pflanzenbeständen*. Mitteilungen aus dem Leichtweiss – Institut für Wasserbau der TU Braunschweig, H. 75.

Lindner, K. (1982), *Der Strömungswiderstand von Pflanzenbeständen*. Mitteilungen aus dem Leichtweiss – Institut für Wasserbau der TU Braunschweig, H. 75.

Nuding, A. (1991), *Fließwiederstandsverhalten in Gerinnen mit Ufergebusch. Entwicklung eines Fließgewasser mit und ohne Geholzufer, unter besonderer Berucksichtigung von Ufergebusch*, Wasserbau-Mitteilugen Nr.35, Technische Hochschule Darmstadt.

Pasche, E. (1984), *Turbulenzmechanismen in naturnahen Fließgewässern und die Möglichkeit ihrer mathematischen Erfassung*. Thesis presented for the degree of Doctor in Applied Sciences, RWTH, Aachen.

Pasche, E., and G. Rouve (1985), Overbank flow with vegetatively roughened flood plains, *J. Hydraul. Eng*. **111**, 9, 1262-1278.

Swiatek, D. (2007), Unsteady 1D Flow Model of Natural Rivers with Vegetated Floodplain, *Publs. Inst. Geophys. Pol. Acad. Sc*. **E-7** (401), 237-244.

Accepted November 13, 2008

PUBLS. INST. GEOPHYS. POL. ACAD. SC., E-10 (406), 2008

Building Wall Boundary Condition in Mathematical Modelling of Built-up Area Rapid Inundation

Michał SZYDŁOWSKI

Gdańsk University of Technology, Faculty of Civil and Environmental Engineering
Narutowicza 11/12, 80-952 Gdańsk, Poland
e-mail: mszyd@pg.gda.pl

Abstract

The paper concerns mathematical modelling of rapid flooding flow in urban (built-up) area. The two dimensional Saint Venant equations are assumed as the model of free surface water flow. The model equations are solved using finite volume method. The mass and momentum fluxes are computed applying the Roe scheme of Godunov problem solution. The built-up area is exactly represented in city inundations simulation. Each separate building is excluded from the computational domain. The numerical mesh is generated in flow area between buildings only. An influence of the type of boundary conditions imposed on buildings walls on simulation results is investigated in the paper. The results of numerical computations are examined against laboratory measurements. The laboratory experiment carried out in hydraulic laboratory of the Gdańsk University of Technology is presented in the article.

1. Introduction

The problem of urban flood simulation has recently become one of the most important research subjects of modern hydrology. The mathematical modelling of rapid inundation in urban areas is the main tool for assessment of risk in the city exposed to flash flooding. Numerical simulations of floods are performed to predict and analyze the parameters of catastrophic flows. Then, the predicted flow parameters (water depth and velocity) can be used to estimate and mitigate the flood influence on city infrastructure (Kelman and Spence 2004) and to increase citizens security (Jonkman *et al*. 2002). When estimating the urban flood parameters, the mathematical model of wave propagation and the digital terrain model of flood area are needed. The former is considered in the paper only. The shallow water equations (Tan 1992) are chosen to represent the free surface water flow in built-up flood plain.

There are several techniques that can be applied for buildings representation in two dimensional shallow water flow modelling. The choice depends on dimensions of flow area and buildings. If the distances between buildings are close to the lengths of buildings walls, the buildings can be simply excluded from numerical mesh. In such case, the buildings walls make the closed boundaries of the computational domain and the mesh is generated in the area outside the buildings. However, if the spaces between buildings are significantly smaller than dimensions of flow, area the proper mesh generation is often impossible due to high disproportion of mesh elements size inside and outside the built-up area. Therefore, the explicit exclusion of the buildings from the numerical mesh can be impossible in this case, and the buildings have to be embedded into simulation as the sub-grid effect, using the urban porosity technique for example (Soares-Frazao *et al*. 2008). The buildings exclusion method is applied in the example presented in this paper.

The buildings representation with the technique of exclusion of the areas covered by buildings, needs to define the boundary conditions on the solid buildings walls. Two types of closed boundary conditions can be imposed on the wall in the simulation – no-slip boundary (velocity vector equal to zero) and free-slip boundary (only normal to the wall direction component of velocity reduced to zero). In the second case, the tangential component can be different from zero. However, its derivative in the direction normal to the wall equals zero. The influence of the boundary condition type on numerical results of rapid urban flood computation is investigated in the paper. The computations obtained using both boundary condition types are compared to laboratory measurements of water depth in model built-up area.

2. Shallow water flow model and solution method

The mathematical model used in the study to simulate urban rapid flooding is a system of shallow water equations. It can be derived from the Navier–Stokes equations assuming hydrostatic pressure and uniform velocity distribution along water depth. The model can be presented in conservative form as (Abbott 1979):

$$\frac{\partial \mathbf{U}}{\partial t}+\frac{\partial \mathbf{E}}{\partial x}+\frac{\partial \mathbf{G}}{\partial y}+\mathbf{S}=0 \tag{1}$$

$$\mathbf{U}=\begin{pmatrix} h \\ uh \\ vh \end{pmatrix}, \qquad \mathbf{S}=\begin{pmatrix} 0 \\ -gh(S_{ox}-S_{fx}) \\ -gh(S_{oy}-S_{fy}) \end{pmatrix} \tag{2a,b}$$

$$\mathbf{E}=\begin{pmatrix} uh \\ u^2h+0.5gh^2 \\ uvh \end{pmatrix}, \qquad \mathbf{G}=\begin{pmatrix} vh \\ uvh \\ v^2h+0.5gh^2 \end{pmatrix} \tag{2c,d}$$

In the system of Eqs. (1) and (2), t = time; (x, y) = horizontal coordinates; (u, v) = depth-averaged velocities in x and y directions; h = local depth; S_{ox}, S_{oy} = bed slopes in

x and y directions; S_{fx} , S_{fy} = bottom friction terms in x and y directions defined by Manning formula; g = gravity. Equation (1) can be presented in another vector form as (LeVeque 2002):

$$\frac{\partial \mathbf{U}}{\partial t} + \nabla \mathbf{F} + \mathbf{S} = 0, \tag{3}$$

where vector $\mathbf{F}$ is defined as $\mathbf{Fn} = \mathbf{E}n_x + \mathbf{G}n_y$ and $\mathbf{n} = (n_x, n_y)^T$ is an unit vector.

In order to solve the mathematical model of free surface water flow (Eq. 3) a numerical method of partial difference equations integration has to be implemented. To integrate the model in space, one of the grid methods known as finite volume method (LeVeque 2002) is applied. This method requires to calculate the fluxes of mass and momentum through the computational cells (volumes) interfaces. It is ensured applying the Roe scheme (1981) of Godunov problem solution. Detailed description of the method is available in the literature (Toro 1997); therefore, it is not presented in this paper. The solution of Eq. (3) must be completed with time integration scheme. The two-step explicit scheme of finite difference method is used in solution algorithm. The computational code for numerical simulation of the rapid floods was prepared at Hydroengineering Department of Gdańsk University of Technology (Szydłowski 2003) and it has been tested for the flow in urban area problems (Szydłowski 2007).

The model is used here to investigate the influence of the type of boundary conditions imposed on the solid buildings walls on the quality of the numerical simulation results. Two types of closed boundary conditions can be implemented in solution of water flow problem – no-slip boundary condition or free-slip boundary condition. Both of them require the normal component of the velocity vector Vn to be equal to zero. If the no-slip boundary condition is imposed, the second velocity component Vs (tangential to the boundary) is also equal to zero. This condition is consistent with the idea of boundary layer, where the flow velocity is reduced to the velocity of the boundary. This type of condition is usually used in computational fluid dynamics for Navier–Stokes equations solution. For the solution of shallow water equations the free-slip condition is most widely imposed. There is no restriction for the tangential velocity component Vs to be zero in this approach. Only Vs derivative in normal direction to the boundary should be equal to zero. The schematic representation of both types of boundary conditions on the building wall is presented in Fig. 1.

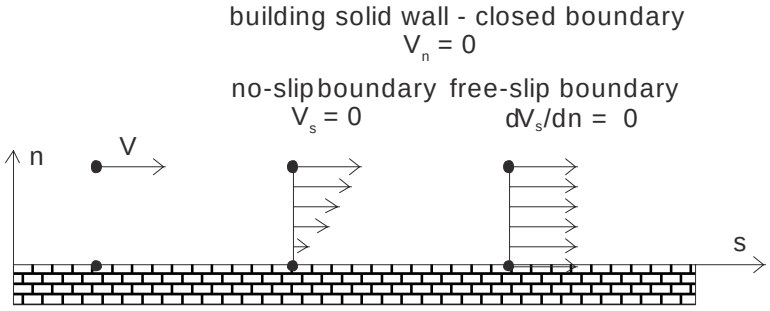

Fig. 1. Types of boundary condition on building wall.

3. Laboratory and numerical experiments

The experiments on urban rapid flooding were carried out in the hydraulic laboratory of Gdańsk University of Technology (Szydłowski 2007). For laboratory measurements, the hydraulic test stand was built (Fig. 2). It is composed of the reservoir (3.0 m long, 3.5 m wide) and the horizontal flat plate (3.75 m long, 3.0 m wide). The plate is separated from the reservoir with the wall (0.12 m wide). Three other boundaries of the plate are open. The 0.5 m wide rectangular breach in the wall can be closed and suddenly open. The gate opening process is automatic. During test experiments, the Manning friction coefficient of the plate and reservoir bottom was estimated as $n = 0.018$ m$^{-1/3}$s. Then, it was used for numerical simulation of flow on the plate surface.

The depth variation can be measured at the control points A1-A8 (Fig. 3). In order to simulate rapid flood in built-up, area the models of buildings are installed on the plate.

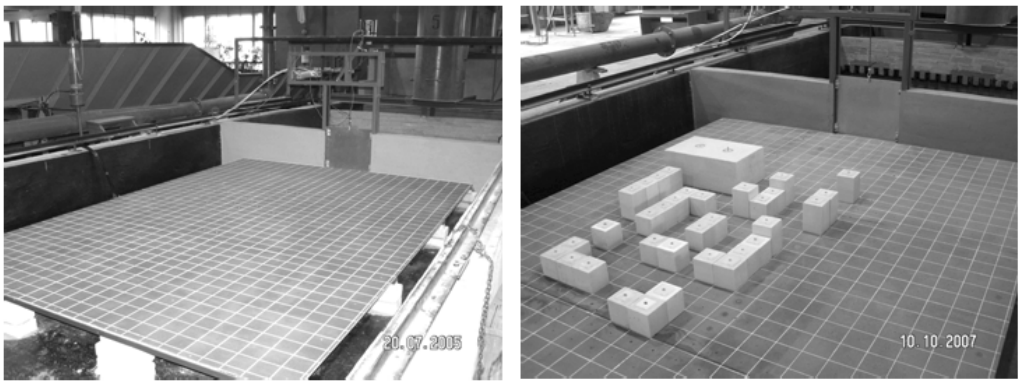

Fig. 2. General view of hydraulic test stand (left) and built-up area test case configuration (right).

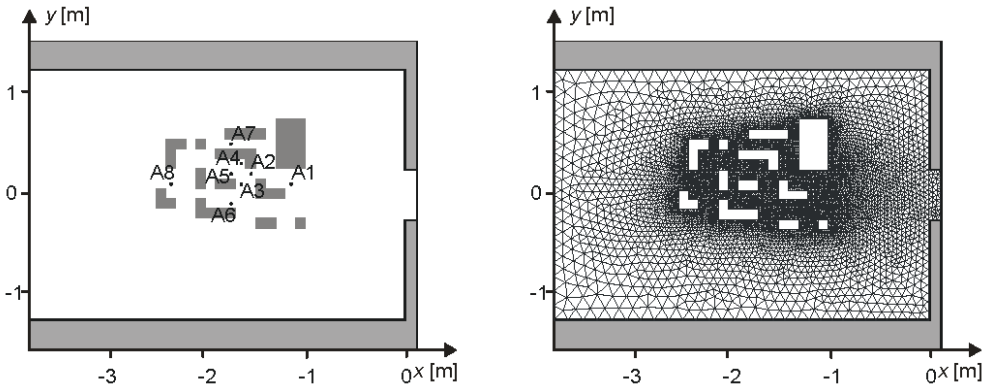

Fig. 3. Model city configuration, gauging points location (left) and part of numerical mesh (right).

Few configurations of building layout have been investigated during research. The unsteady water flow phenomenon known as the dam-break problem was simulated in the laboratory and calculated using the shallow water flow model with free-slip boundary condition imposed on buildings walls. It was observed (Szydłowski 2007), that, in general, computed water depth inside the built-up area is underestimated in relation to the measurements. It seems that this can be a result of insufficient urban area friction representation. In the shallow water model, only the bottom friction is incorporated and buildings walls friction is neglected. Considering the rapid flow between buildings it is clear that the influence of walls on the flow should not be neglected. The friction observed on the walls surface reduces the velocity in the vicinity of buildings walls. In this paper it is proposed to replace the free-slip boundary condition on the solid buildings walls with the no-slip boundary condition, it means, to artificially reduce the tangential velocity on the wall surface to zero.

In order to verify the influence of the type of boundary condition on the quality of the numerical simulation of urban rapid flood, the steady flow experiment has been carried out. The flow in unstructured buildings configuration is considered. In this test case, the streets have made the complex system of open channels bounded with solid walls of buildings models (Fig. 3).

In order to ensure the constant water discharge through built-up area, the gate was fully open during the experiment. The discharge was controlled by the Thompson weir installed at reservoir inflow section and it was equal to 43.56 l/s.

For numerical calculation the domain was covered by unstructured mesh composed of 13787 computational cells (Fig. 3). The mesh was refined between buildings. The size of computational cells around each building was about 0.02 m and it was increasing to 0.15 m near the boundaries of flow area. The steady flow laboratory experiment was simulated numerically starting from unsteady dam-break problem. As the initial condition, the hydrostatic state was assumed with water depth equal to 0.21

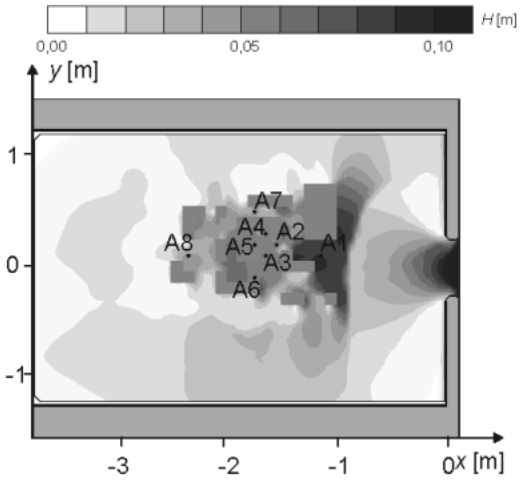

Fig. 4. Computed water depth for built-up area steady flow simulation with free-slip boundary condition.

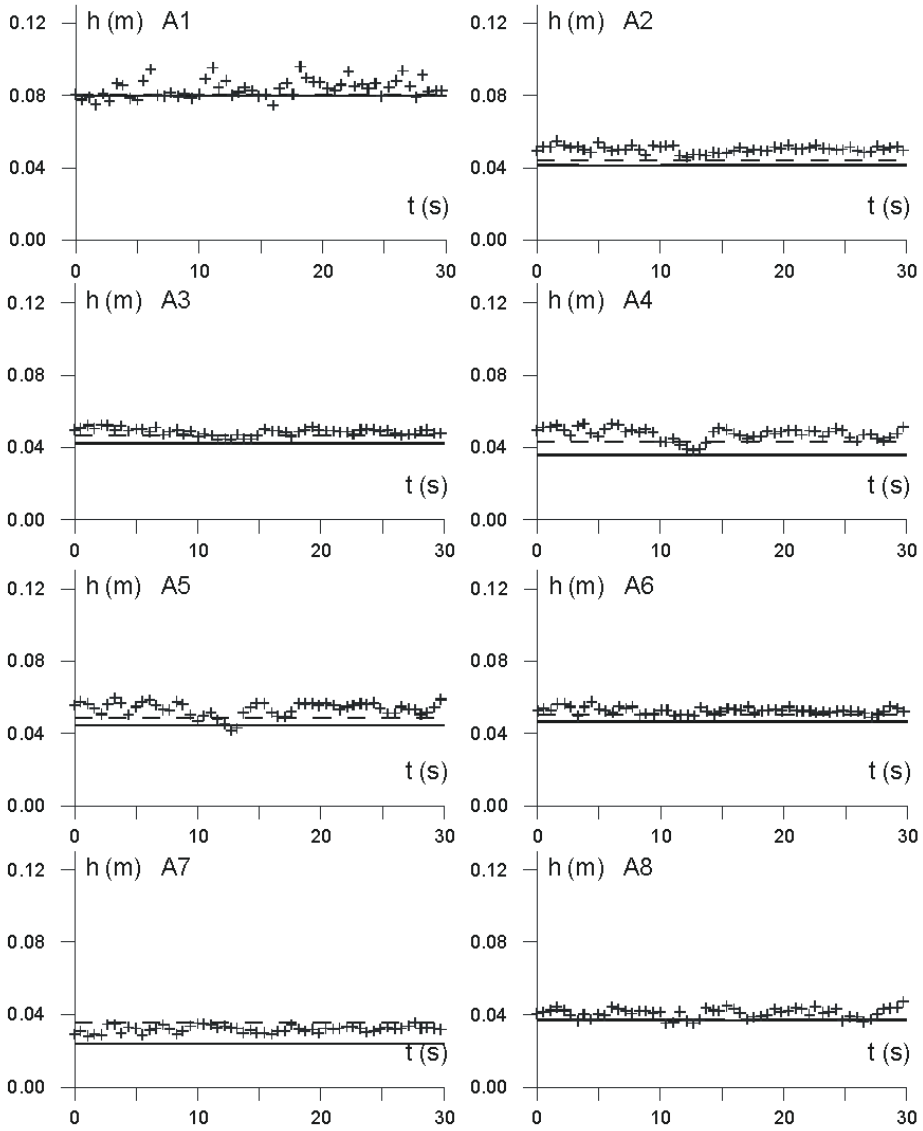

Fig. 5. Depth at the control points: (+ +) measured, (—) calculated using free-slip boundary condition, (– –) calculated using no-slip boundary condition.

and 0.0001 m in reservoir and flood plain, respectively. After about 30 s from the gate opening the steady state was achieved. The boundary conditions were imposed in accordance with experiment. Two side walls of the reservoir were treated as closed boundaries. Additionally, the reservoir was supplied with constant discharge through the inflow section. At the open boundaries of the plate, the free outflow condition was imposed. The flow in built-up area was simulated two times. The first calculation was carried out imposing the free-slip boundary condition at the buildings walls, then the no-slip boundary condition was used in the simulation. The calculations were carried out with the time step $\Delta t = 0.001$ s. The total simulation time was equal to 60 s.

The distribution of computed water depth for steady state (t = 45 s after gate opening) is presented in Fig. 4. The flow structures simulated using free-slip and no-slip boundary conditions are very similar to each other and this type of results presentations makes comparison impossible.

The comparison between depth measurements and results of both calculations for 30 second period of steady flow is presented in Fig. 5. It can be seen that the depth calculated using the no-slip boundary condition (dash line) better fits the measurements (crosses) for the majority of the control points located between buildings than depth simulated imposing free-slip boundary condition (solid line).

4. Conclusion

In the urban rapid flood simulation, two types of boundary conditions can be implemented on the closed buildings walls – free-slip boundary or no-slip boundary. When the first type of boundary condition was imposed in the simulations, the underestimation of computed depth was observed in the previous research. It can be due to incomplete friction representation in water flow model in built-up area. It was proposed to impose the no-slip boundary condition on the buildings wall except for the free-slip boundary condition. The better agreement between computed and measured water depth was observed. It seems that the no-slip boundary condition can substitute (imitate) the wall friction, improving the quality of numerical simulations of rapid floods in urban areas using the shallow water equations as the mathematical model of flow.

References

Abbott, M.B. (1979), *Computational hydraulics: Elements of the theory of free-surface flows*, Pitman, London, 324 pp.

Jonkman, S.N., P.H.A.J.M. van Gelder, and J.K. Vrijling (2002), *Loss of life models for sea and river floods*. **In**: Wu *et al*. (eds.), Flood defence, Science Press, New York, 196-206.

Kelman, I., and R. Spence (2004), An overview of flood actions on buildings, *Engineering Geology* **73**, 3-4, 297-309.

LeVeque, R.J. (2002), *Finite volume method for hyperbolic problems*, Cambridge University Press, New York, 558 pp.

Roe, P.L. (1981), Approximate Riemann solvers, parameters vectors and difference schemes, *J. Comput. Phys.* **43**, 357-372.

Soares-Frazao, S., J. Lhomme, V. Guinot, and Y. Zech (2008), Two-dimensional shallow-water model with porosity for urban flood modelling, *J. Hydraul. Res.* **46**, 1, 45-64.

Szydłowski, M. (editor) (2003), Mathematical modelling of dam-break hydraulic effects, *Monographs of Water Management, Committee of Polish Academy of Science*, 22, Warsaw, 170 pp. (in Polish).

Szydłowski, M. (2007), Mathematical modelling of flood waves in urban areas, *Monographs of Gdańsk University of Technology*, 86, Gdańsk, 149 pp. (in Polish).

Tan, W.Y. (1992), *Shallow Water Hydrodynamics Mathematical Theory and Numerical Solution for a Two-Dimensional System of Shallow Water Equations*, Amsterdam, Elsevier, 434 pp.

Toro, E.F. (1997), *Riemann Solvers and Numerical Methods for Fluid Dynamics: A Practical Introduction (Hardcover)*, Berlin, Springer-Verlag, 592 pp.

Accepted November 13, 2008

CONTENTS

„Publications of the Institute of Geophysics, Polish Academy of Sciences" appears in the following series:

A – Physics of the Earth's Interior

B – Seismology

C – Geomagnetism

D – Physics of the Atmosphere

E – Hydrology (formerly Water Resources)

M – Miscellanea

Every volume has two numbers: the first one is the current number in the series and the second one (in brackets) is the consecutive number of the journal.

PUBLICATIONS OF THE INSTITUTE OF GEOPHYSICS
POLISH ACADEMY OF SCIENCES

E. HYDROLOGY

E-1 (295) Impact of climate change on water resources in Poland.
E-2 (325) Water quality issues in the Upper Narew Valley.
E-3 (365) Modelling and control of floods.
E-4 (377) Potential climate changes and sustainable water management.
E-5 (387) Computational modeling for the development of sustainable water-resources systems in Poland. US-Poland Technology Transfer Program.
E-6 (390) Environmental Hydraulics.
E-7 (401) Monographic Volume, Transport Phenomena in Hydraulics.
E-8 (404) Monographic Volume, Numerical Solutions of Two-Dimensional Mass Transport Equation in Flowing Surface Waters.
E-9 (405) Monographic Volume, Management of the Storage Reservoir Influencing the Protected Natural Environment – Upper Narew River System Case Study.

ISBN-978-83-88765-79-7

Visit our homepage:

http://www.igf.edu.pl/pl/publikacje/publs_inst_geophys_pas